Modelling and Analysis of Rotary Airborne Wind Energy Systems – a Tensile Rotary Power Transmission Design

PhD Thesis

Oliver Tulloch

Wind and Marine Energy Systems Centre for Doctoral Training
Department of Electronic and Electrical Engineering
University of Strathclyde, Glasgow

April 24, 2021

This thesis is the result of the author's original research. It has been composed by the author and has not been previously submitted for examination which has led to the award of a degree.

The copyright of this thesis belongs to the author under the terms of the United Kingdom Copyright Acts as qualified by University of Strathclyde Regulation 3.50. Due acknowledgement must always be made of the use of any material contained in, or derived from, this thesis.

Signed: *O. Tulloch*

Date: April 24, 2021

Abstract

Airborne wind energy is a novel form of wind power. Through the use of lightweight wings and tethers it aims to access locations out of reach to current wind harvesting devices, at a lower cost and with a lower impact on the environment. There are multiple airborne wind energy systems currently under development, one group of these, referred to as rotary systems, use multiple wings networked together to form rotors. This thesis presents an analysis on the design and operation of rotary systems, with a particular focus on the power transmission from the airborne components down to the ground. There are various power transmission methods used for rotary systems, among them tensile rotary power transmission uses multiple networked tethers held apart by a small number of rigid components to transfer torque from a flying rotor down to a ground station.

The aim of this research is to improve the design and operation of rotary airborne wind energy systems that incorporate tensile rotary power transmission, and to assess system performance based on mathematical modelling and test data. It focuses on the Daisy Kite system design, a rotary system, being developed by Windswept and Interesting. Included in this thesis work is the development of three mathematical representations to support systematic analysis and design improvement. The first representation, a steady state model, is used to analyse rotary system design. The second and third models are dynamic representations of varying complexity. Also included is an experimental campaign conducted on the Daisy Kite in collaboration with Windswept and Interesting. Field tests are carried out on nine different Daisy Kite prototypes at their test site on the Isle of Lewis, Scotland. Measured data is collected for the various prototype designs

under different operating conditions. The measured data is used to assess the reliability of the three mathematical representations. This allows the models to be validated and compared to one another in terms of their accuracy and computational efficiency. During the experimental campaign several design and operational improvements are made that increase the power output and lead to more reliable operation. The mathematical representations are used to identify key design factors and to optimise rotary system design. Improved understanding and design of the rotary airborne wind energy system has been achieved through this holistic investigation.

Contents

List of Figures

List of Tables

Nomenclature

Acronyms

AR   Aspect Ratio

Re   Reynolds Number

AWE   Airborne Wind Energy

AWES Airborne Wind Energy System

BEM   Blade Element Momentum

CFD   Computational Fluid Dynamics

HAWT Horizontal Axis Wind Turbine

HTOL Horizontal Take-Off and Landing

KPS   Kite Power Systems

LCOE Levelised Cost of Energy

LTA   Lighter Than Air

NREL National Renewable Energy Laboratory

NTM   Normal Turbulence Model

RMSE Root Mean Square Error

RRP   Rotating Reeling Parotor

TRPT Tensile Rotary Power Transmission

UHMWPE Ultra High Molecular Weight Polyethylene

VESC Vedder Electronic Speed Controller

VTOL Vertical Take-Off and Landing

W&I   Windswept and Interesting

WATTS Wind Airborne Tethered Turbine System

Reference Frames

$(\mathbf{e}_x^a, \mathbf{e}_y^a, \mathbf{e}_z^a)$ Ring reference frame unit vectors   m

(x_w, y_w, z_w) Wind reference frame

(x_t, y_t, z_t) Tether reference frame

$(x_a, y_a, z_a), (x_b, y_b, z_b)$ Ring reference frames

Symbols

α Angle of attack   *deg*

β Elevation angle   *deg*

$\gamma, \gamma_a, \gamma_1, \gamma_2$ Tether attachment angles   *deg*

δ Torsional deformation   *deg*

δ_{crit} Torsional deformation for maximum torque transmission   *deg*

Δt Time step used within numerical integration   *s*

Δl_t Change in tether length   *m*

ζ Power harvesting factor

η Distance along the tether   *m*

θ Rotational position   *rad*

t_x^r, t_y^r, t_z^r	Tether point component vectors in the ring reference frame	m
$\dot{\theta}$	Rotational velocity	rad/s
$\ddot{\theta}$	Rotational acceleration	rad/s^2
$\boldsymbol{\theta}$	Vector of TRPT rings rotational positions	rad
$\dot{\boldsymbol{\theta}}$	Vector of TRPT rings rotational velocities	rad/s
$\ddot{\boldsymbol{\theta}}$	Vector of TRPT rings rotational accelerations	rad/s^2
λ	Tip speed to wind speed ratio	
λ_t	Tether speed to wind speed ratio	
μ	Air dynamic viscosity	kg/ms
ρ	Air density	kg/m^3
σ_{max}	Maximum allowable stress	N/m^2
τ	TRPT radius to rotor radius ratio	
φ	TRPT section tether length to radius ratio	
ψ	Wind shear exponent	
ω	Rotational velocity	rad/s
A	Swept area	m^2
$AeroP$	Power output of a rotor	W
$AeroQ$	Torque produced by a rotor	Nm
$AeroT$	Thrust produced by a rotor	N
b	Wing span	m
c	Aerofoil chord length	m
C	Distance between tether attachment points projected onto one ring plane	m

C_D Drag coefficient

C_{D_t} Tether drag coefficient

C_{f_t} Tether skin friction coefficient

C_L Lift coefficient

C_{L_t} Tether lift coefficient

C_p Power coefficient

$C_{p,\,max}$ Maximum Power Coefficient

C_Q Torque coefficient

C_T Thrust coefficient

d Tether diameter m

D Drag force N

$\mathbf{e}_{F_D,\tau}$ Unit force vector along the tether

$\mathbf{e}_{F_D,\phi}$ Unit force vector tangential to the TRPT radius

$\mathbf{e}_{F_L,\tau}$ Unit force vector perpendicular to $\mathbf{e}_{F_D,\tau}$ and $\mathbf{e}_{F_D,\phi}$

$\mathbf{e}_t$ Tether unit vector

$F_{a,x}^t, F_{a,y}^t, F_{a,z}^t$ Tether aerodynamic force components in the tether reference frame N

$F_{D,\tau}$ Tether aerodynamic force acting tangential to the TRPT radius N

$F_{D,\phi}$ Tether aerodynamic force acting along the tether N

$F_{L,\tau}$ Tether aerodynamic force acting perpendicular to $\mathbf{F}_{D,\phi}$ and $\mathbf{F}_{D,\tau}$ N

F_t Tether force N

F_t^y Tether force component tangential to TRPT radius N

F_x Total axial force magnitude N

$F_{x_{max}}$	Maximum axial force	N
$\mathbf{f}_D$	Function to calculate the tether aerodynamic force	
$\mathbf{f}_S$	Function to calculate the spring force	
$\mathbf{f}_{ext}$	External force vector	$N,\ Nm$
$\mathbf{F}_a$	Aerodynamic force vector of a tether in the wind reference frame	N
$\mathbf{F}_a^t$	Aerodynamic force vector of a tether in the tether reference frame	N
$\mathbf{F}_{D,\tau}$	Tether aerodynamic force vector acting tangential to the TRPT radius	N
$\mathbf{F}_{D,\phi}$	Tether aerodynamic force vector acting along the tether	N
$\mathbf{F}_{L,\tau}$	Tether aerodynamic force vector acting perpendicular to $\mathbf{F}_{D,\phi}$ and $\mathbf{F}_{D,\tau}$	N
$\mathbf{F}_t$	Tether force vector	N
G	Glide ratio, lift force to drag force	
G_{eff}	Effective glide ratio, lift force to drag force (including tether drag)	
$GenQ$	Generator torque	Nm
H_{ref}	Reference height	m
H_z	Height	m
J	Moment of inertia	kgm^2
$\mathbf{J}$	Moments of inertia matrix	kgm^2
k	Torsional stiffness	Nm/rad
kr	Ring stiffness	N/m
kt	Tether stiffness	N/m
$\mathbf{k}$	Torsional stiffness matrix	Nm/rad
l_s	Distance between adjacent TRPT rings	m

l_t	Tether length	m
$l_{t,x}, l_{t,y}, l_{t,z}$	Vector components of a tether in the wind reference frame	m
lk_D	Lift kite drag force	N
lk_L	Lift kite lift force	N
lk_T	Lift line tension	N
L	Lagrangian function	
$\mathbf{l}_s$	Vector of section lengths within a TRPT	m
$\mathbf{l}_t$	Vector of tether lengths within a TRPT	m
m	Mass	kg
$\mathbf{M}$	Mass and inertia matrix	$M, \ kgm^2$
N_r	Number of rings	
N_t	Number of tethers	
$p_{A,x}, p_{A,y}, p_{A,z}$	Vector components of point A in the wind reference frame	m
$p_{B,x}, p_{B,y}, p_{B,z}$	Vector components of point B in the wind reference frame	m
P	Power	W
$\mathbf{p}$	Force vector applied to a TRPT	$N, \ Nm$
$\mathbf{p}_A, \mathbf{p}_B$	Tether attachment point vectors in the wind reference frame	m
Q	Torque	Nm
Q_{loss}	Torque loss due to tether drag	Nm
$\mathbf{Q}_{ext}$	Torque vector applied to a TRPT	Nm
R, R_1, R_2	Radius	m
$\mathbf{R}$	Vector of ring radii within a TRPT	m

S	Wing area	m^2
t	Time	s
t_x, t_y, t_z	Tether point component vectors in the wind reference frame	m
T	Kinetic energy, Tension	J, N
$\mathbf{t}$	Tether point vector in the wind reference frame	m
$\mathbf{t}^r$	Tether point vector in the ring reference frame	m
$\mathbf{T}_{rw}$	Transformation matrix from ring reference frame to wind reference frame	
$\mathbf{T}_{tr}$	Transformation matrix from tether reference frame to ring reference frame	
$\mathbf{T}_{tw}$	Transformation matrix from tether reference frame to wind reference frame	
$\mathbf{u}$	Position vector	m
$\dot{\mathbf{u}}$	Velocity vector	m/s, rad/s
$\ddot{\mathbf{u}}$	Acceleration vector	m/s^2, rad/s^2
V	Potential energy	J
V_a	Apparent wind speed	m/s
$V_{a,\tau}$	Apparent velocity of wind that is tangential to the TRPT radius	m/s
$V_{a,\phi}$	Apparent velocity of wind that is parallel to the tether	m/s
$V_{a,x}, V_{a,y}, V_{a,z}$	Apparent wind vector components in the wind reference frame	m/s
V_{ref}	Wind speed at reference height H_{ref}	m/s
V_w	Ambient wind speed	m/s
V_z	Wind speed at height H_z	m/s
$\mathbf{V}_a$	Apparent wind speed vector in wind reference frame	m/s

$\mathbf{V}_{a,\tau}$	Apparent tether velocity vector that is tangential to the TRPT radius	m/s
$\mathbf{V}_{a,\phi}$	Apparent tether velocity vector that is parallel to the tether	m/s
$\dot{x}$	Axial velocity of a TRPT ring	m/s
$\mathbf{x}$	Axial position vector	m
$\dot{\mathbf{x}}$	Axial velocity vector	m/s

Acknowledgements

This work has been made possible by a great many people. Without them I would have found this task far more arduous and, more importantly, much less enjoyable.

Firstly, I thank my supervisor Hong Yue for providing me with excellent guidance and advice throughout this PhD. She has steered me in the right direction often displaying incredible amounts of patience, allowing me the freedom to explore while nudging me back on course when the tangents got a little too long. Without her comments and corrections much of this thesis would be unintelligible. Also, I thank my second supervisor Julian Feutchwang for the numerous philosophical conversations and his essential observations.

I thank Rod Read for developing the Daisy Kite design. Rod has been vital to the experimental progress achieved, he has manufactured all the prototypes in his loft and tested them on his croft. He has always been on hand to provide crucial discussions around design and operation, it is difficult not to be inspired by the enthusiasm and dedication that he has for the world of airborne wind energy! Along with Rod, my thanks go to his family Kirsty, Findlay and Cameron mainly for letting me steal Rod away from them but also for the outstanding hospitality that they have extended to me every time I visit, often with an entourage of inquisitive academics, students or family members.

There are numerous colleagues that have helped me over the last few years. In particular Mehrad, whom I thank for the countless discussions and continual head scratching

over the modelling of tensile rotary power. The wisest move I ever made was to sit at the desk next to him! I also thank all my fellow PhD students, past and present, of the Wind and Marine CDT. They have made my time at Strathclyde all the more enjoyable.

Lastly, and by no means least, I thank my wife, Josie. Who's unwavering love and support over the course of this PhD has kept me afloat. She has had to endure the worst of my never–ending complaining. I am not sure who is more relieved, me or her, that I can now write THE END.

"The use of means never before heard of for the doing of things never before done, cannot fail to excite considerable interest; and the more especially so if the objects accomplished wear any features of public utility"

GEORGE POCOCK

THE AEROPLEUSTIC ART

Chapter 1

Introduction

This thesis details an investigation into rotary airborne wind energy systems (AWES). It includes an experimental campaign on the Daisy Kite design, being developed by Windswept and Interesting Ltd (W&I), and the development of three rotary kite system mathematical models. The systems design and operational characteristics are analysed based on data from field tests and simulations using the developed mathematical representations. This introductory chapter provides details on the motivation for this thesis, the aims and objectives, its contributions to knowledge and a brief summary of its contents.

1.1   Motivation of Research

Airborne wind energy (AWE) is a relatively new form of wind power. The motivation behind AWE is to reduce the cost of wind energy and to operate in locations that are out of reach to horizontal axis wind turbines (HAWT). It is envisaged that this will be achieved by using less material, compared to HAWT, and by reaching higher altitudes, where stronger and more consistent winds are present. The AWE industry is still in its infancy and there are many prototypes currently under development, creating a wide variety of unique designs. At present there is no consensus within the industry as to which system architecture is most advantageous for power generation.

Previous literature focuses primarily on two system architectures, often referred to as fly–gen and pumping cycle systems. Fly–gen systems use a series of turbines mounted on a rigid wing. As the wing flies through the air the turbines generate electricity, this is transmitted down the tether to a ground station. Pumping cycle systems fly a wing, in figure of eights or circles, to reel a tether off a drum on the ground. As the drum rotates electricity is generated. Once the maximum tether length is achieved the tether must be reeled back onto the drum, consuming a portion of the power generated in the reel out phase.

A less explored AWE system architecture is the rotary design. Rotary AWES use multiple wings networked together, often forming rotors similar to that of HAWT. The flight paths of networked wings are constrained, this can lead to more simple control requirements. It can also result in lower amounts of tether drag, improving the devices efficiency. Of particular interest are rotary AWES that use multiple tethers to transfer torque from the flying rotor down to the ground station, referred to as tensile rotary power transmission (TRPT). TRPT allows for continuous power generation while having the generator located on the ground, therefore, keeping the airborne components lightweight. Several small scale AWE prototypes that use TRPT have been manufactured and tested, however, the design and operating characteristics of TRPT systems are relatively unexplored in the academic literature. No analysis on the dynamic behaviour of a TRPT system has taken place. This work is motivated by the desire to further the understanding of the design and operation of rotary AWES that use TRPT.

1.2   Aims and Objectives

The aim of this research is to improve the design and operation of rotary AWES that incorporate TRPT, and to assess the system performance based on mathematical modelling and test data. It will focus on the Daisy Kite system design being developed by Windswept and Interesting Ltd (W&I). To achieve this, this thesis is broken up into three main areas of research.

1. **Development of mathematical models** – To better understand the working principles of rotary AWES and to improve their design, mathematical representations will be produced. This will include a dynamic representation of the power extraction and transmission. A focus will be made on the TRPT modelling and its analysis in static and dynamic modes.

2. **Construction and testing of a small-scale prototype** – To assess the suitability of the mathematical model a small–scale Daisy Kite prototype will be designed, manufactured and tested. Empirical data must be obtained as there are no other AWES similar to the Daisy Kite for which experimental data is available. With the experimental data, the accuracy of the mathematical representations can be evaluated, and the models improved.

3. **Model–based system analysis of rotary AWES** – At present a small scale 500W Daisy Kite system has been produced. This prototype was developed through several experimental campaigns to refine the device into its current form. The developed mathematical models will be used to conduct a system analysis. This will include a sensitivity analysis to identify the most crucial design factors. An improved system design based on this analysis will be proposed.

1.3   Contribution to Knowledge

Rotary AWES are very different to most AWE devices currently under development. In particular, TRPT allows for continuous power generation while keeping the heavier components, mainly the generator, located on the ground. Many aspects of rotary designs have received very little research attention, especially TRPT. The main contributions to knowledge of this thesis are:

- An experimental campaign on the Daisy Kite system detailed in Chapter 3, including the testing of nine different prototype configurations. This has resulted in a comprehensive experimental data set for a rotary AWES that utilises TRPT.

- The development of three rotary AWES models based on the Daisy Kite design and described in Chapter 4. The first is a steady–state representation, the second two are dynamic representations of varying complexity. These are the first dynamic representations of a TRPT system.

- Within Chapters 3 and 5 key design drivers and several operational characteristics of rotary AWES, that incorporate TRPT, are identified. These are primarily found through model based analysis of the systems performance, including a sensitivity analysis. Observations made during the experimental campaign along with measured data are also used to identify them.

- A refined Daisy Kite system design, given in Chapter 5, based on simulation results from the steady–state mathematical model.

1.4   Outline of Thesis

This thesis is structured as follows:

Chapter 1 – Introduction

Chapter 1 sets out the main motivation behind this thesis, the aims and objectives, its contributions to knowledge and provides a brief overview.

Chapter 2 – An Overview of Airborne Wind Energy and Rotary Airborne Wind Energy Systems

In Chapter 2, relevant background information on AWES and their advantages over horizontal axis wind turbines (HAWT) are given. A classification system for the multitude of different AWES designs is introduced along with an overview of the most developed concepts and the leading industrial companies. The group of concepts referred to as rotary AWES are introduced and their main components detailed, with particular attention given to the power transmission from the airborne wings down to the ground stations. This chapter is concluded by setting out some of the major challenges that face the AWE industry.

Chapter 3 – Experimental Campaign and Design Improvement on Rotary Airborne Wind Energy Systems

Chapter 3 details an experimental campaign that was conducted, in collaboration with W&I, on a rotary AWES, the Daisy Kite. Several different prototype Daisy Kite systems were tested as part of the campaign, the design of each is given. The design improvements that were made over the course of the field tests are also described. Finally the operating characteristics, that were identified through observations during the experimental tests, are detailed.

Chapter 4 – Model Development for Tensile Rotary Power Transmission Systems

In Chapter 4, mathematical representations of the Daisy Kite are given. Three different system models are developed. The first is a steady–state representation, the second two are dynamic representations of varying complexity. The focus of these representations is on the novel tensile rotary power transmission (TRPT) method used to transmit power harvested at the airborne rotor down to the ground station. The complex and less known operational behaviour of TRPT and the torque loss due to tether drag within it have motived the development of these mathematical models.

Chapter 5 – Simulations and Analysis of Rotary Airborne Wind Energy Systems

Chapter 5 presents analysis of the simulation and experimental results. The measured data from experimental tests are used to assess the accuracy of the developed mathematical models. This comparison leads to improvements being made to the dynamic representations. The two dynamic mathematical representations are compared and the more appropriate one is selected for analysing the system further. A design review of the Daisy Kite system is undertaken, this results in a new system design being proposed and key design drivers being identified. The operation of the proposed system is explored which leads to the identification of the optimal combination of TRPT length, elevation angle and tip speed ratio. Finally this chapter is concluded by a discussion on

the Daisy Kite's operating characteristics.

Chapter 6 – Conclusions and Future Work

Chapter 6 summaries this thesis work. Conclusions are drawn and potential future work is identified.

Following this are the appendices and bibliography.

1.5 Publications and Dissemination

O. Tulloch, A. K. Amiri, H. Yue, J. Feuchtwang, and R. Read, "Tensile rotary power transmission model development for airborne wind energy systems," *Journal of Physics: Conference Series*, vol. 1618, sep 2020, https://doi.org/10.1088/1742-6596/1618/3/032001

O. Tulloch, A. K. Amiri, H. Yue, J. Feuchtwang and R. Read, "Modelling Studies on Tensile Rotary Power Transmission for Airborne Wind Energy Systems," in *Airborne Wind Energy Conference 2019 Book of Abstracts*, R. Schmehl and O. Tulloch, Eds. Delft University of Technology and University of Strathclyde, p.158-159, http://resolver.tudelft.nl /uuid:fa2a20d6-51d7-4f85-9f64-65b6df1ca3e0

O. Tulloch, H. Yue, J. Feuchtwang and R. Read, "Power transmission for rotary airborne wind energy systems," presented at *Wind Energy Science Conference 2019*, University of Cork, Ireland, june 2019, https://doi.org/10.5281/zenodo.3383986

O. Tulloch, R. Read, H. Yue and J. Feuchtwang, "Modelling and simulation studies of a networked rotary kite system," in *The International Airborne Wind Energy Conference 2017: Book of Abstracts*, M. Diehl, R. Leuthold, and R. Schmehl, Eds. Albert Ludwig University Freiburg and Delft University of Technology, p.39, http://resolver.tudelft.nl/ uuid:9213be48-e3d3-4ac6-92ca-09874c302eda

Chapter 2

An Overview of Airborne Wind Energy and Rotary Airborne Wind Energy Systems

This chapter gives a brief overview of the airborne wind industry and a detailed introduction to rotary airborne wind energy systems. Airborne wind energy systems (AWES) use tethered aircraft to harness wind power in locations and at altitudes beyond the reach of current market leading wind energy technologies. It is envisaged that by doing so, and by using less material, they will reduce the cost of wind energy. Section 2.1 begins by providing a review of airborne wind energy (AWE), the motivation for AWE and a classification system for the range of devices currently being developed are introduced. Industry trends are highlighted before three of the more developed AWES are detailed, a basic analysis on the power output of an AWE device is given.

This work has focused on the rotary class of AWES. Section 2.2 gives on overview of rotary AWES. The main components that form a rotary system are identified, followed by an introduction to the different power transmission methods that are used to transmit the power, harnessed by the airborne components, down to a ground station. Existing rotary AWES prototypes are then described. Section 2.3 goes on to provide a review of rotary AWES, presenting the motivation for their continued development and providing

a qualitative analysis of the different rotary AWE prototypes. The main challenges that the AWE industry faces are presented in Section 2.4. Section 2.5 presents the conclusions from this chapter.

2.1   Airborne Wind Energy Overview

Humans have been using kites to harness the power in the wind for millennia. It is unknown exactly when and by whom the kite was invented, it is widely credited to China and to Lu Ban (also Gongshu Ban), who in around 500 BC constructed a flying magpie using silk and pieces of bamboo [21]. The Chinese developed kites for a wide variety of applications. Often those applications were motivated by military needs. Examples include sending signals and messages, delivering bombs and even lifting people. Kites were first invented to perform useful tasks, whereas modern kites are mainly seen as kids play things. The Oxford English Dictionary [22] defines a kite as:

> *"A toy consisting of a light frame, usually of wood, with paper or other light thin material stretched upon it; mostly in the form of an isosceles triangle with a circular arc as base, or a quadrilateral symmetrical about the longer diagonal; constructed (usually with a tail of some kind for the purpose of balancing it) to be flown in a strong wind by means of a long string attached. Also, a modification of the toy kite designed to support a man in the air or to form part of an unpowered flying machine."*

The Oxford English Dictionary definition shows that kites are thought of primarily as toys, but it does at least acknowledge their ability to do useful work. Although kites were initially invented to perform useful functions their practical applications are currently limited. In recent history there are only a handful of examples of kites being used to perform useful tasks including: Benjamin Franklin's experiment in 1752, where he famously used a kite to show the electrical nature of lightning.

Just prior to this in 1749 Thomas Melvill and Alexander Wilson used a series of kites on the same line, a kite train, to measure the air temperature at different altitudes. In 1824 the Bristol school teacher G. Pocock published his book, *The Aeropleustic Art*, [1] which gives details of Pocock's invention, the Charvolant. Using simple kites and a modified horse drawn carriage, the Charvolant was able to reach speeds of 20 mph using solely wind power. An artists impression of the Charvolant can be seen in Figure 2.1. Pocock's *The Aeropleustic Art* was the first piece of literature that is dedi-

Figure 2.1: An artists impression of George Pocock's Charvolant [1].

cated to AWE. The late 1800's and early 1900's are often referred to as the golden age of kites [23], due to the rapid development they experienced during this period. This was due to kites being able to fulfil the requirements for the following interests; meteorological measurements, aerial photography, lifting men for military applications and powered human flight. Unfortunately for kites, the exploration of powered flight and the invention of the aeroplane in the early 20th century meant that they were no longer needed for these situations. More recently, the increase in popularity of kite sports has motivated the development of power kites capable of pulling humans at high speeds. Kite surfers have achieved speeds in excess of 60mph. The AWE industry is now at the forefront of using kites, tethered wings and other tethered airborne devices to harness the power in the wind for useful work.

2.1.1   Motivation Behind Airborne Wind Energy

Numerous AWES have now successfully harnessed wind power, many of them showcased
at recent airborne wind energy conferences, the two most recent being in 2017 and
2019 [4, 10].   There are several designs that have received over a decade of research
and development, but at present no system is commercially available.   To achieve a
commercially successful product AWE must demonstrate significant advantages over
current leading wind energy technology, in at least some locations and situations.   Over
the past four decades the three bladed horizontal axis wind turbine (HAWT) has come
to dominate the wind energy industry.   The AWE industry must therefore show that it
is able to produce systems that are cheaper, more reliable or can be deployed in places
that current HAWT's cannot.   The three main reasons behind continued investment in
AWE, as highlighted by Diehl [24], are:

1. The amount of power in the wind

2. The altitudes at which much of the wind resource is located

3. The potential low mass and cost per unit of usable power

Wind power is one of the few natural resources that has the potential to satisfy global
energy demand.   The International Energy Agency (IEA) calculates that total global
energy demand was 168PWh in 2018 [25].   Estimates of the potential for global wind
power can vary greatly.   Lu et al. [26] calculated that the global potential for onshore
and offshore wind, within 50 nm of the coast, is 840PWh per year.   This is based on
HAWTs with a hub height of 100m and excludes land areas unsuitable for HAWT, e.g.
areas of permanent snow or ice.   Castro et al. [27] concluded that 1TW, or 8.7PWh
per year, of wind power is available in the lower 200m with geographical and technical
constraints around areas suitable for wind turbine deployment, and the spacing and
conversion efficiency of turbines within wind farms.   Similar to these two studies, most
estimates only consider current HAWT technologies.

The wind resource is not uniformly distributed within the atmosphere, due to the bound-
ary layer caused by the Earth's surface, close to the Earth's surface wind speed generally

increases with altitude [28]. As current HAWT are restricted to the first few hundred
meters above the ground they are only able to access a small portion of the available
wind resource. Archer and Calderia [29] produced an assessment on the potential of
high altitude wind power. They presented the variation in wind power density with
geographical location and altitude, thus showing the potential for a device that is able
to reach altitudes beyond current HAWT. Marvel et al. [30] found that ground based
turbines could feasibly extract 400TW whereas high altitude devices could extract over
1800TW. Devices that are capable of reaching higher altitudes are able to access more
power dense regions of the wind resource. Relatively small scale AWE prototypes are
already able to reach altitudes of 400–500 meters.

AWES have more flexibility to alter their operational altitude, this allows them to op-
erate at or close to the optimal height. Bechtle et al. [31] assessed the optimal altitude,
in relation to wind speed and wind power density, over Europe. They show the increase
in available wind power, with maximum altitudes of 300m, 500m, 1000m and 1500m, at
the optimal height compared to a fixed height of 100m, around the hub height of many
HAWT's. The wind power density experienced 95% of the time increases by a factor of
2 over most of Europe when comparing the optimal altitude up to 500m to a fixed height
of 100m. This results in an increased amount of time spent above the cut–in conditions,
assumed to be a wind power density of 40W/m^2, and therefore greater capacity factors
for AWE devices compared to HAWT. The power available in the wind, and the ability
of AWES to harness that power, presents a compelling argument for their continued de-
velopment. However, given the success of the three bladed HAWT, AWES must prove to
be more advantageous to be considered desirable over them, for at least a few situations.

The third key motivation behind AWES is their low mass and predicted levelised cost
of energy (LCOE). Figure 2.2 shows Twing Tec's 20kW prototype next to a 20kW wind
turbine. The turbine weighs 20 tons compared to Twing Tec's device weighing only 1
ton [2]. The ground footprint of an AWES is also much smaller as there is no need
for concrete foundations to cope with the large tower bending moments. The rela-

Figure 2.2: TwingTec's 20kW prototype system next to a wind turbine with the same
rated power (28th August 2019). [2]

tively small mass and reduced foundations open up locations where current HAWT are
not suitable. For example; in remote locations with limited access and in regions that
experience extreme cold where it is not possible to lay concrete foundations. The ad-
vantages listed so far all lead to the prediction that AWES will reduce the cost of wind
energy. In the UK's most recent contracts for difference round offshore wind came in
at £39.65/MWh [32], for wind farms that are due to come online in 2023/24. S.Mann
forecasts that AWE could achieve a LCOE of £30/MWh by the year 2030 [33], showing
that AWE is predicted to become cost comparable and potentially cheaper than current
wind turbine technology.

A fourth motivation for AWE that could be added to Diehl's list above are the low
emission associated with AWE devices. By using less material compared to HAWT,
AWES have lower equivalent carbon emissions per unit of power produced. Predic-
tions have shown that AWES could be one of, if not the, cleanest method of elec-
tricity production in the future. AWES have predicted equivalent carbon emissions of
5.6g/kWh of CO_2 compared to 11.5g/kWh for a wind turbine of similar rated power [34].

KiteKraft estimate CO_2 equivalent emissions of 3.3g/kWh for their 20kW device [35] and they envisage that this will reduce further for larger systems. Table 2.1 shows the emissions associated with various energy sources used for electricity generation [18]. The lower values within the range for hyrdo power are associated with run–of–river systems, this is the only current electricity generation method to have similar emissions to those predicted for AWE. As the social and political will to reduce the impact that we have on our environment continues to increase, the low emissions associated with AWES could become a key advantage moving forward.

Energy Source	g-CO_2/kWh
Coal	975.3
Oil	742.1
Gas	607.6
Biomass	35 - 178
Nuclear	24.2
Solar	13.6 - 250
Wind	9.7 - 123.7
Hydro	3.7 - 237

Table 2.1: Emissions found during life cycle assessments for different energy sources used in electricity generation [18]

The potential AWE has to access locations that are out of reach of today's HAWT's, coupled with their reduced mass, lower emissions and cheaper LCOE clearly shows the motivation behind their continued research and development.

2.1.2 Device Classification

The abundance of the wind resource and the continued reduction in the cost of HAWT's, have meant that in the last four decades wind energy has increased its presence within the global energy mix. In the first round of the UK's contracts for difference scheme in 2015 offshore wind had a strike price of £115 per MWh [36], in the most recent round in 2019 the price had fallen to £40 per MWh [32]. In 2018 overall wind energy capacity reached 591GW, a 9% increase from 2017, and produced 5.5% of global electricity supply [37]. Despite the advantages highlighted previously AWE has not seen the same growth as the wider wind industry, there is not yet a commercially available AWES for utility scale power generation. Unlike the rest of the wind industry, with the three bladed horizontal axis turbine, there is no consensus within AWE as to the optimal

system architecture. Over 60 organisations are directly involved in AWE research and
development [4,38]. This has resulted in there being a wide range of concepts at various
levels of maturity. What follows is a brief overview of the current AWE industry and the
most advanced concepts, more detailed reviews are given in [39–41]. It is noted that this
work focuses on systems designed for electricity production. There are several AWES
that are designed for other applications, e.g. ship propulsion, that are not considered
here.

In general AWES consist of three main components:

1. A ground station

2. At least one wind harvesting device e.g. kite, wing or rotor

3. At least one tether that mechanically, and sometimes also electrically, connects
   the wind harvesting device to the ground station

AWES can be classified depending on several design factors relating to these three main
components.

Location of Electricity Generation

The main difference between AWES is the location at which electricity is generated.
This can either be at the ground station, referred to as Ground–Gen, or in the air,
referred to as Fly–Gen. With Ground–Gen, electricity is produced by transmitting the
aerodynamic forces generated by the airborne components to the ground via tethers.
These forces are then used to turn a generator within the ground station. German
based Enerkite [42] are developing a Ground–Gen system. They have a 30kW proto-
type that has achieved several hundred hours of operation and are in the process of
designing and manufacturing a 100kW product. Although most Ground–Gen devices
use a fixed ground station, some utilise moving ground stations. For example the Kite-
Gen Carousel concept [43], where wings pull multiple small vehicles around a track. The
relative movement between the small vehicles and the track is used to power multiple

15

generators.

Fly–Gen systems carry electrical generation equipment on their airborne components.
This usually consists of one or more generators, each attached to a rotor, mounted on a
wing or other device able to support their weight. The generated electricity is then trans-
mitted to the ground station via a conducting tether. German based kiteKRAFT [44]
are developing a Fly–Gen concept, they are currently working on a 20kW prototype
system.

Airborne Component Construction

Another key difference between AWES is the construction of the wind harvesting device.
These can vary from being completely soft, similar to those used in various kite sports,
to completely rigid, more similar to a glider. Netherlands based kitepower [45] are
developing a soft wing Ground–Gen system and are currently testing a 100kW prototype
system. Ampyx Power [5], also based in the Netherlands, use a rigid wing for their
Ground–Gen system. They have a 20kW prototype and are currently manufacturing a
150kW prototype.

Flight Path

The flight path of the airborne components varies considerably between designs. The
most simple is a path that is aligned to the tether, as used by the Laddermill concept
proposed by Ockels and the Delft University of Technology [46]. The most common
flight path is referred to as crosswind, in this case the airborne device is flown across
the wind either in a figure of eight or circular path. A crosswind flight path is used
by the majority of AWES currently under development. A third potential flight path,
that is similar to crosswind circular paths, is a rotational path. Systems that employ
a rotational flight path incorporate multiple networked wings with a common axis of
rotation or a rotor, similar to a HAWT.

Multi–Wing Systems

Most AWES have been designed to use a single wing but there are several designs that
incorporate multiple wings. These multiple wings can either be flown independently and
tethered to a common ground station, or networked together in the air such that each
directly influences the others flight path. Kiteswarms [47] are a German based company
developing a Ground–Gen system that uses networked rigid wings with crosswind flight
paths.

Rotary Systems

Rotary AWES use rotors or several wings networked together to form rotors. These ro-
tors then use the principle of autorotation to provide both aerodynamic lift and torque.
This torque can be converted into electrical power in the air or transmitted to the
ground station via the tethers. It is noted that all rotary AWES use a rotational flight
path but not all AWES that rely on a rotational flight path are rotary systems. Section
2.2 provides an in depth review of rotary systems. UK based Windswept and Inter-
esting (W&I) are developing a Ground–Gen rotary device, the Daisy Kite. They have
manufactured and tested numerous prototype systems, rated less than 1kW, and have
achieved several hundred hours of testing.

Lighter Than Air Systems

There are also a number of AWES that rely on aerostatic lift as opposed to aerodynamic
lift to remain airborne. They use large balloons or shrouds filled with a lighter than
air gas, such as helium, to provide lift. They are referred to as lighter than air (LTA)
systems. US based Altaeros Energies produced and tested a 25kW LTA system [48].

Take-off and Landing

A final major variation between AWES is the take–off and landing procedures used.
Most Fly–Gen devices are able to use vertical take–off and landing (VTOL) , similar to
drones. In this case the generators are used as motors to power the rotors, providing
the lift required to safely take–off and land the wing, US based Windlift [49] use this
method. Another proposed method is to use horizontal take–off and landing (HTOL),
similar to an aeroplane. In this case the wing is accelerated on a runway, until sufficient
aerodynamic lift is created, allowing for take–off. The wing can either be accelerated
by onboard motors or by a catapult or winch. The runways can be utilised for landing
with ground space requirements reduced by slowing the wing down more quickly once
it is grounded, similar to methods used on aircraft carriers. This system is used by
Ampyx Power.

Some AWES also use stationary masts to lift the wing away from surrounding structures
into higher wind speeds. It can then, hopefully, generate sufficient aerodynamic lift for
take–off. For landing, the wing is winched back onto the same mast. German based
SkySails [50] have successfully used this method to launch and retrieve a 2MW soft
wing for ship propulsion [51]. Some AWES designs use a rotating mast. In this case the
mast rotates while the wing is winched out or in from the end of the mast. EnerKite use
a rotating mast for take–off and landing. Many smaller systems use a lift kite that is
launched and then used to pull the main airborne components into the air. For landing
the components are winched back onto the ground, the lift kite ensuring sufficient lift,
to oppose the systems weight, is always maintained. This method is common for rotary
AWES. The Daisy Kite, developed by W&I [52] uses this method. For LTA systems the
buoyancy of the device allows the tethers to be winched out or in, in a controlled manner.

Figure 2.3 shows a chart of AWES classifying them based on these categories, this chart
has been adapted from [3]. It is noted that the AWE industry is in its infancy, therefore
system designs are under constant review. Future design alterations will likely cause
several concepts to move between categories. As the industry progresses classification
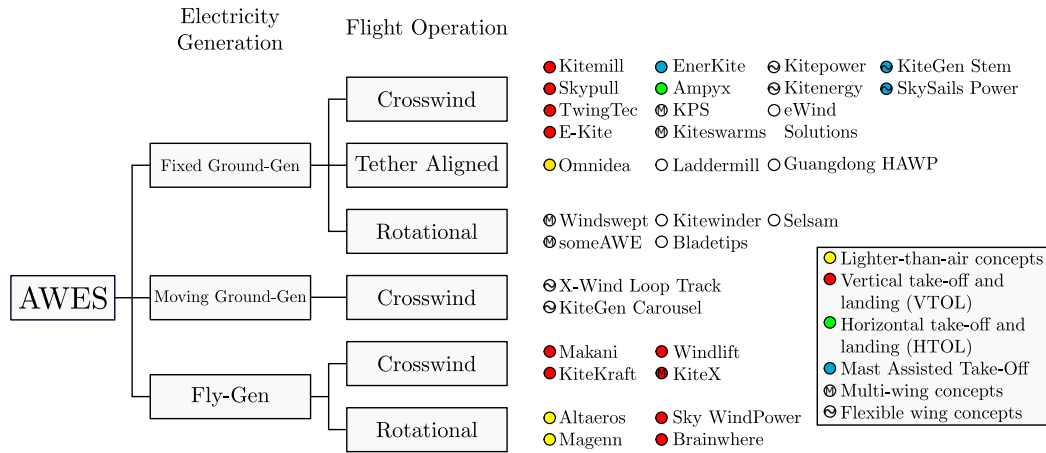
Figure 2.3: Classification of AWES, adapted from [3]

categories may be altered, added or removed if an industry consensus is reached regarding a particular design variable.

2.1.3   Airborne Wind Energy Industry Trends

A series of observations can be made regarding trends within the AWE industry by analysing the chart shown in Figure 2.3. Firstly Ground–Gen systems are much more abundant than Fly–Gen. Of the 31 systems included in Figure 2.3 only 8 are Fly–Gen, the remaining 23 are Ground–Gen. Ground–Gen devices have the advantage of keeping the majority of the heavy components on the ground, making the airborne parts of the device lightweight and relatively simple. In comparison Fly–Gen systems have much greater flying mass as the generators are located on the airborne components. They also have thicker heavier tethers, as they must incorporate a conductive element to transmit the electricity down to the ground station. Although this makes their airborne components much bulkier, complicated and increases the tether drag it allows for VTOL, as the turbines can be used to provide thrust. The only Fly–Gen systems that do not use VTOL are LTA systems. Several Ground–Gen designs include small motors and rotors on the airborne components so that they are able to utilise VTOL. This of course adds weight and negates some of the advantages of having the generator located on the

ground. The success of VTOL is shown by Figure 2.3 as it is the most popular method
for take–off and landing.

The most popular systems are fixed Ground–Gen designs that use a crosswind flight
path. These systems are often referred to as pumping cycle or yo–yo systems. As the
wing fly's in a crosswind motion the tether is reeled off a drum on the ground, this
rotates the drum which is connected to a generator and therefore generates electric-
ity. Once a defined tether length has been reached the wing is flown back towards the
ground station and the tether is reeled back onto the drum, hence the term pumping
cycle/yo–yo. This generation method results in non–continuous power generation as
a small amount of power must be consumed during the reel in phase. Despite this
pumping cycle systems are by far the most abundant generation method with 16 of the
systems shown in Figure 2.3 employing it. Pumping cycle systems have also dominated
the contributions to AWES from the academic community. The two AWE books [38,53],
published in 2013 and 2018, combined have 65 Chapters, with contributions from mul-
tiple authors. 60% of these Chapters are focused on pumping cycle systems. It is noted
that the wing does not need to fly in a crosswind motion to operate in pumping mode,
for example Bladetips Energy employ a pumping cycle with a rotational flight path.

In can also be seen from Figure 2.3 that the majority of devices use rigid wings. In the
past many AWE developers have used soft wings due to their low cost, crash surviv-
ability and lightweight structure. Although many developers continue to use soft wings,
there has been a slight trend towards rigid wings, especially as the wing size increases.
This is due to the improved aerodynamic performance and relative ease of control of
rigid wings. Several systems also use wings that are a hybrid of soft and rigid materials.

LTA systems in the first instance may appear to hold a number of advantages over
other systems. Crucially, they are able to remain airborne in light winds, their take–off
and landing procedures are fairly straight forward and, due to their bouncy, are more
inherently stable than most other AWES. However, they require very large volumes of

a lighter than air gases, usually helium, which is very expensive. The need for sizeable
shrouds makes it difficult for LTA systems to reach larger scales. This is reflected by
the relatively small number of LTA systems currently being developed.

2.1.4   Airborne Wind Energy State of the Art

Although there are numerous different concepts for AWE, two designs have dominated
AWE research in this nacent industry. These are pumping cycle and crosswind Fly–
Gen systems. Both systems were first analysed by Loyd [54] who termed them lift and
drag generation modes respectively. The development of crosswind Fly–Gen systems
has been led by US based Makani Power. They manufactured and tested a 600kW
prototype, the highest rated power of any AWE device to date. Pumping cycle systems
currently dominate the AWE industry, both in terms of number of organisations devel-
oping prototypes, as shown in Figure 2.3, and the quantity of academic research [38,53].
Ampyx Power and UK based Kite Power Systems (KPS) developed rigid wing pumping
cycle systems. These three companies represent some of the most developed prototypes.
More detail on the systems developed by Makani Power, Ampyx Power and KPS are
given in the following sections.

Makani Power

US based Makani Power had the largest and most developed crosswind Fly–Gen system.
Founded in 2006, Makani built and tested a series of wings. Starting with a 2kW
Ground–Gen system that used a soft wing and generated power using a pumping cycle,
they progressed to a crosswind Fly–Gen 600kW prototype. This is the highest power
rating of any AWES for electricity production flown to date. Their 600kW system uses
eight 80kW turbines mounted on a 26m rigid kite, allowing for VTOL. Once airborne
the kite flies in a circular path to generate power, it can fly at altitudes of up to 300m

using the 500m long tether. In August 2019, using a floating spar buoy, they tested their system offshore. The 600kW kite was flown off the coast of Norway in water depths of over 200m. Figure 2.4 shows an image from the system during these tests. In early 2020 it was announced that Makani would no longer be supported by technology company Alphabet. Shortly afterwards Makani Power came to an end, they did however release

Figure 2.4: Makani's M600 being tested off the coast of Norway (August 2019) [4]

a wealth of material on their device including a technical report and flight controls available on their website [55]. They have also released a non-assertion pledge for their patents.

Kite Power Systems

KPS, founded in the UK in 2011, developed a multi kite pumping cycle system. They produced a 40kW prototype and had began manufacturing a 500kW system. Their

Figure 2.5: A rendered image of Kite Power Systems 500kW system

design used two rigid wings in anti–phase, as one wing is reeling the tether out the other is being reeled in. Therefore as one is reeled in, consuming power, the other is reeling out generating power. The aim of using this two wing set up is to achieve a more constant power output for the system as a whole. Using a hydraulic power take off the mechanical power is smoothed before being converted into electricity. Figure 2.5 shows an im-

age of KPS's proposed 500kW system design. In early 2020 Norway based Kitemill,
who are also developing a rigid wing pumping cycle system, acquired KPS's intellectual
property [56].

Ampyx Power

Ampyx Power, founded in 2008, is a spin–out from the Delft University of Technology.
Their device is a rigid wing Ground–Gen system. Similar to KPS, Ampyx Power employ
a pumping cycle generation mode. However, the Ampyx Power wing flys in figures of
eight as power is generated. They are in the process of developing a 150kW prototype
system, AP3. AP3 will have a wing span of 12m and be capable of flying up to an
altitude of 450m. Their AP3 device uses a 20m platform for take–off and landing. The
wing is launched using a 17m catapult to get the wing, from stationary, up to a speed
of 20m/s before the wing leaves the platform. With the wing downwind, the tether is
then used to winch the wing up to an altitude of 250m, similar to a conventional glider
launch. To land, the wing is decelerated in the air using the winch and tether before
coming into contact with the platform. A series of springs and dampers are then able
to bring the wing to a standstill on the platform. Two rotors on the wing also provide
additional propulsion for these HTOL procedures. AP3 will be used as a demonstrator
unit, designed to prove the fully automatic operation of their system. The next iter-
ation, AP4, will be Ampyx's first commercial product. Figure 2.6 shows a rendered
image of AP4 deployed on a floating platform.

There are several companies at similar stages of development to Makani Power, KPS
and Ampyx Power. Many are in the process of developing and manufacturing larger pro-
totypes with rated powers in the range of hundreds of kW. Although there are multiple
organisations developing systems, some for over a decade, there is not yet a commer-
cially available AWES.
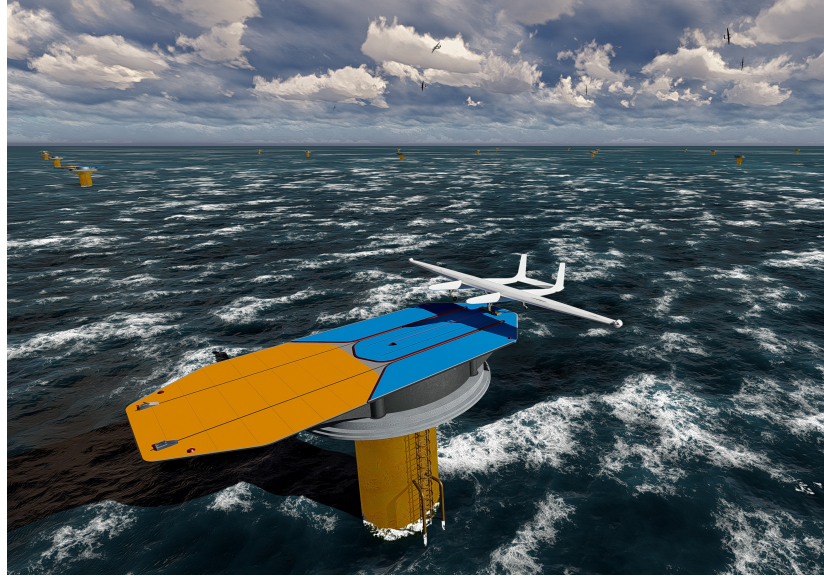
Figure 2.6: Computer generated image of Ampyx Powers AP4 [5]

2.1.5 Airborne Wind Energy Basic Analysis

There have been various studies analysing the potential of a tethered wing to generate power. The first such analysis was conducted by Loyd [54] in 1980. Using analytical models Loyd defines an upper bound for the power harnessed by a tethered wing. This analysis is particularly applicable to pumping cycle and crosswind Fly–Gen systems, referred to as lift and drag modes by Loyd. Loyd's simple analytical models are still widely used and they show the key aspects that must be considered when analysing an AWES. Loyd's analysis first highlights the importance of crosswind flight. Crosswind flight is the term used to describe the motion of a wing as it flys across the wind, perpendicular to the wind vector. In doing so the apparent speed of the wing can be much greater than the wind speed, therefore the power produced by a wing flying crosswind will be much greater. Almost all AWES being developed today use crosswind motion, as shown in Figure 2.3. The power output from a tethered wing using Loyd's analysis can be found from (2.1), [57].

$$P = \frac{1}{2}\rho V_w^3 \cos^3\beta A C_L G^2 \frac{4}{27} \tag{2.1}$$

where ρ is the air density, V_w the wind speed, β the systems elevation angle, A the kite
area, C_L the wings lift coefficient and G the wings glide ratio. The glide ratio is the
ratio between the wings lift and drag coefficients. A simple calculation based on Loyd's
analysis can be used to show the importance of tether drag. To incorporate tether drag
into (2.1), an effective glide ratio G_{eff} defined by (2.3) [58] is used in place of the basic
glide ratio.

$$G = \frac{C_L}{C_D} \tag{2.2}$$

$$G_{eff} = \frac{C_L}{C_D + \frac{C_{Dt}dl}{4A}} \tag{2.3}$$

where C_D is the wings drag coefficient, C_{Dt} is the tethers drag coefficient, d is the tether
diameter and l is the tether length . Using (2.1), (2.2) and (2.3) an example calculation
is performed, Table 2.2 shows the wing and tether parameters that are used in this
calculation, an operating altitude of 400m is used.

Air Density, ρ	1.225 kg/m^3
Wind Speed, V_w	12m/s
Wing Area, A	35m^2
Elevation Angle, β	20°
Kite Lift Coefficient, C_L	1.5
Kite Drag Coefficient, C_D	0.1
Tether Length, l	425m
Tether Diameter, d	0.016m
Tether Drag Coefficient, C_{Dt}	1.2

Table 2.2: System parameters used in calculations based on Loyd's analysis. These are
chosen to be representative of Makani Power's 600kW AWES prototype [19]

Neglecting tether drag results in a predicted power output of 1.5MW, once the tether
drag is included this becomes 613kW, a reduction of 60%. This simple calculation
shows the importance of incorporating tether drag into the analysis of an AWES. The
importance of tether drag is also highlighted in [24, 57, 59, 60]. Due to the significant
impact that tether drag has there are several AWE concepts that have been proposed

specifically aimed at reducing it [61,62]. These include fairing tethers, giving them more
aerodynamic profiles [63], and using multiple tethers configured such that large sections
of tether are held stationary [64, 65]. Many of the systems aimed at using multiple
tethers to reduce drag also use multiple wings.

In his initial analysis Loyd also includes the weight of the kite and tether. However it
has since been shown that the weight of the system can often be neglected for initial
power estimations as the lift generated by the wing is orders of magnitude greater than
the weight of the airborne components [24,57]. It is noted that this assumption is de-
pendant on the system architecture and not valid for low wind speeds where the lift
generated is often low. The power estimation given by (2.1) is therefore a reasonable
first approximation for the power output from a wing that flys in a crosswind motion
for both pumping cycle and Fly–Gen systems.

From the outset academic research and company prototypes have focused on pumping
cycle and Fly–Gen systems. Therefore, these power generation methods are far move
developed than other AWE designs. However, even with several companies developing
them for over a decade, no system is currently commercially available. There are al-
ternative AWES architectures which have received very little research and development
even though they show considerable promise.

This section has given a brief overview of the airborne wind industry; the motivation
behind its continued research, an introduction to classification of the different design
configurations, an update on the current industry with an introduction to some of the
more developed prototypes and a basic analysis of the most common AWES. The re-
mainder of this chapter focuses on the group of concepts referred to as rotary AWES.

2.2   Rotary Airborne Wind Energy Systems

A rotary AWES, or kite turbine, is an AWE device that exploits the principle of autorotation to provide both aerodynamic lift and torque. This section gives a detailed overview of rotary AWES. A brief history of rotary AWE is presented in Section 2.2.1 before the main components within rotary AWES are introduced in Section 2.2.2. Section 2.2.3 briefs several power transmission methods for rotary AWES, including tensile rotary power transmission (TRPT). There are several rotary systems currently under development, these are described in Section 2.2.4.

2.2.1   A Brief History of Rotary Airborne Wind Energy Systems

The invention of rotary kites is first documented in the patent granted to Ansboro in 1891 for a revolving kite [66]. Although the principle by which they work, referred to as autorotation, was not understood until the 1910's. Autorotation is the term that defines the self–sustained rotation of a rotor in a wind field without any externally applied torque [67]. As air passes through the rotor, the aerofoil profile of the blades results in the generation of lift and drag. This provides a torque force causing the rotor to rotate and a thrust force that can be used to support the rotors weight. This principle came about during the development of helicopters in the early 20th Century, as it allows them to land in the event of engine failure. As the helicopter loses altitude, air passes through the rotor causing autorotation, this generates lift which slows the aircraft's descent. The principle of autorotation led to the development of the autogyro or gyroplane, a type of aircraft that uses an unpowered rotor to provide lift [68]. In this case forward velocity is usually generated by an engine connected to a small push prop rotor mounted at the rear of the craft. The forward propulsion causes air to pass through the inclined main rotor, leading to autorotation, allowing the autogryo to sustain flight. It is also possible to have an unpowered autogryo.

During World War II the Germans developed the Focke Achgelis 330 (FA–330) [6]. The FA–330 was an unpowered autogyro that was towed behind submarines, the forward motion of the submarine provided the necessary forward velocity. It was used to lift a pilot up to a height of 400 feet. This allowed the pilot to see 25 miles and relay any sightings of enemy vessels to the submarine below using an inbuilt telephone. A photo of a FA–330 is shown

Figure 2.7: Image of a Focke Achgelis 330 on display in the RAF museum Cosford, Shropshire [6]

in Figure 2.7. This is the first example of a rotary AWE device, although not used for electricity production the FA–330 was an unpowered tethered airborne device that used autorotation to provide useful work. There were around 200 FA–330's built, making them the most widely produced rotary AWES to date.

In terms of rotary AWES used for electricity production, a handful of patents appeared in the late 1970's that detail the use of rotary kites to generate electricity. These appeared during the 1970's oil crisis, as more interest was being paid to alternative forms of energy. Poulsen [69] proposed a rotor on the end of a shaft inclined upwardly in the downwind direction from the generator. This recognised the ability of the rotor to generate torque but also supply sufficient thrust to maintain the shafts elevation angle. Fry and Hise [70] envisaged several vertical axis turbines in series on a single shaft. As this concept uses vertical axis turbines it does not rely on autorotation to remain airborne. Instead the top of the shaft must be connected to a device that is able to support the weight of the shaft and turbines. This could be a solid structure or, to be classified as an AWES, a LTA device could be used.

Fletcher and Roberts [71] proposed an airborne platform to harness the jet–stream winds. This became the first rotary AWES that was built and tested in Australia in

the 1980's [72]. This Fly–Gen design used pairs of counter rotating rotors, similar to a quad–copter, to generate power aloft. It was envisaged that the craft would be flown at very high altitudes in order to access the strong winds within the jet streams. Initial tests done at low altitudes and in wind tunnels were successful.

After this initial development of rotary AWES progression stagnated, the energy industry recovered from the oil crisis and the demand for alternative sources of energy receded. Widespread recognition of the environmental impact of energy production at the start of the 21st Century increased the level of research into sustainable sources of energy, resulting in progress in AWES and rotary systems once again.

2.2.2   Rotary Airborne Wind Energy System Components

As with any AWES, rotary systems comprise of three main components; a ground station, at least one wing and at least one tether. Many rotary AWES also utilise a lift kite to provide additional lift. What follows is a description of the main components for rotary systems and methods used in various rotary designs. Figure 2.8 shows a diagram of a rotary AWES highlighting these main components.

Rotor

A key component of any rotary AWES is the rotor. The rotor, though autorotation, is able to generate torque and lift, which are in turn used to generate electricity. In many cases the rotors are similar to helicopter or wind turbine rotors, as the wings are all connected to one central hub. A rotor can also be formed by networking multiple wings, that rotate around a central axis, together. In this case there is no central hub, instead the wings are connected, via light weight materials, at a given radius from the rotors axis of rotation. This type of rotor is shown in Figure 2.8 and is referred to as an open centre rotor.
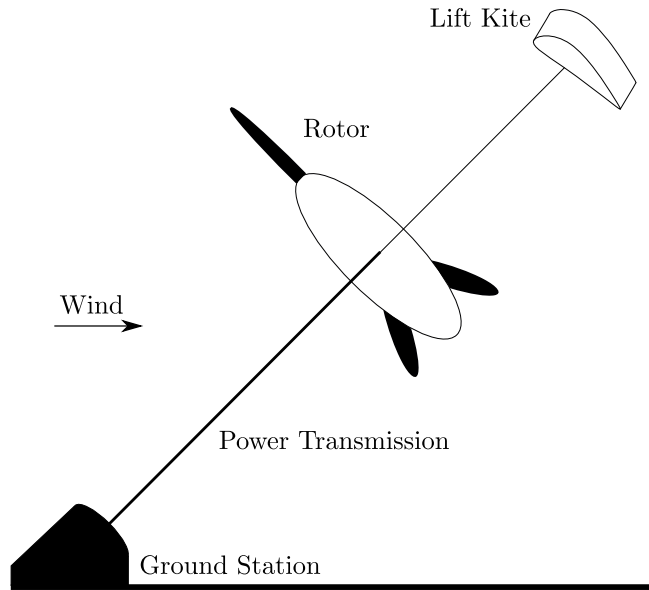
Figure 2.8: Diagram showing the main components of a rotary AWES

Similar to all AWES the wings can either be totally soft, rigid or a hybrid of the two.
Some rotary AWES designs use multiple rotors, in a few concepts a common shaft is
used for several rotors. Due to the use of a rotor for power harvesting, rotary AWES
share many similarities with HAWT in terms of how energy is extracted from the wind.

Ground Station

The ground station, as with all AWES, is the main point of contact with the ground.
However, it is not necessarily the only point of contact with the ground, several AWE
designs have multiple attachment points. The airborne components of a rotary AWES,
again, similar to all AWES, will be pulled towards the downwind side of the ground sta-
tion. Therefore, all tether attachment points on the ground must be able to stay aligned
with the wind direction. The ground station design is dependent on the design of the
systems airborne components. For systems that generate electricity on the ground, the
ground station will house the generator and much of the electrical infrastructure. The
ground station is also likely to incorporate the take–off and landing system.

Lift Kite

Many rotary AWES prototypes currently include a lift kite. For these systems it is often crucial for the take–off and landing process. On small systems and prototypes the lift kite is launched by hand, similar to a traditional kite launch. The most commonly used lift kites are passively stabilised single line kites, such as those used for kite aerial photography. Actively stabilised and controllable kites bring further advantages for take–off, landing and alignment of the whole system. Once airborne the lift kite is then used to pull the rest of the system into the air. A passively stable lift kite can be used to control the elevation angle and the downwind alignment of the system, by altering the lift kite used or by setting or actively altering its bridle lines the aerodynamic forces created can be changed. Depending on the power transmission used the lift kite can aid in the operation of the device by increasing the tension on tethers used for power transmission within the system. At present all rotary AWES prototypes are relatively small compared to other AWES. As rotary systems increase in size the take–off and landing process is likely to be altered so that it can be achieved autonomously, these new processes may or may not include a lift kite. Future larger systems may dispense with the lift kite altogether. However, it is envisaged that for small to medium scale rotary systems the lift kite will be crucial for take–off, landing and operational control.

2.2.3   Power Transmission for Rotary Airborne Wind Energy Systems

The power transmission takes the energy extracted at the rotor and transfers it down to the ground station. As with all AWES the energy transfer is a key component within rotary systems. To achieve the desired altitude it must be feasible and cost effective to transmit the power extracted back down to the ground. Altitudes of 500–600m are desirable, and given the necessary elevation angle, this results in power transmission lengths of over 1km. For rotary AWES there are several methods that are being developed to achieve this. Five proposed methods are introduced below.

Pumping Cycle

As described in Section 2.1.4 some of the most developed AWES use a pumping cycle. The tether is attached to a winch and generator at the ground station, the thrust from the rotor pulls the tether off the winch, generating power. Once a certain tether length is reached, it is wound back onto the winch, using the generator as a motor. The power extracted by the rotor is therefore transmitted down to the ground station as a tensile force within the tether. There are a number of advantageous that arise from using a rotor as opposed to a single wing for a pumping cycle AWES. Schutter et al. [73] highlight the simplified control requirements. The tether drag is also reduced as the tether remains more stationary compared to a single wing crosswind pumping cycle system [62]. Although pumping cycle generation is widely used within the AWE industry, very few rotary AWES utilise this method of power transmission.

Electrical

Similar to other AWES, rotary systems can use mechanical and/or electrical power transmission. Electrical power transmission for rotary AWES provides many of the same advantages and disadvantages as other AWE devices as detailed in Section 2.1.3. The main disadvantage being the requirement to have heavy electrical generation equipment located on the airborne components. The greatest advantage being the ease of take–off and landing utilising VTOL. Similar to rotary systems which use pumping cycle generation, rotary AWES that use electrical power transmission can result in reduced tether drag compared to single wing designs.

Shaft

Using a rotor to extract power from the wind produces torque. Therefore, similar to a wind turbine, the rotor can be mechanically connected to a generator to convert this torque into electricity. AWES that use electrical power transmission do this using very short shafts between the rotor and the generator on the aircraft. There are several ro-

tary systems that use the torque generated at the rotor for power generation, but locate
the generator on the ground. The torque must therefore be transmitted to the ground
station. The most intuitive method is to use a long lightweight hollow shaft, usually
made from carbon fibre. Shaft's are frequently used to transmit torque however, this
is mostly done over relatively short distances. By using a shaft the heavy components
are kept on the ground and power generation is continuous.

Belt Drive

Another method by which a rotary AWES has transmitted the power from the rotor
down to the ground is through the use of a belt drive, or rope drive. The tether is held
between two pulleys, one on the ground station the other just underneath the rotor.
The torque produced at the rotor is rotated by 90° so that the airborne pulley is driven
by the rotor. The tether is then pulled over this airborne pulley as it rotates. As this
happens the tether is also pulled over the ground station pulley causing it to spin. The
ground station pulley is coupled to a generator for electricity production. The use of
rope drives to transmit power over large distances was explored and used in the 19th
century [74, 75].

Tensile Rotary Power Transmission

The final method for transferring the torque from the rotor down to the ground station
is tensile rotary power transmission (TRPT). By using a series of networked tethers
held apart by a small number of rigid components it is possible to transmit torque. In
its simplest form a TRPT system resembles a rope ladder. Two tethers running straight
down the outside of several equally spaced rigid rods. If sufficient tension is applied to
the system then torque can be transmitted from one end of the tethers to the other.
There are multiple configurations of tethers and rigid components that can be used to
achieve a TRPT system. It shares many of the advantages of using a shaft, but it is
able to do so using less material and mass. A disadvantage however, is that with many

tethers passing through the air the aerodynamic drag will likely be greater than that
experienced by a shaft. The use of TRPT is investigated in more detail throughout this
thesis work.

These five methods for power transmission with rotary AWES are summarised in Table
2.3. Similar to other AWES power can be transferred electrically or using the tether ten-
sion. Additionally rotary systems can also transfer torque. Rotary AWES have received
very little research attention and as such these various power transmission methods have
also seen minimal development, in particular TRPT. Out of these five methods TRPT
is the only one, or a variation of it, that is not used in another application . Rotary
AWES are therefore the only example of TRPT. Given this and the various advantages
that TRPT has, as discussed in Section 2.3.2 and Chapter 5, this work focuses on the
research and development of TRPT.

Transmission Method	Description
Pumping Cycle	The thrust generated by the rotor reels the single tether off a drum on the ground. Once the maximum tether length is reached it must be winched back onto the drum by the motor/generator.
Electrical	The rotor is directly connected to an airborne generator. The electricity is transmitted down the tether to the ground station.
Shaft	Uses a lightweight hollow shaft to transfer torque generated at the rotor down to the ground station.
Belt Drive	The tether passes over two pulleys, one at the ground station connected to a generator and one in the air attached to the flying rotor. The torque generated by the rotor is rotated by 90° before being passed to the airborne pulley. As the rotor drives the airborne pulley, the tether is pulled over it which in turn drives the ground station pulley.
TRPT	A series of tethers are held apart by rigid components to form a shaft like structure. With sufficient tension applied to the tethers the system is able to transfer torque.

Table 2.3: Summary of the five power transmission methods used by rotary AWES.

2.2.4   Rotary Airborne Wind Energy System Prototypes

The previous two sections have introduced the main components that make up any
rotary AWES; a rotor, power transmission, ground station and often a lift kite. There
are several rotary AWES that are currently under development. Each of those with a
working prototype are introduced below:

The Daisy Kite

Windswept and Interesting Ltd. (W&I) have been developing the Daisy Kite since 2012.
The Daisy Kite uses one or more rotors all connected to a common TRPT. W&I have
manufactured and tested multiple prototypes with various configurations from a single
rotor using soft wings, as shown in Figure 2.9, to multiple rotors using rigid wings.
The multi–rotor versions stack the rotors up the TRPT, each rotor is above the rotor
upwind of it. Their largest prototype achieved a power output of 1.4kW [76], greater
than any other rotary AWES that employs TRPT.

The most recent W&I prototype uses six rigid wings, each with a span of 1m, attached to a carbon fibre ring with a radius of 1.5m. The TRPT consists of six tethers that are equally spaced around several carbon fibre rings. The rings are located at set distances along the tethers. Figure 2.9 shows a shortened version of this TRPT. A lift kite is used for take–off and landing and to provide addition tension to the TRPT during operation. W&I focus on creating networks, as described by W&I owner Read [77]. By networking wings and tethers together the system

Figure 2.9: Image of one of Windswept and
Interesting's Daisy Kite prototypes

passively stabilises the kites flight path. The multiple tethers also provide for greater
levels of redundancy and reduced control requirements. This thesis work concentrates
on the Daisy Kite design, more details on the systems architecture and its testing are
described in Chapter 3.

Rotating Reeling Parotor

The Rotating Reeling Parotor (RRP) is a
rotary AWES developed by Benhaïem, an
image of the RRP is shown in Figure 2.10.
A more detailed description of the system
can be found in [7]. The Parotor uses a
single rotor and TRPT. Its rotor consists
of eight kites equally spaced around a fly-
ing ring. The TRPT uses four tethers uni-
formly distributed around the rotors ring.
The other end of the four tethers are con-
nected to a second ring on the ground.
This ring is parallel to the ground. There-

Figure 2.10: Image of the Rotating Reeling
Parotor prototype [7]

fore, as can be seen in Figure 2.10, the flying kite ring and ground ring have different
axes of rotation. This results in the four tethers changing length as the system rotates.
Each tether has a winch at the ground ring end so that this can occur, this also pro-
vides a second mode of electricity generation. There are also several suspension lines
in addition to the four main tethers. The RRP relies on a lift kite for take–off, landing
and for support in the air. The small scale prototype shown in Figure 2.10 acted as a
proof of concept, this system is analysed by Benhaïem and Schmehl in [7].

Airborne Turbine

someAWE Labs S.L. are developing the rotary AWES shown in Figure 2.11(a). Their
system is very similar to the Daisy Kite. It uses a single rotor with four rigid blades.
The blades are connected to each other to form a square with a blade at each corner.
This rotor is directly connected to a TRPT to transmit the rotor torque to the ground
station. A lift kite is used for take–off, landing and to provide additional tension to the
TRPT during operation. The TRPT consists of eight tethers and a series of straight
carbon fibre rods. The TRPT can be seen in the image in Figure 2.11(b). The rods
are equally spaced up the system and positioned such that each rod is perpendicular to
neighbouring rods, with all rods perpendicular to the TRPT's axis of rotation. Four of
the tethers run straight down the outside of the rods, parallel to the axis of rotation.
Each of these tethers connects to every other rod. The remaining four tethers connect
to one end of every rod and therefore criss–cross their way up the system. This TRPT
geometry is very different to the ones used in the Daisy Kite and the RRP designs.
Having a number of tethers that do not start parallel to the axis of rotation gives the
system greater initial torsional stiffness. No relative displacement between adjacent
rods is needed to transmit torque between them. someAWE Labs S.L have built and
tested several configurations of this system and are currently working towards a power
output of 100W sustained for 100 minutes.

(a) Full prototype
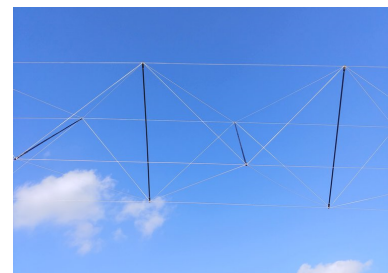
(b) TRPT system

Figure 2.11: Images of someAWE Labs S.L. prototype airborne turbine [8,9]

Kiwee One

KiteWinder are developing the rotary AWES, Ki-
wee One. Kiwee One is a 100W system, it weighs
less than 4.5kg and is designed to fit into a back-
pack to provide portable wind power. As shown in
Figure 2.12 it uses a two bladed rotor with a tail fin,
to keep the rotor pointing into the wind. As with
most rotary AWES it incorporates a lift kite. Kiwee
One is the only rotary AWES that uses a belt drive
form of power transmission, as described in Section
2.2.3. Kiwee One is available for purchase for €900
from KiteWinder [78]. This is the only openly available AWES.

Figure 2.12: Image of a KiteWinder's prototype, Ki-wee One [10]

Bladetips Energy

Bladetips Energy are developing a pumping cycle rotary AWES. Their system uses
a three bladed rotor to pull the tether off the ground based winch. As the name
suggests, and the image in Figure 2.13 shows, they only give the outer part of each
blade an aerofoil profile, the inner portion is a straight rod. Within any rotor the outer

sections of the blades generate the most torque,
therefore to keep weight down Bladetips Energy
only place aerofoils on this more efficient part of
the blade. Their design does not include a lift
kite for take–off and landing. These procedures are
achieved by powering/spinning the rotor such that
sufficient lift is generated to support its own weight.
Bladetips Energy are designing their system for al-
ternative purposes not just electricity production.
Their system is also designed to be used for telecom-

Figure 2.13: Image of Bladetips
Energy's prototype [11]

munications, surveillance and observation purposes.

38

Superturbine

Selsam Innovations have developed the Super-
turbine. The Superturbine uses multiple small
rotors all on a common shaft, as shown in Figure
2.14. By using multiple rotors on a single shaft
rotational speeds remain high removing the need
for a gearbox, a leading cause of wind turbine
failures [79]. Selsam Innovations have developed
multiple wind energy systems using this concept.
Several of these are AWES, similar to that shown
in Figure 2.14, as one end of the shaft is held aloft
by either a lift kite or a shroud/balloon filled with
a lighter than air gas. They have also developed
prototypes that use a tower to achieve the de-
sired altitude, Queen [80] provides an analysis of
one of these tower based systems.

Figure 2.14: Image showing one
of Selsam Innovations Superturbine
prototypes [12]

Wind Airborne Tethered Turbine System

Figure 2.15: Image of one of Sky Wind-
Power's WATTS prototype [13]

Sky WindPower are developing the
Wind Airborne Tethered Turbine System
(WATTS) for power generation. Their
system uses pairs of counter–rotating ro-
tors and generates electricity aloft. It can
therefore be powered for VTOL proce-
dures, similar to a drone. Sky WindPower
has manufactured and flown several pro-
totypes, one of these is shown in Figure
2.15. Due to the stationary tether it is envisaged that very high altitudes could be
reached as the tether drag will be small compared to many other AWES. This quad-

39

copter concept, initially develop by Roberts in the 1980's [72], aims to access the wind
resource within the jet stream.

The seven systems that have been briefly introduced within this section demonstrate
the large variation in rotary AWES design. As mentioned previously there are over 60
organisations researching AWE with limited consensus on the optimal system design,
this case is similar within rotary AWES. It can be seen from the seven rotary AWES
described above that the transfer of torque from the rotor to the ground station is the
most popular method of power transmission, four of the seven rotary designs opting for
this method. Of these four, three use TRPT: the Daisy Kite, RRP and someAWE Labs
S.L. It can also be seen that all but one of the systems, WATTS, are Ground–Gen.

This section has introduced rotary AWES. Their brief history was given before their
main components introduced. Existing rotary AWES prototypes have also been de-
scribed. A comparison between rotary and other AWES is given in the following section.

2.3   Review of Rotary Airborne Wind Energy Designs

This section highlights the motivation for continued research into rotary AWES, through
the comparison of the various rotary concepts with the current leading AWES designs.
It also provides a comparison of the rotary AWES systems introduced in Section 2.2.4.
Finally some of the many challenges that the AWE industry faces are introduced.

2.3.1   Motivation for Rotary Airborne Wind Energy Systems

Currently all rotary prototypes, described in Section 2.2.4, are of a relatively small scale
compared to other AWES prototypes. The power output achieved by rotary systems
is in the order of a few kW, whereas there are many AWES prototypes in the tens of
kW and a handful in the hundreds of kW power rating as shown in Section 2.1.2. As
previously stated the majority of AWE development has focused on pumping cycle and

crosswind Ground–Gen systems. This is shown by the number of companies developing
this type of system in Figure 2.3.

The second most developed systems are crosswind Fly–Gen devices, this is predomi-
nately down to the progress achieved by Makani power with their 600kW prototype.
These two generation methods were analysed by Loyd [54] in his initial assessment of
AWE in 1980. Since then many different concepts and ideas for AWE have been pro-
posed, one of these being rotary systems. There are a number of distinct advantages
that rotary AWES have over the two most developed concepts. Due to the number of
different rotary concepts that are being developed not every advantage listed is appli-
cable to all rotary designs. Three key advantageous that apply to most rotary AWES
are:

1. Ground–Gen systems with continuous power generation

2. No necessity for operational control systems

3. Networked structure leading to inbuilt redundancy making their flight control pas-
   sively stable

As shown in Section 2.2.4, almost all rotary AWES are Ground–Gen devices. This cou-
pled with their ability to continuously generate power gives them a distinct advantage
over most other AWES, especially pumping cycle and crosswind Fly–Gen devices. As
previously stated keeping the generator on the ground keeps the airborne components
as light as possible. The wing can be more simple as it does not need to support the
weight of heavy components. There is less danger posed by the airborne components,
a lighter wing has less potential to cause damage. If a fault occurs on the wing it is
simple and less expensive to replace. Similarly for Fly–Gen devices the tether must
conduct electricity, resulting in their tethers being heavier, more expensive and of a
greater diameter, which increases tether drag. The ability to generate power contin-
uously results in more simple power trains, reducing cost. Pumping cycle systems in
particular suffer from phased operating with periods of power consumption, this may be

41

overcome through using multiple devices in anti–phase, as proposed by KPS. However, this requires complex power systems or more sophisticated drive trains. KPS proposed a hydraulic drive train connected to two wings, the hydraulic system balances the power between the two wings so that the input to the generator can be more smooth. Continuous power output from the wings removes the need for these complex and costly systems.

Most AWES rely on sophisticated control systems to ensure that the wing remains airborne and follows the desired flight path. The modelling and control of AWES has received a large amount of research attention. With most AWE designs it is not possible to run a successful test flight until sensors and controllers are in place. Rotary AWES use kites that are networked together forming rotors. Therefore, the flight path of an individual kite is much more constrained. It is possible to form a network that physically sets the desired elevation and flight path of a network of wings. Thus removing the need for operational control and making it more simple to design, manufacture and test small–scale prototypes at a low cost. This is demonstrated by the multiple small scale rotary prototypes introduced in Section 2.2.4. Although rotary AWES have operated without any operational control [77], it will be necessary for controllers to be incorporated into larger scale systems. It is envisaged that due to their similarities with HAWT, rotary AWE systems will have similar operational strategies to HAWT. Therefore they will be able to utilise a number of the control strategies currently used for HAWT, e.g. pitch and yaw control.

The networking of wings not only reduces the operational control requirements it also makes the system more inherently stable and increases the systems redundancy. Several rotary designs use a network of wings and tethers. Individual wings and tethers can fail and the system is still able to operate, all be it in a reduced capacity. This increased redundancy allows for more flexibility regarding repairs and ensures that a catastrophic failure is less likely to occur. Read [77] describes the networking of wings and tethers and the advantages this brings in more detail.

A forth less explored advantage is around take–off and landing. As will be discussed in
Section 2.4 the reliable and safe launch and landing of AWES presents a challenge for
the AWE industry, particularly for Ground–Gen systems. Most Fly–Gen systems are
able to use the generators as motors to fly the wings up to the desired altitude, either
like a traditional aircraft using HTOL, or a drone using VTOL. At present most rotary
systems use a lift kite for take–off and landing, these also aid in the operation of the
devices by providing additional lift. It is envisaged that it will be possible to power the
rotors to provide the necessary lift for controlled take–off and landing, as is currently
used by the rotary system developed by Bladetips Energy. This has several advantages
over the take–off and landing methods proposed for other devices. For Ground–Gen
devices, as stated in Section 2.1.2, methods include: attaching small motors and rotors
for VTOL, using a winch and/or catapult to achieve sufficient velocity for HTOL and
using a mast to lift or rotate the wing until sufficient lift is generated for launch. These
methods add weight to the airborne components, require a point of no return and can
make for complex ground stations. By running the generator as a motor or using a
lift kite, rotary AWES have demonstrated controlled take–off and landing with minimal
additional components and no added weight to the rotor itself.

Rotary AWES present several advantages over the leading AWES designs, many of
these are qualitative based on observations from prototype testing. To quantify the
advantages of rotary AWES more research is required. Table 2.4 lists the published
scientific papers dedicated to rotary AWES. In 2017 there were 116 published articles
or book chapters on AWE [81], only four of these were focused on rotary systems. It is
noted that in the recent AWE book [38], published in 2018, three out of the 30 chapters
focused on rotary systems showing an increase in interest, there were no chapters in
the initial AWE book [53], published in 2013. Five of the eight publications shown in
Table 2.4 focus on the Fly–Gen system proposed by Sky WindPower. Given the poten-
tial benefits that rotary systems have, more research is required to better understand
these designs, in particular of Ground–Gen rotary systems. It is only through gaining
knowledge on their performance and limitations that more reliable comparisons can be

drawn between them, other AWES and wind harvesting devices.

Authors	System	Year	Title
Benhaïem and Schmehl	Parotor	2018	Airborne Wind Energy Conversion Using a Rotating Reel System.
Read	Daisy Kite	2018	Kite Networks for Harvesting Wind Energy
Roberts	SkyWind Power	2018	Quad-Rotorcraft to Harness High-Altitude Wind Energy
Schutter et al.	Rotokite/ Autogyro	2018	Optimal Control of a Rigid-Wing Rotary Kite System for Airborne Wind Energy
Mackertich and Das	SkyWind Power	2016	A Quantitative Energy and Systems Analysis Framework for Airborne Wind Energy Conversion using Autorotation
Rancourt et al.	SkyWind Power	2016	Design Space Exploration of Gyrocopter-Type Airborne Wind Turbines
Rimkus and Das	SkyWind Power	2013	An Application of the Autogyro Theory to Airborne Wind Energy Extraction
Roberts et al.	SkyWind Power	2007	Harnessing High-Altitude Wind Power

Table 2.4: Scientific publications on rotary AWES.

2.3.2 Discussion of Existing Rotary Airborne Wind Energy Systems

A comparison and discussion based on the seven rotary AWES introduced in Section 2.2.4 is given below. These systems have mostly been developed through experimental experience, by manufacturing and testing multiple prototypes. Each device is at a differing stage of development, there is limited research and openly published data on their performance, as demonstrated by the list of scientific literature in Table 2.4. Therefore a quantitative comparison between them is not possible at present. What follows is a qualitative comparison and discussion between the various rotary AWES.

Sky WindPower's WATTS, shown in Figure 2.15, is the only Fly–Gen rotary AWES prototype. It shares many of the same advantages and disadvantages as other Fly–Gen AWE designs. Housing the generators in the air results in heavy airborne components

and requires the tether to conduct electricity. Equally as the size of the generator in-
creases its power capacity per unit mass will decrease [82]. Therefore, as the system size
increases the weight of the generator will become more of an issue. However, it allows
for VTOL, making the take–off and landing procedures relatively straight forward com-
pared to other rotary designs. A key advantage that this system has over the leading
crosswind Fly–Gen AWES is the reduced tether drag. Using multiple rotors attached
to a stationary frame means that the tether remains relatively static during operation.
This lower tether drag is a key driver for the system, when Roberts first proposed the
design he was able to feasibly target altitudes within the jet stream.

Bladetips Energy's rotary pumping cycle solution, shown in Figure 2.13, again shares
many similarities with crosswind pumping cycle systems. Although it is a Ground–Gen
system, allowing for lightweight wings, it results in non–continuous power generation,
due to the cyclic nature of its operation. Similar to the Sky WindPower concept, due to
the more static tether, the relative tether drag is reduced compared to crosswind pump-
ing cycle designs. Both Bladetips Energy and Sky WindPower use VTOL, providing
scalable take–off and landing procedures. The procedures can be automated and has
already been demonstrated with other larger AWES, e.g. Makani Power. In contrast,
other rotary AWES do not have such robust launch and landing methods at present. An
additional advantage that Bladetips Energy's design has is their potential to alter the
size of the rotor. Using an open centre rotor means that the radius the wings operate
at can be altered. The swept area of the rotor can therefore be altered which leads to
several possible advantages. It could be used for operational control to limit system
power output in winds above rated speeds. It also means that the rotor size could be
reduced for take–off and landing, minimising the footprint of the ground station.

WATTS and Bladetips Energy's are similar to the leading AWES designs of crosswind
pumping cycle and crosswind Fly–Gen. They use the same methods of power generation
and are therefore subject to similar advantages and limitations. The other five rotary
AWES have more unique architectures compared to leading AWES concepts. All five

other designs offer continuous power with ground based generation.

Kitewinder's Kiwee One achieves continuous generation with a Ground–Gen system by using a rotor and lopped rope drive. The company have been able to manufacture a small scale 100W product, however, the ability of their design to scale up is unknown. The rotors prime function is to generate torque, this torque must be reacted to avoid the entire airborne structure rotating. Coupled with this, the observation that if the two sides of the tether in the rope drive were to become twisted, its ability to transmit power would be reduced and could potentially lead to the system failing. It is noted that Bladetips Energy are not likely to have a similar issue as their rotor is used to primarily generate thrust. Sky WindPower, similar to Kiwee One, generate power from the rotor torque. By using pairs of counterrotating rotors they are able to overcome this issue of tether twisting. This could be a possible solution for Kitewinder when they scale up their design. There are no published studies looking at the use of a rope drive for AWE.

The Daisy Kite, RRP, someAWE Labs S.L. and the Superturbine all transfer power to the ground using torque. The transmission of torque is usually done over relatively short distances, whereas, in the case of AWE it must be done over much longer distances with minimal mass. Torque transmission, similar to a rope drive, allows for continuous power generation using a Ground–Gen device. The take–off and landing of these systems currently relies on a lift kite or other lifting device. The systems are laid out on the ground before being hoisted into the air by the lift kite/lifting device. Although this is a controllable and robust method for launching small scale systems, it will likely need to be adapted for larger systems. At present it requires a considerable amount of human intervention and land space to lay the system out prior to launch.

The Superturbine uses a hollow shaft for torque transmission. A key design principle of the Superturbine is the use of multiple small rotors. This allows the rotational speed to remain high, removing the need for a gearbox. The use of multiple smaller rotors

instead of a single large rotor also allows the system to benefit from economies of scale much earlier. This may help to reduce manufacturing costs and operation and maintenance cost. If a single blade becomes damaged the cost of replacing it, or even replacing an entire rotor, will be minimal. However, the use of multiple rotors on a single shaft presents several issues. Firstly the downwind rotors will likely be effected by the wakes of the upwind rotors. Newman used actuator disc theory to analyse the effect of multiple rotors inline [83]. Newman showed that the combined maximum power coefficient for two rotors, one directly downwind of the other, is $\frac{16}{25}$, this is only slightly higher than the maximum for a single rotor, $\frac{16}{27}$. As the Superturbine is inclined to the oncoming wind the rotors are not directly downwind of each other, also this inclination results in the wake of upwind turbines being directed away from the downwind rotors [84]. Although these factors may help to reduce the wake effects, it is likely that downwind rotors will be effected by the wakes from upwind rotors.

Another factor that must be considered for the Superturbine is the design of the rotors. With several rotors on an inclined shaft, not all rotors will experience the same wind field. Higher up rotors will, on the whole, experience higher wind speeds. It will therefore be very challenging to keep all rotors operating at an optimal tip speed ratio. It may even result in several rotors reducing the power produced by the system, if a rotor was forced to operate at speeds outside of the power producing range. There are no published studies that analyse the wake effect of multiple AWES rotors on a common shaft in open flow, or how multiple rotors on a common shaft could be designed to ensure that all rotors are operating close to their maximum power coefficient.

The Daisy Kite, RRP and someAWE Labs S.L are the most similar rotary AWES prototypes. They all utilise TRPT and have similar operating principles, but the architecture of the TRPT is very different between the three designs. To the best of our knowledge, other than this thesis work, there is only one published study by Benhaïem and Schmehl analysing the operation of a TRPT [7]. More research and analysis is required to identify an optimal TRPT configuration. The use of a TRPT allows for the transmission of

torque without the weight of a shaft. The weight reduction is advantageous, however
it brings with it various disadvantages as well. Firstly, the use of tethers instead of
a solid shaft reduces the torsional stiffness. Although the generators reaction torque
has been used to control the system [76], this only applies for relatively short TRPT
lengths. It is currently unknown if this will be possible for longer TRPT lengths given
the torsional flexibility. Another key factor is likely to be the tether drag. A TRPT has
multiple tethers rotating at potentially high speeds, this leads to losses due to tether
drag. However, within the Daisy Kite and someAWE Labs S.L prototype the tether
lengths are short between rigid components. The tethers could therefore potentially
be given an aerodynamic profile to reduce the tether drag. There is currently no pub-
lished analysis on the tether drag within a TRPT system. More research is required
to fully understand the dynamic response of a TRPT and the impact of tether drag
before analysis on the optimal design, and the corresponding operating characteristics,
is undertaken.

A key advantage that systems using TRPT have over other AWES is less tether fatigue.
Most methods that use tethers to transmit mechanical power cause large cyclic loads
and abrasion on the tether. TRPT configurations are able to greatly reduce these two
factors, potentially prolonging the tethers useful life. Although collectively within the
AWE industry there have been several thousand flying hours, very few AWES failures
are openly discussed. One that is, for a crosswind pumping cycle system, [85] demon-
strates the safety implications of having a single tether and therefore a single point
of failure. Designs that incorporate TRPT have multiple tethers which increasing the
systems redundancy, improves safety and enhances their ability to avoid catastrophic
failures [86].

Most rotary AWES designs utilise a lift kite. Beside providing controlled take–off and
landing, this additional lift also allows the system to operate at lower elevation angles.
The elevation angle of the system dictates the angle between the rotor plane and the
wind vector. As the elevation angle increases the rotors ability to extract power from

the wind decreases. Equally as the elevation angle increases the rotors ability to provide
lift and counteract the systems weight improves. The optimal elevation angle will likely
be dependant on the specific system architecture. Using a lift kite, to provide addi-
tional lift to the system, allows the elevation angle to be reduced and therefore more
power generated. At present the lift kites in rotary AWES remain static. However, if
the lift kite were to fly in a crosswind motion the additional lift that it provides to the
system could be greatly increased [54]. It is envisaged that as rotary systems scale, the
systems that incorporate lift kites will begin to fly them in a crosswind motion. It may
also become apparent that lift kites provide few advantages for larger scale systems.
Some designs may opt to remove them completely and rely solely on the rotor for lift
generation, as with Bladetips Energy's device.

This section has reviewed current rotary AWES. It has discussed the various limitations
and advantages that the different rotary AWES have compared to one another and to
leading AWES. It is clear from this discussion that there are multiple unanswered ques-
tions regarding the design of rotary AWES. Given the vast number of AWE designs and
the different stages of development that each design is at, a detailed comparison of all
the concepts is somewhat challenging. There is no clear sign of the industry converging
towards a single system architecture. It is possible that different designs are optimal so-
lutions at different scales and that certain systems are optimal for specific niche markets.
Given this and the disproportionate amount of research that has been directed towards
rotary AWES the remainder of this work focuses solely on rotary AWES. Within rotary
AWES it can also be seen that almost half of the tested prototypes use TRPT. However
there is very limited analysis of this power transmission method. This research has
therefore focused on improving the knowledge and understanding surrounding rotary
AWES that utilise TRPT. The following section sets out some of the numerous chal-
lenges that face the AWE industry.

2.4   Main Challenges Facing Airborne Wind Energy

The concept of using airborne devices to generate electricity is not a new idea. In just
over the last decade improved materials, greater computational power, increase in the
use of wind turbines and the continued drive for more sustainable electricity generation
has seen greater development in AWE. However, there are still several challenges that
face the industry. These must be overcome if AWE is to ever contribute to reducing our
societies environmental impact. What follows is a brief introduction to the major chal-
lenges currently facing AWE. A more detailed description of these are given in [87,88].

Power Efficiency Measure in Airborne Wind Energy

Several AWES were introduced in Section 2.1, showing the vast range of system archi-
tectures. This is somewhat analogous to the wave energy industry where hundreds of
designs have been proposed [89]. Such a diverse range of concepts makes it more difficult
for AWE to progress. If, within the AWE industry, there is no consensus on the most
advantageous design, potential investors and clients external to the industry will find it
hard to identify the systems with the greatest potential. This creates a barrier to more
organisations becoming involved with the industry. The lack of design convergence, in
part, is due to the lack of metrics for comparing different systems. HAWT uses the
power coefficient, the portion of power passing through the turbine that it is able to
extract. The power harvesting factor (ζ) has been proposed for AWE [24]. It is the
amount of power that a wing can extract compared to the power passing through an
area equal to the wings area. For a modern wind turbine $\zeta \approx 6$. A maximum possible
value of $\zeta = 30$ for any given wing has been proposed [24], this is analogous to the
Betz limit for HAWT. It is yet to be seen if the power harvesting factor is a reliable
metric for comparing AWES. It may transpire that different designs are more suited to
different scales or that particular designs are the best for niche situations or locations.
For example, wind turbines with power ratings of less than 1kW often have more than
three blades whereas almost all larger sized HAWT use three blades. A challenge that
faces the AWE community is to show a trend towards a smaller number of system ar-

chitectures. This will likely occur as more research and development on the different
designs takes place.

Autonomous Control of In-Flight Operation, Take-Off and Landing

A lot of research has focused on the in–flight operation of AWE. Both on the modelling
of the airborne components and on the development of control algorithms to keep the
wings on the desired flight path. Although multiple systems have demonstrated auto-
mated flight, none have done so without human supervision or for extended periods of
time. Operational times for single flights are at most several hours to days long. To
prove the reliability of the in–flight control, flights of several weeks, months and years
with automated operation are necessary. The in–flight controllers must also demon-
strate their ability to operate in a wide range of weather conditions. Although models
and control systems have been developed for several systems, a challenge for the AWE
industry is to prove the reliability and robustness of these over the expected operational
time and environmental conditions.

Leading on from the in–flight operations are take–off and landing procedures. As high-
lighted by Fagiano [90], for a wind farm of AWES there will be many thousands of
take–off and landings. For a wind farm of 300 units, assuming each unit lands and
takes off once every ten days, results in 10,950 take–off's and landings every year. As
shown in Figure 2.3, VTOL is the most widely adopted approach within the industry.
Fagiano and Schnez [91] investigate four methods for a rigid wing pumping cycle sys-
tem, concluding that a winch aided HTOL is optimal. This work is expanded on in [92].
Rieck et al. [93] investigate three methods also for a rigid wing pumping cycle but they
conclude that a rotating arm launch is optimal. Thus showing that different launch
and land methods will be optimal depending on the systems design. Coupled with the
need for extended flight times, a challenge that AWE faces is to demonstrate consistent
automated take–off and landing.

Reliability of Component Materials

AWE uses a range of relatively new lightweight materials. Such as ultra high molecular
weight polyethylene (UHMWPE) fibre tethers and composite wings. Given the aim for
AWES to operate for over 8,000 hours a year, the reliability of these materials must
be well understood. Scheduled maintenance and replacement of parts to maximise the
component life, while minimising the risk of catastrophic failure, is only possible when
materials and the loading they are subject to is well understood. Many of the materials
used within AWES are relatively new and are being loaded in new ways, the life of mul-
tiple components is currently unknown. For example, with most designs it is assumed
that the tether will need to be replaced every 1–2 years. However, until more extensive
testing is done the expected life of tethers can only be estimated. The AWE industry
needs to better understand material degradation to identify the optimal time to replace
components.

Understanding of Wind Resource and Other Environmental Factors

A key motivation for AWE, as explained in Section 2.1.1, is the altitude that much of
the wind resource is located at. The ability of an AWE to not only reach higher alti-
tudes but also alter its height of operation, indicates that AWES could achieve higher
capacity factors compared to HAWT. A higher capacity factor is associated with a lower
LCOE. To take full advantage of this, AWES must know what the optimal operational
height is in real time.

The impact that wind energy has on the local and global environment has been studied
in detail [94, 95]. These studies are focused on HAWT. There are a small number of
studies that assess the environmental impact of AWES [96, 97]. The UK's renewable
energy planning database [98] shows that just over 50% of wind energy projects are
either refused or have their applications withdrawn. Proposed wind farms often face
strong local opposition with the environmental impacts frequently cited as reasons for
the opposition [99]. This is likely to also effect the AWE industry. Bruinzeel et al.

show [96] that the greatest environmental impact of a AWES is the *'mortality caused
by the moving aircraft or tether'*, which are predominately bird strikes. As AWE is still
in the design stage, this presents a unique opportunity to incorporate mitigation for
impacts into the systems design from an early stage. A challenge that faces the AWE
industry is to increase the knowledge around the environmental impact of devices. Once
better understood these impacts can be removed, reduced or mitigated against.

Regulation, Approval and Commercialisation

The final challenge highlighted here is around the approval and regulation of systems.
The airspace industry is highly regulated. The aircraft, maintenance regime, pilot (or
remote pilot) and device operation must be certified and approved before flights can oc-
cur. AWES are very different to what the aviation authorities are used to. Currently the
approval of testing for AWES is done by local aviation authorities. These approvals are
for individual devices at specific test sites. As there are only a handful of test sites, the
requirements imposed on each are independent with a large variation between sites [88].
The European Aviation Safety Agency are developing regulations for remote piloted
aircraft systems, or drones. It is expected that AWES will fall into this type of opera-
tion, seen as a tethered drone. Airborne Wind Europe is a consortium of organisations
actively pursuing AWE. They have established five working groups with one dedicated
to airspace regulation. The AWE industry, in collaboration with the various aviation
authorities, will need to establish specific regulation and approval procedures for AWES.

Although several companies are planning to commercialise their systems in the near
future, there are numerous challenges still to overcome. Reliability is the greatest of
these, AWE must demonstrate continuous autonomous operation before investors and
potential customers will view it as a viable energy option. Most systems have only
demonstrated a few hours of automated operation and therefore must greatly increase
this. That said there are several larger energy and technology companies that have
taken an interest in AWES. It is likely that if AWE is able to at least partially prove

reliability more financial support will become available. AWE currently has a technology readiness level of 3-5 [87, 100], product development is still required prior to any device being commercially available. It is expected that smaller scale, off–grid systems, will be the first to market as these often demand lower capacity factors, reducing the operational time and reliability requirements, compared to utility scale grid connected energy systems.

2.5   Summary

This chapter has provided an overview of the airborne wind industry, with a focus on the class of devices referred to as rotary AWES. There are several advantages that AWE have compared to the HAWT. Using lightweight tethered wings, or a lighter than air gas, AWES can reach higher altitudes than HAWT. This gives AWE access to more of the wind resource. It also ensures that less material is used, reducing CO_2 equivalent emissions and providing the potential for higher capacity factors. This leads to a predicted LCOE that is lower than HAWT, providing the motivation for continued research into AWE.

There are over 60 organisations currently investigating AWE. This has resulted in a variety of different AWES architectures being proposed. A classification system for the many designs is given in Section 2.1.2. The classification system identified several trends within the industry and highlighted the most popular generation method: a crosswind Ground–Gen also referred to as a pumping cycle system. The second most popular system category, crosswind Fly–Gen, is being developed by fewer organisations. However, the largest AWE prototype to date, Makani Power's 600kW wing, uses this system architecture. The power outputs for both pumping cycle and crosswind Fly–Gen systems can be calculated using a basic analysis for a wind harvesting wing. This basic analysis highlights the significance of tether drag.

Rotary AWES use rotors or multiple wings to form rotors. These systems utilise the

principle of autorotation to remain airborne and generate power. The various compo-
nents that make up a rotary AWES are detailed in Section 2.2.2 and a review of rotary
AWE designs is given in Section 2.3. All AWES must transfer the energy that is har-
vested aloft down to the ground. There are five power transmission methods currently
used by rotary AWES, these are: tether tension using a pumping cycle, electrically,
a hollow shaft, TRPT and a rope drive. Seven existing rotary AWE prototypes are
introduced in Section 2.2.4, each has demonstrated several advantages that rotary sys-
tems have over the two most developed AWES, pumping cycle and crosswind Fly–Gen
systems. Three key advantages, that apply to most rotary designs, are:

1. Ground–Gen systems with continuous power generation

2. No necessity for operational control systems

3. Networked structure leading to inbuilt redundancy, making them more inherently
   stable

To further develop rotary systems more research is required to confirm and quantify the
advantages of each rotary system design. This will allow for a more informed compari-
son between them and other wind harvesting devices.

Key challenges facing the AWE industry were set out in Section 2.4. The most crucial
of these is proving the reliability of any given AWE concept. Over the last two decades
multiple organisations have proved that the concept of AWE is possible. More develop-
ment is needed if AWES are to become commercially viable and contribute to societies
energy demands. It is possible that different AWE designs are best suited to different
situations.

Chapter 3

Experimental Campaign and Design Improvement on Rotary Airborne Wind Energy Systems

This chapter gives details of an experimental campaign conducted on the rotary AWES developed by W&I. The testing has been conducted in collaboration with W&I, all field tests took place at their test site on the Isle of Lewis, Scotland. Over one hundred hours of testing on multiple prototypes has taken place, this represents the most comprehensive experimental campaign of any rotary AWES utilising TRPT. Along with this chapter details of the W&I experimental campaign can also be found in [52, 76, 77, 101].

The two key aims of the experimental campaign have been;

1. Improve the knowledge around the operational characteristics of rotary AWES.

2. Provide data for comparison with the mathematical models developed as part of this thesis work, these models are described in chapter 4.

Both of these have been achieved, previously unknown operational behaviour has been identified and data collected from several Daisy Kite prototypes is compared to the developed mathematical representations in Section 5.1.

W&I's rotary AWES, the Daisy Kite, was briefly introduced in Section 2.2.4, a more thorough description of the Daisy Kite and the systems components are provided in Section 3.1. The W&I test site is described in Section 3.2, along with the testing procedures used during the collection of empirical data. Section 3.3 provides details of the design changes that have been implemented throughout the campaign. These improvements have been made to; (1) facilitate the collection of performance data and, (2) increase the power output of the prototype system. The data collected is analysed in Section 3.4. Observations made during the experimental campaign, on the Daisy Kites performance characteristics, are introduced in Section 3.5. Finally this chapter is summarised in Section 3.6.

3.1 Daisy Kite System Configuration

W& I have been developing their rotary AWES, the Daisy Kite, since 2012. Their first prototype consisted of four kites attached to the circumference of an inflatable trampoline, this was mounted on a line with rotary snap shackles and tensioned between two windsurfing masts so that it could spin freely. Since then W&I have manufactured and tested a large number of prototypes achieving several hundred flying hours. The development of the Daisy Kite has been reliant on experience, gained through testing the various prototypes. From the initial prototype the design has seen considerable modification. Figure 3.1 shows a diagram of a recent Daisy Kite design, the main components have been labelled. The Daisy Kite design uses the principle of tensegrity, putting as many of the structural loads into tensile load paths as possible, while minimising compressive load paths. This allows lightweight tethers to be used for much of the structure. Minimising the weight for any AWES is crucial as it improves the overall aerodynamic efficiency of the system. In the remainder of this section each of the components highlighted in Figure 3.1 are described. For almost all of the components multiple versions with differing designs have been tested. Several of the design alterations have been minor, e.g. slight movement of tether attachment points or changing of the attachment mechanism between components. All of the different component
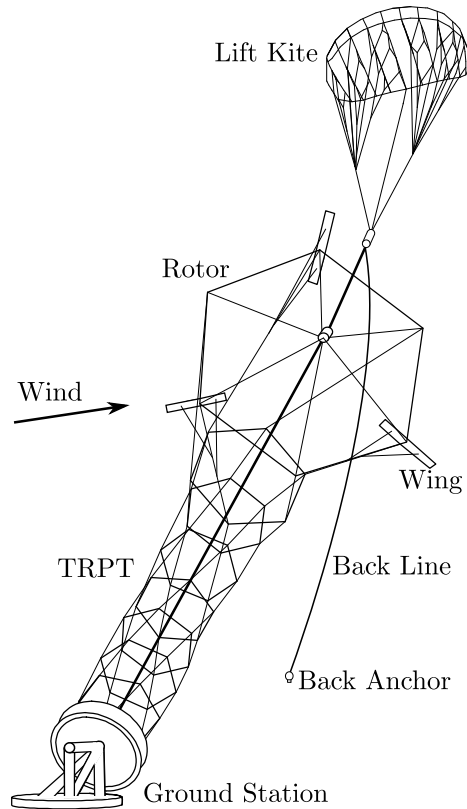
Figure 3.1: Diagram of the Daisy Kite AWES with the main components labelled

versions tested throughout the experimental campaign are detailed, however, any minor alterations are not included within the following descriptions.

3.1.1 Rotor

Several rotors have been used by various Daisy Kite prototypes, all are analogous to the rotor of a HAWT. Many Daisy Kite designs have also used multiple rotors, much like the Superturbine introduced in Section 2.2.4. Similar to a HAWT, the Daisy Kite rotor converts the kinetic energy of the wind into rotational motion for electricity generation. However, unlike a HAWT, the Daisy Kite rotor also provides aerodynamic lift so that it is able to remain airborne at the desired operating altitude. To provide this lift force the rotor must be pitched/tilted down into the incoming wind. This causes a misalignment between the incoming wind and the rotors axis of rotation. A portion of the thrust

force produced by the rotor is therefore in the vertical direction, thus providing lift to support at least some of the systems weight. This is often referred to as the principle of autorotation [67]. Although it allows the rotor to generate lift, the misalignment of the rotors axis of rotation and the incoming wind reduces the rotors ability to convert the kinetic energy in the wind into rotational power. The tilting of the rotor is analogous to a yawed HAWT [28,102]. There is a trade off between the rotors ability to generate lift or to generate power.

Much like a HAWT the Daisy Kite's rotor uses several blades, or wings, equally spaced around the rotor. Prototypes using three and six bladed rotors have been tested. Unlike a HAWT, the wings on the Daisy Kite rotor do not all connect to a central hub. Instead the wings are connected to a carbon fibre ring at a distance from the rotors centre, as can be seen in Figure 3.1. The span of each wing is much less than the rotors radius, thus leaving the centre of the rotor unfilled. This is referred to as an open centre rotor. On a HAWT the outer 30% of the blades produce around 50% of the power. The outer portion of the blades produce the most power per unit blade area. Minimising weight is advantageous for any AWES, the Daisy Kite design only incorporates the most efficient outer portion of the blades. By leaving the centre of the rotor open the weight of the rotor can be reduced while limiting the impact on the rotors swept area and power output.

On a HAWT rotor the inner section of the blades support the outer blade portions, it also transfers the power generated by the outer portion to the central hub, which is connected to the end of the drivetrain. Without the inner section of the blade the Daisy Kite rotor must utilise alternative methods to support the wings and transmit the wing forces to the drivetrain. The wings on the Daisy Kite rotor are all connected to a carbon fibre ring. The ring is constructed from several straight rods that are joined and bent to form the ring. The ring, for all prototypes, has a radius of 1.52m and is encased in a dacron sleeve. Six radial tethers are sewn into the dacron sleeve with their other ends connected together at the centre of the rotor. These are referred to as radial tethers. The six radial tethers are equally spaced around the ring. The carbon fibre ring and six

radial tethers help to support each wing. The bank angle, and on some rotors tested the anhedral arc, of the wings provide a radial force that acts to expand the ring. The centrifugal forces, on the rotors components as they rotate, provide an additional radial force that also acts to expand the rotor. The expansion of the rotor ensures that many of the load paths within the rotor are tensile, thus using the tensegrity principle. It is also crucial to the transmission of torque down to the ground station, further detail is given in Section 3.1.3. Earlier prototypes also included a ring kite that aids ring expansion. The ring kite is a conically shaped kite with its circular leading edge connected to the carbon fibre ring, Figure 3.4 shows a diagram of a rotor that incorporates a ring kite.

The ring, in particular, ensures that the wings follow the desired flight path. The radial tethers main role is to limit the radial deformation of the ring, ensuring that it maintains a circular shape. The radial forces act to expand the rotor and keep the structure in tension. These components ensure that the rotor is adequately supported when airborne. Figure 3.2 shows a diagram of the Daisy Kite's rotor showing the rotors components and its design. To remain airborne, as mentioned previously, the rotor is pitched down into the oncoming wind. This results in a lift force being produced that
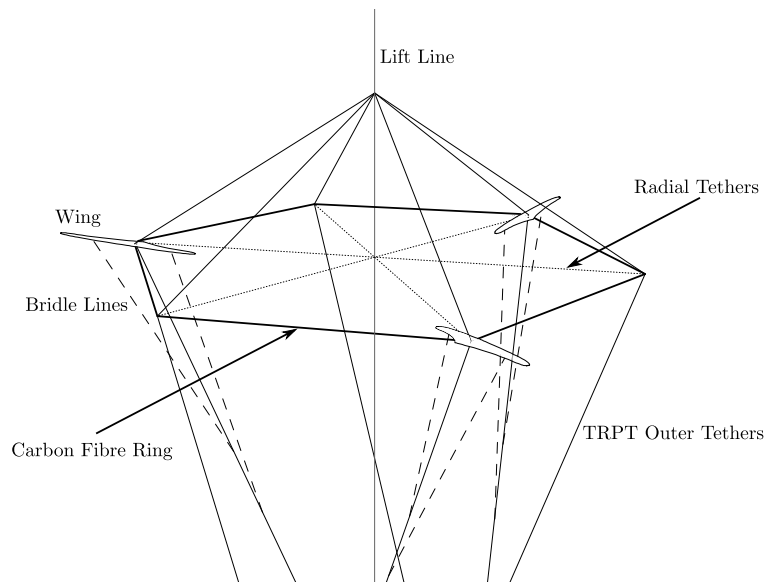
Figure 3.2: Diagram of the Daisy Kite's rotor design

60

acts to oppose the weight of the rotor, and the entire systems weight. The lift kite also
supplements this lift force.

The power is transmitted from the rotor down to the ground station using TRPT. The
Daisy Kite's rotor is incorporated into the TRPT, as is described in Section 3.1.3, the
rotors ring and wings form the first ring of the TRPT. The main difference between the
various Daisy Kite prototype rotors are the wings. Two different wings have been used
within the multiple configurations tested, the following sections introduce both wings.

Soft Wings

The HQ Symphony Beach III 1.3 [103] is a symmetric parafoil kite with a span of
1.3m and a chord length that various from 0.55m at its centre to 0.16m at the tips.
These HQ kites are low cost and readily available, they are a steerable two line kite
intended for use by beginner kite flyers.   They are able to operate in a wide range
of wind speeds and, despite their symmet-
ric form, can perform small radius turns.

Figure 3.3 shows an image of a HQ Sym-
phony Beach III 1.3 kite as used on the
Daisy Kite.   Due to their low cost and
wide range of acceptable operating condi-
tions, these kites were used extensively on
early Daisy Kite prototypes.

Figure 3.3: Image of a HQ Symphony Beach
III 1.3 kite as used in the Daisy Kite

The kites are sewn onto the dacron sleeve which surrounds the rotors carbon fibre ring.
The attachment point between the ring and the distance along the kites span has varied
between prototypes. On prototypes, for which power data has been collected, the kites
are attached to the rotor ring roughly a third of the distance along their span, with 2/3
of the kite outside the ring. When the kites are flat their outer tips are at a radius of
2.43m. 0.36m of the kite's span sits inside of the rotor ring. Earlier prototypes had

larger portions of the kite outside of the rotor ring. On these prototypes any portion of the kite that would have been inside of the ring was removed, the kites span was therefore reduced on these iterations of the device. Figure 3.4 shows a diagram of such a rotor.

The leading edge of the kites is stiffened using a 3mm carbon fibre rod. This ensures that the kite does not collapse in the spanwise direction. Earlier prototypes also included a series of overdrive rods, these ran from various points on the kites leading edge to the rotor ring. These rods were to prevent the kite from flying ahead of the rotor ring, they have been removed for later prototypes and from all prototypes for which performance data has been collected.

The position of the kites is set when manufacturing the different rotors. It is possible to make minor alterations to the kites tuning between tests, once flying it is not possible to alter their set up on existing prototypes. The sweep angle of the wing, as shown in Figure 3.4, is set at the point it is sewn onto the dacron sleeve. The overdrive rods helped to ensure that the sweep angle was maintained during operation. The anhedral bank angle and arc are defined by the setting of the kites bridle lines. The bridle lines are connected to the TRPT outer tethers connecting the rotor and the next TRPT ring, towards the ground. By altering the length, or the connection points, of the bridle lines, the kites bank angle is increased or decreased. Increasing the bank angle increases
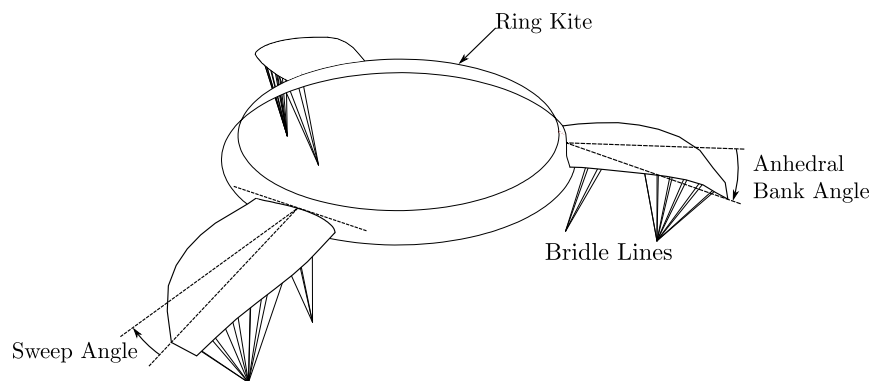
Figure 3.4: Diagram of a Daisy Kite rotor, incorporating a ring kite, showing the kites anhedral bank angle and sweep angle.

the kites aerodynamic force component that acts to expand the rotor. The bridle lines can also be set to cause a spanwise twisting of the kites. By setting the TRPT outer tethers forward of the kites the bridle lines are pulled ahead of the kite causing it to twist about its span. The TRPT system deforms torsionally during operation, the relative position of the rotor ring and the adjacent TRPT ring will vary depending on the systems operation point. The TRPT outer tethers will retreat further behind the kite as more torque is generated, this altering the twist along the kites span.

Due to the flexible nature of the soft kites and the Daisy Kite design, the orientation of the kites will change depending on the systems operating point. It is envisaged that it may be possible to use this to influence the Daisy Kites operating characteristics in a beneficial way. For example, overspeed protection could be incorporated by ensuring that the kites depower at higher rotational speeds. This could be achieved by setting the bridle lines so that the tip of the kite twists to spill wind when high rotational speeds are reached or large rotational deformations are experienced. This is analogous to a windsurfing sail twisting to depower. Given the complex nature of the aeroelastic behaviour of the soft kites, and their configuration within the Daisy Kite, more inves-

Figure 3.5: Image of a Daisy Kite prototype undergoing field tests. Three soft rotors are shown (September 2016).

tigation is required to confirm to what extend these kite reactions can be achieved.

W&I have tested multiple prototypes that utilise soft winged rotors. All these rotors use three HQ kites equally spaced around the rotor. Prototypes using up to three rotors, stacked up the TRPT have been tested. Figure 3.5 shows an image of a Daisy Kite prototype in the first test associated with this thesis work. Three soft winged rotors, each with a ring kite, are shown in the image.

Rigid Wings

More recent Daisy Kite prototypes have used rigid wings. These wings have a span of 1m and a constant chord length of 0.2m. They use the NACA 4412 aerofoil profile and do not incorporate any twist in the spanwise direction. Similar to the soft wings they are mounted on a carbon fibre ring with a radius of 1.52m. The outer tip of the wings, when flat to the rotor plane, have a radius of 2.22m. Therefore, 0.3m of the wings span is inside of the rotor ring.

The wings are constructed from foam and coated in a plastic film for additional protection. They are attached to the ring using a custom 3D printed fuselage, a diagram of these fuselages is shown in Figure 3.6. The fuselage slides over the rotor ring and dacron sleeve and is secured in place using the attachment loops. The inner and outer sections of the wing fit into either side of the fuselage. Two carbon fibre spars run the length of the wing. The insert for the spar, closest to the wings trailing edge, on the fuselage can be seen in Figure 3.6.
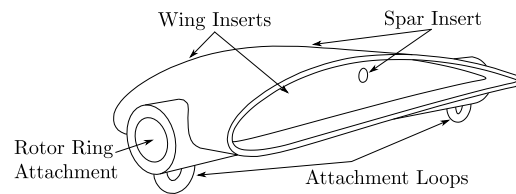
Figure 3.6: Diagram of the rigid wing fuselage for connecting the wings to the rotor ring.

Similar to the soft wings the rigid wings also incorporate bridle lines, although far fewer

are used. A bridle line is connected to the midpoint between the fuselage and the outer tip of the wings. There is a second bridle line attached to the midpoint between the fuselage and the inner tip of the wings. These can be seen in the diagram shown in Figure 3.2. The bridle lines are connected to the TRPT outer tethers. As with the soft kites, the length and connection point will dictate the bank angle of the wings.

The fuselages are used to set the pitch angle of the wings. The angle of the wing inserts on the fuselage relative to the rotor ring attachment define the wings pitch angles. Two different pitch angles have been trailed, 0° and 4°. In the 4° case the leading edge is pitched down relative to the ring. The sweep angle of the rigid wings is always set to zero.

Rigid wing test have been conducted using single set ups, most of the tests use three wings with a small number of tests conducted using six wings on a single rotor. Figure 3.7 shows an image of a three bladed rigid winged rotor undergoing field tests.

Figure 3.7: Image of a rigid rotor Daisy Kite prototype undergoing field tests (August 2019).

3.1.2 Lift Kite

As with many small scale rotary AWES the Daisy Kite design incorporates a lift kite. The lift kite is crucial in assisting the take–off and landing procedures of the Daisy kite. It also provides additional lift to the system during operation. As mentioned in Section 3.1.1 there is a compromise between the rotors ability to generate power or lift, which is determined by the elevation angle. A smaller elevation angle will result in more power being generated but less lift. By including a lift kite to supplement the lift generated by the rotor, the rotors elevation angle can be reduced. The misalignment between the rotors plane and the wind vector, or tilt angle, is decreased, increasing the rotors ability to generate power. Analysis of the Daisy Kite's optimal elevation angle is given in Section 5.4.1.

The additional force generated by the lift kite increases the tension within the TRPT. As discussed in Section 3.1.3, the ability of the TRPT to transfer torsion is dependant on the axial force, or tension, that is applied to it. By increasing the tension in the TRPT larger amounts of torque can be transmitted from the flying rotor down to the ground station.

The lift kite used by the Daisy Kite prototype is a single skin lifting kite developed by Peter Lynn, [104]. Lifting kites have been developed to provide stable lift. They are mainly used for kite aerial photography and within kite displays, to lift camera equipment and display kites into the air respectively. The single skin, single line, lift kite used in the Daisy Kite design is a lightweight lifting kite with a surface area of 3.2m^2. An image of the lift kite is shown in Figure 3.8. A single tether or lift line, as can be seen in Figure 3.8, connects the lift kite to a thrust bearing at
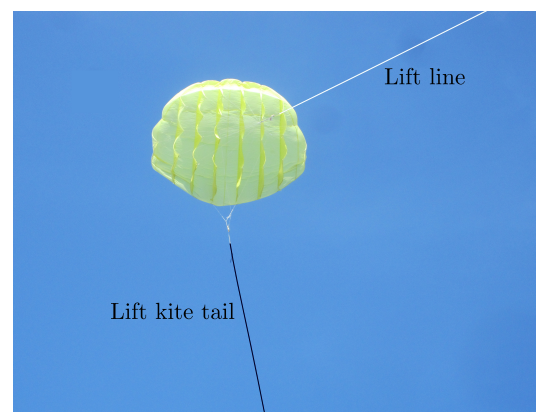
Figure 3.8: Image of the single skin lifter kite used by the Daisy Kite.

the top of the Daisy Kite turbine. The lift kite has multiple bridle lines, as shown in
the diagram in Figure 3.1. The length of these bridle lines can be altered to adjust the
kites flying position. For example, the bridle lines can be used to change the kites angle
of attack, this in turn alters the lift to drag ratio of the kite which determines the kites
elevation angle. The lift kite can therefore be used to control the elevation angle of the
entire system.

The lift kite ensures the downwind alignment of the entire system. A tail has been
added to the lift kite as it was found that this stabilised the kite. With the tail in place
fluctuations in the kites lateral position are reduced. It is crucial to have a stable lift
kite to ensure that the downwind alignment of the system is reliable. The ability of
the lift kite to control the systems elevation angle and downwind alignment presents
a simple method for increasing or reducing the systems power output as required. By
increasing the misalignment, or yaw, between the rotor and the wind vector, the rotors
power output is reduced. This method has been successfully applied during field tests
to reduce the systems rotational speed prior to landing.

Several different lift kites have been used with various Daisy Kite prototypes. The single
skin lifter described above was found to have the best power to weight and provided
sufficient position stability. Other lift kites are used in different wind conditions, for
example in higher wind speeds a less powerful lift kite is preferred. The data collected
for this thesis work has been measured with the single skin lifter shown in Figure 3.8.

Multiple tests have been run using a 4.8m tall mast in place of the lift kite. In these
experiments the lift line is connected to the top of the mast instead of the lift kite.
Initially the mast was used to mitigate against the risk of ground strikes during the first
rigid wing tests, it was found that being able to fix the systems elevation angle provided
a number of advantages. The mast tests are described in Section 3.2.2.

3.1.3 Tensile Rotary Power Transmission

The Daisy Kite uses TRPT to transfer torque from the flying rotor to the ground station, where the electrical generation equipment is located. The TRPT is the most novel aspect of the Daisy Kite's design. Usually torsion is transmitted over relatively short distances using solid or hollow shafts. Although a reliable method of power transfer these shafts are often heavy, and at larger scale are too heavy for AWE applications. Given the need for lightweight components within AWE, TRPT aims to transfer torsion over large distances while minimising weight. Figure 3.9 shows a diagram of Harburg's coaxial multi–turbine generator. This TRPT, detailed by Harburg in his 1990 patent [14], is the first known example of TRPT. It is not used much in other applications and it is perhaps most suited for AWE.

The Daisy Kite's TRPT Design

As discussed in Section 2.2.4 there are multiple possible configurations that a TRPT could take. In principle it consists of multiple tethers that are separated by rigid components. In its simplest form it consists of two tethers that are connected to either end of a series of rods. This simple configuration looks similar to a rope ladder. As torsion is applied to one end of the tethers, so long as there is sufficient tension on the

Figure 3.9: Diagram of Harburg's coaxial multi–turbine generator [14].

68

Figure 3.10: Diagram of the first TRPT configuration used within the Daisy Kite for this work, TRPT–1

tethers, the torque will be transmitted to the opposite end of the tethers. W&I have previously tested a TRPT that was similar to this simple configuration. Their design also included a third tether that ran through the middle of each rod. This third central tether acted as the axis of rotation about which the rods and the outer two tethers rotated. W&I found this configuration impractical, the straight rods would easily get caught inside the tethers and the system required large amounts of tension to reliably transfer torque. W&I have experimented with several TRPT designs. Later iterations of the Daisy Kite's TRPT all consist of six tethers that are equally spaced around the circumference of several carbon fibre rings. Figure 3.10 shows a diagram of the first TRPT system that has been used within the Daisy Kite for this work.

The rings are made of one or more straight carbon fibre tubes that are bent into shape. As with the rotor, the rings are encased in a dacron sleeve. The tethers are sewn onto the dacron sleeve at the six attachment points on each ring. A central tether runs through the centre of each ring acting as the axis of rotation of the TRPT. Similar to the rotor, each ring has six radial tethers. These run from the tether attachment points on the ring to the central tether. The radial tethers are joined to each other at the central tether using a small plastic disc. The disc acts to join the radial tethers and allows the TPRT to rotate independently of the central tether. As with the rotor, the radial tethers constrain the rings radial deformation.

69
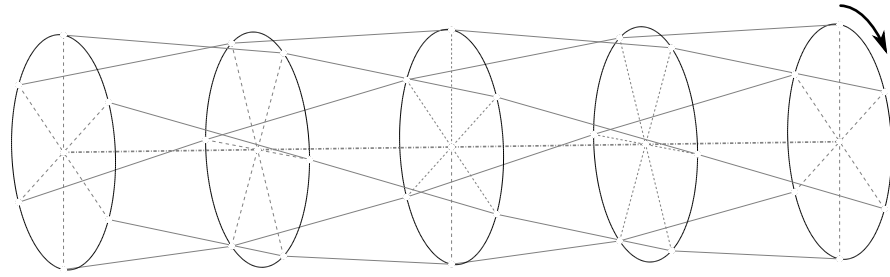
Figure 3.11: Diagram of a torsionally deformed Daisy Kite TRPT.

The TRPT shown in Figure 3.10 is used for a number of the experiments conducted as part of this work. It consists of five carbon fibre rings, the top ring is also the Daisy Kite's rotor. The ground station has a steel wheel with a diameter of 0.42m that the tethers at the bottom of the TRPT connect on to. The TRPT shown in Figure 3.10 was designed to have a cone angle of 22°. This is to avoid any abrupt changes in the TRPT's diameter. As torsion is applied to the TRPT, the system deforms. Figure 3.11 shows an example of this. The Daisy Kite's TRPT must deform rotationally before it is able to transmit torque. In its initial state the tethers are parallel to the axis of rotation, and therefore unable to react any torsional force. Once two adjacent rings have different rotational positions relative to one another, the tethers are no longer parallel to the axis of rotation. The tethers are then able to react against the torsion and transmit torque along the TRPT.

As the TRPT deforms the outer tethers move inwards towards the axis of rotation. If the six outer tethers reach the axis of rotation they will cross and the transmittable torque collapses to zero. The rings within the TRPT act to resist this compression force, keeping the outer tethers away from the central axis. When designing the TRPT it was feared that an abrupt change in the TRPT diameter would increase the compression force beyond the rings ultimate strength, causing the rings to fail. By slowly decreasing the TRPT diameter from the flying rotor down to the ground stations wheel, the compressive forces within the TRPT are kept low.

W&I have experimented with various TRPT configurations for the Daisy Kite. They
settled on a general design that consists of six tethers equally spaced to form a cylinder,
where the tethers are held apart by lightweight rigid components. This set up was cho-
sen as it provides smooth continuous power transmission and has proven to be resistant
to component failure during operation. The detailed design of the Daisy Kite's TRPT
is still under development, as is evident by the five different variations, detailed below,
that have been tested within this experimental campaign.

The RRP rotary AWES system introduced in Section 2.2.4 uses a TRPT system similar
to the Daisy Kite. The steady state analysis of the RRP, conducted by Benhaïem and
Schmehl [7], shows the importance of the TRPT's dimensions in relation to its ability to
transfer torque. Within the RRP four outer tethers are used and there are no interme-
diate rigid components between the flying rotor and the ground station. This reduces
the weight of the airborne components, however, it means that to transfer the required
torsion the diameters of the flying and ground rotors must increase as the distance be-
tween them becomes larger. If high altitudes are to be reached the required diameter
of the ground rotor in particular could become a limiting factor.

If rotary AWES that utilise TRPT are to reach altitudes of 400–500m, as current
AWES prototypes have done, TRPT lengths in the region of 1km are necessary. The
longest TRPT at present is someAWE's open tensegrity shaft, at a length of 30m [8].
someAWE's TRPT, described in Section 2.2.4, is very different compared to the Daisy
Kite or RRP designs. someAWE's open tensegrity shaft design results in a more tor-
sionally stiff system, this may prove crucial as TRPT based systems move to larger scale
prototypes.

TRPT Configurations

Five main TRPT configurations have been tested throughout the experimental cam-
paign. The first of these is shown in Figure 3.10. Figure 3.12 shows the dimensions
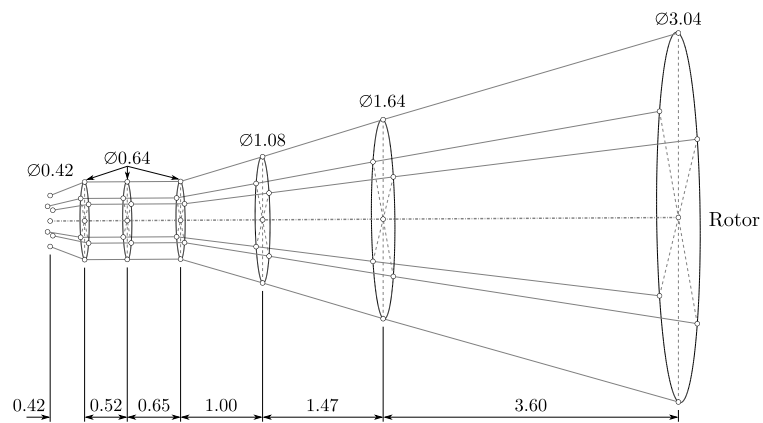
(a) TRPT–2.
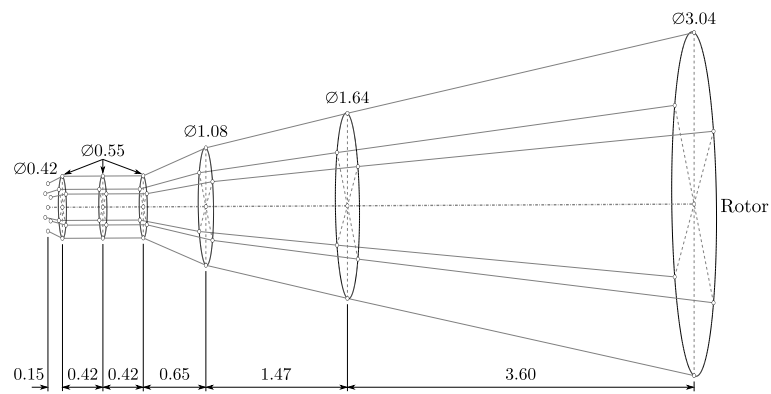
(b) TRPT–3.
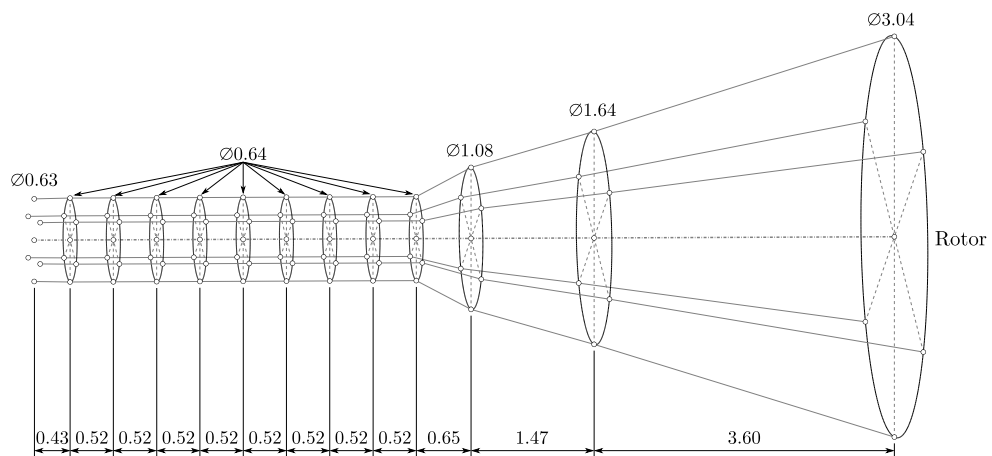
(c) TRPT–4.

Figure 3.12: Diagrams of TRPT iterations 2, 3, and 4 used throughout this work.

used for TRPT iterations 2, 3, and 4. The TRPT versions 1 to 4 are similar, the main difference between them being the number of carbon fibre rings, the diameter of the rings and the length of tethers between the rings. The ground station wheel in versions 1, 2, and 3 has a diameter of 0.42m, for versions 4 and 5 this was increased to a diameter of 0.63m. W&I have found that in general the Daisy Kite's TRPT configuration is less capable of transferring torsion as the distance between rings becomes larger and the ring diameter is reduced [77]. The ground station wheel diameter was increased to allow for larger amounts of torque to be transmitted.

The most recent power transmission configuration, TRPT–5, has included a series of significant changes from TRPT–4. Figure 3.13 shows a diagram of TRPT–5. Most noticeably several of the rings are hexagonal in shape instead of circular, including the rotor. The circular rings are constructed by bending several straight carbon fibre tubes to form a ring. The rings therefore have a residual force that is attempting to straighten the tubes. It is believed that this has increased the chance of a ring failing. Usually when the system is not in use the carbon fibre tubes are stored in their straightened form. On several occasions when they have been stored in their ring form, the rings have failed while in storage. Moving from a circular to a hexagonal shape removes the need to bend the tubes and therefore eliminates any residual stress, stress in a material under no load.
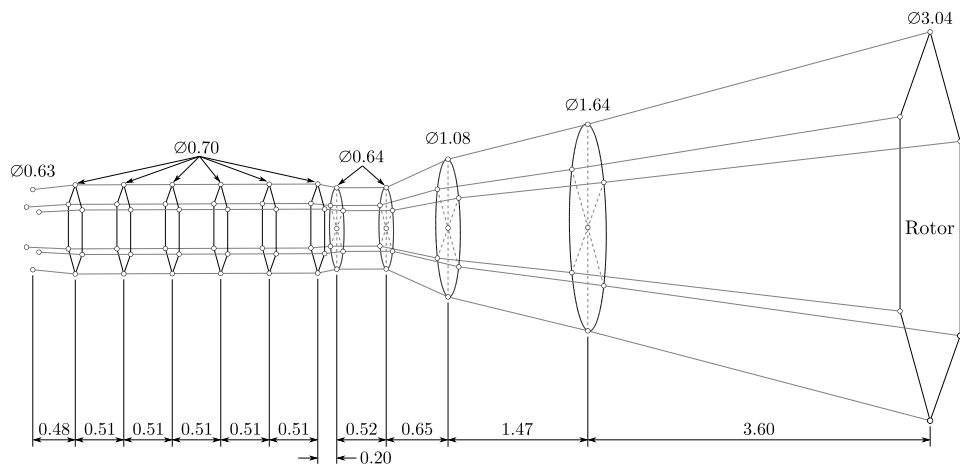
Figure 3.13: Diagram of the most recent TRPT configuration, TRPT–5.

The hexagonal rings do not use a dacron sleeve or radial tethers. The straight rods are connected to one another using a small cuff that fits over the end of two tubes, joining them at the required 120° angle. This cuff also incorporates a short dacron tab that the outer tethers are sewn onto. As can be seen in Figure 3.13 TRPT–5 utilises a mixture of hexagonal and circular rings.

The second major change made for TRPT–5 is the removal of the central tether within the TRPT. As highlighted previously in Section 3.1.3, the ability of the TRPT to transfer torsion is dependant on the axial force, or tension, that is applied to it. It is the axial force on the outer tethers that determines this. The tension on the central tether does not directly change the systems ability to transfer torque. It does however reduce the tension that is present within the outer tethers. By removing the central tether within the TRPT, the outer tethers react the full axial force generated by the rotor and the lift kite. This increases the axial force on them, which in turn improves the TRPT's ability to transfer torque.

TRPT Failure

As mentioned previously, if the outer tethers reach the central axis and cross, the transmittable torque collapses to zero. This will occur if the TRPT is overloaded with torque such that the torsional deformation between two adjacent rings exceeds 180°. At this point the system is said to have failed, the rotor side of the TRPT will continue to rotate but the ground station side will either become stationary or rotate at a slower speed and with reduced torque. The tethers within the TRPT will therefore become excessively twisted. This failure mode does not necessarily lead to full system failure. If the ground station end of the TRPT is powered, such that it rotates faster than the rotor end, it is possible to untwist the tethers. The TRPT can then resume normal operation. It is also noted that if the tethers are allowed to continually twist round each other, such that the torsional deformation between adjacent rings becomes much larger than 180°, the compression force on the rings will increase beyond their ultimate

74

strength, causing the rings to fail. The distance between adjacent rings dictates the point at which this occurs. If the diameter of the rings is larger than the length of the tethers between two adjacent rings, it is not possible for the torsional deformation to reach 180°. In this case the tethers or rings will fail if the TRPT is overloaded with axial tension or torque.

The TRPT has three main failure modes; 1) Tethers cross due to excessive torsional deformation, 2) tethers fail due to excessive tension and 3) rings fail due to excessive compression force. Depending on the TRPT's geometry the first failure mode acts as an indicator prior to the second and third failure modes occurring. The second and third modes both result in component failure whereas it is possible to recover from the first before they occur. Even if a tether or ring component fails it is not necessarily catastrophic to the system. Experiments have demonstrated that tethers and rings can fail and the Daisy Kite continues to produce power, but at a reduced capacity.

3.1.4   Ground Station

The ground station is the Daisy Kite's main point of contact with the ground. It connects to the end of the TRPT and houses all the electrical generation equipment. It must withstand the forces applied to it by the airborne components, transferred via the end of the TRPT. As previously mentioned the TRPT connects onto a wheel on the ground station. Figure 3.14 shows an image of the Daisy Kite's ground station with the key components labelled.

The six outer tethers connect to the outer rim of the wheel and the central tether, not included for TRPT–5, attaches to the wheels centre. Two repurposed bicycle wheels have been used, with diameters of 0.42m and 0.63m. The wheel shown in Figure 3.14 is the 0.42m diameter wheel. The wheel is connected to a 500W generator via a chain drive. The chain drive has a gear ratio of 1:2.14. The generator is a 500W electric bike motor that has been repurposed so that it can be used as a generator. The 36V

Figure 3.14: Image of the Daisy Kite ground station with key components labelled.

generator is connected to a series of batteries and a Vedder Electronic Speed Controller (VESC) [105]. The generators rotational speed and breaking current are recorded at a frequency of 2Hz to 5Hz depending on the testing requirements. A Quarq Dzero power meter [106] is mounted on the large gear directly behind the wheel, as can be seen in Figure 3.14. This power meter is able to record the power and rotational speed at a frequency of 2Hz. The power meter measures the output from the TRPT. Unless otherwise stated all power, torque and rotational speed data shown are based on these readings.

Operational Control

The VESC is a motor speed controller developed for small electric transport, e.g. bicycles and skate boards. It is used to control the operating point of the Daisy Kite. In

combination with the VESC, W&I have developed several algorithms to set the gener-
ators braking current during operating. It uses the average wind speed and rotational
speed from the past 0.5 seconds to find the tip speed ratio of the system. This is com-
pared to the desired tip speed ratio and the generator current is raised or lowered to
achieve the tracking performance. The rotational speed has also been used to set the
breaking current, this allowed constant speed tests to be run.

The ramp rate of the generator current is kept small to ensure that there are no large
step changes in generator torque. W&I also use a series of supervisory checks to ensure
that the device remains in stable operation. If the rotational speed drops below a set
value the generator current is set to almost zero. If the rotational speed drops below
a lower set point it is assumed that the TRPT has over–twisted, i.e. failure mode 1,
where the TRPT outer tethers have crossed. In this situation the generator is used as
a motor to power the bottom of the TRPT forward for a short period of time. It is
hoped that this will recover the TRPT from the over–twist and that normal operation
can continue. There is also a manual override that can be used to force the generator
into motor mode if the system operator notices the TRPT over–twisting or feels that
the situation is about to occur. If this does not solve the over–twist then the airborne
device must be landed.

Ground Anchors

A key feature of any fixed/non–moving AWES are the foundations or anchor points.
These hold the systems ground station in place and must be able to react any forces
applied to the system. The Daisy Kite's main ground anchor secures the ground station
in place. As can be seen in Figure 3.15, a large screw anchor is used to hold the ground
station in place. The yaw bearing, labelled in Figure 3.14, allows the entire ground
station to rotate around the screw anchor. This ensures that the rotor and TRPT are
always aligned in the downwind direction.

The Daisy Kite design includes a second ground anchor, this is located downwind of the rotor and is referred to as the back anchor. As shown in Figure 3.1, the back line connects the lift kite and central tether to the back anchor. This second point of contact with the ground ensures that if the airborne components become separated form the ground station they will not travel outside of the test area. The length of the back line can be used

Figure 3.15: Image of the Daisy Kite's ground station screw anchor.

to set an upper limit on the systems elevation angle. The back line is key to the Daisy Kite's current take–off and landing procedures, as described in Section 3.2.2.

3.2 Test Site Set Up and Measurement Campaign

3.2.1 Windswept and Interesting Test Site

All tests have been carried out at W&I's test site on the Isle of Lewis, Scotland. The islands airport, Stornoway airport, has an average annual wind speed of 6.7m/s with the prevailing winds coming from the South–West [107]. The test site is located 2 miles East of the Airport. The site is ideally located in terms of the wind resource. However, due to its proximity to Stornoway airport, the site is within the aerodrome traffic zone (ATZ) that surrounds the airport. Several restrictions are in place due to this. Most importantly all components must be kept below an altitude of 30m. This has constrained the altitude the Daisy Kite has been designed for and operated at. The mass of the airborne components must be kept under 2kg which has also limited the size of system that can be tested at the site. Clearance must be granted by local air traffic control prior to each test.

The W&I test site is located in the village of Aignish and is surrounded by predominantly single storey dwellings and crofts. The requirement to fly below an altitude of 30m often results in the system being tested in highly turbulent wind conditions. A Vector Instruments A100L2 anemometer is used to measure the wind speed [108]. The anemometer is located on a 4.8m mast, this is similar to the height of the rotors centre. The wind speed is measured at a frequency of 1 to 4Hz depending on the test set up. A Vector Instruments wind vane has also been used to measure the wind direction during several of the tests. When in use, the wind vane is mounted on a 1.5m tripod.

The test site layout is shown in Figure 3.16. The entire set up can be easily relocated between test sessions to adjust for any changes in the wind direction. The distance from the ground station to the rotor launch point and back anchor is dependent on the length of the TRPT being tested. The lift kite is the highest point on the Daisy Kite system. Limiting the distance between the lift kite launch point and ground station to 30m ensures that all airborne components remain under the 30m limit. Due to the
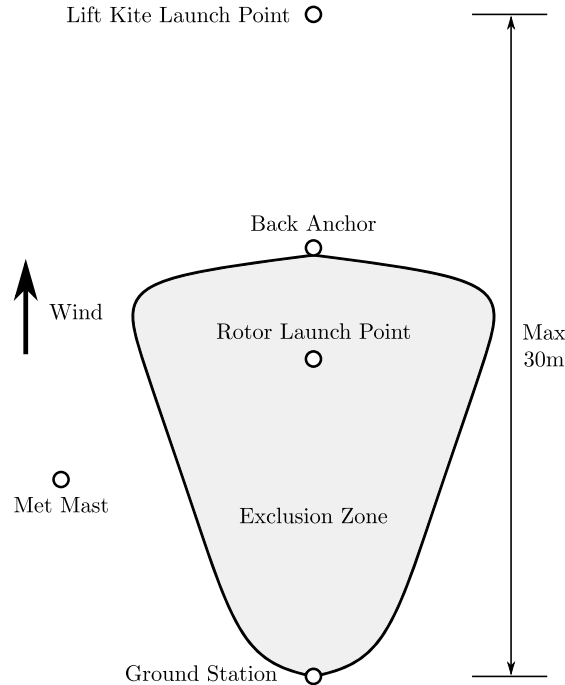
Figure 3.16: Diagram of the Daisy Kite test site layout.

elevation angle of the system the height that the lift kite operates at is usually well below the 30m limit.

3.2.2 Take–off and Landing Procedures

Lift Kite Tests

Prior to launch the Daisy Kite system is assembled and laid out on the ground downwind of the ground station with the layout shown in Figure 3.16. The lift line is initially connected to the back anchor and the top of the Daisy Kite turbine. The lift kite is held open, facing the wind to inflate with air before being released into the air, similar to a traditional kite launch. Once in the air the lift kite is held in place by the back anchor. The lift line is released from the back anchor and the back line is slowly reeled out. As the back line is reeled out the lift kite pulls the rotor and TRPT into the air. Once the rotor is clear of the ground and released it begins to rotate, transferring torque down the TRPT to the ground station.

The process for landing the Daisy Kite is the opposite to the take–off procedure. The back line is reeled in which slowly pulls the rotor and TRPT down to the ground. The lift line is then secured onto the back anchor before it is pulled down. This take–off and landing procedure often results in the rotor wings striking the ground. This is acceptable when using the soft HQ kites but when testing the rigid foam wings this must be avoided. To avoid ground strikes when testing the rigid blades the generators braking current is increased to reduce the systems rotation during take–off and landing. When wind speeds are higher the lift line and back line are also pulled to one side. The rotor is therefore no longer directly downwind of the ground station, thus creating a yaw angle and completely stalling the rotor. These two additional procedures ensure that the rigid wings do not strike the ground while rotating during launch and landing procedures.

Mast Tests

Along with the tests conducted using the lift kite, several tests have been conducted using a mast. In these tests instead of using a lift kite to keep the rotor and TRPT in the air, the central tether, beyond the rotor, is connected to a 4.8m mast. The mast tests are conducted for two main reasons; 1) the take–off and landing procedures are more controlled and 2) the elevation angle is fixed. When testing the Daisy Kite using the lift kite, the systems elevation angle is determined either by the length of the back line or the resultant aerodynamic force on the entire system. This, especially given the often turbulent wind flow, is constantly changing. The elevation angle was seen to vary considerably in short time scales. To allow for greater accuracy within the experimental data, fixed mast tests are implemented to collected data with constant elevation angles.

During the mast tests the wind vane is used to record the wind direction. When using the mast the system does not align itself downwind of the ground station as it is constrained by the mast. By recording the winds direction during these tests, any yaw error that arises due to this misalignment of the system and the incoming wind can be accounted for.

3.2.3 Tensile Rotary Power Transmission Laboratory Experiments

Along with the field tests at W&I's test site a set of laboratory experiments were also conducted in a laboratory at the University of Strathclyde. These laboratory experiments focused on TRPT and were completed by an internship student. Tests were carried out on a single TRPT section which consisted of two 0.62m diameter wheels connected by 6 tethers equally spaced around the circumference of the wheels, replicating the Daisy Kite's TRPT. The tethers have a length of 0.65m. One of the wheels was fixed in place while the second was free to move in the longitudinal and lateral directions. A series of experiments were carried out using this laboratory set up, these involved varying the tension on the six tethers while applying increased amounts of torsion. The aim of these experiments was to assess the steady state operation of a

single TRPT section. The rotational speed was kept constant throughout the tests.

The torque on each wheel was measured using two torque transducers and the rotational deformation between the wheels was determined using images taken during each experiment. The axial force applied to the set up was measured using a load cell. A more detailed description of these experiments and analysis of the results obtained are given in the final report produced by the intern student in Appendix A.

3.2.4   Data Summary

The experimental campaign consists of 45 different tests conducted on 41 days from May 2017 to May 2020. This has resulted in 120 hours of test data on 9 different Daisy Kite prototype configurations. A list of the individual tests, showing the configurations tested and the length of each test is given in Appendix B. Table 3.1 provides a summary of the total testing time for each of the 9 prototype configurations.

Configuration Number	Wing	Number of Rotors	TRPT Version	TRPT Length (m)	Total Test Length (hours)
1	Soft	1	1	6.7	27.5
2	Soft	1	2	7.7	12.5
3	Soft	1	3	6.7	9.0
4	Soft	2	1	6.7	21.0
5	Soft	2	2	7.7	5.5
6	Soft	3	2	7.7	18.5
7	Rigid	1	3	6.7	8.0
8	Rigid	1	4	10.3	13.5
9	Rigid (6 Wing)	1	5	9.5	1.5

Table 3.1: Summary of the total testing time on each Daisy Kite prototype configuration.

It can be seen from Table 3.1 that some of the configurations have relatively small

amounts of flying time, in particular configuration 9. Analysis of the collected data is given in Section 3.4. Although all configurations are analysed, the single rotor systems are focused on. The mathematical models described in Chapter 4 are based on these single rotor configurations.

3.3 Design Improvement of Daisy Kite Prototypes

As seen in the previous section, tests have been run on multiple Daisy Kite prototypes. Prior to and during the test campaign improvements have been made to the Daisy Kite's design. The aim of these improvements was to increase the reliability and accuracy of the data collected and to increase the power output of the device. An image of the initial Daisy Kite prototype, that was assessed as part of this work, is shown in Figure 3.5.

3.3.1 Design Improvements Prior to Experimental Campaign

Prior to field tests commencing in May 2017 a series of alterations were made to the Daisy Kite, this included the addition of sensors and the redesign of some components. This section details two main design alterations during this stage.

Ground Station

Figure 3.17 shows an image of the original Daisy Kite ground station. It used a repurposed ebike. By turning the ebike upside down and securing it to the ground, a bespoke attachment could be used to connect the bottom of the TRPT to one of the pedal cranks. The rotor and TRPT, using the bikes drivetrain and motor, were able to recharge the ebike's battery. This was a highly practical set up as the bike could be cycled and and then recharged anywhere, where space allowed. The bikes variable gear ratio,

reaction torque from the motor and the bikes brakes were used to control the rotational speed of the system. Although this proved to be a low cost and practical ground station it had several limitations that were addressed before any data could be collected.

Figure 3.17: Image of the old Daisy Kite Ground Station.

The ground station's most crucial role is to secure the airborne components to the ground. During operation the ebike could be seen to move violently and components on it would often fail. A new bespoke ground station was therefore designed. An image of the upgraded ground station is shown in Figure 3.18.

The refined ground station allowed for a more robust connection between the TRPT and the ground station, via a wheel, and more secure anchoring of the ground station, as introduced in Section 3.1.4. The bespoke ground station is also able to freely rotate about the anchor point. This ensures that the system is able to always align itself to the downwind direction if the wind direction changes during operation, the ebike in the initial design was not able to achieve this. With the bespoke ground station it is possible to alter the angle that the TRPT connection wheel makes with the ground. This angle can therefore be adjusted depending upon the elevation angle of the system, although it cannot be altered while the system is operational.

Figure 3.18: Image of the upgraded Daisy Kite Ground Station.

Along with making the ground station more secure and minimising the misalignment between the ground station and the airborne components the redesign also enhanced the drivetrain and measurement equipment. As described in Section 3.1.4, the ground station redesign included a power meter so that the devices power output and rotational speed could be measured. Although the resisting torque applied at the ground station could be varied when using the ebike, it could not be accurately controlled. The generator reaction torque was varied without knowing the torque value. The gear ratio was also varied to achieve the desired operation point. As shown in Figure 3.14 a chain drive is still used, however, unlike the bike, the gear ratio is fixed in the redesign. Initially on the redesigned ground station the reaction torque was altered using a disc brake.

Ring Kite Removal

As shown in Figure 3.5, and mentioned in Section 3.1.1, earlier Daisy Kite prototypes incorporated ring kites. The purpose of these rings kites was to aid the expansion of the rotor and ensure that the wings followed the desired flight path. Although the ring kites did aid in expanding the rings they also increased the overall weight and drag of the system. Observing the system operation, in Figure 3.5, it was identified that the ring kites were not always inflated and could be seen to back fill, counteracting any expansion force, at certain rotational positions. The ring kites were therefore removed from any future prototypes.

Figure 3.19: Image of the first Daisy Kite prototype for which performance data has been collected (May 2017).

Figure 3.19 shows an image of the first Daisy Kite prototype that was used to record data within this experimental campaign. The bespoke ground station and removal of the ring kite can be clearly seen.

3.3.2 Design Improvements During the Experimental Campaign

The Daisy Kite design is constantly under review, therefore during the experimental campaign multiple prototypes have been tested. The reasoning behind the various improvements that have been made during the experimental campaign are detailed within this section.

Addition of Vedder Electronic Speed Controller

Initially the reaction torque at the ground station was set using a mechanical disc brake. The brake was altered manually with the aim to increase the systems power output. This proved to be a simple and robust method for controlling the rotational speed. The system could easily be held stationary or allowed to spin freely with simple adjustments made by an operator. However, it required near constant supervision especially in variable wind conditions.

To provide automated operation the VESC, as described in Section 3.1.4, was added to the system. The VESC is used to set the generators reaction torque to keep the system operating at or close to its optimal tip speed ratio. By providing a set braking current, as described in Section 3.1.4, the internal VESC software determines the required braking current and therefore the generators reaction torque. The VESC has been developed for use with multiple small motors. Prior to it being used within any tests it is connected to the Daisy Kite generator and the inbuilt software provides a tuning function. When adjusting the desired braking current the VESC accounts for the response of the drivetrain, however, it does not account for the response of the TRPT and rotor. The VESC has been used to operate the Daisy Kite at a set tip speed

ratio and at constant rotational speeds.

Rigid Wings

The initial prototypes all used soft wings. This was due to their low cost and crash survivability. However, the flexibility of the wings results in low aerodynamic efficiency. Increasing the power output would require larger soft wings or a larger rotor radius. It is also possible to increase to Daisy Kite's power output by using more aerodynamically efficient wings. This was achieved using foam wings as described in Section 4.2.1. The foam wings have a smaller surface area compared to the soft wings but, even with a smaller swept area, produce more power. A drawback is that the foam wings and 3D printed fuselages are more easily damaged by ground impacts. The take–off and landing procedures were adapted to minimise the chance of the wings being subject to large impacts.

Towards the end of the experimental campaign a higher solidity rotor was trialed. Given the relatively low rotational speed and tip speed ratio of the Daisy Kite system, it was predicted that a higher solidity rotor would be advantageous in relation to the power output. A six bladed rotor was therefore manufactured and tested. The six bladed rotor uses the same foam wings and fuselages as the three bladed design.

Tensile Rotary Power Transmission

As shown in Section 3.1.3, five different TRPT's have been manufactured and tested. The latest TRPT incorporated the most significant design improvements. Mainly the use of straight tube's to form hexagons, instead of bending the tubes into circles, and the removal of the central tether within the TRPT. As detailed in Section 3.1.3, these alterations eliminate any residual stress within the TRPT rings and increase the axial force within the TRPT.

The fourth and fifth TRPT versions were both longer than the earlier versions. A key motivation for any AWES, is the ability to reach higher altitudes where stronger and more consistent wind is present. To reach higher altitudes the length of the Daisy Kites TRPT must be increased. The increase in the TRPT length on versions 4 and 5 were to see if the impact of increasing the length could be observed while ensuring that the height restriction at the W&I test site was adhered to.

At the start of the experimental campaign the maximum power output achieved by the Daisy Kite was a little over 300W, for a triple soft winged rotor set up. The maximum power output achieved during the experimental campaign was 1.4kW, on a single rigid winged rotor set up. The maximum power output has therefore increased by a factor of just under five while the swept area of each individual rotor has remained relatively constant. This shows the impact that the various design improvements have made over the course of the testing period.

3.4 Analysis of Collected Data

Over 120 hours of data were collected during the experimental campaign including wind speed, power generation and rotor speed. The analysis of these measurements is presented within this Section.

3.4.1 Data Processing

Prior to any analysis the measured data is processed. Figure 3.20 shows the wind speed and power output that was collected during a test on a single mast mounted rigid winged rotor on the 31$^{\text{st}}$ August 2018. The power and rotational speed data are logged using the power meter, this is extracted after each test session. The VESC and wind data are logged using arduino's, these are connected to a PC and are regularly saved throughout a test session. The steps involved in processing the data are outlined below:
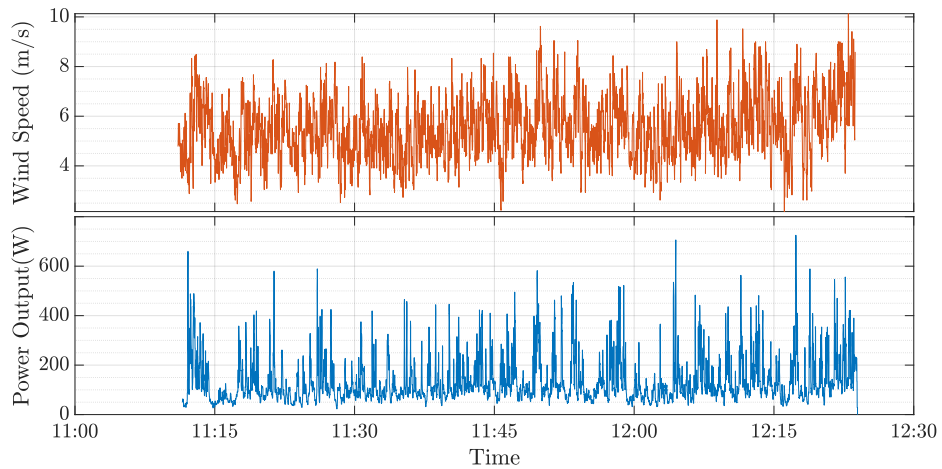
Figure 3.20: Wind speed and power data from 31st August 2018.

1. As multiple data logging devices are used the first step is to match the start and end time stamps for each data set.

2. Any corrupt data points are removed. Any logging errors are removed. As mentioned in Section 3.1.4 the generator can be used as a motor to drive the system forward if required. It is therefore necessary to remove any data points where this is the case. The VESC records at which points such removals are required, this is cross checked with data from the power meter.

3. As the frequency of data varies between the three logged files, the data is averaged so that is can be collated into a single file. The time scales which the data is averaged over are varied from one second up to five minutes depending on what analysis is to be done. If there is insufficient data within the desired averaging time scale the averaged data point is removed. The threshold is set at three quarters of the expected number of readings. For example, the power data has a frequency of 2Hz therefore one minute of data should include 120 readings, if averaging over one minute and there are less than 90 power readings that data is not included in the analysis.

4. Finally any averaged data points that do not include both wind and power data are removed.

After processing all available data, 55 hours of one minute averaged data is suitable for analysis.

3.4.2 Comparing Daisy Kite Configurations

Metrics for Power Generation Efficiency

The following sections compare the various Daisy Kite configurations shown in Table 3.1 to one another. Data from multiple test sessions are used for each configuration. The main metric for comparison is the systems power coefficient, C_p, the ratio between the power extracted by the device to the available power within the swept area, calculated by

$$C_p = \frac{P}{\frac{1}{2}\rho V^3 A} \tag{3.1}$$

where P is the power produced, ρ the air density, A the swept area of the device and V the wind speed. For the soft rotors, where the inner kite tip is at a radius of 1.16m and the outer tip is at a radius 2.43m, this corresponds to a swept area of 14.3m^2. For the rigid rotors, with inner tip radius of 1.22m and outer tip radius of 2.22m, the swept area is 10.8m^2. For systems that use multiple rotors the swept area is multiplied by the number of rotors.

The tip speed ratio, λ, is also used. This is the ratio of the rotors tip speed to the wind speed. Plotting the tip speed ratio against the power coefficient gives the non–dimensional power curve and is frequently used to compare the power generation efficiency of wind turbines. This has been used to compare the various Daisy Kite configurations.

As introduced in Section 2.4 the power harvesting factor, ζ, is the ratio between the power extracted and the power available in a cross–sectional area equal to the wing area of the device. It is calculated by

$$\zeta = \frac{P}{\frac{1}{2}\rho V^3 S} \tag{3.2}$$

where S is the wing area. For the Daisy Kite the three bladed soft and rigid rotors have
wings areas of 1.38m^2 and 0.60m^2 respectively.

Number of Rotors

A key design principle of W&I is to network multiple smaller kites together instead of
increasing the size of the kites to increase the power output. Several of their prototypes
have used multiple rotors stacked up a common TRPT. A series of tests were conducted
to compare the efficiency of stacked rotors. These tests used TRPT–2 with 1, 2 and 3
soft rotors, these correspond to configurations 2, 5 and 6 as labelled in Table 3.1. Each
of the individual rotors used during these tests are identical. Figure 3.21 shows the
power and C_p vs λ curves for Daisy Kite configurations 2, 5, and 6. The plots show one
minute averaged data.

The power curve data shown in Figure 3.21(a) indicate that, as would be expected,
the power output increases with the number of rotors. However, the increase is not
proportional to the increase in swept area.

The C_p vs λ plot shown in Figure 3.21(b) gives a clearer comparison between the three
configurations. It can be seen that the single and dual rotor set ups have similar C_p
values, but that the C_p values for the triple rotor configuration are lower. With the
systems tested, as rotors are added the spacing and elevation angle is such that down-
wind rotors will be partially in the wake of upwind rotors. This reduces the wind speed
and increases the turbulence that rotors further downwind will experience. The C_p for
downwind rotors will therefore be lower, reducing the overall systems power coefficient.
This can be seen in the reduction in C_p for the triple rotor configuration compared to
the single and dual rotor cases.

The power coefficients for the single and dual rotor cases are similar due to the relatively
low tip speed ratios that the system is being operated at. At lower tip speed ratios the

rotor blades will disturb less of the air passing through them, therefore downwind rotors
will be less affected by the wake of upwind rotors. It is likely with the prototypes tested,
that a single rotor upwind did not interact with the flow enough to be visible in the
data but when two upwind rotors were present, as in the triple rotor case, the power
reduction in the third rotor is noticeable.
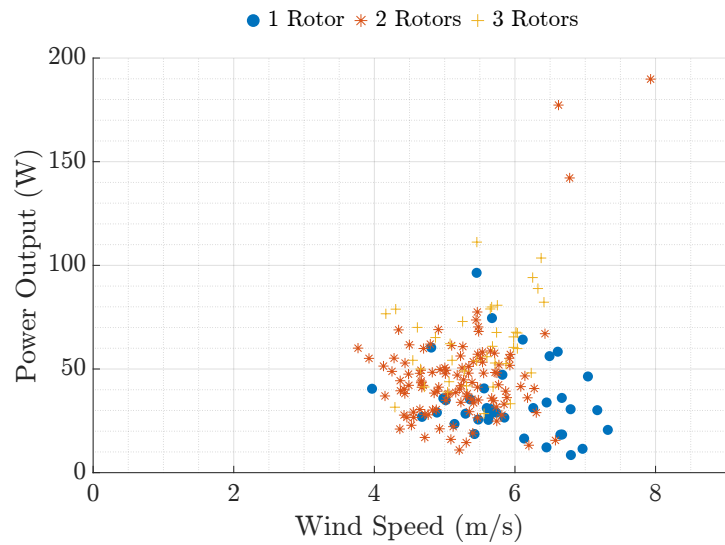
(a) Power output
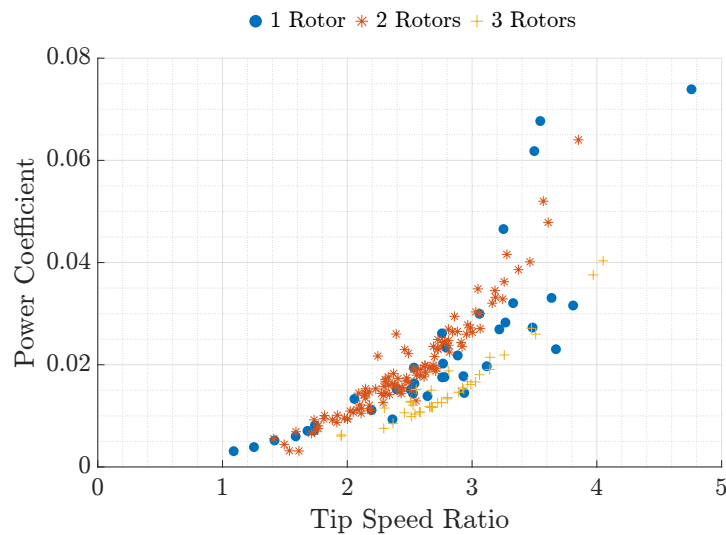
(b) Power coefficient

Figure 3.21: Comparison of 1, 2, and 3 soft rotors using TRPT–2.

As discussed in Section 2.3.2 the stacking of multiple rotors on a common shaft presents several challenges. It is desirable to avoid the rotors operating in the wake of upwind rotors if possible. Increased spacing between rings may reduce the effects of the turbulent interaction between rotors. The design of each individual rotor should be refined, to ensure that each rotor contributes to the overall power and operates close to its optimal rotational speed, for the wind conditions that it experiences. This work does not focus on the use of multiple rotors on a common shaft. The collected data highlights that if multiple rotors are to be used more research is required to better understand how this impacts individual rotors and the system as a whole.

Wing Material

A crucial improvement made during the experimental campaign was the transition from soft kites to rigid blades. The motivation for this transition was to increase the power output of the Daisy Kite. Figure 3.22 shows the power output and C_p vs λ curves for single rotors, using TRPT–3, for both soft kites and rigid blades. The prototypes used for this comparison correspond to configurations 3 and 7 in Table 3.1. The data points shown are one minute averages.

Figures 3.22(a) and 3.22(b) show that the rigid blades have a power output that is much larger than the soft kites. The power coefficient of the soft kites is around 0.05, whereas for the rigid blades C_p values of greater than 0.2 are achieved. In terms of power harvesting factor the soft kites have maximum values of 0.75 whereas the rigid blades achieve ζ values of over 4.

It can also be seen from Figure 3.22(b) that the rigid blades were operated at a higher tip speed ratio. The Daisy Kite's rotor is similar to a HAWT, it will therefore have an optimal tip speed ratio at which a maximum power coefficient is achieved. For the Daisy Kite this optimal tip speed ratio is dependant upon the aerodynamics of the rotor and the TRPT. As TRPT–3 was used for both the soft and rigid wings in this comparison

93

the change in tip speed ratio is due to the improved aerodynamic efficiency of the foam blades.

The soft kites were selected primarily due to their low cost and resistance to impacts. They were designed as a beginners two line kite, not for use within an AWES. By comparison the foam blades profile were selected specifically for the Daisy Kite rotor, to
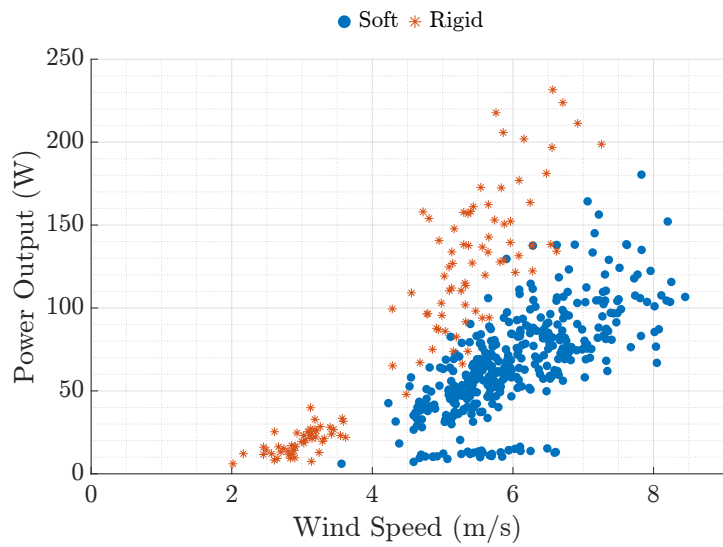
(a) Power output
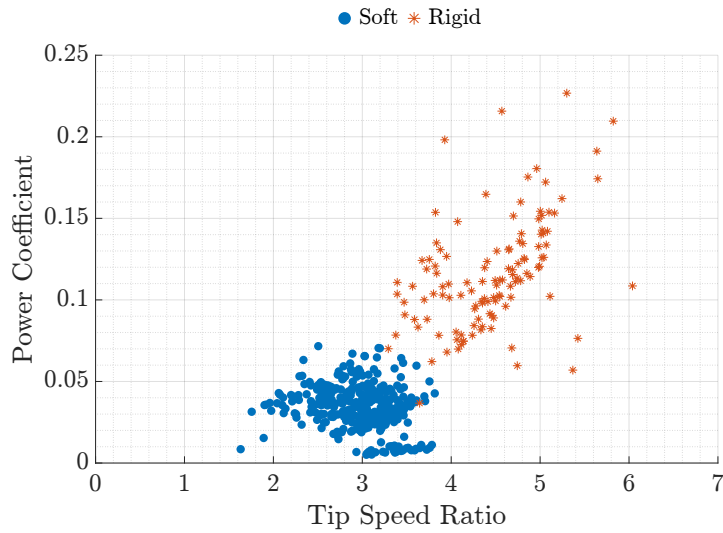
(b) Power coefficient

Figure 3.22: Comparison between a single soft and rigid winged rotor using TRPT–3.

increase power output. This coupled with the improved aerodynamic performance of a rigid wing compared to a soft wing explains the significant rise in power output by moving to the foam blades.

Although the rigid blades allow for higher power generation it may still be advantageous to use soft kites. The soft kites are lighter and are able to survive larger impacts compared to the foam wings. Figure 3.23 shows the standard deviations of the one minute averaged points shown in Figure 3.22(a). It can be seen in Figure 3.23 that for similar variations in wind speed the rigid blades produce larger variations in power output. This demonstrates that the rigid wings are more susceptible to wind speed fluctuations. Although the flexible nature of the soft kites reduces their aerodynamic performance, it allows them to dampen some of the flow turbulence. This highlights another potential advantage of using soft kites over rigid blades. A Daisy Kite system that uses rigid wings will have larger variations in power output, this will put additional strain on the systems components which must be accounted for within the systems design.

As mentioned in Section 2.1.3 there seems to be a trend towards rigid wings within the AWE community but there are several organisations still developing systems based on
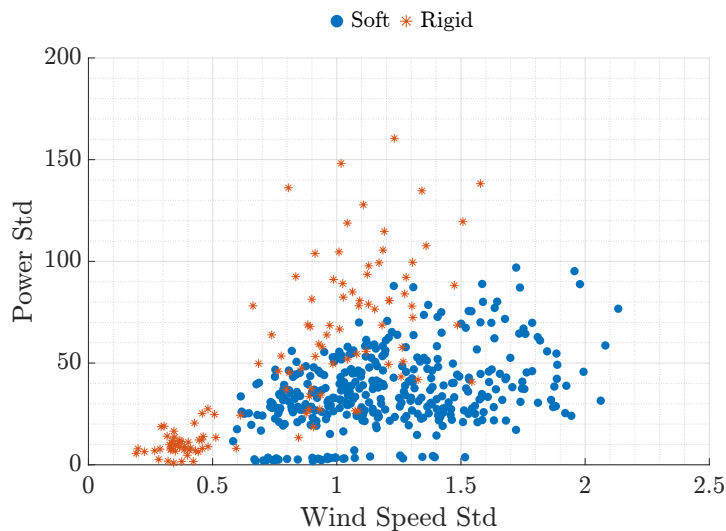
Figure 3.23: Comparison between the standard deviations, of the one minute averaged, power output for the soft and rigid winged rotor.

soft kites. It is clear from the tests conducted on the Daisy Kite that the foam blades result in higher power generation. However, depending on the systems application soft kites may by more suitable, due to their weight, crash survivability and smaller storage volume. It is also envisaged that a soft kite designed specifically for use within the Daisy Kite would improve the performance of a soft wing based system.

Rigid Blade Pitch

The blades angle of attack will vary along its length and as the rotor rotates. On the rigid blades the pitch of the blade is set at it's root, where it connects into the fuselage socket. The pitch that the blades are set to will alter the blades angle of attack, affecting the performance of the rotor. During the experiments two different pitch angles were tested, 0° and 4°. Figure 3.24 shows the plots of the power coefficient against the tip speed ratio for both pitch angles. In these tests a rigid winged rotor with TRPT–3 was used, this corresponds to configuration 7 in Table 3.1. The points shown are one minute averages.

Figure 3.24 shows that there is only a small difference in the collected data between
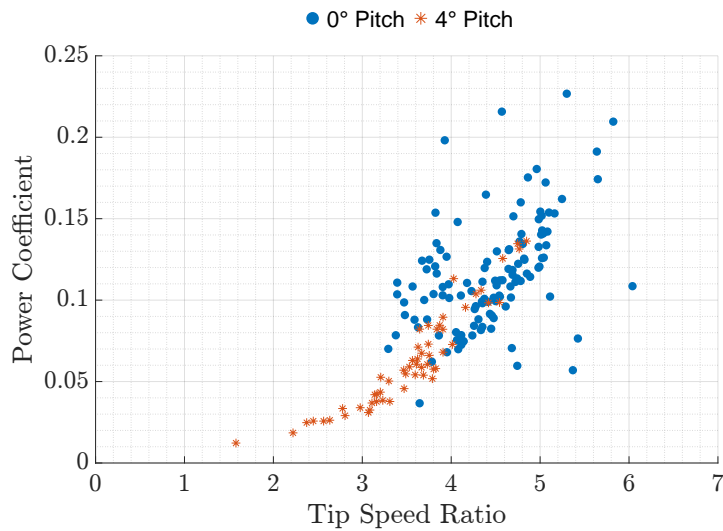
Figure 3.24: Power coefficient for single rigid rotor with 0° and 4° blade pitch.

96

the 0° and 4° blade pitch angle. The C_p vs λ plots for both blade set ups are similar,
however, the power coefficient for the 0° pitched blades cover a larger range for similar
values of λ. The comparison between different blade pitch angles is expanded upon
in Section 5.3.2, using the mathematical models described in Chapter 4. All the rigid
wings on configurations 8 and 9 were manufactured with a blade pitch angle of 4°.

Length of TRPT and Tether Drag

Five different TRPT have been tested with the overall length varying from 6.74m up
to 10.31m. As discussed in Section 2.1.5 the tether drag for an AWES can cause a
significant amount of power loss. To investigate the tether drag within the Daisy Kite,
data collected using TRPT–3 and TRPT–4 are compared. TRPT–3 has a total length
of 6.91m and TRPT–4 a length of 10.31m. Figure 3.25 shows a comparison between
configurations 7 and 8. It is noted that data shown from configuration 7, using TRPT–
3, includes data using both 0° and 4° pitched blades. As the comparison between the
different pitch angles, shown in Figure 3.24, shows only a small difference for the two
pitch angles. The data points shown are one minute averages.

The power output shown in Figure 3.25(a) shows that the power output from TRPT–3,
with the shorter overall length, is similar to that produced using TPRT–4. The com-
parison of the power coefficients in Figure 3.25(b) shows that the values for the shorter
TRPT appear to be slightly higher for similar tip speed ratios. It can also be stated
from analysing the C_p values in Figure 3.25(b) that the C_p for TRPT–4 reduces as λ is
increased above a value of 4.5, whereas for TRPT–3 the values continue to increase. As
the TRPT increases in length the impact of tether drag will become larger. This will
cause two effects in relation to the C_p vs λ plots. Firstly, as the tether drag is increased
the power output of the system will decrease, reducing the power coefficient. Secondly,
the higher the tip speed ratio, the faster the system rotates. As the system rotates faster
the tether drag will become larger. The increased tether drag experienced by longer
TRPT will reduce the power output by a larger proportion at higher tip speed ratios

compared to lower tip speed ratios. These two factors will cause the C_p vs λ curve to move towards lower values of C_p and λ simultaneously as the TRPT length is increased.

The impact of tether drag on the Daisy Kite is investigated further in Section 5.3.3, utilising the mathematical models that are introduced in Chapter 4.
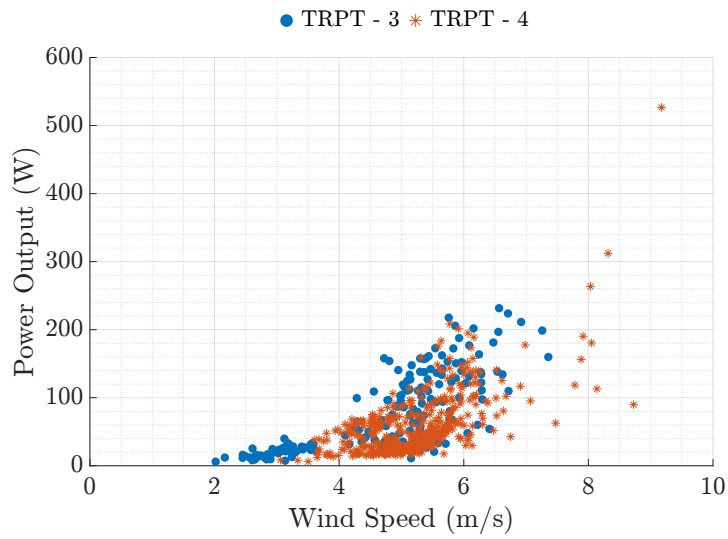
(a) Power output
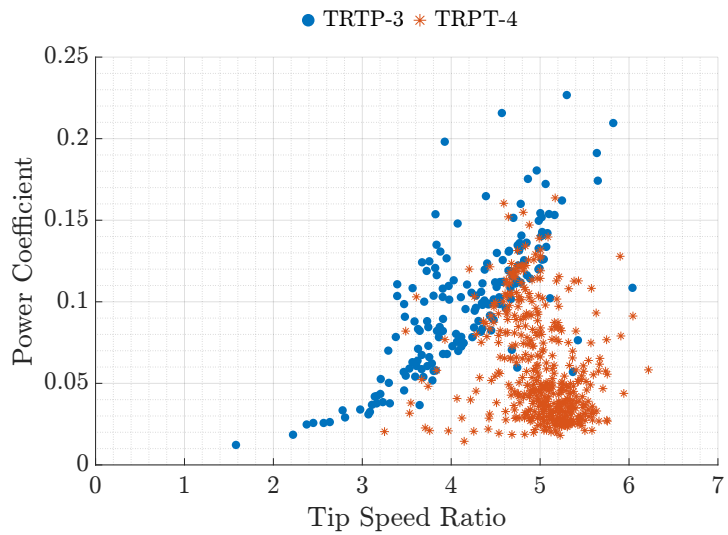
(b) Power coefficient

Figure 3.25: Comparison between TRPT–3 and TRPT–4.

Number of Blades

Most Daisy Kite prototypes use rotors that consist of three equally spaced blades or wings, similar to large HAWT. The most recent prototype, configuration 9, used six foam blades. The collected data for these tests are compared with the results from a three bladed rotor in Figure 3.26, the points shown are one minute averages. The Daisy Kite configuration 9 is the only prototype tested that uses TRPT–5. The 6–bladed
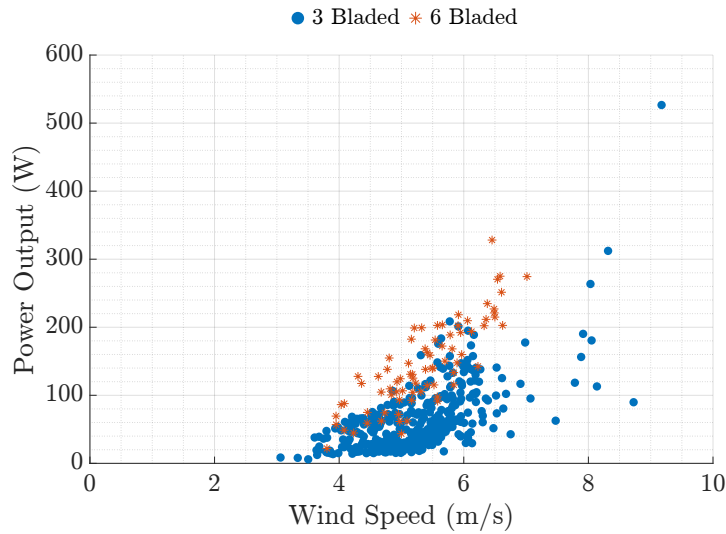
(a) Power output
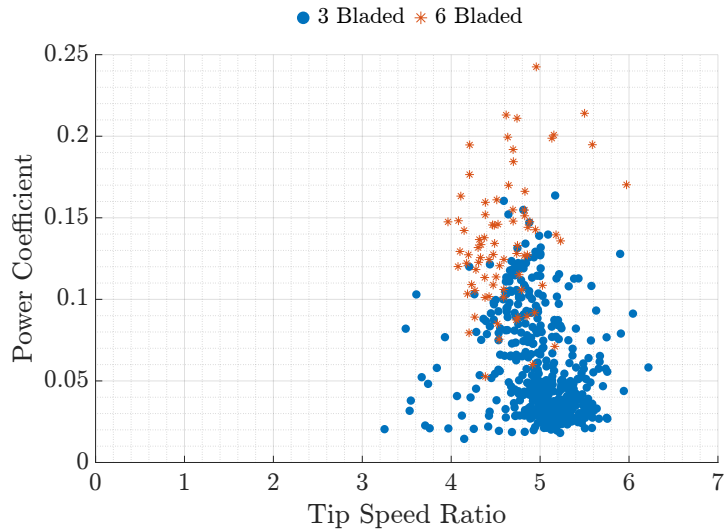
(b) Power coefficient

Figure 3.26: Comparison between a single rigid rotor using 3 and 6 blades

99

rotor is therefore compared to configuration 8, which uses a three bladed ridged winged
rotor and TRPT–4. As can be seen from Figures 3.12(c) and 3.13, TRPT–4 is 0.8m
longer than TRPT–5 and the first six rings on TRPT–5 have a slightly larger diameter
than those on TRPT–4. It is expected that these two TRPT will perform similarly in
relation to the power output. As described in Section 3.1.3, the main changes made
from TRPT–4 to 5 were aimed at increasing the axial force on the six outer tethers and
removing any residual stress within the rings.

The power output from the two prototypes is shown in Figure 3.26(a). It can be seen
that the 6–bladed rotor produces more power than the 3–bladed in similar wind speeds.
The C_p vs λ plot shown in Figure 3.26(b) also confirms this as the 6–bladed rotor is
able to achieve higher power coefficients at similar tip speed ratios. A rotors solidity
is defined as the percentage of the swept area occupied by the blades. The 3–bladed
rigid rotors have a solidity of 5.5%, this is similar to large HAWT. Large HAWTs have
a optimal tip speed ratio in the region of 6 or 7. From analysing the C_p vs λ results
shown in Figures 3.25(b) and 3.26(b), it can be stated that C_p values reduce as the tip
speed ratio is increased above a value of 4.5 for the 3–bladed rotors . This indicates
that they have an optimal λ less than 4.5. A lower tip speed ratio indicates that a rotor
solidity that is more than a large HAWT would increase the power output for the Daisy
Kite. The tests using the 6 blades confirm this as the higher solidity has resulted in
more power being generated.

3.5   Daisy Kite Observed Operational Behaviour

As well as comparing the various Daisy Kite configurations the collected data has been
used to analyse the Daisy Kites operational behaviour. The Daisy Kite's rotor is very
similar to that of a HAWT, the rotor in isolation will therefore share some operating
characteristics with HAWT. The use of TRPT to connect the flying rotor to the sys-
tem's generator is only seen within rotary AWES. The experimental data has been used
to identify previously unknown operating characteristics.

3.5.1 Constant Speed Tests

During the experimental campaign several constant speed tests were run. The aim of these tests was to provide data so that more complete C_p vs λ curves for the Daisy Kite could be used for analysis. Figure 3.27(a) shows the rotational speed of the Daisy Kite during constant speed tests on the 5th June 2018. In this test a single soft rotor using TRPT–2, configuration 4, was run at multiple rotational speeds for short periods of time. In can be seen from Figure 3.27(a) that the rotational speed was held relatively constant at several set points. After processing the data, six periods of constant speed operation are selected for further analysis. Figure 3.27(b) shows the processed one minute averaged data for the six selected periods.
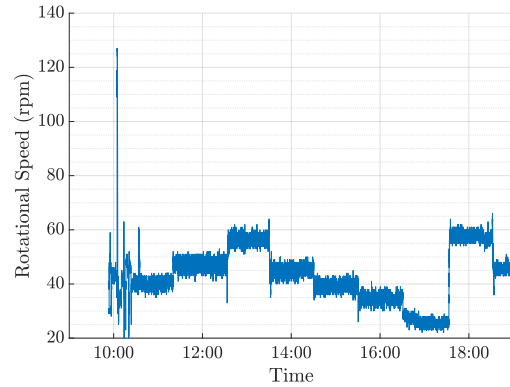
(a) Raw data
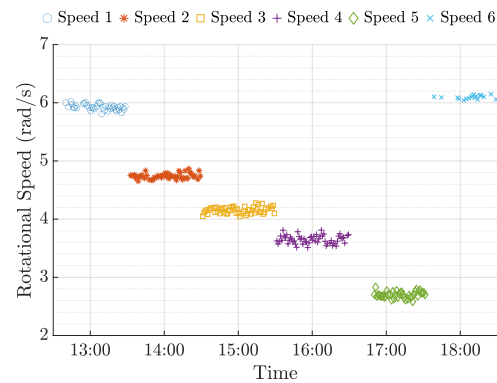
(b) Processed one minute averaged data

Figure 3.27: Rotational speed data collected during constant speed tests on 5th June 2018.

Figure 3.28 shows the power coefficient against tip speed ratio for the data shown in Figure 3.27(b). The different constant speeds can be clearly seen to occupy different regions of this C_p vs λ plot. Due to concerns about running the prototype at very high rotational speeds, close to overspeed, there is limited data for higher tip speed ratios.
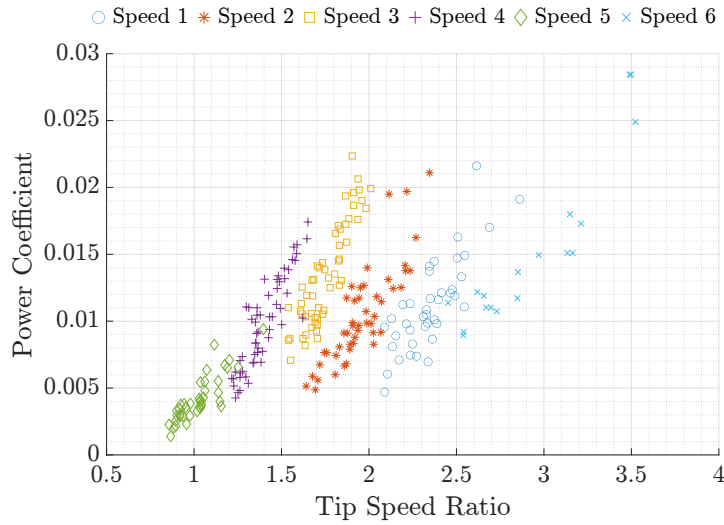
Figure 3.28: C_p vs λ plot for the constant speed test conducted on 5th June 2018.

Constant speed tests were also attempted using a rigid winged rotor, TRPT–3, configuration 7. Figure 3.29 shows the rotational speed data for the constant speed test on 23rd August 2018. Comparing this data with the soft winged rotor, shown in Figure 3.27(a), it can be seen that the variations in rotational speed are much greater for the rigid winged ro-
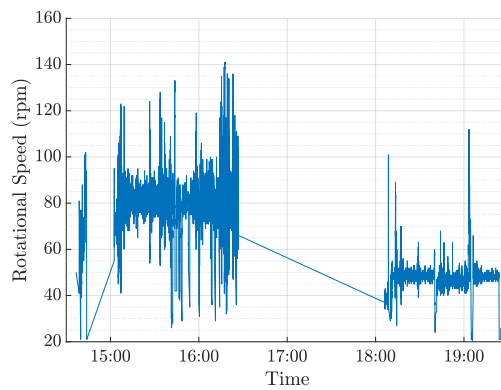
Figure 3.29: Rotational speed for constant speed test conducted on 23rd August 2018.

tor. Given these large fluctuations only two constant speed periods were identified from the test data, the higher speeds risked causing catastrophic damage to the system. During these tests it was noted that the speed variation was oscillating periodically. By analysing videos taking during the tests the period of oscillation was estimated to be around 8 seconds. To investigate this further the power spectral density of the normalised power data was calculated.

Figure 3.30 shows the power spectral density for the rigid winged data from the 23rd August 2018, during constant speed tests, and from 20th September 2018 during a non–
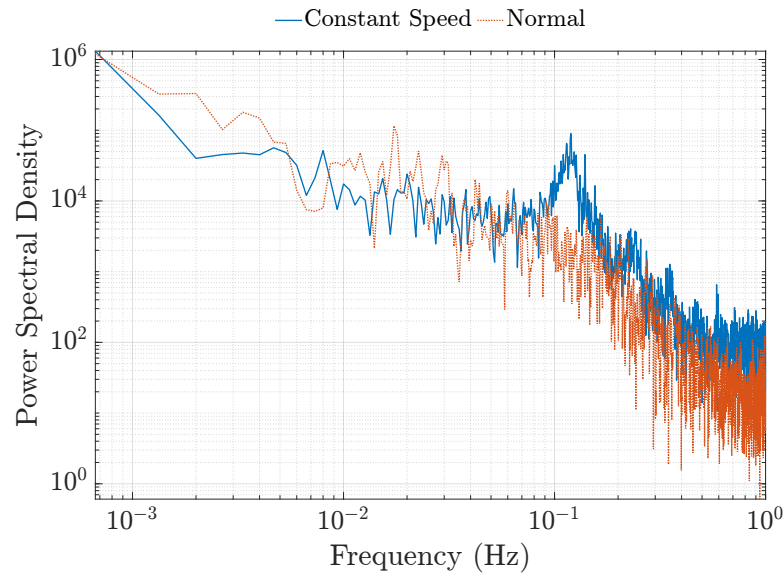
Figure 3.30: Power spectral density for both constant speed and non-constant speed tests on a single rigid winged rotor.

constant speed, or normal, test. It can be seen that there is a large peak at a frequency of 0.12Hz in the constant speed data, this corresponds to an oscillation period of just over 8 seconds. This peak is not present within the non–constant speed data. This suggests that while attempting to control the rotational speed of the system, harmonic oscillation has been introduced. This may be due to the controller used, it does not account for the response of the TRPT and has therefore resulted in unstable motion. The non–constant speed, or normal, operation does not show any significant peaks in Figure 3.30. The constant speed tests were run using the VESC's inbuilt constant speed controller, during normal operation the VESC is combined with the control algorithm developed by W&I, described in Section 3.1.4. The W&I algorithm reduces the controller action, as the ramp rate of the generators reaction torque is limited. It is noted that the data is recorded at a frequency of 2Hz, it is therefore not possible to identify oscillations at higher frequencies.

The power spectral density for soft winged rotor tests was also calculated. Figure 3.31 shows the power spectral density of the data collected during constant speed tests on the 5th June 2018 and non–constant speed tests on 28th August 2018. Similar to the
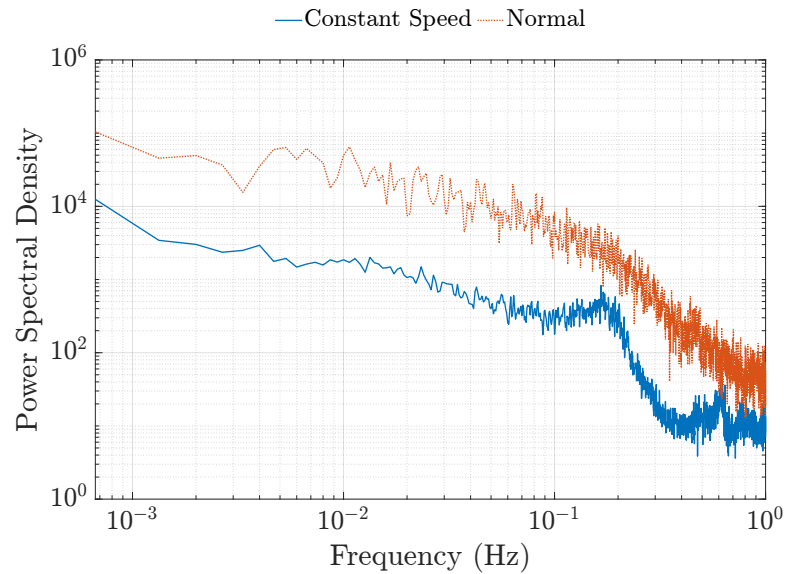
Figure 3.31: Power spectral density for both constant speed and non-constant speed tests on a single soft winged rotor.

rigid case it can be seen that during the constant speed tests a peak is present. The peak within the soft blade data is much lower explaining why these oscillations were not noticed during the tests. In the case of the soft wings, this peak occurs at a slightly higher frequency of 0.17Hz corresponding to an oscillation period of just under 6 seconds. Again this peak does not appear under non–constant speed, or normal, operation. This again suggests that it might be the constant speed control that causes the undesirable harmonic behaviour.

If constant speed control is implemented in the future it must be improved to remove the large oscillations. The harmonic behaviour increases the fatigue loading on the device, reducing its operational lifetime.

Response to Gusts

During the multiple tests the Daisy Kite's behaviour during gusts was of particular interest. Two characteristics of the system were identified in relation to its response to changes in wind speed, the first due to the flexible nature of the TRPT. The more

104

torque that is applied to the TRPT the larger the rotational deformation. As the TRPT deforms rotationally the distance between the rings becomes smaller, the rings are pulled together reducing the overall length of the TRPT. If the wind speed increases over a short period of time, for example, during a gust of wind, the torque applied to the TRPT is temporarily increased. This causes the TRPT length to shorten pulling the rotor towards the ground station. As the rotor is pulled towards the ground station it travels upwind, increasing the relative wind speed that it experiences and in turn increasing the torque that it produces. Thus creating a positive feedback loop as the wind speed increases. The reverse is true for a decrease in wind speed as the rotational deformation of the TRPT will reduce, causing the rotor to travel downwind. Figure 3.32 shows diagrams of TRPT–4 before and during a gust passing through the Daisy Kite system. In Figure 3.32(b), during the gust, the rotor is pulled upwind by 1.2m compared to Figure 3.32(a), just prior to the gust.

Is was also noticed that during a gust, if using a lift kite, the elevation angle of the system would decrease. This reduction in the elevation angle results in the misalignment between the rotor and the oncoming wind becoming smaller. This increases the power and torque output of the rotor and further adds to the positive feedback loop caused by the flexible nature of the TRPT. These two characteristics result in the Daisy Kite's power output increasing by a larger amount, than would be initially expected, from the

(a) Prior to gust   (b) During gust
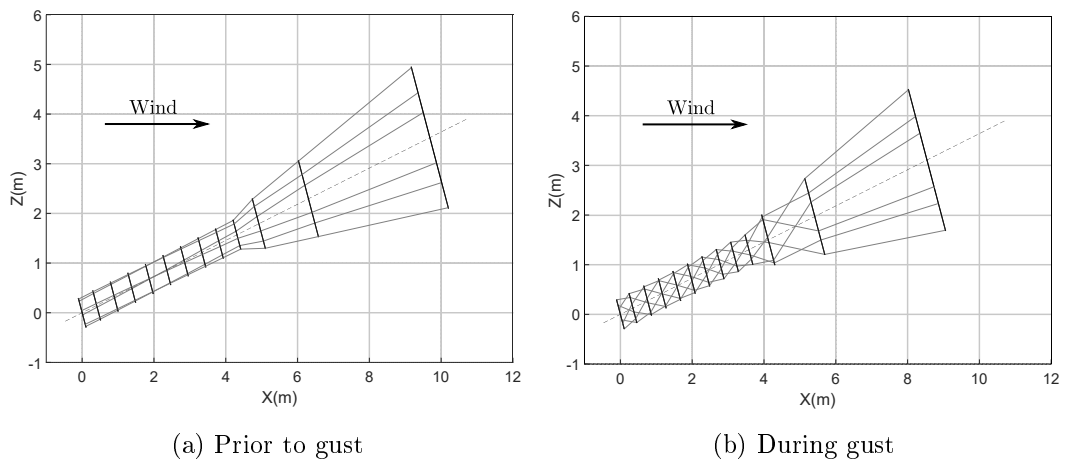
Figure 3.32: Diagrams of TRPT–4 before and during a gust.

increase in wind speed. It also highlights the highly dynamic operation of the Daisy Kite. The movement of the Daisy Kite's rotor and TRPT during operation affects the relative wind speed that the rotor experiences and therefore the power output and loading on the system. Operational characteristics such as these must be better understood if the Daisy Kite's design and operational control is to be improved. The Daisy Kite's operational behaviour is discussed further in Chapter 5.

3.6 Summary

This chapter has detailed the experimental campaign that has been conducted in collaboration with W&I. The 9 configurations of the Daisy Kite that have been tested were introduced along with the testing procedure. The two aims of this experimental works were to:

1. Improve understanding of the Daisy Kite's design characteristics and operational behaviour.

2. Provide empirical data to compare with the mathematical representations of the Daisy Kite.

Through analysing the collected data the understanding of the Daisy Kite's operating characteristics have been improved. This is demonstrated through the various design upgrades that were made throughout the experimental campaign. These have resulted in the devices power output increasing by a factor of almost five. Observations made during the multiple testing sessions have identified the highly dynamic nature of the system, in particular its behaviour during gusts. As the Daisy Kite system is scaled up in size and power output, its dynamic characteristics must be explored in more depth. The Daisy Kite's operational behaviour is explored further in Chapter 5.

Over 120 hours of operational data, using 9 different rotor and TRPT configurations, has provided empirical data for comparison with the mathematical representations that are described in Chapter 4. The testing of several Daisy Kite prototypes has ensured

that the developed models can be compared to experimental data from a wide range of rotor and TRPT configurations. This provides additional reassurance regarding the models accuracy and reliability.

Chapter 4

Model Development for Tensile Rotary Power Transmission Systems

This chapter describes the steps that have been taken to develop a mathematical representation of rotary AWES. The model focuses on designs that use TRPT and is based on the Daisy Kite system developed by W&I. As mentioned in Chapter 2 rotary AWES are unique in design and operation, where holistic investigation is expected to improve the systems performance. The mathematical representations described in this chapter will help to improve the understanding and knowledge surrounding rotary AWES, specifically those that utilise TRPT. Accurate modelling of the systems dynamics is a prerequisite for a number of development tasks, including design optimisation, system analysis and controller design.

4.1   System Model Overview

Other than this work, the only mathematical representation of a rotary AWES, that incorporates TRPT, was undertaken by Benhaïem and Schmehl [7]. They analyse the steady state operation of the RRP system described in Section 2.2.4. The aim of the

mathematical model, presented in this chapter, is to develop an initial dynamic representation of a rotary AWES, that utilises TRPT. As highlighted in Section 3.5, the Daisy Kite has several operating characteristics that require further investigation, primarily the dynamic behaviour of the TRPT.

4.1.1   Modelling Objectives

Alongside the aim of producing an initial dynamic representation, the key objectives for the models development are as follows:

1. Improve the understanding of rotary AWES, specifically those that use TRPT. TRPT is academically an unexplored method of power transmission. The creation and use of a mathematical representation for rotary AWES improves the knowledge surrounding this method of power transmission.

2. Improve the design of the Daisy Kite and systems of similar design.
   With a full system model a comprehensive design review of rotary AWES is possible. The devices can be analysed and individual/groups of components can be optimised to improve the overall performance of the system.

The method of transmitting power using rotating taut lines is not a new concept [14]. However, very little research has been undertaken on it in relation to wind energy generation. Usually torque is transmitted over short distances using rigid shafts. TRPT aims to transmit torque over very large distances while minimising weight. Previously the development of TRPT has been driven by trial and error using small scale prototypes mainly the Daisy Kite [77], the RRP [7] and someAWE airborne turbine, [8] as introduced in Section 2.2.4. By incorporating model based analysis it is possible to develop a systematic view of the TRPT mechanism, speeding up and reducing the cost of the development process.

4.1.2   Overall System Model Configuration

The full system model consists of a series of connected individual modules. These individual modules are established by analysing rotary AWES and identifying their main component groups and modelling parameters. Similar to any other AWE device there are three main component groups, these are:

1. Power extraction

    The airborne components that are responsible for harnessing the power from the wind. This is usually a series of wings that follow a set flight path. In the case of Fly–Gen rotary AWES this also includes the generator.

2. Power transmission

    The power transmission transfers the power between the airborne wings and the ground station. This can be achieved either mechanically or electrically. Communication between the ground station and airborne device is often achieved using these components e.g. signals are sent up the tethers, either mechanically or electrically, to alter the airborne components operating state.

3. Ground station

    All the airborne components are connected to the ground through the ground station. For Ground–Gen system this also houses the generator.

A block diagram of the individual modules used within the rotary AWES model are shown in Figure 4.1. This shows how the modules are connected and how they are combined to form the three main component groups. The two–way connections between modules expresses the existing coupling between system components. For several modules there are multiple versions of varying complexity and computational demand. This has allowed the development of three full system representations, these are briefly outlined below:

1. The first, and most simplistic, provides an initial prediction for the power output, efficiency and overall forces for a given system geometry in steady conditions.

2. The second model provides an initial representation of the Daisy Kite's dynamic behaviour.

3. The third, and most complex representation, allows for a more detailed analysis of the the systems dynamic response.

The remainder of this chapter introduces each of the individual modules, describing the theory behind each and how they have been implemented to form the full system representation. The full representation has been developed in MATLAB and includes a number of third party open source software packages. The power extraction subsystem and its key modules are presented in Section 4.2. The ground station is described in Section 4.3. The modules that make up the power transmission subsystem are detailed in Sections 4.4, 4.5, 4.6 and 4.7. Finally this chapter is concluded in Section 4.8.
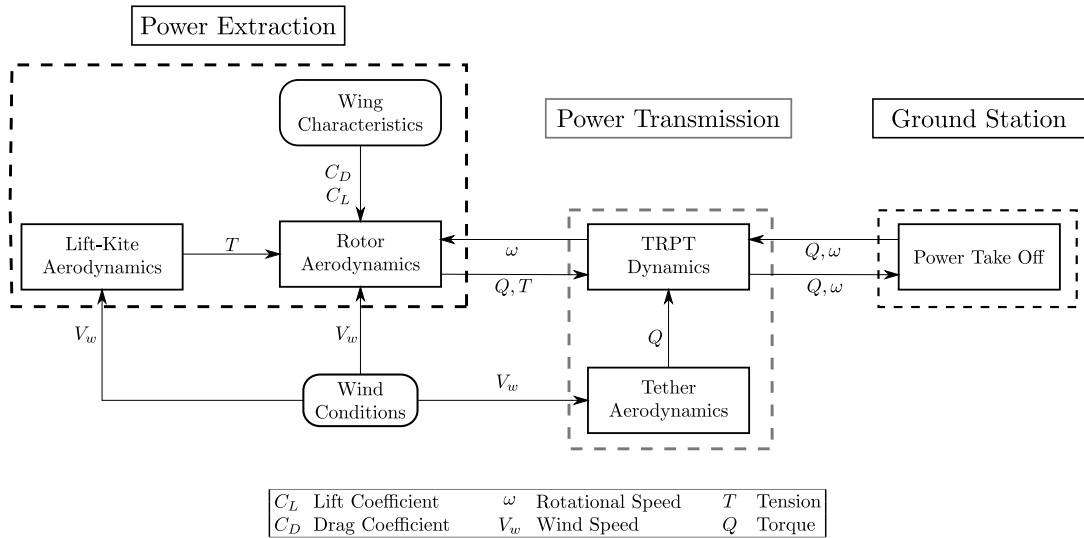
Figure 4.1: Block diagram of the rotary AWES and its modules, the key variables are indicated.

4.2   Power Extraction

4.2.1   Rotor Aerodynamics

The rotor aerodynamics module is the central module within the power extraction group. In the most simple context the power extraction of an AWES is represented by a point force. In this case the aerodynamic forces on the wing, calculated using the 2D aerofoil lift and drag equations, are assumed to act at a single point at the end of a tether. This representation, used by Loyd [54] in the first analytical analysis of an AWES, provides a first approximation for the power that an AWES can harvest. This representation is still widely used due to its simplicity and low computational requirements. As the AWE industry has developed, the complexity and accuracy of the modelling methods, used to estimate the power harvesting potential of various AWES, have also increased. The level of accuracy and details of a model can be decided depending on the modelling requirements and computational resources. From the point representation used by Loyd to sophisticated multi–body representations such as that described by Breukels and Ockels [109].

The methods developed to model the power extraction of AWES have focused mainly on single–wing devices. There are several studies that have investigated the power harvesting potential of rotary AWES. The majority of these have focused on devices similar to the WATTS developed by Sky WindPower, introduced in Section 2.2.4. As this rotary AWE device is similar to the autogyro and helicopter, many of these studies are based on the modelling of autogyro's and helicopters. Rimkus and Das [110], Mackertich and Das [111] and Roberts [112] all use blade element momentum theory (BEM), first employed by Glauert [68] to analyse autogyros, to predicted the forces produced by the rotor.

Due to the configuration of multiple wings to form rotors, the power extraction of rotary AWES share more similarities with horizontal axis wind turbines (HAWT) than with most other AWES. Similar to HAWT, rotary AWES use several wings/blades that

rotate around a central point or hub. Due to this, and the well developed methods that are used to mathematically model HAWT, this research has used modelling methods usually associated with HAWT to represent the rotor aerodynamics. However, due to the required elevation angle for rotary AWES, β, the rotor is tilted/pitched down into the oncoming flow. This causes a misalignment between the rotor plane and the wind vector. This is analogous to a yawed wind turbine as the resulting misalignment of the rotor plane and the wind vector causes similar effects. The modelling of yawed HAWT's is used as a datum for modelling the rotor aerodynamics of rotary AWES. It is also noted that the blades of a HAWT are all connected to a central hub, whereas this is not always the case for rotary AWES. As shown in Section 2.2.4 the rotors of rotary AWES often have open centres. The wings are connected to each other at a distance from the centre of rotation, therefore the centre of the rotor is unfilled. This means that the length of the wings used within rotary AWES can be far smaller than the radius of the rotor. Within this analysis this open centre is accounted for based on existing models of HAWT blade roots.

Two rotor modelling methods, widely used within the wind industry, have been used for the rotary AWES representation. These are the actuator disc model and blade element momentum theory. Both are described in the following two sections.

Actuator Disc Model

The actuator disc model, based on the conservation of axial momentum, provides a simple method for estimating the power generated by a rotor [28]. It is widely used within the wind industry. In actuator disc theory the rotor is treated as a disc or ring that extracts a portion of the available wind energy passing though it. The portion of energy that the rotor is able to extract is referred to as the power coefficient, C_p. Betz used actuator disc theory to show that the maximum theoretical power coefficient for a wind turbine is $\frac{16}{27}$ [113]. Actuator disc theory can also be used to estimate the torque and thrust forces from a rotor based on the torque coefficient C_Q and thrust

coefficient C_T. As an initial estimate of the main forces and the power output from a rotary AWES, actuator disc theory provides a simple and quick method. It also provides an estimate of how a systems elevation angle impacts the power output. As described in [28], applying actuator disc theory to a yawed rotor results in a reduced power output equivalent to $\cos^3 \beta$, where β is the misalignment between the rotors axis of rotation and the wind vector. An elevation angle of $30°$ results in a 35% reduction in the rotors power output. Noura et al. [114] show that this approximation for the power reduction of a yawed turbine provides reliable results through comparison with experimental data. Benhaïem and Schmehl [7] use actuator disc theory to estimate the power output from a rotary AWES. Using the actuator disc model, the power output from a rotor is estimated using (4.1) where ρ is the air density, V_w the wind speed and A the swept area of the rotor.

$$P = \frac{1}{2}\rho V_w^3 A C_p \cos^3 \beta \qquad (4.1)$$

The actuator disc model provides initial estimates of what power output a given rotor geometry can achieve in certain wind speeds at a given elevation angle. It assumes that the performance coefficients of the rotor are known and that the rotor disc is uniform. If more detailed analysis of the rotor is required during operation, e.g. to investigate how the variation in wind speed over the rotor affects or impacts its performance, or how different wings affect the rotors operation, a more sophisticated rotor model is required.

Blade Element Momentum

Blade element momentum theory (BEM) is another rotor modelling method that is widely used within the wind industry. BEM is a combination of blade element theory and the conservation of momentum. BEM theory states that by splitting the rotor into a series of rings, the blade forces at each blade segment can be calculated using the aerofoil performance coefficients and ensuring conservation of momentum. The results from each ring can then be summed to give the overall rotor performance [28,102]. BEM is the most widely used rotor aerodynamic modelling tool within the wind industry due

to its low computational requirements and its proven accuracy [115,116]. As mentioned previously, it has also been used to analyse rotary AWES [110–112,117].

A key assumption with BEM is that each blade section is independent of other sections, therefore the flow over each section can be taken as two dimensional with no flow passing between the sections. As the rotor plane is yawed the flow over the blades becomes more three dimensional contradicting this assumption. The necessary elevation angle of a rotary AWES causes the misalignment of the rotor plane with the incoming wind. Rotary AWES rotors are therefore constantly yawed. This brings into question whether BEM is a suitable modelling method for rotary AWES. There are numerous studies within the wind industry investigating the impact of yaw and the applicability of BEM to yawed rotors. Micallef and Sant [118] provide an overview on the aerodynamics of yawed wind turbines and highlight potential modelling methods. Castellani et al. [119] compare the results obtained from FAST, a BEM based wind turbine modelling tool, their BEM code and wind tunnel experiments for yaw angles of up to 45°. They show that FAST and their BEM code can reliably estimate the rotors power and thrust coefficients, C_p and C_T. Rahimi et al. [120] give a comparison between the results from BEM, computational fluid dynamics (CFD) and wind tunnel experiments for yaw angles of 0° and 30°. This study shows there is good agreement between the different modelling techniques and experimental data for 0° yaw. When the yaw angle is increased to 30° the error between the predicted and experimental blade forces is larger, particularly towards the blade root and tip. Micallef et al. [121] provide a comparison between BEM and wind tunnel tests at a yaw angle of 30°. Their results show that the discrepancy in the power output between the two increases from 0° yaw to the 30° case and that the inaccuracy is greatest for higher wind speeds and higher tip speed ratios.

As highlighted in [118] rotor yaw results in the rotor seeing an asymmetric flow field. Therefore, the magnitude and direction of the apparent wind speed that any individual blade section sees varies over time. This means that yawed rotors may experience unsteady aerodynamic effects which result in the blades experiencing dynamic stall.

Within BEM the lift and drag coefficients are assumed to vary with the angle of attack based on steady flow values. The phenomena of dynamic stall produces hysteresis effects for both the lift and drag. Therefore, the use of steady state 2D lift and drag coefficients, when modelling yawed rotors experiencing dynamic stall, will produce unreliable results. There have been several adaptations developed for BEM to account for this effect. Holierhoek et al. [122] compare three methods: the ONERA, Beddoes-Leishman and the Snel models to experimental results. Their study highlights the improvement gained in predicting the aerofoils lift coefficient from using any of the three models. None of the models significantly outperform the others in terms of their ability to predict the lift coefficient.

The studies in [118–121] demonstrate that for yaw angles of up to 45° the results from BEM are comparable to experimental data but that BEM becomes less accurate as the yaw angle becomes larger. They also show that BEM is less accurate at the blade tip and root, for high wind speeds and for higher tip speed ratios. Given this evidence, the use of BEM to represent the rotor aerodynamics of rotary AWES is only suitable for low elevation angles of 30° or less, for wind speeds of less than 14m/s and for tip speed ratios of less than 7. [122] highlights the advantages of using a dynamic stall model, it is therefore necessary that the BEM code used to model the rotary AWES rotor aerodynamics includes one of the available dynamic stall models.

Given BEM's wide use within the wind energy industry there are several commercial, and openly available, software packages that use it to analyse wind turbine rotor aerodynamics. Examples include; DNV GL's Bladed, HAWC2 developed by the Technical University of Denmark and FAST developed by the National Renewable Energy Laboratory (NREL). This research uses NREL's FAST [123] for a number of reasons. Firstly it is open source software, making it accessible and easy to obtain. Another key advantage of FAST is its modular structure. It is possible to run the rotor aerodynamics module, AeroDyn [124], as a stand alone program. This makes it more simple and less computationally expensive to integrate into a rotary AWES model. AeroDyn has undergone

extensive validation [125–127] and has been used in multiple studies investigating wind turbine rotors [119, 120, 128]. Rancourt et al. [117] used AeroDyn to model the rotors on the rotary AWES, WATTS, developed by Sky WindPower.

In this work, AeroDyn v15 is used as the *Rotor Aerodynamics* module within the rotary AWES mathematical representation. AeroDyn requires input parameters that are explained in [124], several of which are detailed in the following sections. An example of the AeroDyn input files used within the simulations are shown in Appendix C.

4.2.2   Wing Characteristics

A key input into the *Rotor Aerodynamics* module are the aerodynamic properties of the wings used within the rotor. AeroDyn requires the lift and drag coefficients of each wing, for all possible angles of attack, from $0°$ to $360°$. As introduced in Section 3.1.1 there are two wings used by various Daisy Kite prototypes, the HQ Symphony Beach III 1.3 kite and the bespoke foam blades using the NACA 4412 aerofoil profile.

HQ Symphony Beach III 1.3

The HQ Symphony Beach III 1.3 kite is widely available. The wings performance coefficients are estimated from the available literature. The HQ kite is a ram–air kite with a span of 1.3m and a chord that varies from 0.55m at the centre to 0.16m at the tips. The planform of the wing, as used within the mathematical representation, is shown in Figure 4.2.

To identify relevant aerodynamic characteristics the Reynolds number (Re) and aspect ratio (AR) of the wing are required. The Reynolds number is calculated using (4.2), where ρ is the air density, taken to be 1.225 kg/m^3, V_w the wind velocity, assumed to be 10 m/s as a representative value for the Daisy Kite wings, c the chord length and μ the dynamic viscosity of the air, taken as 1.7894×10^{-5} kg/ms. The AR is calculated

Figure 4.2: Planform of the HQ Symphony Beach III 1.3 kite as used within the mathematical representation.

using (4.3) where b is the span of the wing, 1.3m, and S is the wing area, calculated as $0.46\mathrm{m}^2$ using the wings planform shown in Figure 4.2.

$$Re = \frac{\rho V c}{\mu} \tag{4.2}$$

$$AR = \frac{b^2}{S} \tag{4.3}$$

The Re varies from 1.1×10^5 at the tips to 3.8×10^5 in the centre of the kite, the AR is 3.7. These values match with relevant literature. Ghoreyshi et al. [15] present wind tunnel tests on the Clark Y–M15 aerofoil with an AR equal to 3 and a Re equal to 2×10^5. Their experimental study is of particular interest as it is aimed at predicting the aerodynamic characteristics of ram–air parachutes. The wind tunnel tests are conducted using a rigid Clark Y–M15 aerofoil profile with an open leading edge similar to ram–air kites. The results from the wind tunnel tests presented in [15] are used to predict the lift and drag coefficients of the HQ Symphony Beach III 1.3 kite for angles of attack from $0°$ to $30°$ in this thesis work. Outside of this range the performance coefficients are calculated using NREL's AirfoilPrep [129]. AirfoilPrep is a open source package that is designed to extrapolate aerofoil performance coefficients to give the full $360°$ range required by AeroDyn. Figure 4.3 shows the lift and drag coefficients, for all possible angles of attack, that are used for the HQ Symphony Beach III 1.3 kites within

118

(a) Lift Coefficient
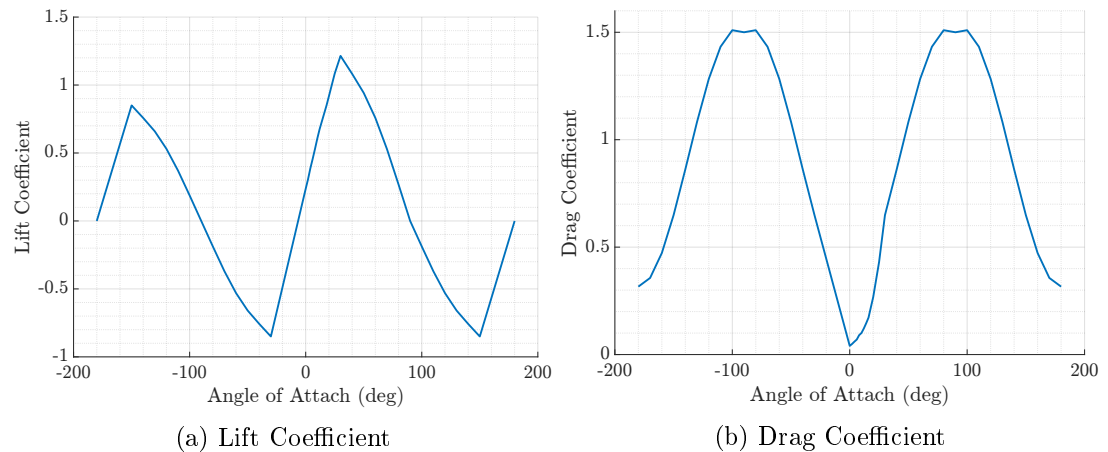
(b) Drag Coefficient

Figure 4.3: The lift and drag coefficients for the HQ Symphony Beach III 1.3 kites used within the mathematical representation. Data from 0° to 30° is taken from [15], outside of this range AirfoilPrep is used to calculated the coefficients.

the mathematical representation. It is assumed that these values do not change along the wings span and, excluding dynamic stall effects, are constant in time. Therefore the aeroelastic nature of the kites are neglected.

NACA 4412

Given the wide and extensive use of NACA aerofoil profiles, the aerodynamic performance coefficients for the NACA 4412 foam blades are defined based on wind tunnel test data from available literature and Xfoil. Xfoil is an open source software developed by the Massachusetts Institute of Technology (MIT). Provided with the 2D shape of an aerofoil, Xfoil calculates the lift and drag coefficients for a given Re and Mach number. The foam blades have a span of 1m and a constant chord length of 0.2m. Using (4.2), (4.3) with the values of ρ, V_w and μ used previously, it can be stated that the Re and AR for the foam blades are equal to 1.4×10^5 and 5 respectively. Ostowari and Naik [16] conducted a series of wind tunnel tests on the NACA 44xx aerofoil series. One of these tests used a NACA 4412 profile with AR of 6 and Re of 2.5×10^5. The results presented in [16], along with the predictions from Xfoil [17], are used to define the lift and drag coefficients for the foam blades for angles of attack in the range from $-10°$ to 110° . For values outside of this range, similar to the HQ kites, the coefficients are

119

(a) Lift Coefficient
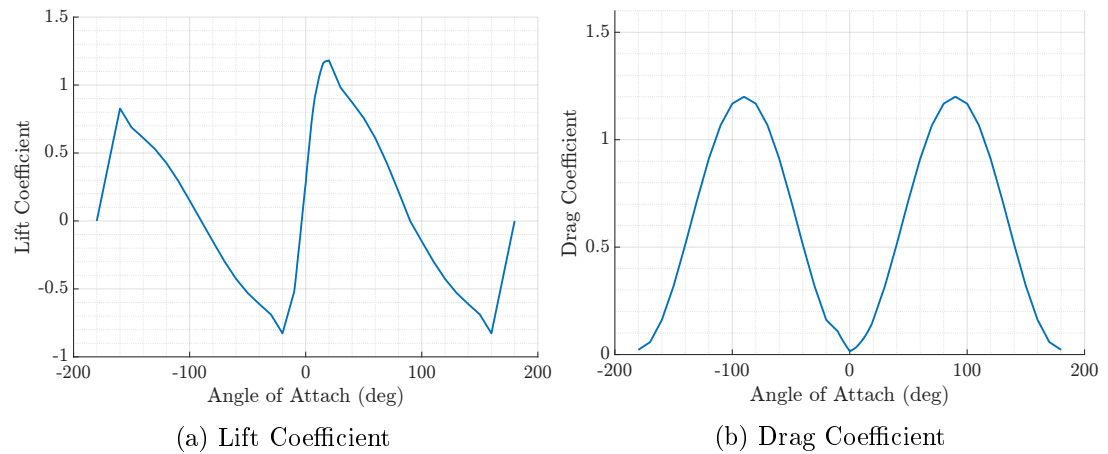
(b) Drag Coefficient

Figure 4.4: The lift and drag coefficients used for the foam blades used within the mathematical representation. Data from $-10°$ to $110°$ is taken from [16, 17], outside of this range AirfoilPrep is used to calculated the coefficients.

calculated using NREL's AirfoilPrep. Figure 4.4 shows the lift and drag coefficients for all possible angles of attack that are used for the NACA 4412 foam blades within the mathematical representation.

4.2.3   Lift Kite Aerodynamics

The lift kite is represented as a static point force. Using the lift kite area S, the lift coefficient, C_L, and the drag coefficient, C_D, the lift kites aerodynamic forces are calculated using (4.4) and (4.5). The values used throughout this analysis are given in Table 4.1. Assuming the elevation angle of the lift kite tether is equal to the elevation angle, β, of the TRPT and rotor, the lift kites aerodynamic force that is

Lift Coefficient	1
Drag Coefficient	0.2
Kite Area	3.2 m^2

Table 4.1: Properties of the Daisy Kite's lift kite.

in–line with the lift kite tether, lk_T, can be calculated from (4.6).

$$lk_L = \frac{1}{2}\rho V_w^2 S C_L \tag{4.4}$$

$$lk_D = \frac{1}{2}\rho V_w^2 S C_D \tag{4.5}$$

$$lk_T = lk_L \sin\beta + lk_D \cos\beta \tag{4.6}$$

Assuming that the lift kite tether is straight, has constant length and has negligible tether drag the aerodynamic force, lk_T, can be taken as the additional axial force that the lift kite provides to the rotor and TRPT.

4.2.4   Wind Conditions

Three different wind models have been used throughout the modelling and simulation process:

1. The first, and most basic representation, assumes that the wind field is both uniform and constant. Therefore there is no variation in wind speed with location and time. This simple representation of the wind is used to analyse the steady performance of the three system models.

2. The second wind model assumes that the wind speed varies with time but is uniform in the plane perpendicular to the winds direction. This wind representation allows for investigation into the dynamic response of the system.

3. The third wind field representation used accounts for the variation of wind speed in both time and altitude. The variation of wind speed with altitude is taken into account using the power law below [102]

$$V_z = V_{ref} \left(\frac{H_z}{H_{ref}}\right)^\psi \tag{4.7}$$

where V_{ref} is the wind speed at reference height H_{ref}, V_z is the wind speed at

height H_z and ψ is the shear exponent that depends on the surface roughness. Table 4.2 shows values of the shear exponent, ψ, for different types of terrain. Unless otherwise states the shear exponent, ψ, is assumed to be 0.2 throughout this analysis. AeroDyn uses the power law in (4.7) to represent the wind shear. Using the same wind shear model for the entire system ensures that it is straight forward to integrate all modules into the same modelling scheme. The power law model is widely used within the wind industry as a simple representation of the variation of wind speed within the atmospheric boundary layer [102, 130]. It is noted that several simulations have been run incorporating wind shear but assuming the the wind speed does not vary with time.

Terrain	Shear Exponent ψ
Smooth hard ground, calm water	0.10
Tall grass on level ground	0.15
High crops, hedges and shrubs	0.20
Wooded countryside, many tress	0.25
Small town with trees and shrubs	0.30
Large city with tall buildings	0.40

Table 4.2: Shear exponent for various terrain types [20].

The second and third wind models use NREL's TurbSim [131] to generate the wind files used within the simulations. TurbSim is a software package, developed by NREL, for generating flow fields for wind and tidal flows. Within TurbSim the Kaimal spectra model is used to model the wind turbulence. Turbulence intensities are based on the normal turbulence model (NTM) as set out in IEC 64100-1 [132].

4.3   Ground Station – Power Take Off

The ground station consists of several components and houses the systems drivetrain. The components that make up the drivetrain include, a wheel, that the TRPT connects

to, a chain drive, a power meter, a disc brake and the generator. To account for the rotating mass of the drivetrain the mass of the bottom TRPT ring is made to be heavier then upper rings in the TRPT. The bottom ring of the TRPT represents the wheel on the ground station that the

Generator mass	5.5 kg
Generator outer radius	0.12m
Wheel mass	0.85 kg
Wheel radius	0.21 m
Other moments of inertia	0.002 kgm^2

Table 4.3: Properties of the rotating components within the Daisy Kite ground station.

TRPT connects to. Within the Daisy Kite, this wheel is made from stainless steel and therefore has a larger mass compared to the other rings of the TRPT. The rings within the TRPT are constructed from carbon fibre tubes. This wheel and the generator account for most of the rotating mass within the ground station. Other moments of inertia, as referred to in Table 4.3, include the inertia due to the chain drive, disc brake and power meter. The generator and wheels moments of inertia, J, are calculated using (4.8) where m is the components mass and R the components outer radius. The moments of inertia of the generator and wheel are 0.040 kgm^2 and 0.019 kgm^2 respectively.

$$J = \frac{1}{2}mR^2 \tag{4.8}$$

The load from the generator is represented as a resisting torque applied to the lowest ring of the TRPT. For initial simulations this is kept at a constant value before step changes are applied to analyse the step response of the TRPT and rotor. The torque measured at the bottom of the TRPT during experimental tests is also used to set the generator torque within simulations. This allows for a more direct comparison between the model and the field tests. As described in Section 3.1.4 the torque data is recorded at a frequency of 2Hz. This data is disaggregated via linear interpolation so that the frequency of the data matches the sampling time used within the simulations.

So far all the modules in the power extraction and ground station subsystems, as shown in Figure 4.1, have been described. The following sections describe the several mathe-

matical representations of the power transmission system, including an analytical model of the static system and two dynamic models, which makes a key contribution of this thesis work.

4.4   Steady State Modelling of Tensile Rotary Power Transmission Systems

An analytical representation of the TRPT used within the Daisy Kite is defined by analysing the steady state equilibrium of a single section. This consists of two rings and several tethers that connect these rings, as shown in Figure 4.5. This equilibrium analysis is adapted from work by Benhaïem and Schmehl [7]. This analysis assumes that the rings are rigid and rotate around a common axis of rotation that passes through their centres, the rings are orthogonal to the axis of rotation. All points on a ring will be the same distance from the axis of rotation at all times and there is no relative deformation between any two points on the same ring. It is also assumed that the tethers are straight and do not stretch. Therefore, tethers are of constant length forming the shortest path between the attachment points at both ends. Aerodynamic effects are neglected. The system is assumed to be massless.

If we consider points A and B at either end of a tether that join two rings. Point A is fixed to ring one with radius R_1 and point B is fixed to ring two with radius R_2. The two rings are parallel and share the same axis of rotation which is in line with the wind direction, inclined by angle β . The wind reference frame (x_w, y_w, z_w) is set up as follows: x_w is parallel to the wind velocity vector V_w which is parallel to the ground, y_w is perpendicular to the wind vector and also parallel to the ground. z_w is perpendicular to the $x_w - y_w$ plane. The origin, O_1, is at the centre of ring one. The rotating reference frame for ring one, (x_a, y_a, z_a), is defined as follows: the origin is at O_1, x_a lies on the systems axis of rotation, y_a and z_a are in the plane of ring one, where z_a is towards point A. The corresponding rotating reference frame for ring two,
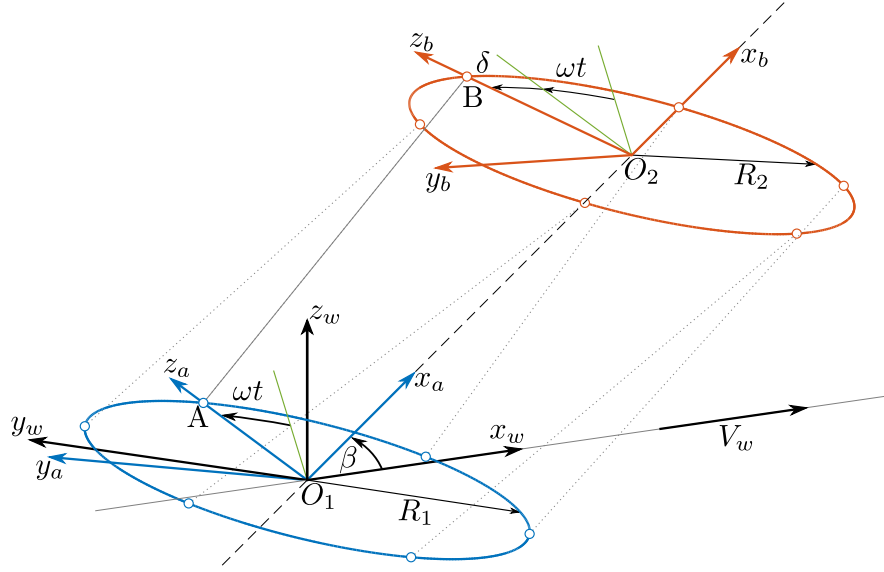
Figure 4.5: Representation of one section of the TRPT within the Daisy Kite system.

(x_b, y_b, z_b), is defined similarly: the origin is at O_2, x_b lies on the axis of rotation, y_b and z_b are in the plane of ring two, z_b is towards point B. Both rings rotate around x_a and x_b respectively at angular velocity ω with point A lagging behind point B by angle δ.

The relationship between the two points can be defined by analysing the steady state case of the TRPT system as shown in Figure 4.5. Firstly the locations of point A and B are defined in relation to the wind reference frame (x_w, y_w, z_w). With the rotational deformation set to zero, $\omega t = \delta = 0$, the transformation matrix $\mathbf{T}_{rw}$ gives the rotational transformation of the two ring reference frames, (x_a, y_a, z_a) and (x_b, y_b, z_b), to the wind reference frame by the elevation angle, β.

$$\mathbf{T}_{rw} = \begin{bmatrix} \cos\beta & 0 & -\sin\beta \\ 0 & 1 & 0 \\ \sin\beta & 0 & \cos\beta \end{bmatrix} \tag{4.9}$$

The position vector of point A, $\mathbf{p}_A$, in the wind reference frame is given by

$$\mathbf{p}_A = \begin{bmatrix} p_{A,x} \\ p_{A,y} \\ p_{A,z} \end{bmatrix} = \mathbf{T}_{rw} \begin{bmatrix} 0 \\ \sin(\omega t) \\ \cos(\omega t) \end{bmatrix} R_1 \tag{4.10}$$

similarly the position vector of point B, $\mathbf{p}_B$, in the wind reference frame is given by

$$\mathbf{p}_B = \begin{bmatrix} p_{B,x} \\ p_{B,y} \\ p_{B,z} \end{bmatrix} = \mathbf{T}_{rw} \begin{bmatrix} 0 \\ \sin(\omega t + \delta) \\ \cos(\omega t + \delta) \end{bmatrix} R_2 + \begin{bmatrix} \cos\beta \\ 0 \\ \sin\beta \end{bmatrix} l_s \tag{4.11}$$

where l_s is the distance between the centre of the two rings. With the locations of points A and B in the wind reference frame described, the vector between points A and B, which corresponds to the tether originating at A, can be defined.

$$\mathbf{p}_B - \mathbf{p}_A = \begin{bmatrix} l_{t,x} \\ l_{t,y} \\ l_{t,z} \end{bmatrix} = \begin{bmatrix} -\sin\beta\cos(\omega t + \delta) \\ \sin(\omega t + \delta) \\ \cos\beta\cos(\omega t + \delta) \end{bmatrix} R_2 + \begin{bmatrix} \cos\beta \\ 0 \\ \sin\beta \end{bmatrix} l_s - \begin{bmatrix} -\sin\beta\cos(\omega t) \\ \sin(\omega t) \\ \cos\beta\cos(\omega t) \end{bmatrix} R_1 \tag{4.12}$$

The distance l_t between points A and B, which is also the tether length, is given by.

$$l_t = |\mathbf{p}_B - \mathbf{p}_A| = \sqrt{l_{t,x}^2 + l_{t,y}^2 + l_{t,z}^2} \tag{4.13}$$

To analyse the ability of a TRPT section to transmit torque, the tether angle γ, which is the angle between the tether and the rings plane, must first be calculated. Considering the attachment of the tether at point A in Figure 4.5, using the unit vectors at point A, $\mathbf{e}_x^a$, $\mathbf{e}_y^a$ and $\mathbf{e}_z^a$, in the ring reference frame (x_a, y_a, z_a) and the unit vector, $\mathbf{e}_t$, for the tether between points A and B, as shown in Figure 4.6, the tether angle for attachment point A can be defined as

$$\cos\gamma_a = \mathbf{e}_y^a \cdot \mathbf{e}_t = (\mathbf{e}_z^a \times \mathbf{e}_x^a) \cdot \mathbf{e}_t = (\mathbf{e}_t \times \mathbf{e}_z^a) \cdot \mathbf{e}_x^a \tag{4.14}$$
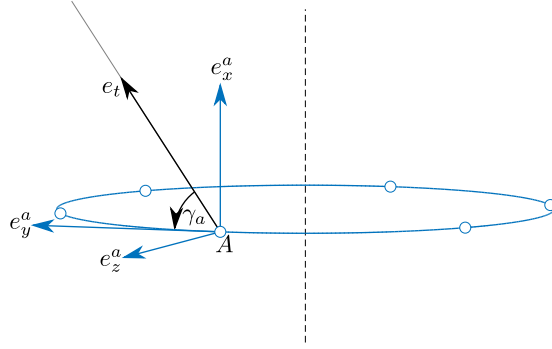
Figure 4.6: Unit vectors for point A and the tether between point A and point B.

where $\times$ and $\cdot$ correspond to vector cross and dot products respectively. The unit vectors $\mathbf{e}_t$, $\mathbf{e}_z^a$ and $\mathbf{e}_x^a$, in the wind reference frame, are defined by.

$$\mathbf{e}_t = \frac{\mathbf{p}_B - \mathbf{p}_A}{l_t} \tag{4.15}$$

$$\mathbf{e}_z^a = \frac{\mathbf{p}_A}{R_1} \tag{4.16}$$

$$\mathbf{e}_x^a = \begin{bmatrix} \cos\beta \\ 0 \\ \sin\beta \end{bmatrix} \tag{4.17}$$

Evaluating (4.14) using the unit vector definitions in (4.15), (4.16) and (4.17) leads to the following expression for the tether attachment angle at point A.

$$\cos\gamma_a = \frac{1}{R_1 l_t}\left((l_{t,y}p_{A,z} - l_{t,z}p_{A,y})\cos\beta + (l_{t,x}p_{A,y} - l_{t,y}p_{A,x})\sin\beta \right) \tag{4.18}$$

In this steady state analysis it is assumed that the forces are shared equally among all the tethers connecting the two rings. The tether attachment angle must be identical for each tether. The equation in (4.18) applies to all tether attachment points on ring one. Substituting the tether and point A vector components from (4.10) and (4.12) into (4.18) gives the following definition for the tether attachment angle at all tether attachment points on ring one.

$$\cos\gamma_1 = \frac{R_2}{l_t}\sin\delta \tag{4.19}$$

Repeating this tether attachment angle analysis for point B, leads to the following expression for all the tether attachment points on ring two.

$$\cos \gamma_2 = \frac{R_1}{l_t} \sin \delta \tag{4.20}$$

It can be seen from (4.19) and (4.20) that the tether attachment angle is determined by the ring radius, tether length and the torsional deformation. For the TRPT section to be in equilibrium the torque, Q, that is transferred is balanced by the tethers force contribution to the moments about the axis of rotation. Assuming that the forces are shared equally among all tethers, the magnitude of the torque transmitted from the tethers to ring one is given by

$$Q = -\sum_{i=1}^{N_t} F_{t,i}^y R_1$$
$$= -N_t F_t^y R_1 \tag{4.21}$$

where F_t^y is the tether force component that is tangential to the ring at each tether attachment point, N_t the number of tethers connecting the two rings and the subscript i the index for the ith tether. The magnitude of force F_t^y is given by

$$F_t^y = F_t \cos \gamma_1 \tag{4.22}$$

where F_t is the magnitude of the tether force. The tether force vector is given by the following.

$$\mathbf{F}_t = F_t \, \mathbf{e}_t \tag{4.23}$$

With the TRPT section in equilibrium the magnitude of the total axial force applied to the section, F_x, must be balanced by the axial components of the tether force. As the axial force is shared equally between all the tethers, the magnitude of the total axial

force is given by

$$F_x = -\sum_{i=1}^{N_t} \mathbf{F}_{t,i} \cdot \mathbf{e}_x^a$$

$$= -N_t \mathbf{F}_t \mathbf{e}_x^a$$

(4.24)

Substituting (4.23) into (4.24) and rearranging, the magnitude of the tether force is given by

$$F_t = -\frac{F_x}{N_t(\mathbf{e}_t \cdot \mathbf{e}_x^a)}$$

(4.25)

where, by substituting in the tether vector components from (4.12), the vector dot product $\mathbf{e}_t \cdot \mathbf{e}_x^a$ is given by

$$\mathbf{e}_t \cdot \mathbf{e}_x^a = \frac{1}{l_t}\Big(l_{t,x}\cos\beta + l_{t,z}\sin\beta\Big)$$

$$= \frac{l_s}{l_t}$$

(4.26)

By substituting (4.19), (4.22) and (4.25) into (4.21) the following expression for the magnitude of the torque transferred from the tethers to ring one is determined.

$$Q = R_1 F_x \frac{\cos\gamma_1 l_t}{l_s}$$

$$= R_1 R_2 F_x \frac{\sin\delta}{l_s}$$

(4.27)

Repeating this process for the torque transferred from ring two to the tethers yields exactly the same result. Therefore the torque shown in (4.27) can be seen as a general expression for the magnitude of torque that can be transmitted by a single TRPT section under steady state operation. As the ring radii and tether length are assumed to be fixed, the distance between the rings, l_s, can be identified by analysing the TRPT geometry. Figure 4.7 shows a single TPRT section with two rings of different radius. The distance C is the distance between the tether attachment points at either end of the same tether, projected onto one ring plane.

The distance l_s between two rings can therefore be defined as

$$l_s = \sqrt{l_t^2 - C^2} \tag{4.28}$$

where C can be calculated using triangular geometry.

$$C^2 = R_1^2 + R_2^2 - 2R_1R_2 \cos \delta \tag{4.29}$$

The distance between the two rings, l_s, is given by

$$l_s = \sqrt{l_t^2 - R_1^2 - R_2^2 + 2R_1R_2 \cos \delta} \tag{4.30}$$

and is a function of tether length, ring radii and torsional deformation. Substituting (4.30) into (4.27), the torque that a single TRPT section can transmit is given by.

$$Q = R_1R_2F_x \frac{\sin \delta}{\sqrt{l_t^2 - R_1^2 - R_2^2 + 2R_1R_2 \cos \delta}} \tag{4.31}$$
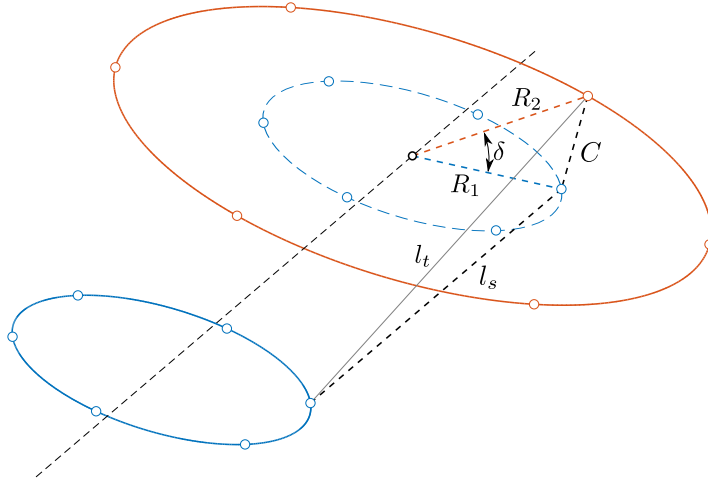
Figure 4.7: Geometry analysis to find the distance between adjacent rings within the TRPT.

By rearranging (4.31) the torsional deformation is given by.

$$\cos\delta = \frac{-Q^2 \pm \sqrt{Q^4 - F_x^2 Q^2 (l_t^2 - R_1^2 - R_2^2) + F_x^4 R_1^2 R_2^2}}{R_1 R_2 F_x^2} \qquad (4.32)$$

Therefore the torsional deformation can be found for any steady state operating condition. The deformation of a single TRPT section can vary from $0°$ to $180°$. As discussed in Section 3.5, beyond $180°$ the tethers will cross with each other. Once this happens the amount of torque that the TRPT section can transfer is largely reduced. The deformation between the two rings will increase rapidly causing the tethers to twist around one another. The system is therefore said to have failed if any single TRPT section reaches a torsional deformation of greater than $180°$.

It is noted that positive values of torque correspond to power being transmitted towards the ground station. A negative value indicates that power is being transferred towards the rotor, a situation that may occur depending on the operating strategy and state of the system. Equation (4.32) shows that there are two possible torsional deformations, δ, for a given TRPT geometry, torque and axial force. To investigate these two solutions the torsional stiffness of a TRPT section is calculated. By differentiating (4.31) with respect to the torsional deformation, δ, the torsional stiffness, k, of a TRPT section can be found.

$$k = \frac{dQ}{d\delta}$$

$$= R_1 R_2 F_x \left(\frac{\cos\delta}{\left(l_t^2 - R_1^2 - R_2^2 + 2R_1 R_2 \cos\delta\right)^{\frac{1}{2}}} + \frac{R_1 R_2 \sin^2\delta}{\left(l_t^2 - R_1^2 - R_2^2 + 2R_1 R_2 \cos\delta\right)^{\frac{3}{2}}} \right) \qquad (4.33)$$

The torsional stiffness provides information about the stability of the two torque solutions. A positive torsional stiffness shows that the steady state solution is in equilibrium as the tether forces are acting in the opposite direction to the torque being transmitted, therefore cancelling each other. Whereas a negative torsional stiffness shows that the

system is not in equilibrium as the tether forces are acting in the same direction as the torque being transmitted. Before a negative stiffness occurs there is an operating point at which the stiffness becomes zero, this corresponds to the torsional deformation at which the maximum amount of torque can be transmitted. By setting the torsional stiffness, k, equal to zero in (4.33) the torsional deformation, δ_{crit}, at which the maximum torque can be transmitted is derived to be.

$$\cos \delta_{crit} = \frac{R_1^2 + R_2^2 - l_t^2 \pm \sqrt{l_t^4 + R_1^4 + R_2^4 - 2R_1^2 l_t^2 - 2R_2^2 l_t^2 - 2R_1^2 R_2^2}}{2R_1 R_2} \tag{4.34}$$

It can be seen from (4.34) that the value of torsional deformation for maximum torque transmission is dependant only on the geometry of the TRPT section. The steady state analysis results in (4.31), (4.32), (4.33) and (4.34) being identified and used to determine steady state values of torque, torsional deformation and stiffness. These equations can be used to assess the TRPT performance and examine the relationship between the factors that affect a TRPT ability to transmit torque. Analysis of the TRPT steady state operation using these equations is detailed in Section 5.3.

4.5 Torque Loss in Tensile Rotary Power Transmission - Tether Drag Models

Tethers mechanically connect the wings to the ground and are used to transmit the energy harvested aloft down to the ground, either mechanically or electrically. For all AWES currently under development they are a critical component. The long tether lengths required to reach the desired altitudes, combined with the high wing velocities, leads to vast lengths of tether moving through the air at great speed. As shown in Section 2.1.5 this results in significant tether drag that reduces a systems ability to generate power. Several AWES have been designed specifically to reduce the tether drag [61, 62]. It is important to analyse the tethers impact on any proposed AWES design. The tether drag is investigated to firstly quantify its effect on TRPT systems and the

current Daisy Kite design. Secondly to take tether drag into account in prototype design and during the development of operation strategies. Two models of the aerodynamic forces on the tethers have been developed. Details for each model are presented in the following section, an overview of each is as follows:

1. An initial estimate of the torque loss within the TRPT is calculated assuming no torsional deformation, each TRPT ring is of equal radius, tethers are straight and do not stretch, all tethers are of equal length and diameter and the axial tension applied to the TRPT is distributed equally among all tethers.

2. An improved estimate of the aerodynamic forces on the tethers within the TRPT is calculated by accounting for torsional deformation and varying TRPT radius. This improved analysis allows for the torque loss and the axial and radial forces, that arise due to the aerodynamic forces on the tethers, to be calculated. This is based on work in [59].

4.5.1   Simple Tether Drag Model for Steady State Tensile Rotary Power Transmission Representation

An initial analysis of the tether drag within the Daisy Kite's TRPT follows. It is assumed that there is no torsional deformation within the TRPT, each ring within the TRPT has the same radius, tethers are straight and do not stretch, all tethers are of equal length and diameter and the axial tension applied to the system is distributed equally between the tethers. Assuming that the wind is uniform in both space and time, the drag, D_i, experienced by a unit length of a single tether, i, is given by

$$D_i = \frac{1}{2}\rho V_{a,i}^2 dC_{D_t} \tag{4.35}$$

where d is the tether diameter, C_{D_t} the tethers drag coefficient and $V_{a,i}$ the tethers apparent velocity in the direction of rotation. The drag experienced by the tether is directly proportional to its diameter. The smallest allowable tether diameter, to minimise the drag force, can be identified from the maximum allowable stress in the tether

material σ_{max}. Assuming that the axial tension applied to the TRPT is reacted equally by the N_t tethers and that all tethers are the same diameter, for a given maximum TRPT axial tension, $F_{x_{max}}$, the diameter of the tethers can be defined as.

$$\sigma_{max} = \frac{4F_{x_{max}}}{\pi d^2 N_t}$$

$$d = 2\sqrt{\frac{F_{x_{max}}}{\sigma_{max}\pi N_t}}$$

$$(4.36)$$

Substituting (4.36) into (4.35) and accounting for the N_t tethers. The unit length drag, D, experienced by a TRPT is given by.

$$D = \sum_{i=1}^{N_t} \rho V_{a,i}^2 \sqrt{\frac{F_{x_{max}}}{\sigma_{max}\pi N_t}} C_{D_t} \qquad (4.37)$$

For a TRPT that is inclined to the horizontal, the relative velocity, $V_{a,i}$, that a tether experiences will vary as the system rotates. The apparent velocity of the tether in the direction of rotation, $V_{a,i}$, is formed from two components. From the wind, V_w, and from the rotational motion of the system, ωR. The apparent wind speed in the direction of rotation experienced by the tether is a combination of these two. ωR acts parallel to $V_{a,i}$ and is equal for all tethers. The component of V_w that acts in the direction of the TRPT rotation is dependant on the tethers rotational position θ_i and the systems elevation angle β. It is calculated from $V_w \sin\theta_i \sin\beta$. The apparent velocity of the tether in the direction of rotation is given by

$$V_{a,i} = \omega R + V_w \sin\theta_i \sin\beta \qquad (4.38)$$

Defining the tether speed ratio λ_t, analogous to the tip speed ratio of a rotor, as

$$\lambda_t = \frac{\omega R}{V_w} \qquad (4.39)$$

substituting (4.39) into (4.38) gives the apparent tether velocity as.

$$V_{a,i} = V_w(\lambda_t + \sin\theta_i \sin\beta) \qquad (4.40)$$

Substituting (4.40) into (4.37) and assuming that the TRPT is of constant radius the torque loss, Q_{loss}, per unit length of TRPT due to tether drag is given by.

$$Q_{loss} = R\rho V_w^2 \sqrt{\frac{F_{x_{max}}}{\sigma_{max}\pi N_t}} C_{D_t} \sum_{i=1}^{N_t} (\lambda_t + \sin\theta_i \sin\beta)^2 \qquad (4.41)$$

The steady state torque loss of the TRPT can be calculated by determining the energy lost due to tether drag in one revolution and averaging this over one rotation. The steady state torque loss due to tether drag is given by.

$$Q_{loss} = R\rho V_w^2 \sqrt{\frac{F_{x_{max}}}{\sigma_{max}\pi N_t}} C_{D_t} \sum_{i=1}^{N_t} \frac{1}{2\pi} \int_0^{2\pi} (\lambda_t + \sin\theta_i \sin\beta)^2 d\theta_i \qquad (4.42)$$

Under steady state conditions the energy loss caused by each tether, over one revolution, will be equal. By accounting for this and evaluating the integral in (4.42), the steady state torque loss per unit length of the TRPT can be calculated by.

$$Q_{loss} = R\rho V_w^2 \sqrt{\frac{F_{x_{max}}}{\sigma_{max}\pi N_t}} C_{D_t} N_t \frac{1}{2\pi} \int_0^{2\pi} (\lambda_t + \sin\theta \sin\beta)^2 d\theta$$

$$= R\rho V_w^2 \sqrt{\frac{N_t F_{x_{max}}}{\sigma_{max}\pi}} C_{D_t} \left(\lambda_t^2 + \frac{\sin^2\beta}{2}\right) \qquad (4.43)$$

From analysing (4.43) it can be seen that the torque loss, that arises from tether drag, is dependant on a number of factors including: the number of tethers N_t, the elevation angle β, the tether speed ratio λ_t, the maximum stress of the tether material σ_{max} and the maximum total axial force $F_{x_{max}}$. This initial analysis allows for the Daisy Kite's torque loss to be estimated for a range of steady state operating conditions. It also shows the relationship that the torque loss has with several design variables. Analysis of the torque loss, due to tether drag, using (4.43) is given in Section 5.3.3.

4.5.2 Improved Tether Drag Model for Dynamic Tensile Rotary Power Transmission Representations

The torque loss shown in (4.43) does not take into account any torsional deformation within the TRPT. It also neglects the components of the tethers aerodynamic force that are not in the direction of the TRPT rotation. As the TRPT deforms torsionally the tethers are no longer parallel to the axis of rotation which in turn alters the angle of attack between the apparent wind and the tether. A change in the tethers angle of attack will alter the aerodynamic force and the resulting torque loss. The torsional deformation of the TRPT also results in the tethers distance from the axis of rotation varying along its length. The tethers distance from the axis of rotation affects the torque loss. By taking into account any torsional deformation and calculating the total aerodynamic force, the accuracy of the torque loss representation will be more complete. The following analysis removes these assumptions made within the simple tether drag analysis. The model development is based on [59].

The vector for the ith point on a tether, $\mathbf{t}_i$, can be defined in the wind reference frame using (4.10) and (4.15) to give

$$\mathbf{t}_i = \begin{bmatrix} t_{i,x} \\ t_{i,y} \\ t_{i,z} \end{bmatrix} = \mathbf{p}_A + \mathbf{e}_t \eta \qquad (4.44)$$

where η is the distance along the tether with the constraint $0 < \eta < l_t$. The tether reference frame, (x_t, y_t, z_t), is defined, with origin at $\mathbf{t}_i$, such that x_t is parallel to the TRPT's axis of rotation, y_t is tangential to the TRPT radius pointing towards the direction of rotation and z_t is perpendicular to x_t and y_t pointing away from the axis of rotation. The tether reference frame is defined by two successive rotational transformations onto the wind reference frame, as shown in Figure 4.8. The first is given by $\mathbf{T}_{rw}$ in (4.9) which describes the rotation from the ring reference frame (x_a, y_a, z_a), with no rotational displacement $\omega t = 0$, to the wind reference frame (x_w, y_w, z_w) by angle β . By using this the tether point vector in the ring reference frame, $\mathbf{t}_i^r$ is given

by.

$$\mathbf{t}_i^r = \begin{bmatrix} t_{i,x}^r \\ t_{i,y}^r \\ t_{i,z}^r \end{bmatrix} = \mathbf{T}_{rw}\mathbf{t}_i \tag{4.45}$$

The rotational position within the TRPT, θ_i, and the distance from the axis of rotation, R_i, of the ith tether point are then given by.

$$\tan\theta_i = \frac{t_{i,z}^r}{t_{i,y}^r} \tag{4.46}$$

$$R_i = \sqrt{t_{i,y}^r{}^2 + t_{i,z}^r{}^2} \tag{4.47}$$

The rotational matrix, $\mathbf{T}_{tr}$, that describes the rotation from the tether reference frame, at the ith tether point, to the ring reference frame is given by.

$$\mathbf{T}_{tr} = \begin{bmatrix} 1 & 0 & 0 \\ 0 & \cos\theta_i & \sin\theta_i \\ 0 & -\sin\theta_i & \cos\theta_i \end{bmatrix} \tag{4.48}$$
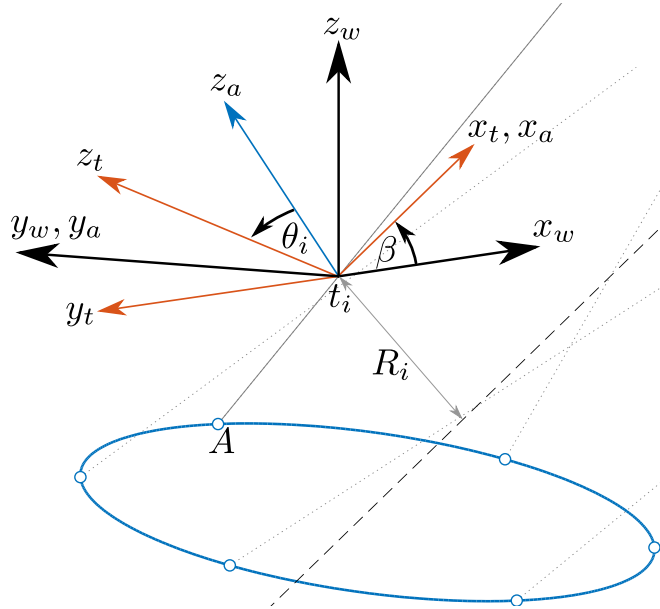
Figure 4.8: Diagram showing the tether reference frame

The transformation from the tether reference frame, at the ith tether point, to the wind reference frame can then be calculated by combining $\mathbf{T}_{rw}$ and $\mathbf{T}_{tr}$ to give.

$$\mathbf{T}_{tw} = \mathbf{T}_{rw}\mathbf{T}_{tr} = \begin{bmatrix} \cos\beta & \sin\beta \, \sin\theta_i & -\sin\beta \, \cos\theta_i \\ 0 & \cos\theta_i & \sin\theta_i \\ \sin\beta & -\cos\beta \, \sin\theta_i & \cos\beta \, \cos\theta_i \end{bmatrix} \quad (4.49)$$

This rotational transformation can then be used to define the apparent wind velocity, at the ith tether point, in the wind reference frame. The apparent velocity vector, $\mathbf{V}_a$ of the tether point is again given by a combination of the wind velocity, V_w, and the rotation of the tether point about the axis of rotation. The rotation of the tether is calculated from $\omega_i R_i$, where ω_i is the rotational speed of the ith tether point. It is noted that in the dynamic representations the rotational speed of the tether point is calculated through linearly interpolating the rotational speeds of the rings or tether attachment points at either end of the tether. The rotational speeds of each ring or each tether attachment point are calculated as described in Sections 4.6 and 4.7 for the two dynamic TRPT representations respectively. The apparent wind velocity vector, $\mathbf{V}_a$, at the ith tether point defined in the wind reference frame is given by.

$$\mathbf{V}_a = \begin{bmatrix} V_{a,x} \\ V_{a,y} \\ V_{a,z} \end{bmatrix} = \begin{bmatrix} V_w \\ 0 \\ 0 \end{bmatrix} + \mathbf{T}_{tw} \begin{bmatrix} 0 \\ \omega_i R_i \\ 0 \end{bmatrix} \quad (4.50)$$

To define the aerodynamic force vector $\mathbf{F}_a$ acting on the ith tether point, the force is decomposed into three components: (1) acting tangential to the tether points radius, $\mathbf{F}_{D,\tau}$, aligned with the velocity component $\mathbf{V}_{a,\tau}$; (2) axial force acting along the tether, $\mathbf{F}_{D,\phi}$, aligned with the wind velocity component $\mathbf{V}_{a,\phi}$; and (3) transverse force $\mathbf{F}_{L,\tau}$ acting perpendicular to $\mathbf{F}_{D,\tau}$ and $\mathbf{F}_{D,\phi}$, as shown in Figure 4.9 [59,133], where α is the angle between the tether and the tether points apparent wind vector, the tethers angle

of attack. The unit vectors for each of the aerodynamic forces are given by.

$$\mathbf{e}_{F_{D,\phi}} = \mathbf{e}_t \tag{4.51}$$

$$\mathbf{e}_{F_{D,\tau}} = \mathbf{e}_t \times \mathbf{e}_{F_{L,\tau}} \tag{4.52}$$

$$\mathbf{e}_{F_{L,\tau}} = \mathbf{e}_{V_a} \times \mathbf{e}_t \tag{4.53}$$

The tethers angle of attack, α, is calculated from the dot product of the apparent wind vector, $\mathbf{V}_a$, given by (4.50) and the tether unit vector, $\mathbf{e}_t$, given by (4.15).

$$\cos \alpha = \mathbf{V}_a \cdot \mathbf{e}_t \tag{4.54}$$

The magnitudes of the the two velocity components $V_{a,\phi}$ and $V_{a,\tau}$ are given by.

$$V_{a,\phi} = V_a \cos \alpha \tag{4.55}$$

$$V_{a,\tau} = V_a \sin \alpha \tag{4.56}$$

The magnitudes of the three aerodynamic forces, in the wind reference frame, are given
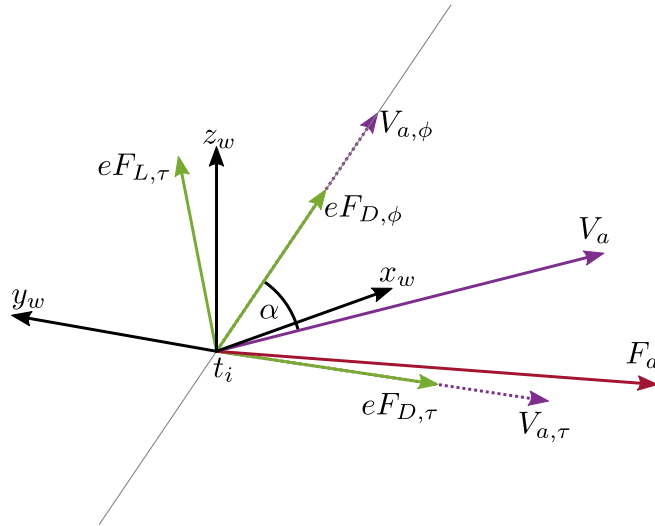
Figure 4.9: Diagram showing the aerodynamic force on a tether point

by

$$F_{D,\phi} = \frac{1}{2}\rho d V_{a,\phi}^2 \pi C_{f_t} \tag{4.57}$$

$$F_{D,\tau} = \frac{1}{2}\rho d V_{a,\tau}^2 C_{D_t} \tag{4.58}$$

$$F_{L,\tau} = \frac{1}{2}\rho d V_{a,\tau}^2 C_{L_t} \tag{4.59}$$

where C_{D_t} is the tethers drag coefficient, C_{f_t} the tethers skin friction drag coefficient and C_{L_t} the tethers lift coefficient. The force magnitudes in (4.57), (4.58) and (4.59) are multiplied by the force unit vectors in (4.51), (4.52) and (4.53) respectively to give the three aerodynamic force component vectors. Treating the tether as a cylinder results with a lift coefficient of 0, the force $F_{L,\tau}$ will equal 0. The aerodynamic force components can be summed to give the resultant aerodynamic force vector, per unit length of tether, in the wind reference frame.

$$\mathbf{F}_a = \mathbf{F}_{D,\phi} + \mathbf{F}_{D,\tau} + \mathbf{F}_{L,\tau} \tag{4.60}$$

To determine the torque loss due to this aerodynamic force, the force vector is transformed into the tether reference frame.

$$\mathbf{F}_a^t = \begin{bmatrix} F_{a,x}^t \\ F_{a,y}^t \\ F_{a,z}^t \end{bmatrix} = \mathbf{T}_{tw}^{-1}\mathbf{F}_a \tag{4.61}$$

The $F_{a,y}^t$ component of the aerodynamic force vector is tangential to the tether points radius, it can be used to determine the torque loss, due to tether drag, for a unit length around the ith tether point given by.

$$Q_{loss,i} = F_{a,y}^t R_i \tag{4.62}$$

The torque loss on the TRPT system can be obtained by applying (4.62) to several segments on each tether, adjusted for the segment length. The result from each seg-

ment can then be summed to give an overall TRPT torque loss. Although only the $F^t_{a,y}$ component of the aerodynamic force in (4.61) contributes directly to the torque loss, the $F^t_{a,x}$ and $F^t_{a,z}$ components are still of interest. The $F^t_{a,x}$ component is parallel to the axis of rotation and will effect the axial tension experienced by the tether. The $F^t_{a,z}$ component is perpendicular to $F^t_{a,x}$ and $F^t_{a,y}$, it acts to pull the tether towards or away from the axis of the TRPT.

In this thesis , the simple tether drag model is used to assess the torque loss within the TRPT under steady state operation. The improved tether drag is used within the two dynamic representations of the TRPT that are introduced in the following two sections.

4.6   Spring–Disc Tensile Rotary Power Transmission Model

For an initial dynamic representation of the TRPT several assumptions about the system have been made. This simplified dynamic model uses aspects of the steady state model, introduced in Section 4.4, in which it is assumed that the tension and torque applied to a single TRPT section are shared equally between all tethers. It is also assumed that the tethers do not stretch and therefore have constant length. By making these two assumptions it is possible to replace all the tethers, in a single section of the Daisy Kite's TRPT, with a torsional spring, where the torsional stiffness is defined using (4.33) as derived in Section 4.4. By assuming that the rings are rigid and uniform, each ring can be represented by a single moment of inertia J. It is assumed that all rings within the TRPT share the same axis of rotation and that all rings are orthogonal to this axis. A schematic of this representation, showing several TRPT sections, is given in Figure 4.10, each ring is shown as an inertial disc and the tethers as torsional springs. This representation is hence referred to as the spring–disc model. Disc 6, at the far left hand side of the schematic, is towards the ground station end of the TRPT, disc 1 is towards the rotor.

As the tethers are assumed to not stretch and are of equal length, the axial position
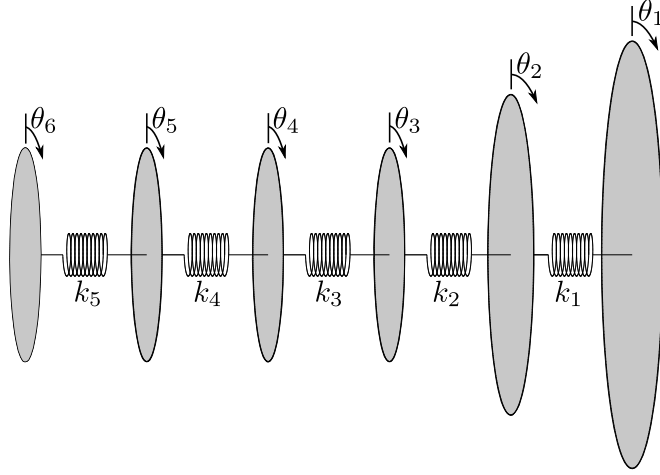
Figure 4.10: Schematic of the spring-disc TRPT representation. Each ring is described by a moment of inertia, J, and the multiple tethers in each section are replaced by a single torsional spring of stiffness k. Disc 6, on the left hand side of the schematic, represents the ground station end of the TRPT.

of the discs is defined by their torsional displacement. As the torsional deformation between adjacent discs increases, the constant tether length forces the discs to move towards each other. The torsional deformation defines the axial deformation and the distance between discs. The disc at the ground station end of the TRPT is constrained to a fixed axial position. Each disc has one degree of freedom in rotation as indicated in Figure 4.10, the number of discs dictates the number of degrees of freedom of the spring–disc representation. The moment of inertia of each ring is calculated based on the properties of the carbon fibre tubes, shown in Table 4.4, and the diameter of each ring.

The moments of inertia for each disc and the torsional stiffness of each spring, found at each operating point using (4.33), make up inertia and stiffness matrices for the TRPT. Equations (4.63) and (4.64) show the inertia and stiffness matrices respectively. Both matrices have size $N_r \times N_r$, where N_r represents the

Outer Diameter	4 mm
Inner Diameter	2.5 mm
Density	1600 kg/m^3

Table 4.4: Properties of the carbon fibre tubes used within the Daisy Kite's TRPT system.

number of rings in the TRPT. The moment of inertia of the first ring, J_1 is increased to account for the mass of the wings, the moment of inertia of the last ring, J_{N_r}, is increased to account for the drivetrain components, as described in Section 4.3. For a given TRPT geometry the stiffness matrix $\mathbf{k}$ is defined by the discs rotational positions $\boldsymbol{\theta}$ and the axial force applied to the TRPT F_x, as shown by (4.33). The axial force, F_x, is the combination of the thrust from the rotor and the aerodynamic force produced by the lift kite.

$$\mathbf{J} = \begin{bmatrix} J_1 & 0 & 0 & \cdots & 0 \\ 0 & J_2 & 0 & \cdots & 0 \\ 0 & 0 & J_3 & \cdots & 0 \\ \vdots & \vdots & \vdots & \ddots & \vdots \\ 0 & 0 & 0 & \cdots & J_{N_r} \end{bmatrix} \tag{4.63}$$

$$\mathbf{k} = \begin{bmatrix} k_1 & -k_1 & 0 & \cdots & 0 \\ -k_1 & k_1 + k_2 & -k_2 & \cdots & 0 \\ 0 & -k_2 & k_2 + k_3 & \cdots & 0 \\ \vdots & \vdots & \vdots & \ddots & \vdots \\ 0 & 0 & 0 & \cdots & k_{N_r-1} \end{bmatrix} \tag{4.64}$$

The torsional stiffness of each TRPT section will vary as the axial force, F_x, and the rotational positions of the rings, $\boldsymbol{\theta}$, change. The torsional stiffness calculated from (4.33) assumes the system is under steady state conditions. The values of torsional stiffness are updated continually to correspond to the current operating point. This leads to the stiffness matrix, $\mathbf{k}$, varying with time. The torsional spring forces are the product of the stiffness matrix, $\mathbf{k}$, and the rings rotational positions, $\boldsymbol{\theta}$. A time varying function, $\mathbf{f}_S$, that is dependant on the rotational positions of the rings and the axial force is defined to calculate the torsional spring force, $\mathbf{f}_S(\boldsymbol{\theta}, F_x)$.

The aerodynamic forces experienced by the tethers of any AWES reduce the amount of energy reaching the ground station. The energy that is lost due to tether drag can significantly reduce the energy produced by the system, as shown in Section 2.1.5. To account for this energy loss within the spring–disc representation the tether drag is converted to a torque loss, as described in Section 4.5.2. This torque loss is applied such that it opposes the rotational motion of the TRPT. In the spring–disc representation each tether is split into two segments of equal length, the torque loss due to each segment is applied to the nearest disc. Each disc will have an opposing torque applied to it that arises from half the tether length above the disc and half the tether length below the disc. The first and last discs within the TRPT only have tethers above and below them respectively, it is expected that a lower opposing torque is applied at these two discs.

As shown in Section 4.5.2, the torque loss, due to tether drag, for a unit length around the ith tether point is dependant on: the systems elevation angle β, the wind velocity V_w, the rotational position θ_i and the speed of the tether point $\omega_i R_i$. The position of the tether point t_i and its speed $\omega_i R_i$ are calculated from the positions and speeds of the TRPT discs, $\boldsymbol{\theta}$ and $\dot{\boldsymbol{\theta}}$ respectively. The position vector, $\mathbf{t}_i$, and its radius from the axis of rotation, R_i, are calculated from the discs rotational positions. The rotational velocity of a tether point is calculated by linearly interpolating between the rotational velocities, $\dot{\theta}$, of the discs that are at either end of the tether. The central point of each tether segment and each tether segments length are used to calculated the torque loss that arises from each segment. For a fixed elevation angle the opposing torque, due to tether drag, is a function of the wind speed V_w, the discs rotational positions $\boldsymbol{\theta}$ and the discs rotational velocities $\dot{\boldsymbol{\theta}}$. A time varying function, $\mathbf{f}_D$, is defined to calculated the opposing torque that is applied to each disc as a result of the tether drag, $\mathbf{f}_D(\mathbf{V}_w, \dot{\boldsymbol{\theta}}, \boldsymbol{\theta})$.

So that pure torques can be applied to the system the calculation uses cylindrical coordinates. Using the inertia matrix, $\mathbf{J}$, the function for spring force, $\mathbf{f}_S$, and the function

for torque loss, $\mathbf{f}_D$, the equations of motion of the spring–disc model are represented by

$$\mathbf{J}\ddot{\boldsymbol{\theta}} + \mathbf{f}_D(\mathbf{V}_w, \dot{\boldsymbol{\theta}}, \boldsymbol{\theta}) + \mathbf{f}_S(\boldsymbol{\theta}, F_x) = \mathbf{Q}_{ext} \qquad (4.65)$$

where $\mathbf{Q}_{ext}$ is the external torque applied to the system, which includes the rotor torque and the generator torque. In this instance material damping has been neglected. It is assumed that the aerodynamic damping due to tether drag is much larger than any internal material damping. The torque loss, $\mathbf{f}_D$, and the stiffness matrix, $\mathbf{k}$, are non-linear functions which indicates that an analytical solution is not suitable to solve the equations of motion. A numerical method is therefore required. Given its simplicity and ease of implementation the central difference integration method [134] has been used to solve (4.65). The algorithm used to solve the spring–disc representation for a fixed generator torque is given in Table 4.5. The torque, $\mathbf{Q}$, applied to each ring is the combination of the rotor torque $AeroQ$, generator torque $GenQ$ and the torque loss due to tether drag $\mathbf{f}_D$.

Inputs	Wind speed V_w, TRPT geometry $\mathbf{R}$ and $\mathbf{l}_s$, elevation angle β, initial conditions $\boldsymbol{\theta}_2$ and $\dot{\boldsymbol{\theta}}_2$, generator torque $GenQ$
Line 1	Find $\mathbf{l}_t$ and $\mathbf{J}$
Line 2	Find $AeroQ_2$, $AeroT_2$ and $AeroP_2$
Line 3	Find lk_T, $F_{x,2}$ and $\mathbf{k}$
Line 4	Find $\mathbf{f}_{D,2}$ and $\mathbf{Q}_2$
Line 5	$\ddot{\boldsymbol{\theta}}_{\mathbf{2}} = \dfrac{\mathbf{J}}{\mathbf{Q}_2} - \mathbf{k}\boldsymbol{\theta}_{\mathbf{2}}$
Line 6	$\boldsymbol{\theta}_1 = \boldsymbol{\theta}_2 - \Delta t \dot{\boldsymbol{\theta}}_2 + \dfrac{\Delta t^2}{2}\ddot{\boldsymbol{\theta}}_2$
Line 7	$\mathbf{a} = \dfrac{\mathbf{J}}{\Delta t^2}, \quad \mathbf{b} = \dfrac{2\mathbf{J}}{\Delta t^2}$
Line 8	**For** each time step, i
Line 9	Find $AeroQ_i$, $AeroT_i$ and $AeroP_i$
Line 10	Find lk_T, $F_{x,i}$ and update $\mathbf{k}$
Line 11	Find $\mathbf{f}_{D,i}$ and $\mathbf{Q}_i$
Line 12	$\mathbf{c} = \mathbf{Q}_i - \mathbf{a}\boldsymbol{\theta}_{i-1} - \mathbf{k}\boldsymbol{\theta}_i + \mathbf{b}\boldsymbol{\theta}_i$
Line 13	$\boldsymbol{\theta}_{i+1} = \dfrac{\mathbf{a}}{\mathbf{c}}$
Line 14	$\dot{\boldsymbol{\theta}}_i = \dfrac{\boldsymbol{\theta}_{i+1} - \boldsymbol{\theta}_{i-1}}{2\Delta t}, \quad \ddot{\boldsymbol{\theta}}_i = \dfrac{\boldsymbol{\theta}_{i+1} - 2\boldsymbol{\theta}_i + \boldsymbol{\theta}_{i-1}}{\Delta t^2}$
Line 15	**End For**
Outputs	$\boldsymbol{\theta}, \dot{\boldsymbol{\theta}}, \ddot{\boldsymbol{\theta}}, \mathbf{AeroQ}, \mathbf{AeroT}, \mathbf{AeroP}, \mathbf{Q}, \mathbf{F}_x$

Table 4.5: Pseudo code for the spring–disc TRPT representation. $\mathbf{R}$ is the vector for the discs radii, $\mathbf{l}_s$ is the vector containing the TRPT section lengths, $\mathbf{l}_t$ the vector for tether lengths in each TRPT section, $\mathbf{J}$ the inertia matrix, $AeroQ$ the rotor torque, $AeroT$ the rotor thrust, $AeroP$ the rotor power, lk_T the lift kite line tension, F_x the axial force, $\mathbf{f}_D$ the torque loss due to tether drag, $\mathbf{Q}$ the torque applied to each disc, $\mathbf{k}$ the stiffness matrix, Δt the time step length and $\boldsymbol{\theta}, \dot{\boldsymbol{\theta}}, \ddot{\boldsymbol{\theta}}$ the vectors containing the discs rotational positions, velocities and accelerations respectively. $\mathbf{a}, \mathbf{b}, \mathbf{c}$ are variables used within the algorithm.

4.7 Multi–Spring Tensile Rotary Power Transmission Model

The second more complex TRPT representation, the multi–spring model, considers more degrees of freedom for each TRPT section. The main additional feature, compared to the previously described spring–disc representation, is that each tether within a section is represented by a separate linear spring with stiffness kt, removing the assumption that the tethers do not change length. The tethers are assumed to be straight and all tethers in the same TRPT section have the same unloaded length. The rings of the TRPT are split into N_t segments, N_t represents the number of tethers and is equal to six in the current Daisy Kite TRPT design. The mass of each segment is represented by a point mass located at the tether attachment position. A linear spring is assumed for each mass between the neighbouring two tether attachment points with stiffness kr. The point masses are constrained to move around the circumference of the ring and all the masses on the same ring are constrained to move axially together. All the masses on a single ring have the same axial displacement. Each ring has N_t rotational degrees of freedom and one axial degree of freedom, the total number of degrees of freedom for each ring within the TRPT is therefore N_t+1. For the current Daisy Kite TRPT design each ring has seven degrees of freedom. Figure 4.11 shows a schematic of the model for
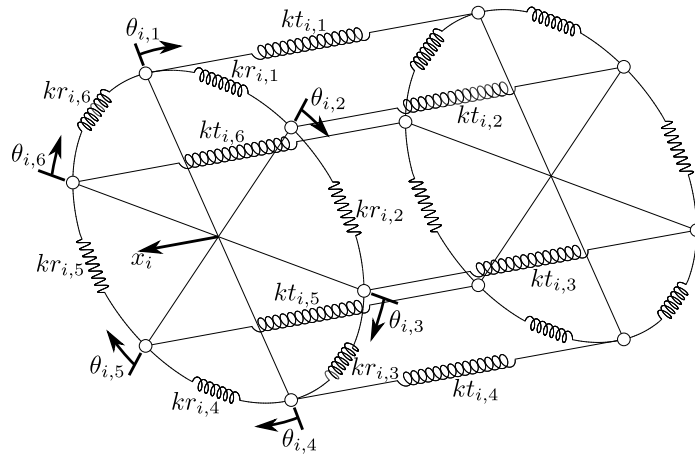
Figure 4.11: Schematic of the multi-spring TRPT representation. Each ring is represented by N_t ($N_t = 6$ in this design) linear springs with stiffness kr and the tethers by linear springs with stiffness kt. The number of degrees of freedom for a single ring is $N_t + 1$.

one section of the Daisy Kite's TRPT, where $N_t = 6$. The seven degrees of freedom for one of the rings are shown. Similar to the spring–disc representation the system is defined and solved using cylindrical coordinates.

As with the spring–disc representation, the multi–spring model incorporates the torque loss due to tether drag as described in Section 4.5.2. Again each tether is split into two equal segments, the aerodynamic force for each segment is calculated using the location of its mid point and its length. The multi–spring model includes an axial degree of freedom for each ring, therefore the axial force that arises due to the aerodynamic forces on the tether can be taken into account. With the aerodynamic force on the tether transformed into the tether reference frame, as given by (4.61) for a unit length, the $F_{a,x}^t$ component corresponds to the axial force that arises due to the airflow around the tether. The axial force for all tethers on a single ring are combined and applied to the rings axial degree of freedom. The torque loss and axial force applied to each mass and ring respectively are a result of the aerodynamic forces on half the tether above and half the tether below it. It is noted that the first and last rings within the TRPT only have tethers above and below them respectively.

Given the more complex nature of the multi–spring model Lagrangian dynamics are used to define the dynamics of motion. The general from is given by

$$\frac{d}{dt}\frac{\partial L}{\partial \dot{\mathbf{u}}} - \frac{\partial L}{\partial \mathbf{u}} = 0 \qquad (4.66)$$

where $\mathbf{u}$ is the position vector that includes the rotational positions of the masses $\boldsymbol{\theta}$ and the axial positions of the rings $\mathbf{x}$, $\dot{\mathbf{u}}$ is the corresponding velocity vector.

$$\mathbf{u} = \begin{bmatrix} \mathbf{x} \\ \boldsymbol{\theta} \end{bmatrix} \quad , \qquad \dot{\mathbf{u}} = \begin{bmatrix} \dot{\mathbf{x}} \\ \dot{\boldsymbol{\theta}} \end{bmatrix}$$

The Lagrangian function L is formed from $L = T - V$ where T is the kinetic energy and V the potential energy within the TRPT. The kinetic energy and potential energy

148

of the system are written as

$$T = \sum_{i=1}^{N_r} \sum_{j=1}^{N_t} \frac{1}{2} m_{i,j} (\dot{x}_i^2 + R_i^2 \dot{\theta}_{i,j}^2) \tag{4.67}$$

$$V = \sum_{i=1}^{N_r} \sum_{j=1}^{N_t} \frac{1}{2} kt_{i,j} \Delta l_{t_{i,j}}^2 + \frac{1}{2} kr_{i,j}^2 (\theta_{i,j} - \theta_{i,j+1})^2 \tag{4.68}$$

where N_r is the number of rings, i denotes the ith ring, N_t the number of tethers, j denotes the jth mass on a ring, $m_{i,j}$ the mass of the jth mass on the ith ring, x_i the axial position of the ith ring, R_i the radius of the ith ring, $\theta_{i,j}$ the rotational position of the jth mass on the ith ring, $kt_{i,j}$ the tether stiffness, $\Delta l_{t_{i,j}}$ the change in tether length from its unloaded length and $kr_{i,j}$ the stiffness of each ring segment. The change in tether length, Δl_t, is calculated from analysing the diagram in Figure 4.12. The length C in Figure 4.12 defines the distance between the ends of the tether in the plane of one
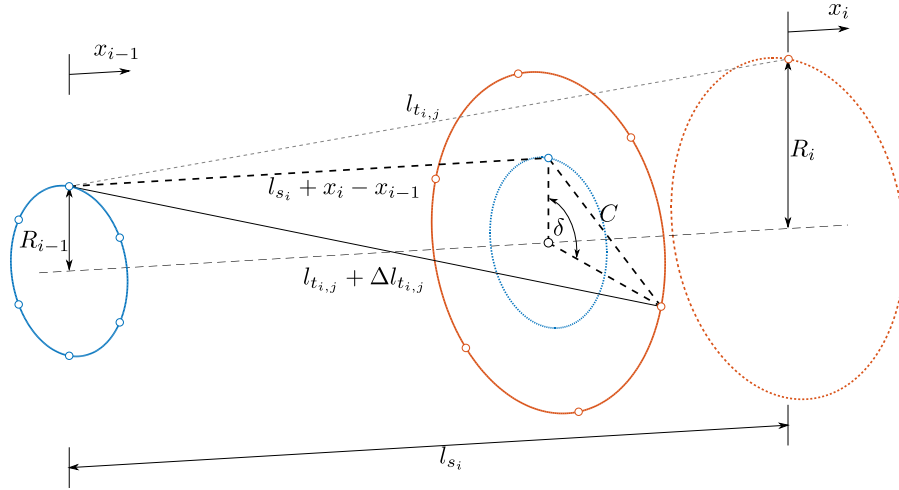
Figure 4.12: Diagram showing the change in tether length, $\Delta l_{t_{i,j}}$, of the jth tether within the ith TRPT section.

ring. Similar to (4.29) in Section 4.4 the distance C is calculated from

$$C = R_i^2 + R_{i-1}^2 - 2R_i R_{i-1} \cos(\delta) \tag{4.69}$$

where $\delta = \theta_{i,j} - \theta_{i-1,j}$. The change in tether length, $\Delta l_{t_{i,j}}$, for the jth tether on the ith ring is therefore given by

$$\Delta l_{t_{i,j}} = \sqrt{(l_{s_i} + x_i - x_{i-1})^2 + R_i^2 + R_{i-1}^2 - 2R_i R_{i-1} \cos(\theta_{i,j} - \theta_{i-1,j})} - l_{t_{i,j}} \tag{4.70}$$

By substituting (4.67), (4.68) and (4.70) into (4.66) the equations of motion, excluding the aerodynamic forces on the tethers, can be defined. For simplicity let

$$A_1 = (l_{s_i} + x_i - x_{i-1})^2 + R_{i,j}^2 + R_{i-1}^2 - 2R_i R_{i-1} \cos(\theta_{i,j} - \theta_{i-1,j}) \tag{4.71}$$

$$A_2 = (l_{s_{i+1}} + x_{i+1} - x_i)^2 + R_i^2 + R_{i+1}^2 - 2R_i r_{i+1} \cos(\theta_{i+1,j} - \theta_{i,j}) \tag{4.72}$$

The equation of motion for the axial degree of freedom, x_i, of the ith ring is

$$\frac{d}{dt}\frac{\partial L}{\partial \dot{x}_i} - \frac{\partial L}{\partial x_i} = \sum_{j=1}^{N_t} m_{i,j} \ddot{x}_i + \sum_{j=1}^{N_t} k t_{i,j} \left(\frac{(l_{s_i} + x_i - x_{i-1})\left(\sqrt{A_1} - l_{t_{i,j}}\right)}{\sqrt{A_1}} \right)$$

$$- \sum_{j=1}^{N_t} k t_{i+1,j} \left(\frac{(l_{s_{i+1}} + x_{i+1} - x_i)\left(\sqrt{A_2} - l_{t_{i+1,j}}\right)}{\sqrt{A_2}} \right) \tag{4.73}$$

and the equation of motion for the rotational degree of freedom, $\theta_{i,j}$, of the jth mass on the ith ring is

$$\frac{d}{dt}\frac{\partial L}{\partial \dot{\theta}_{i,j}} - \frac{\partial L}{\partial \theta_{i,j}} = m_{i,j} R_i^2 \ddot{\theta}_{i,j} + k t_{i,j} \left(\frac{R_i R_{i-1} \sin(\theta_{i,j} - \theta_{i-1,j})\left(\sqrt{A_1} - l_{t_{i,j}}\right)}{\sqrt{A_1}} \right)$$

$$- k t_{i+1,j} \left(\frac{R_i R_{i+1} \sin(\theta_{i+1,j} - \theta_{i,j})\left(\sqrt{A_2} - l_{t_{i+1,j}}\right)}{\sqrt{A_2}} \right)$$

$$+ 2k r_{i,j}^2 \theta_{i,j} - k r_{i,j+1}^2 \theta_{i,j+1} - k r_{i,j-1}^2 \theta_{i,j-1} \tag{4.74}$$

The aerodynamic forces on the tether are accounted for with additional terms within the equations of motion. Similar to the spring–disc model, for a fixed elevation angle, the aerodynamic forces on the tether are dependant on the wind speed, V_w, and the position and velocity of the system, $\mathbf{u}$ and $\dot{\mathbf{u}}$ respectively. The function $\mathbf{f}_D$ determines the axial force and opposing torque that is a result of the tether aerodynamics, $\mathbf{f}_D(V_w, \mathbf{u}, \dot{\mathbf{u}})$. For a given elevation angle (β) the equations of motion can be written in the general form

$$\mathbf{M}\ddot{\mathbf{u}} + \mathbf{f}_D(\mathbf{V}_w, \mathbf{u}, \dot{\mathbf{u}}) + \mathbf{f}_S(\mathbf{u}) = \mathbf{f}_{ext} \qquad (4.75)$$

where $\mathbf{M}$ is the mass and inertia matrix, defined in (4.76), $\mathbf{u}$ the position vector that includes the rotational and axial positions, $\mathbf{f}_D$ the aerodynamic forces on the tether, $\mathbf{f}_S$ the spring forces and $\mathbf{f}_{ext}$ the forces from the rotor, generator and lift kite. The rotor torque, $AeroQ$, is split between three of the rotational degrees of freedom on the first ring. This torque is applied to alternate points on the ring to account for the three wings of the Daisy Kite rotor. The resisting generator torque, $GenQ$, is applied to the last ring in the TRPT. It is split equally between the rotational degrees of freedom on this last ring. Similar to the spring–disc representation the mass and moment of inertias of the last ring is increased to account for the increased mass of the ground station ring and the inertia within the drivetrain. The mass and moment of inertia of the first ring is also increased to account for the rotor.

The first term in (4.75), $\mathbf{M}\ddot{\mathbf{u}}$, corresponds to the first terms in (4.73) and (4.74), the acceleration terms. The spring forces, $\mathbf{f}_S(\mathbf{u})$, are calculated using all but the acceleration terms in equations (4.73) and (4.74).

The aerodynamic forces on the tether, $\mathbf{f}_D$, and the spring forces, $\mathbf{f}_S$, are non–linear terms. Similar to the spring–disc representation, an analytical solution is not suitable. The central difference integration method has been applied to solve the equations of motion, defined in (4.75). The algorithm implemented to solve this multi–spring representation, for a fixed generator torque, is given in Table 4.6.

$$\mathbf{M} = \begin{bmatrix} \sum_{j=1}^{N_t} m_{1,j} & 0 & 0 & \cdots & 0 & 0 & 0 & \cdots & 0 \\ 0 & J_{1,1} & 0 & \cdots & 0 & 0 & 0 & \cdots & 0 \\ 0 & 0 & J_{1,2} & \cdots & 0 & 0 & 0 & \cdots & 0 \\ \vdots & \vdots & \vdots & \ddots & \vdots & \vdots & \vdots & \ddots & \vdots \\ 0 & 0 & 0 & \cdots & J_{1,6} & 0 & 0 & \cdots & 0 \\ 0 & 0 & 0 & \cdots & 0 & \sum_{j=1}^{N_t} m_{2,j} & 0 & \cdots & 0 \\ 0 & 0 & 0 & \cdots & 0 & 0 & J_{2,1} & \cdots & 0 \\ \vdots & \vdots & \vdots & \ddots & \vdots & \vdots & \vdots & \ddots & \vdots \\ 0 & 0 & 0 & \cdots & 0 & 0 & 0 & \cdots & J_{N_r,N_t} \end{bmatrix} \qquad (4.76)$$

Inputs	Wind speed V_w, TRPT geometry $\mathbf{R}$ and $\mathbf{l}_s$, elevation angle β, initial conditions $\mathbf{u}_2$ and $\dot{\mathbf{u}}_2$, generator torque $GenQ$, number of tethers N_t.
Line 1	Find $\mathbf{l}_t$ and $\mathbf{M}$
Line 2	Find $AeroQ_2$, $AeroT_2$ and $AeroP_2$
Line 3	Find lk_T, $\mathbf{f}_{S,2}$ and $\mathbf{f}_{D,2}$
Line 4	Find $\mathbf{p}_2$
Line 5	$\ddot{\mathbf{u}}_2 = \dfrac{\mathbf{M}}{\mathbf{p}_2 - \mathbf{f}_{S,2}}$
Line 6	$\mathbf{u}_1 = \mathbf{u}_2 - \Delta t \dot{\mathbf{u}}_2 + \dfrac{\Delta t^2}{2}\ddot{\mathbf{u}}_2$
Line 7	$\mathbf{a} = \dfrac{\mathbf{M}}{\Delta t^2}, \quad \mathbf{b} = \dfrac{2\mathbf{M}}{\Delta t^2}$
Line 8	**For** each time step, i
Line 9	Find $AeroQ_i$, $AeroT_i$ and $AeroP_i$
Line 10	Find lk_T, $\mathbf{f}_{S,i}$ and $\mathbf{f}_{D,i}$
Line 11	Find $\mathbf{p}_i$
Line 12	$\mathbf{c} = \mathbf{p}_i - \mathbf{a}\mathbf{u}_{i-1} - \mathbf{f}_{S,i} + \mathbf{b}\mathbf{u}_i$
Line 13	$\mathbf{u}_{i+1} = \dfrac{\mathbf{a}}{\mathbf{c}}$
Line 14	$\dot{\mathbf{u}}_i = \dfrac{\mathbf{u}_{i+1} - \mathbf{u}_{i-1}}{2\Delta t}, \quad \ddot{\mathbf{u}}_i = \dfrac{\mathbf{u}_{i+1} - 2\mathbf{u}_i + \mathbf{u}_{i-1}}{\Delta t^2}$
Line 15	**End For**
Outputs	$\mathbf{u}$, $\dot{\mathbf{u}}$, $\ddot{\mathbf{u}}$, $\mathbf{AeroQ}$, $\mathbf{AeroT}$, $\mathbf{AeroP}$, $\mathbf{f}_D$, $\mathbf{f}_S$, $\mathbf{p}$

Table 4.6: Pseudo code for the multi–spring TRPT representation. $\mathbf{R}$ is the vector for the discs radii, $\mathbf{l}_s$ is the vector containing the TRPT section lengths, $\mathbf{l}_t$ the vector for tether lengths in each TRPT section, $\mathbf{M}$ the mass and inertia matrix, $AeroQ$ the rotor torque, $AeroT$ the rotor thrust, $AeroP$ the rotor power, lk_T the lift kite line tension, $\mathbf{f}_S$ the spring forces, $\mathbf{f}_D$ the aerodynamic forces on the tethers, $\mathbf{p}$ the force applied to each point mass, Δt the time step length and $\mathbf{u}, \dot{\mathbf{u}}, \ddot{\mathbf{u}}$ the vectors containing the masses positions, velocities and accelerations respectively. $\mathbf{a}, \mathbf{b}, \mathbf{c}$ are variables used within the algorithm.

4.8   Summary

This chapter has detailed the mathematical representation of rotary AWES that utilise TRPT. The separate modules, as shown in Figure 4.1, that make up the entire system model have each been described. The use of lightweight tethers to transfer torsion is a novel method of power transmission. Considering this, particular attention has been given to the *TRPT Dynamics* module of the system model as shown in Figure 4.1. The three models that have been developed for the *TRPT Dynamics* module represent a key contribution of this thesis work.

The *Rotor Aerodynamics*, *TRPT Dynamics* and *Tether Aerodynamics* modules have different versions as described throughout this chapter. The different versions of these three modules are listed below:

Rotor Aerodynamic

1. Actuator disc

2. Blade element momentum, NREL's AeroDyn v15

Tether Aerodynamics

1. Simple tether drag

2. Improved tether drag

TRPT Dynamics

1. Steady state

2. Spring–disc

3. Multi–spring

The different version listed above have been combined in to form three separate system models, each based on one of the three models for the *TRPT Dynamics* module. The different configurations that make up the three system models are summarised as follows:

1. **The steady state model** – incorporating the actuator disc model, the steady state analysis of the TRPT in Section 4.4 and the simple tether drag model in section 4.5.1.

2. **The spring–disc model**, as described in Section 4.6 – incorporating AeroDyn, the static analysis of the TRPT in Section 4.4 to define the torsional stiffness of each section and the improved tether drag model in Section 4.5.2.

3. **The multi–spring model**, as described in Section 4.7 – incorporating AeroDyn and the improved tether drag model in Section 4.5.2.

The three models have been developed for rotary AWES that use TRPT, they are based on the Daisy Kite system produced by W&I. The next chapter provides analysis of the rotary AWES, the Daisy Kite, using these three mathematical representations.

Chapter 5

Simulations and Analysis of Rotary Airborne Wind Energy Systems

This chapter details an analysis of the Daisy Kite design using the experimental data, introduced in Chapter 3, and the mathematical representations, described in Chapter 4. Firstly the experimental and simulation results are compared to one another in Section 5.1. Section 5.2 provides a comparison between the simulation results from the two dynamic representations, the multi–spring and spring–disc models. Section 5.3 gives a design analysis of the Daisy Kite system based on the steady state before an improved design is proposed in Section 5.4. Section 5.4 also identifies several operational characteristics of the Daisy Kite. Finally this chapter is concluded in Section 5.5.

5.1 Comparison of Mathematical Models and Experimental Data

Several Daisy Kite configurations have been tested during the experimental campaign, described in Section 3.1. This section provides comparisons between the system models described in Chapter 4 and the experimental data.

As detailed in Section 3.2.4 nine different Daisy Kite configurations have been tested,

156

of which six use a single rotor. The mathematical representations focus on single rotor systems, therefore the data collected from these are used for comparison. The wide range of system designs over a variety of operating conditions, for which experimental data has been collected, allows a comprehensive assessment of the models quality. This provides confidence in the simulation results when using the models to analyse the Daisy Kite design.

5.1.1 Steady State Representations Compared to Collected Data

TRPT Laboratory Experiments

To assess the accuracy of the static TRPT representation developed in Section 4.4, laboratory experiments on a single TRPT section were conducted. These are described in the internship student report given in Appendix A. The experimental results collected are compared to the torsional deformation calculated using (4.32) defined in Section 4.4. The results for the 30kg load case tested during the laboratory experiments are shown in Figure 5.1.
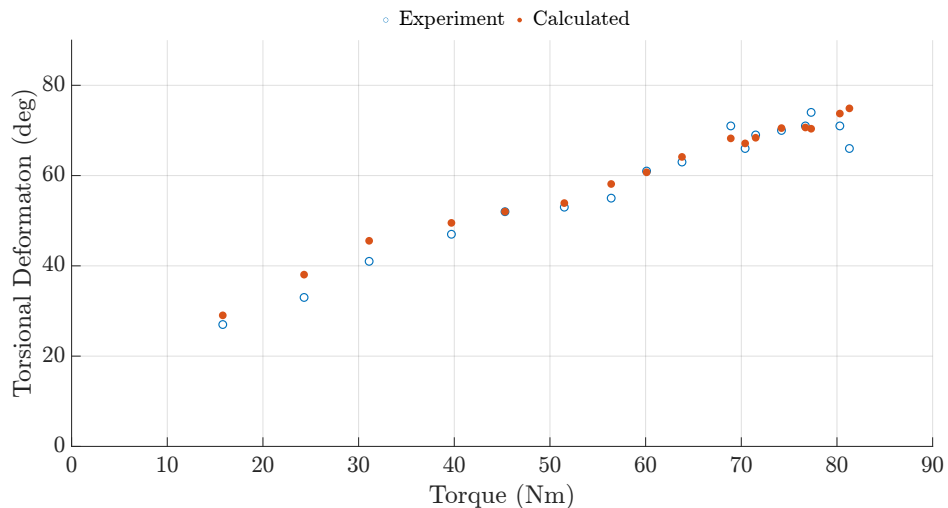
Figure 5.1: TRPT laboratory experimental results compared to calculated torsional deformation for the 30kg load case.

It can be seen in Figure 5.1 that the difference between the measured data and the calculated values is small. As highlighted in the report given in Appendix A, the friction of the pulley's and casters within the laboratory equipment cause the calculated and experimental data to be more closely matched when larger axial tensions are applied. The largest axial tension tested is the 30kg load case. The comparison in Figure 5.1 shows that the modelled relationships between torque and torsional deformation are consistent with experimental results.

Full System

The initial comparison between the developed models and experimental data is based on the steady state response. It is assumed that there is no torsional deformation within the TRPT. The spring–disc model is used to calculate the power coefficient at different tip speed ratios. Figure 5.2 shows the comparison of the calculated and measured C_p over a range of tip speed ratios, for the six single rotor configurations. The experimental data shown are averages over one minute. Table 5.1 shows the test dates that data for each comparison is taken from. The raw test data is processed as described in Section 3.4.1. The configurations with soft wings and rigid wings are discussed separately in the following.

– Configurations with Soft Wings

Figures 5.2(a), 5.2(b) and 5.2(c) show the results using soft wings and TRPT versions 1, 2 and 3 respectively. The maximum values of C_p obtained in the simulation results in Figures 5.2(a) and 5.2(b), at an elevation angle of 40°, are 0.02. The maximum value of C_p in Figure 5.2(c) at 25° is 0.1. It can be seen that the simulation results using TRPT–3 (Figure 5.2(c)), show larger C_p values and reach the maximum C_p at a higher tip speed ratio compared to the simulation results for TRPT–1 and 2. This is due to a lower elevation angle. The experimental results for TRPT–1 and 2, shown in Figures 5.2(a) and 5.2(b), were collected with the Daisy Kite using a lift kite, whereas,

(a) Configuration 1 − Soft wing TRPT−1

(b) Configuration 2 − Soft wing TRPT−2

(c) Configuration 3 − Soft wing TRPT−3

(d) Configuration 7 − Rigid wing TRPT−3

(e) Configuration 8 − Rigid wing TRPT−4

(f) Configuration 9 − Rigid 6 wing TRPT−5
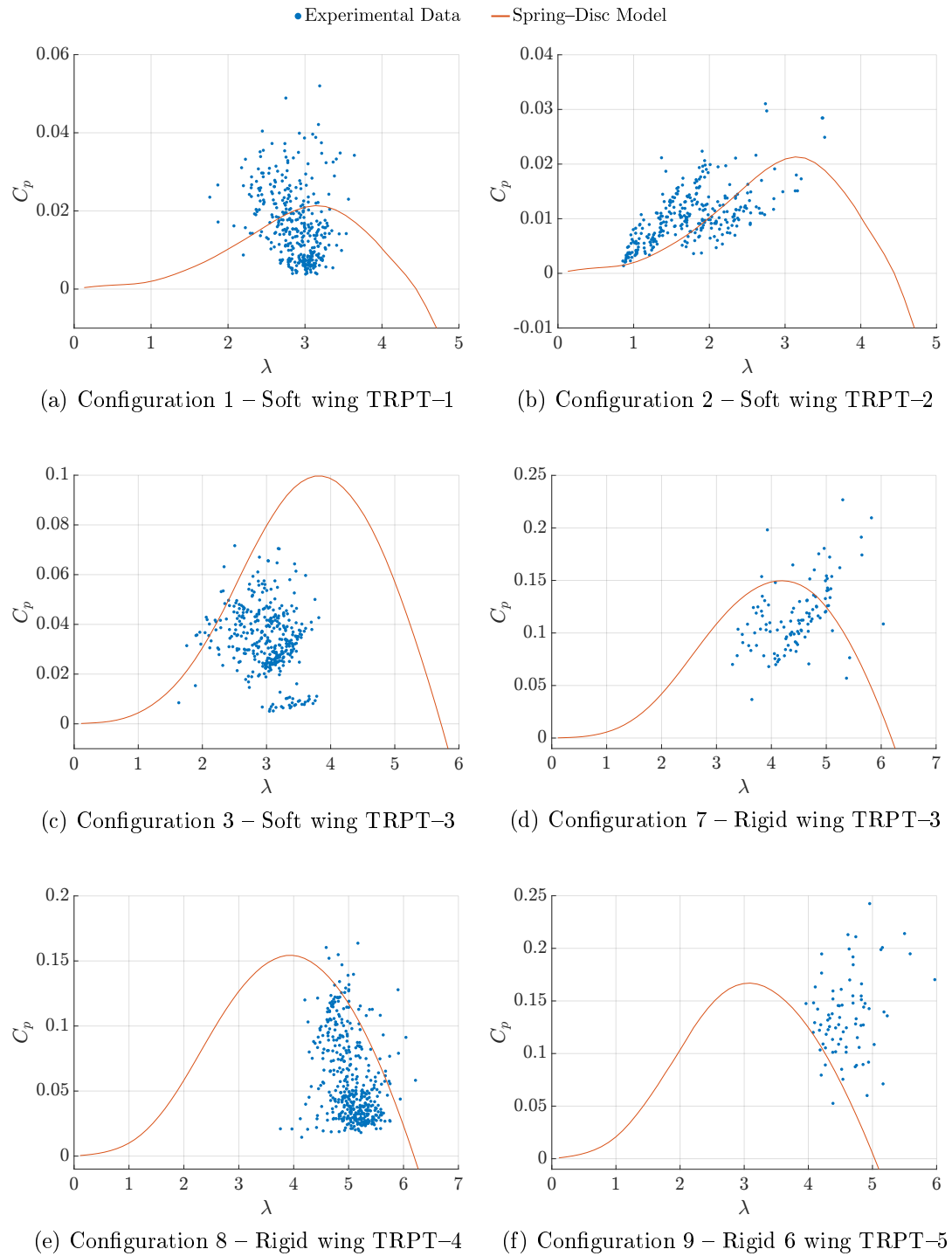
Figure 5.2: Power coefficient against tip speed ratio for various Daisy Kite configurations using the steady state spring–disc model compared to experimental data.

the experimental results for TRPT–3, shown in Figure 5.2(c), are from a mast mounted test. The elevation angle for the mast mounted test is around 25° , using a lift kite the system's elevation angle is much larger at 40°. As highlighted in Section 4.2.1, the BEM theory, used to model the Daisy Kite's rotor aerodynamics, is likely to be less accurate for higher elevation angles. Simulations with the angle larger than 30° are only used to compare the mathematical models with collected data. Due to the reduction in power generation as the elevation angle is increased, it is expected that lower elevation angles will be more advantageous for rotary AWES. The experimental results shown in Figure 5.2(b) are obtained from the constant speed tests, where a wider range of tip speed ratios were tested.

– Configurations with Rigid Wings

Figures 5.2(d), 5.2(e) and 5.2(f) show the results for rigid wings with TRPT versions 3, 4 and 5 respectively. Among the six comparisons made, Figure 5.2(f) displays the largest difference between the simulation and experimental results. Very few of the experimental data points stay close to the simulation results. This suggests possible missing elements in the mathematical representation for the 6–bladed rotor. The rotor aerodynamics package, AeroDyn, used within the mathematical representation does not support rotors with more than three blades. Therefore, to model the six bladed rotor, a three bladed rotor was simulated with increased solidity to match with the six bladed configuration. This was achieved by increasing the blades chord lengths. Although this provides an indication of the performance for the higher solidity rotor, it is less accurate when compared to other simulations.

In can be seen from the plots shown in Figure 5.2 that the model is able to predict the steady state values for the six Daisy Kite configurations. Table 5.1 shows the root mean square errors (RMSE) for C_p between the simulation and experimental data averaged over one minute. It can be seen that the lowest error is found for configuration 2 (Figure 5.2(b)), where constant speed tests were used to provide a wider range of tip speed

Configuration	Test Dates	Total Data Length (min)	RMSE
1	18$^{\text{th}}$ June 2017 27$^{\text{th}}$ June 2017	362	0.0106
2	5$^{\text{th}}$ June 2018 13$^{\text{th}}$ June 2018	293	0.0052
3	17$^{\text{th}}$ Aug 2018 22$^{\text{nd}}$ Aug 2018 28$^{\text{th}}$ Aug 2018	375	0.0494
7	27$^{\text{th}}$ Aug 2018 31$^{\text{st}}$ Aug 2018	112	0.0492
8	13$^{\text{th}}$ Dec 2019 17$^{\text{th}}$ May 2019 5$^{\text{th}}$ June 2019 6$^{\text{th}}$ June 2019 24$^{\text{th}}$ Aug 2019 8$^{\text{th}}$ Sept 2019	442	0.0619
9	29$^{\text{th}}$ Apr 2020 16$^{\text{th}}$ May 2020	78	0.1084

Table 5.1: C_p RMSE between simulation results and experimental data

ratios. Configuration 2 used a lift kite with an elevation angle of around 40° , indicating that the mathematical representation is more accurate at higher elevation angles. The greatest error is seen for configuration 9, (Figure 5.2(f)) which uses the 6–bladed rotor. The modelling of the 6–bladed rotor produces less accurate results due to the limitation of the rotor aerodynamics package used.

The accuracy of the mathematical representation is also assessed by comparing the following Daisy Kite configurations using the spring–disc model:

- Soft wings with rigid wings

- Pitched rigid blades with flat rigid blades

- TRPT–3 (rigid wing) with TRPT–4 (rigid wing)

- 3 rigid blades with 6 rigid blades

These comparisons are shown in Figure 5.3.

Figure 5.3(a) shows the simulation results for both the soft and rigid wings using TRPT–3. It can be clearly seen that the rigid wings achieve higher C_p values over the full range of λ simulated. The maximum C_p achieved by the soft wings is 0.1 at $\lambda = 3.9$, whereas the rigid wings achieved a maximum C_p of 0.15 at $\lambda = 4.2$, a 50% increase. This highlights the improved aerodynamic performance of the rigid wings, as confirmed by the experimental data.

Figure 5.3(b) shows the simulation results for the two different rigid blade pitch angles tested during the experimental campaign for TRPT–3. Feathering the blades by $4°$ increases the maximum C_p value achieved from 0.15 to 0.155 compared to the flat blades. It also lowers the tip speed ratio that the maximum C_p occurs at from 4.2 to 4.0. Within the experimental data it was not possible to identify any significant change in C_p or λ for the different blade pitches. The simulation results show that the increase in performance of the $4°$ pitched blades is only minor, with a 3% increase in the maximum value of C_p. This was not noticeable within the noise of the experimental results.

Figure 5.3(c) shows the simulation results comparing TRPT–3 and TRPT–4. Within the simulation results there is only a minor difference between the two TRPT's. TRPT–4 achieves a lower maximum C_p value by 5×10^{-4}. The increase in tether length from TRPT–3 to TRPT–4 is 3.4m, these simulation results show that the increase in tether drag due to this additional length is minor. The comparison based on the experimental results, shown in Figure 3.25, also showed little difference between the two TRPT's with TRPT–3 having slightly higher values of C_p, especially at higher tip speed ratios. The effect of tether drag on the Daisy Kite system is analysed further in Section 5.3.3.

Figure 5.3(d) shows the comparison between a 3 and 6 bladed rotor. As mentioned previously, the rotor aerodynamics module does not support simulating rotors with more than 3 blades, the 6–bladed rotor is modelled by increasing the chord length of the

(a) Rigid and soft wings

(b) 4° and 0° pitched rigid wings

(c) TRPT–3 and 4

(d) 3 and 6 blades
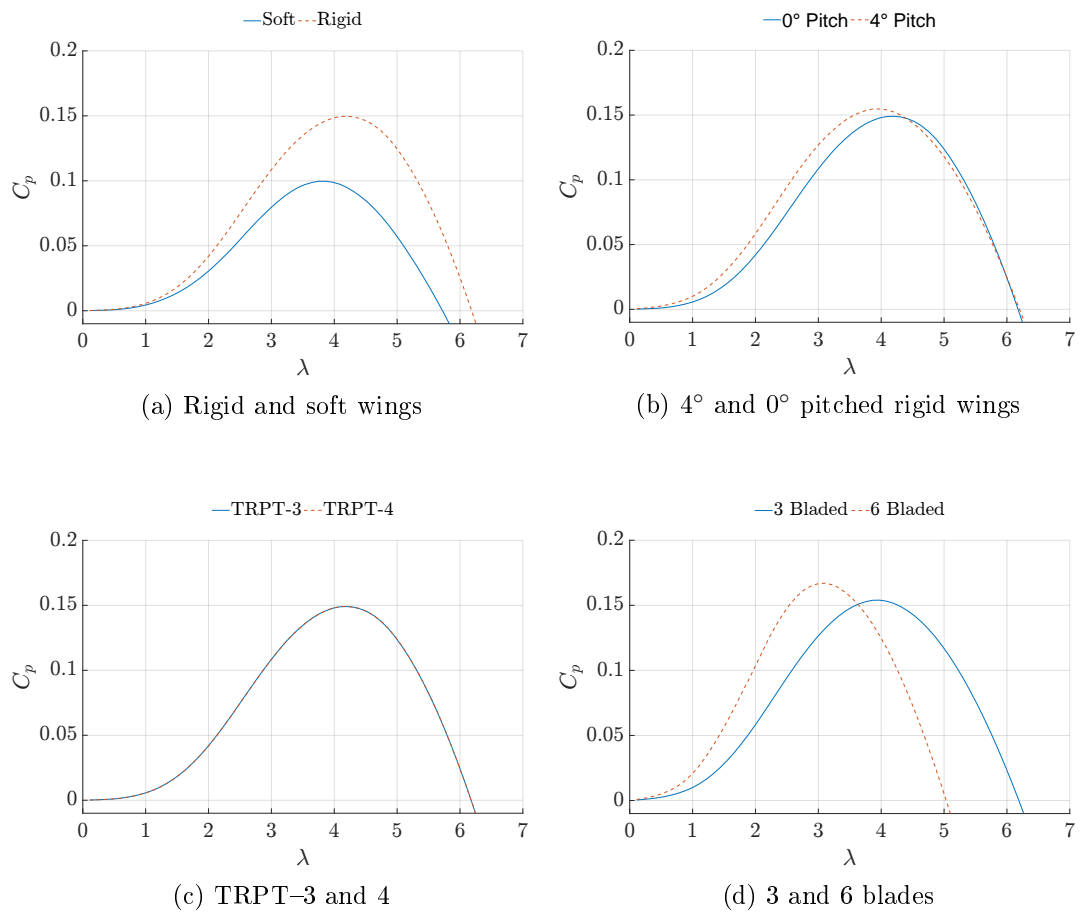
Figure 5.3: Steady state power coefficient against tip speed ratio, Daisy Kite configuration comparisons using spring–disc model.

3–bladed rotor. Both rotors have a 4° blade pitch. The simulation results show that the 6–bladed rotor achieves a higher maximum C_p value at a lower tip speed ratio. The 6–bladed rotor increases the maximum C_p from 0.155 to 0.166 and lowers the optimal tip speed ratio from 4.0 to 3.1 when compared with the 3–bladed rotor. This result is confirmed by the experimental data shown in Figure 3.26.

The steady state comparisons shown in Figures 5.2 and 5.3, along with the RMSE values given in Table 5.1, show that the mathematical model is able to calculate the steady state response of the six different single rotor Daisy Kite configurations tested. The model produces similar results to the experimental tests when comparing different Daisy Kite designs.

5.1.2 Spring–Disc Representation Compared to Experimental Data

To assess the performance of the spring–disc models dynamic behaviour, the measured wind speed and the corresponding output torque, as measured by the power meter during experimental tests, are used as inputs to the dynamic model. As the time step required for the model simulation is much smaller than the sampling frequency of the measured data, linear interpolation was used to disaggregated the experimental data.

Several 5–minute windows were selected from the experimental data for this comparison study. Firstly 5–minute windows with consecutive data were compared to each other based on the wind speed and power output. A window from the rigid wing test on 8th September 2019 using TRPT–4 was selected as the initial comparison case. The measured wind speed and power output have mean values of 5.5m/s and 35W respectively. Figure 5.4 shows the wind speed and power output for this 5–minute period.

It can be seen in Figure 5.4 that the power output experiences several sharp increases and reductions in magnitude which do not correspond to similar changes in wind speed. These changes in power output arise due to adjustments in the generator torque set by the VESC.
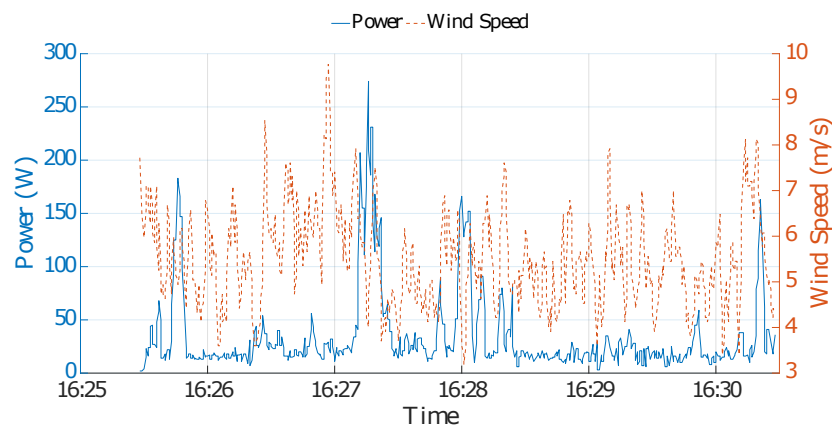
Figure 5.4: 5–minute window from experiential tests on 8th September 2019

During simulations the generator torque and wind speed are kept constant for the first 50 seconds, this ensures that any transient behaviour at the start of the simulation does not affect the comparison. The simulation results in Figure 5.5 show a close match to the experimental data, however, there are several instances where the simulation results deviate more from the experimental data. For example, at around 160 seconds the simulation results contain large oscillations with the predicted power output sharply dropping to 20W while the experimental power output is 110W. To reduce the difference between the simulation results and the collected data the spring–disc model is modified by considering the length of the TRPT subject to wind speed variations, this modification is described next.
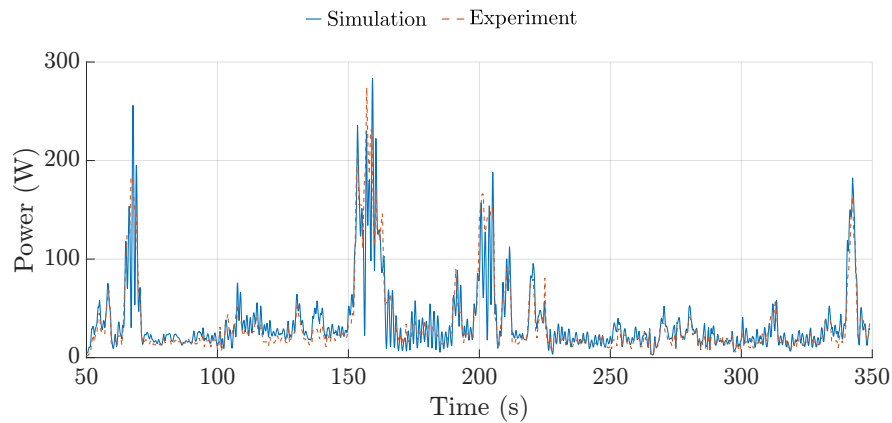
(a) Power output comparison
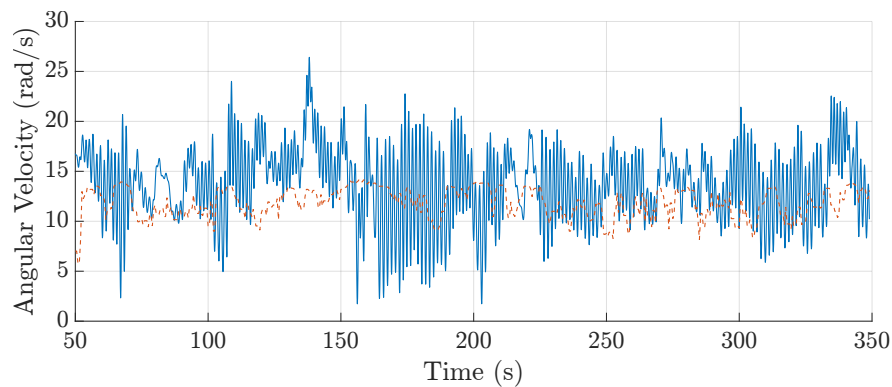
(b) Ground station angular velocity comparison

Figure 5.5: Initial comparison between the spring–disc model and experimental data

Rotor Relative Wind Speed

As described in Section 3.5.1 the length of the TRPT changes due to the change of the relative rotational position between TRPT rings. This is caused by constantly changing torque and axial tension applied to the TRPT due to wind speed fluctuations. The change in length of the TRPT impacts the relative wind speed that the rotor experiences. Initially this effect is neglected within the mathematical representations for simplicity. Figure 5.5(b) shows the evolution of the ground station's angular velocity for the spring–disc model where the change in TRPT length is neglected. It can be seen that the model output has much larger variations compared to the experimental data.

As the TRPT length reduces or increases, the rotor moves towards or away from the ground station. This motion is out of alignment with the wind vector by elevation angle β. An additional component, that is parallel to the wind vector, is added to the wind speed experienced by the rotor. This additional component is calculated using the elevation angle and the speed at which the rotors centre, or hub, moves towards or away from the ground station. The relative wind speed at the rotor, $V_{w_{hub}}$, is calculated using (5.1)

$$V_{w_{hub}} = V_w + \frac{Hub\ Speed}{\sin \beta} \tag{5.1}$$

where V_w is the ambient wind speed and *Hub Speed* is the speed of the rotor parallel to the system's axis of rotation.

Figure 5.6 shows the ground station's angular velocity when the change in TRPT length has been accounted for. Comparing Figures 5.5(b) and 5.6 it can be seen by incorporating the effect of the changing TRPT length, the magnitude of the fluctuations in the ground station's angular velocity has been reduced slightly. For example, in Figure 5.6 between 150 and 200 seconds into the simulation, there are fewer instances at which the angular velocity drops below $5rad/s$ compared to Figure 5.5(b).

Table 5.2 shows the RMSE between the simulated and experimental data, including and
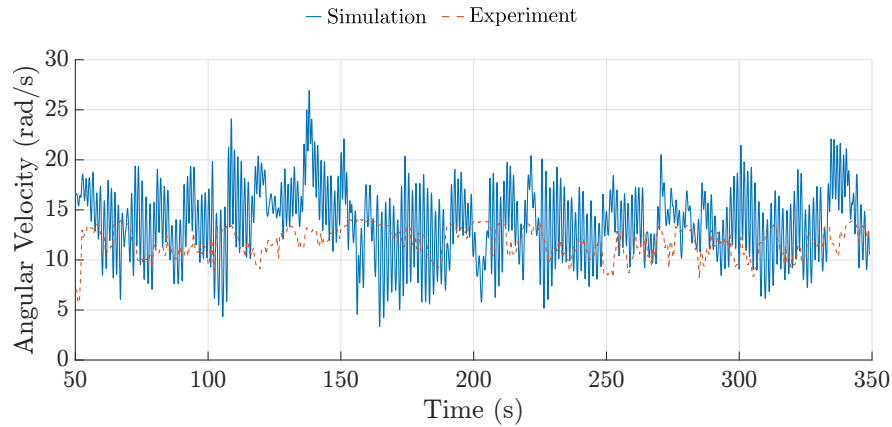
Figure 5.6: Ground station angular velocity accounting for the change in TRPT length within the spring–disc representation.

neglecting the change in TRPT length. It can be seen that by calculating the relative wind speed at the hub, using (5.1), the RMSE of the ground station angular velocity and the power output are reduced.

The error within the power output is reduced by almost 20% by accounting for the change in overall TRPT length. In this simulation the TRPT has an initial length of 10.3m. For longer TRPTs the overall length is likely to change by a larger amount during operation. The change in TRPT length should not be neglected. The improved representation of the rotors relative wind speed is therefore incorporated into both the spring–disc and multi–spring dynamic models.

	Ground Station ω RMSE	Power RMSE
TRPT length change neglected	4.42	17.92
TRPT length change included	4.23	14.54

Table 5.2: Assessment of including the relative motion of the rotor

First Natural Frequency

It can be seen from Figures 5.5(b) and 5.6 that the simulation results of the ground station's angular velocity contain high frequency oscillations that are not seen within the experimental results. To investigate this further the power spectral densities (PSD) of the simulation and experimental data are calculated. These are shown in Figure 5.7. The experimental data is recorded at a frequency of 2Hz therefore the comparison can only be made for frequencies up to 1Hz.

It can be seen from Figure 5.7 that the simulation PSD data contains a peak at a frequency of around 0.7 Hz, whereas the experimental data does not. The peak in the simulation data corresponds to the system's first natural frequency, as predicted by the spring–disc model. The model's natural frequencies can be determined by calculating the eigenvalues, using the mass and stiffness matrices of the system at a given operating point. Due to the non–linear relationship between the system's state and the torsional stiffness of each TRPT section, given by (4.33) in Section 4.4, the natural frequency of the system is constantly changing. Figure 5.8 shows how the first natural frequency changes over the 5–minute simulation.
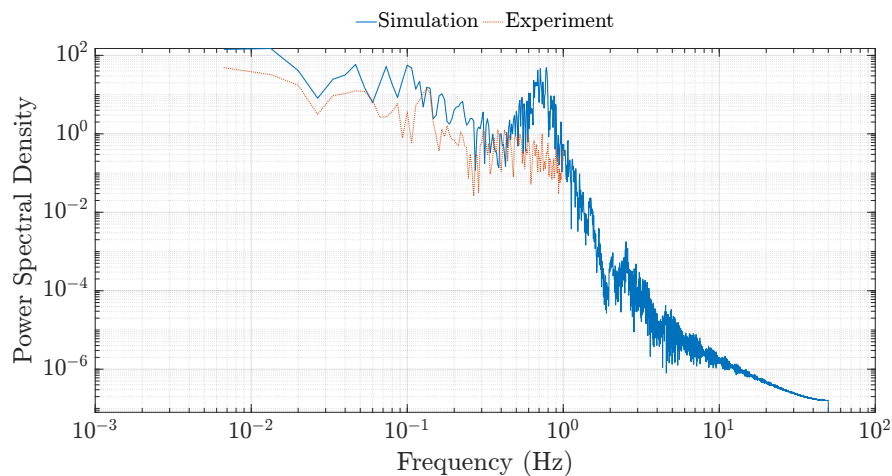
Figure 5.7: Power spectral density of the ground station angular velocity for the spring–disc model compared to the experimental data.

It can be seen from Figure 5.8 that for the given 5–minute window the system's first mode varies from as low as 0.6Hz to as high as 1.1Hz, with a mean value of 0.74Hz. This corresponds to the peak seen within the PSD shown in Figure 5.7. The first mode corresponds to the relative motion of the ground station wheel being in the opposite direction to all other TRPT ring's and the rotational displace-

Figure 5.8: Time profile of first natural frequency as calculated using the spring–disc model.

ment of the TRPT ring's increasing further from the ground station. This first natural frequency is not visible within the collected data.

As the first natural frequency is not present within the experimental data and spans a wide range within the simulated results, a filter is applied to remove the oscillations at the first mode from the simulation data. A low pass Butterworth filter is used to remove the oscillations in the simulation results at frequencies above the first mode. Figure 5.9 shows the PSD with the filter applied compared to the experimental data and the unfiltered model results. It can be seen that the low pass filter has successfully removed the peak in the simulation results at 0.7 Hz. Figure 5.10 shows the power output and the ground station angular velocity for the filtered simulation results compared to the experimental data.

Figure 5.10 shows that with the low pass filter applied to the simulation results they match more with the experimental data. The oscillations around the first natural frequency have been removed from both the power output and angular velocity results. This reduces the error between the mathematical representation and the experimental data. The RMSE between the model and experimental results, with and without the filter, for the ground station angular velocity (ω) and the power output are shown in Table 5.3. It can be seen that the filter reduces the error by around 30% and 20% for

169
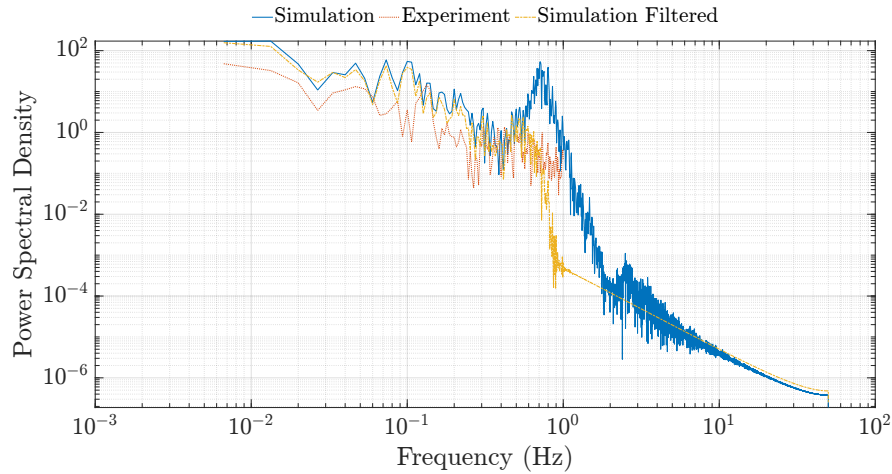
Figure 5.9: Power spectral density of the ground station angular velocity for the spring–disc model with and without a low pass filter applied.

the angular velocity and the power output respectively. It can be seen in Figure 5.10(a) that with the filter applied, the large deviations from the experimental data have been removed. For example, the large oscillations previously highlighted at 160 seconds in the power output are no longer present.

	ω RMSE	Power RMSE
Unfiltered	4.23	14.54
Filter applied	3.05	11.60

Table 5.3: RMSE with and without the low pass filter

Figure 5.9 shows that the impact of frequencies larger than 0.7 Hz within the simulation data are removed with a low pass Butterworth filter. As experimental data is recorded at a frequency of 2Hz it is not possible to assess the accuracy of the model at frequencies above 1Hz. It is also not possible to accurately compare the experimental and simulation data at frequencies close to 1Hz. As shown in Figure 5.7 the first natural frequency predicted by the spring–disc model is close to a frequency of 1Hz. It is therefore not possible to comment on the spring–disc model's characteristics near the system's first natural frequency. There is a risk that by applying the low pass filter important higher frequency dynamics are being neglected. However, given that the filter significantly reduces the error between the simulated and experimental data it is advisable to apply the low pass filter to the simulation results during the comparison.

170
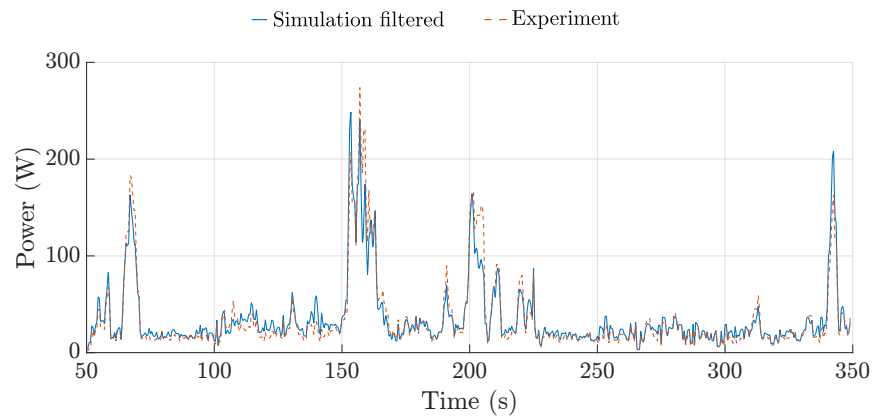
(a) Power output comparison
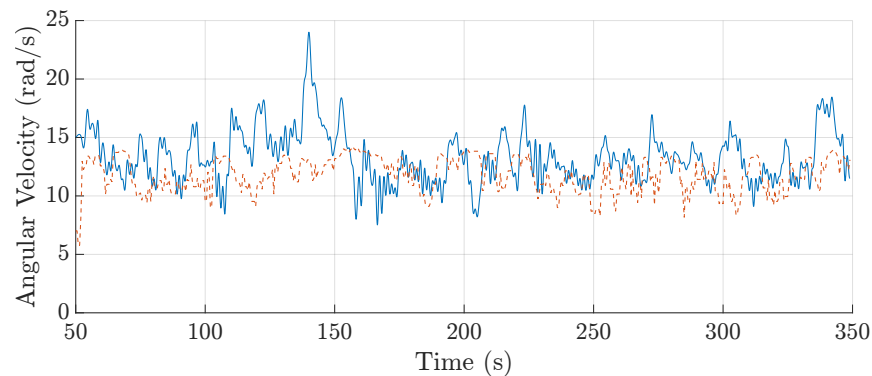
(b) Angular velocity comparison

Figure 5.10: Comparison between the spring–disc model with a low pass filter and experimental data

It can be seen from Figure 5.8 that the frequency of the system's first mode changes during the experiment. The five TRPT versions trialled within the experimental campaign will also have different natural frequencies. Therefore, a different low pass filter must be applied to the simulation results for each comparison with the experimental data. The low pass filter is set based on the mean frequency and the frequency range of the first mode for each 5–minute window. When the first natural frequency is higher than 1 Hz the low pass filter can be set to sample the data to 2 Hz to be compared with the experimental data.

The model has been improved by incorporating the relative wind speed experienced

Case	Test Date	Configuration	Wing	TRPT	Wind Speed (m/s)	Power Output (W)
1	08/09/2019	8	Rigid	4	5.3	35
2	20/09/2018	7	Rigid	3	6.1	50
3	27/08/2018	7	Rigid	3	2.7	10
4	06/05/2018	2	Soft	2	5.8	10
5	18/06/2017	1	Soft	1	5.5	15

Table 5.4: Five experiments used for comparison with the mathematical representations.

by the rotor and the low pass filter. Several sets of experimental data from different single rotor prototype configurations are used to compare with the spring–disc model. Table 5.4 shows the experimental test days from which the 5–minute windows have been taken, the corresponding Daisy Kite configuration, the mean wind speed and the mean power output during the 5–minute window. It is noted that for the rigid wing test conducted on 27th August 2018, case 3, the wings are flat to the ring; in the rigid wing tests conducted on 8th September 2019 and 20th September 2018, cases 1 and 2, the rigid wings are pitched to feather by $4°$.

Table 5.5 shows the results from comparing the spring–disc model to the five experimental cases. It gives the mean frequency of the system's first mode and the RMSE for

Case	1$^{\text{st}}$ Natural Frequency (Hz)	ω RMSE with filter	Power RMSE with filter
1	0.74	3.05	11.60
2	1.43	5.51	25.60
3	0.73	1.63	2.44
4	1.47	2.35	8.26
5	1.52	2.10	3.81

Table 5.5: Summary of comparison between spring–disc representation and experimental data

the ground station angular velocity and the power output with a low pass filter applied. It can be seen from Table 5.5 that the first natural frequency of the system is always less than 2Hz. In general the first mode occurs at a higher frequency when TRPTs with shorter lengths are used or the wind speed is higher. The decrease in the first mode frequency with a longer TRPT can be seen by comparing case 1, the case that incorporated TRPT–4, to the other four cases. TRPT–4 has a length of 10.3m, the length of the other three TRPTs used in this comparison are all less than 7.7m. The increase in first natural frequency with increased wind speed is shown by comparing case 3, which has a much lower mean wind speed, to case 2. Both experimental cases used TRPT–3. The difference in natural frequency is due to the stiffness of the TRPT. A shorter TRPT will be more rotationally stiff than a longer TRPT, so long as the radius of both TRPTs are similar. Equally as the wind speed increases a greater amount of axial tension is applied to the TRPT from the rotor thrust and the lift kite, this increases the rotational stiffness. An increase in the system's rotational stiffness results in the increase in the first mode frequency. It can be seen from Table 5.5 that the frequency of the first mode only drops below 1Hz for simulated results under cases 1 and 3.

Figure 5.11 shows the comparison of the ground station angular velocity for the simulated and experimental results for the four cases in Table 5.5, excluding case 1 as the latter is given in Figure 5.10(b). The experimental data shown in Figure 5.11(c) were collected during constant speed tests. Although in general the simulation is closely matched to the experimental data, it can be seen that there are instances where the simulation and experimental results are considerably different. For example in Figure 5.11(a) at around 120 seconds and 240 seconds the simulation data increases in velocity while the experimental data clearly decreases. Instances similar to this are likely due to the turbulent nature of the wind. During the experimental campaign the met mast is located at a distance from the Daisy Kite. The recorded wind speed that is used as an input to the simulation is therefore not necessarily the wind speed that the Daisy Kite's rotor experiences. As the rotor system was operated near the ground and there are a number of obstacles in the area surrounding the test site, e.g. trees and buildings,

the turbulence is likely to be high. From the measured data the turbulence intensity is found to range from 14% to 20%.

Given the experimental data and the different Daisy Kite configurations tested, it can be stated that the spring–disc model, in general, is able to match with the experimental data to a reasonable degree of accuracy. Taking account of the change in TRPT length and applying a low pass filter to the simulation results have improved the mathematical representation.
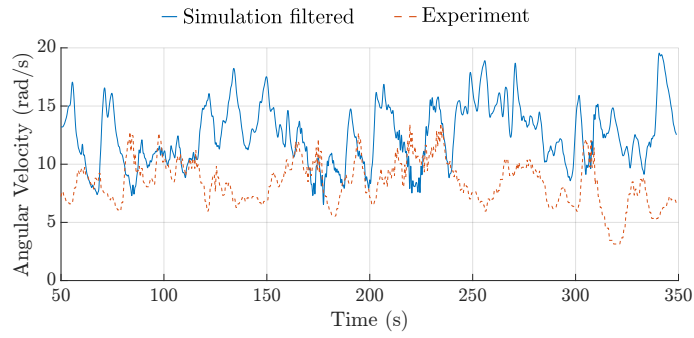
(a) Case 2: rigid wing, TRPT–3
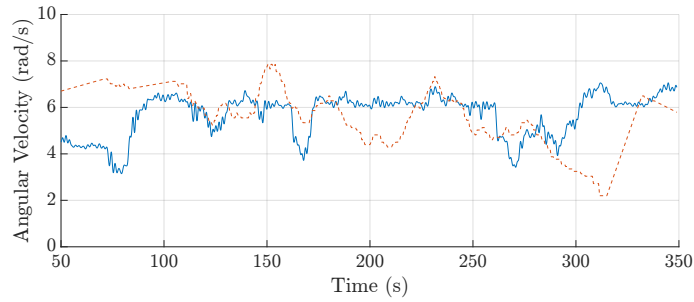
(b) Case 3: rigid wing, TRPT–3
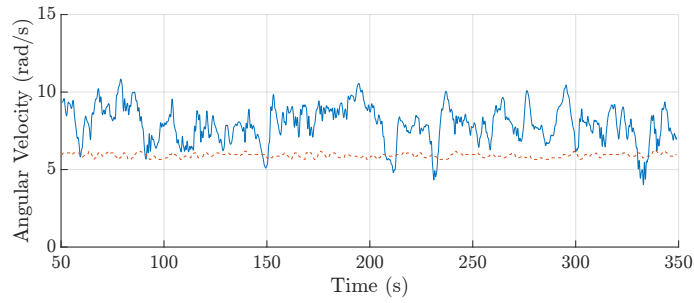
(c) Case 4: soft wing, TRPT–2
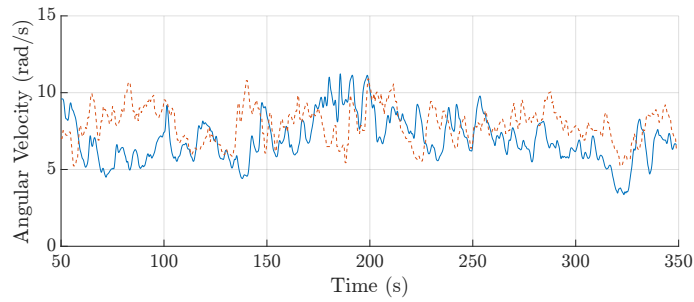
(d) Case 5: soft wing, TRPT–1

Figure 5.11: Comparison of the ground station angular velocity between the spring–disc model and experimental data

5.1.3   Multi–Spring Representation Compared to Experimental Data

The previous section has shown that the spring–disc model gives a reasonable match to the experimental data. This section will compare the multi–spring model developed in Section 4.7 with the same experimental data.

Multi–Spring Model Refinement

Prior to comparing the multi–spring model with the experimental data, it was necessary to modify the representation. The increased complexity of the multi–spring model allows more degrees of freedom to be included. This however, comes at the cost of requiring significantly more computational time, especially when the TRPT representation is coupled to AeroDyn. This is due to the smaller time step required when solving the multi–spring differential equation.

The stability and accuracy of the numerical integration method, the central difference method, depends on the size of the time step used when solving the equations of motion. If the time step is too large the solution becomes less accurate or even unstable. However, smaller time steps require more computational time, therefore, a large time step that gives a stable solution is identified. In the case of the spring–disc model this corresponds to a time step of 0.005s. The size of the suitable time step depends on the operating conditions, as the torsional stiffness increases the time step must decrease. With the same input the multi–spring model requires a time step of 0.00002s. The multi–spring representation therefore needs a time step that is 250 times smaller than the spring–disc model. The stability for a given time step is dependant on the systems stiffness. From the simulation studies in the previous section, it is found that the torsional stiffness of the spring–disc model rarely exceeds 100 N/m. In comparison, in the multi–spring model, the per unit length stiffness of the springs that represent the tethers and rings are set to be 5×10^5 N/m [135] and 4×10^6 N/m [136] respectively. This resulting in a much smaller time step required to achieve a stable solution.

To reduce the computational time required for the multi–spring model the rings are assumed to be rigid. The rings are about one order of magnitude stiffer than the tethers, by assuming rigid rings the size of the time step required for stable integration increases. From observations made during the experimental campaign it can be stated that the carbon fibre rings are seen to deform by a considerable amount. This deformation is usually experienced when the system is close to failure. During normal stable operation very small deformation of the TRPT rings was observed. To assess the impact of the ring deformation on the model's results, comparisons are made for the multi–spring representation using rigid and flexible rings.

Figure 5.12 shows the comparison of the results of the multi–spring representation assuming flexible and rigid rings. In these simulations the model is not coupled to Aero-Dyn, instead a constant torque and thrust of 43Nm and 325N respectively are applied at the rotor. The generator torque is set to 38Nm. These values are set so that the steady state of the system is close to the operating point at the optimal tip speed ratio with a wind speed of 8 m/s for Daisy Kite configuration 8, rigid wing rotor using TRPT–4. In this case the optimal tip speed ratio is 4.0. Once the simulation has reached the steady state the generator reaction torque is reduced by 1Nm for a period of 0.5 seconds to introduce the stimulation. Figure 5.12 shows the initial response to this change in the generator reaction torque.
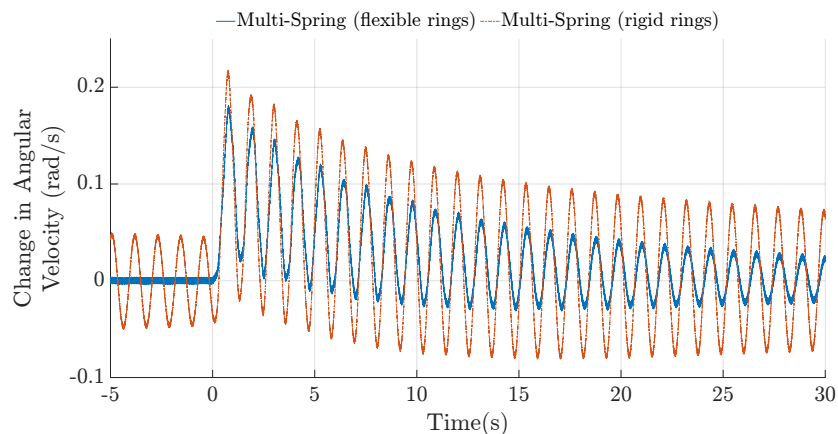
Figure 5.12: Results from the multi–spring representation comparing rigid and flexible carbon fibre rings within the TRPT.

177

It can be seen from Figure 5.12 that the result with rigid TRPT rings shows a similar response pattern as the flexible ring case. Rigid rings produce slightly higher amplitude oscillations in the transient part, also the settling time of the response is longer. The RMSE between the two response series in Figure 5.12 is calculated to be 0.023. Repeating this for inputs that correspond to wind speeds of 6 m/s and 10 m/s gives RMSE values of 0.036 and 0.010 respectively. These results show that neglecting the internal rotational deformation of the TRPT rings has a negligible effect on the model results and that the error between the flexible and rigid ring results reduces as the wind speed increases.

Table 5.6 shows the required time step and computational time for the multi–spring model with and without the assumption of rigid rings. For comparison the spring–disc model is also shown. The computational times are based on a 400 second simulation using MATLAB 2020a and a Intel Core i7–4790 processor. It can be seen that assuming the rings being rigid increases the time step by a factor of 5. The larger time step and fewer degrees of freedom reduces the computational time by a factor of 6. Given the reduced computational requirement and negligible impact on the results all future simulations using the multi–spring model assume that the TRPT rings are rigid.

Representation	Time Step	Computational Time
Multi–Spring (flexible rings)	0.00002 s	464 mins
Multi–Spring (rigid rings)	0.0001 s	77 mins
Spring–Disc	0.005 s	1.5 mins

Table 5.6: Time step and computational time for different mathematical representations.

Multi–Spring Comparison to Experimental Data

The modified multi–spring representation assuming rigid rings is used for comparison to the experimental data. As with the spring–disc model, the same 5–minute window
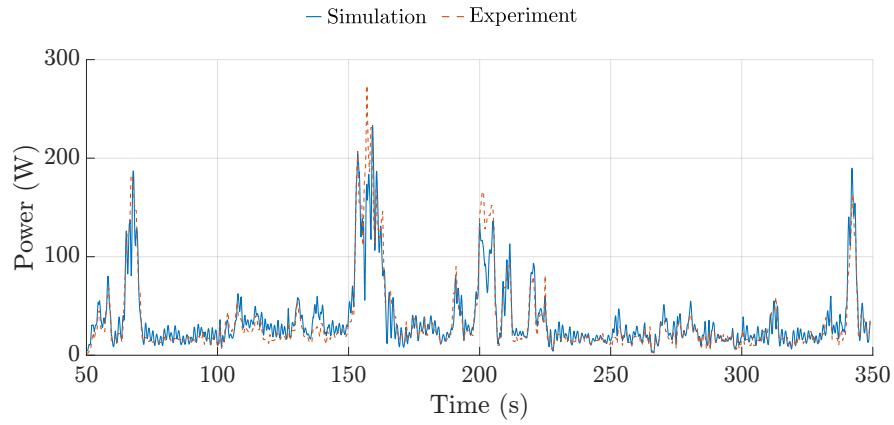
(a) Power output comparison
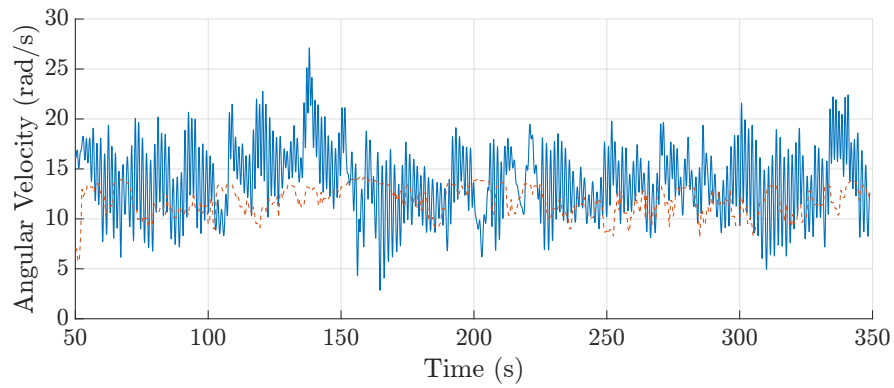
(b) Rotational speed comparison

Figure 5.13: Initial comparison between the Multi–Spring model and experimental data

taken from test data on 8th September 2018 is used for the initial comparison case.
Figure 5.13 shows the time profile comparison for both the systems power output and
the ground station's angular velocity. Again a constant input is applied for the first 50
seconds of the simulation to remove any initial transient effects.

First Natural Frequency

As can be seen from the power output, shown in Figure 5.13(a), the simulation re-
sults are similar to the experimental data. However, similar to the spring–disc model,
large high frequency oscillations can be seen in the simulated angular velocity. Again,
these oscillations found in the simulation results are not present in the experimental

data. To investigate this further, similar to the spring–disc model, the power spectral density of the ground station angular velocity is calculated. This is shown in Figure 5.14.

Figure 5.14 shows that the simulation results contain a large peak in the power spectral density around the frequency of 0.75Hz. This corresponds to the first natural frequency as identified using the spring–disc model and discussed in the previous section. Similar to the spring–disc simulation results, a low pass Butterworth filter is applied to remove the impact of oscillations at and above the first natural frequency for comparison with the experimental data. Figure 5.14 also shows the power spectral density of the simulation results with the low pass filter applied. It can be seen that the filter is able to remove the large peak at 0.75Hz from the original simulation results.

Figure 5.15 shows the power output and ground station angular velocity for the filtered simulation results compared to the experimental data. The filtered simulation results in Figure 5.15 confirm that the low pass filter is able to remove the higher frequency oscillations. By removing these oscillations the error between the model and the experimental data is reduced. For the ground station rotational speed, the RMSE between the simulation results and the experimental data with and without the low pass filter is 3.61
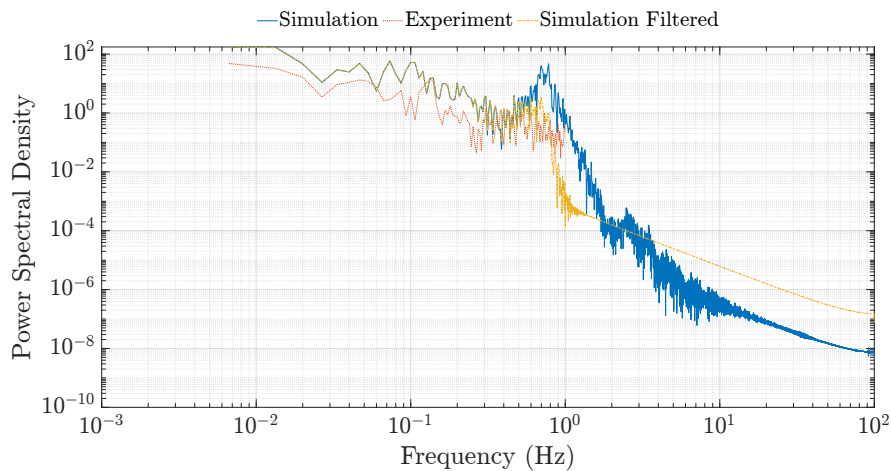
Figure 5.14: Power spectral density of the ground station rotational speed for the Multi–Spring model with and without a low pass filter applied compared to the experimental data.

and 4.20 respectively. The RMSE of the power output is 12.79 and 14.59 respectively with and without the filter. The low pass filter reduces the error between the model and experimental data by around 15%. The low pass filter is applied to all comparisons between the multi–spring model and the experimental data. As can be seen from Figures 5.7 and 5.14 the frequency of the first system mode is similar for the multi–spring and spring–disc models. The same low pass filters used with the spring–disc model are used for the multi–spring model for each comparison case.

Table 5.7 shows the RMSE for both the ground station angular velocity and the power output between the filtered multi–spring representation and the experimental data. By
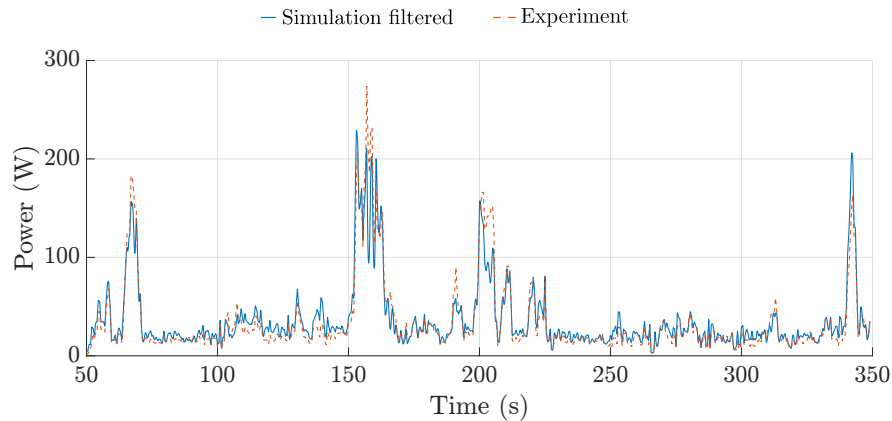
(a) Power output comparison
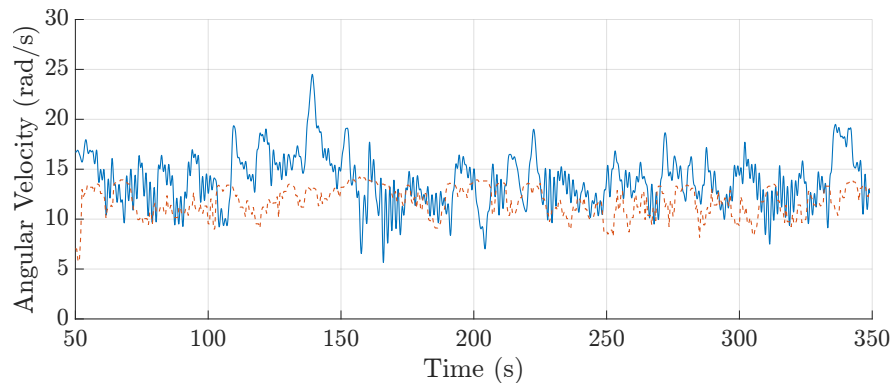
(b) Angular velocity comparison

Figure 5.15: Comparison between the experimental data and the multi–spring model with a low pass filter.

comparing the RMSE values for the multi–spring model in Table 5.7 with the RMSE values for the spring–disc model in Table 5.5, in can be seen that both representations achieve similar modelling accuracy for all cases.

Figure 5.16 shows the ground station angular velocity for the filtered multi–spring results for all cases, excluding Case 1 as this is given in Figure 5.15(b). It can seen from the results given in Table 5.7 and Figures 5.15 and 5.16 that the multi–spring model is able to match the experimental data to a similar degree of accuracy as the spring–disc representation.

Case	ω RMSE with filter	Power RMSE with filter
1	3.61	12.79
2	5.51	25.62
3	1.69	2.47
4	2.36	8.12
5	2.10	3.91

Table 5.7: Summary of comparison between the multi–spring representation and experimental data
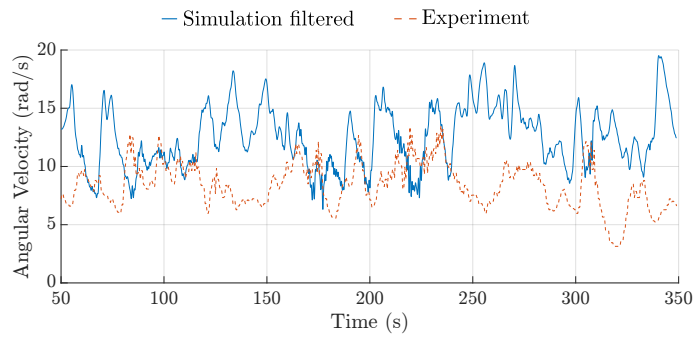
(a) 20$^{\text{th}}$ September 2018: rigid wing, TRPT–3
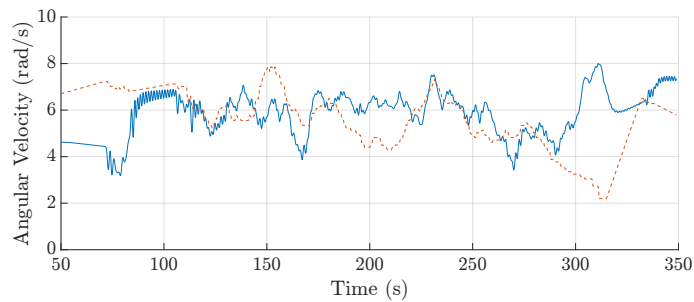
(b) 27$^{\text{th}}$ August 2018: rigid wing, TRPT–3
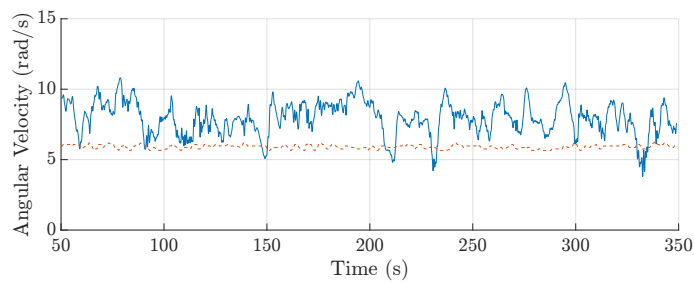
(c) 5$^{\text{th}}$ June 2018: soft wing, TRPT–2
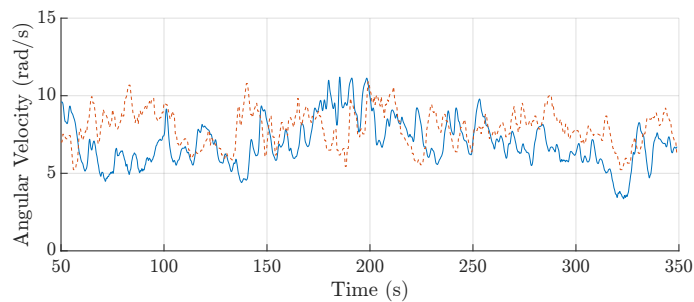
(d) 18$^{\text{th}}$ June 2017: soft wing, TRPT–1

Figure 5.16: Comparison of the ground station angular velocity between the multi–spring model and experimental data

5.2 Comparison of Spring–Disc and Multi–Spring Tensile Rotary Power Transmission Models

A series of simulations are run to compare the responses of the multi–spring and spring–disc models. Initially the TRPT models are run in isolation, the rotor aerodynamic and lift kite modules are used to set constant values of rotor torque, rotor thrust and lift kite force that correspond to a constant wind speed. The generator torque is set such that the system operates at or close to the optimal tip speed ratio. The Daisy Kite configuration 8, rigid wings and TRPT–4, is used for this comparison at a fixed elevation angle of 25°.

5.2.1 Steady State Response

Figure 5.17 shows the comparison between the two TRPT models given the constant input that corresponds to wind speeds of 8 m/s and 12 m/s. The system is initially set to be stationary before the input change is introduced. For 8 m/s the rotor and generator torque are set to 43Nm and 38Nm respectively, the combined rotor thrust and lift kite force is 325N. For 12 m/s the rotor and generator torque are 97Nm and 85Nm respectively, the combined rotor thrust and lift kite force is 733N.
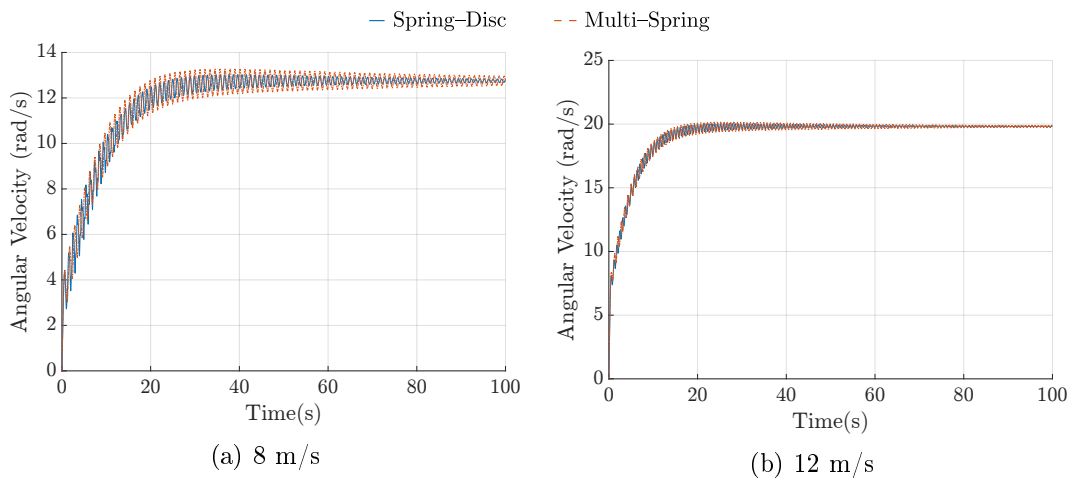
Figure 5.17: Angular velocity of the rotor for the spring–disc and multi–spring representations given constant rotor torque, rotor thrust, lift kite force and generator torque.

Figure 5.17 shows the response profiles of the angular velocity of the two models calculated at two wind speeds. It can be seen that the transient response and the steady state of both representations are similar for the two wind speeds. The constant inputs that correspond to a wind speed of 8 m/s results in a steady state value of close to 12.8 rad/s for both the multi–spring and spring–disc models. The multi–spring model has a slightly lower steady state angular velocity by 3.6×10^{-3} rad/s. At the wind speed of 12 m/s the steady state values of the angular velocity are close to 19.8 rad/s for both models with the multi–spring model again having a slightly lower angular velocity by 1.2×10^{-2} rad/s. The spring–disc model neglects the axial component of tether drag and possible changes in the tether's length, the drag is therefore slightly lower within the spring–disc model which results in the slightly higher steady state angular velocity. However, the difference between the two TRPT representations in the steady state is negligible.

5.2.2   Response to a Change in Torque and Tension

To further investigate the difference between the two TRPT models a variation in generator torque is applied. Starting from the steady state the generator torque is reduced by 1Nm for a period of 0.5 seconds and then returned to the original values of 38Nm and 85Nm for 8 m/s and 12 m/s respectively. Figure 5.18 shows the response of the multi–spring and spring–disc models for this short–period reduction in generator torque. Figures 5.18(a) and 5.18(c) show the response that corresponds to a wind speed of 8 m/s, Figures 5.18(b) and 5.18(d) show the response that corresponds to a wind speed of 12 m/s. Only the change in angular velocity from the initial steady state values are shown so that the response of both models can be more clearly compared.

It can be seen from Figure 5.18 that the responses of the two representations are very similar for both wind speeds and that the system response is highly oscillatory. Figures 5.18(c) and 5.18(d) show that the multi–spring representation has higher amplitude oscillations, it can also be seen that the amplitude of the oscillations are lower for higher

(a) 8 m/s

(b) 12 m/s

(c) magnification of 5.18(a)

(d) magnification of 5.18(b)
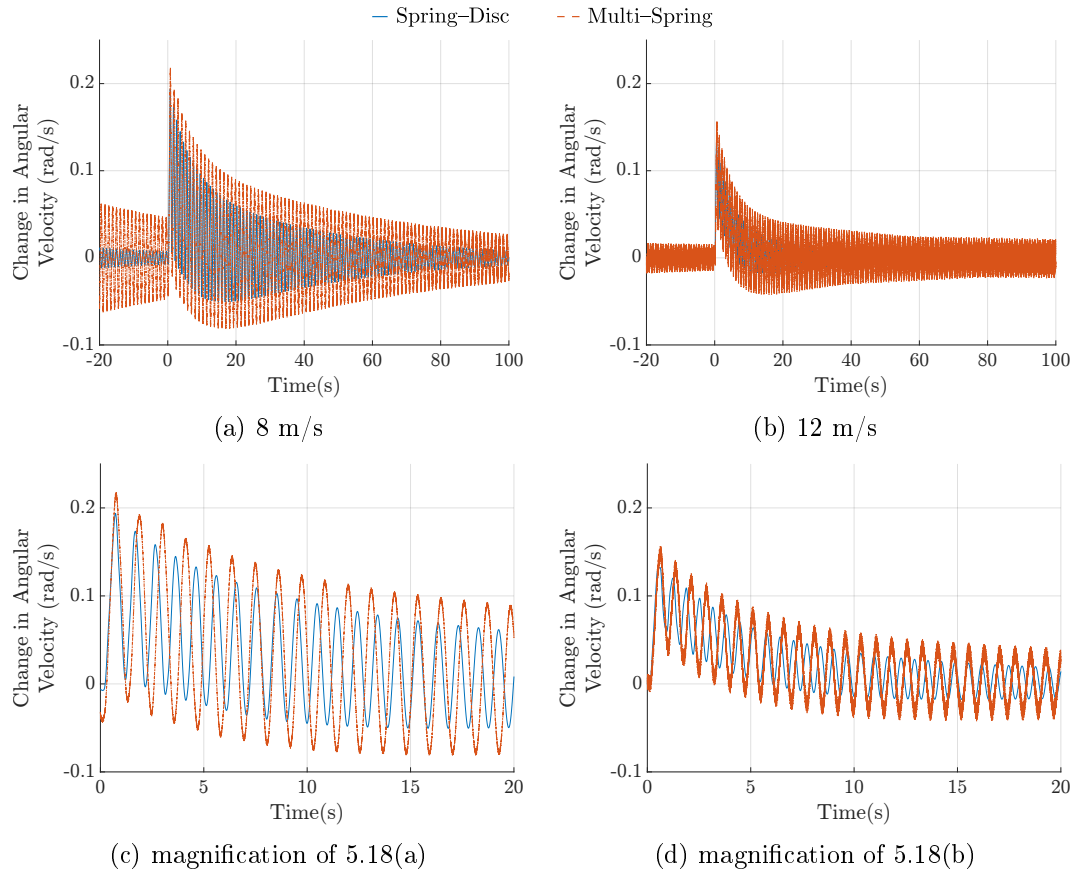
Figure 5.18: Angular velocity of the rotor for the spring–disc and multi–spring representations with a reduction in generator torque by 1Nm for a period of 0.5 seconds.

wind speeds for both representations.

Figure 5.19 shows the responses of both systems to a step change in the axial tension being applied. At the steady state the axial tension is increased by 100N for a period of 0.5 seconds and then decreased to the original value. Simulations are made at wind speeds of 8 m/s and 12 m/s and the response of the angular velocity are shown in Figure 5.19.

Both models produce similar responses to the step change in axial tension but the multi–spring model response exhibits larger amplitude oscillations. Table 5.8 shows the RMSE between the two responses subject to step changes in generator torque and axial

(a) 8 m/s

(b) 12 m/s

(c) magnification of 5.19(a)

(d) magnification of 5.19(b)
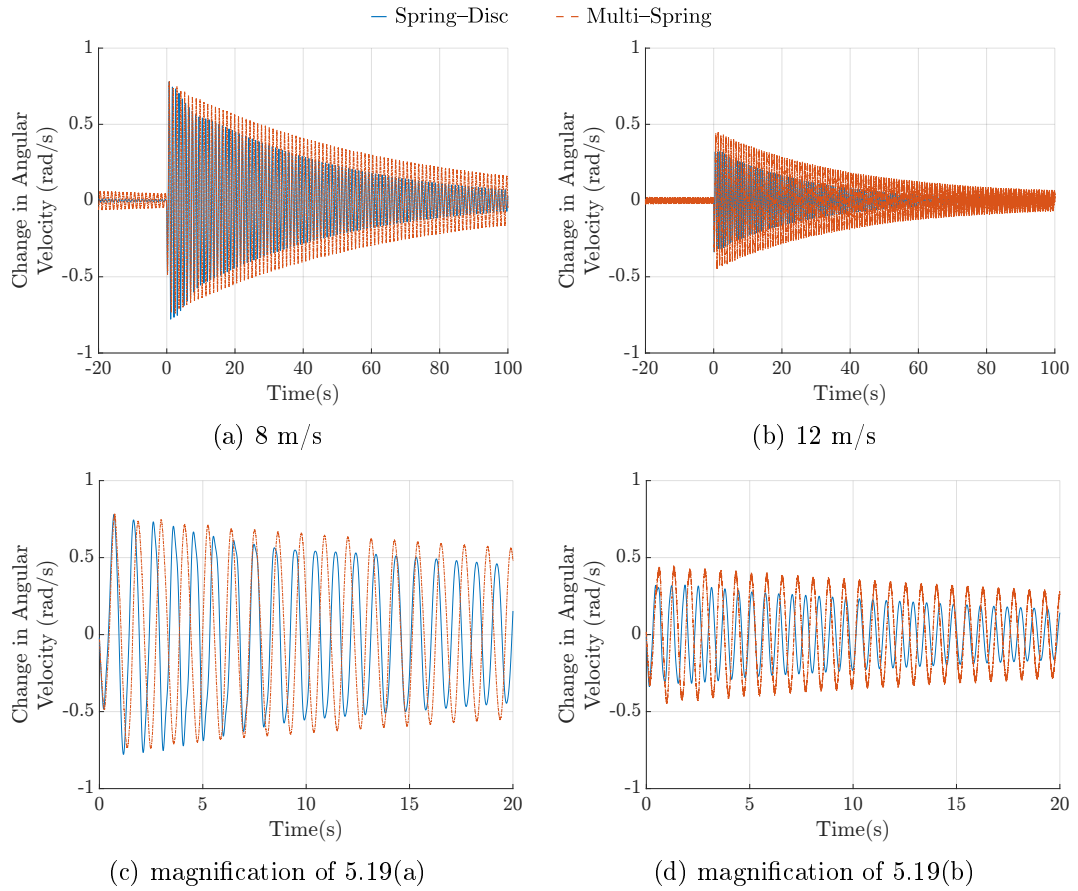
Figure 5.19: Angular velocity of the rotor for the spring–disc and multi–spring representations subject to an increase in axial tension by 100N for a period of 0.5 seconds.

tension at several wind speeds.

It can be seen from Table 5.8 that the error between the two TRPT representations is significantly lower when a change in torque is applied compared to a change in axial tension. A key difference between the two models is on the modelling of the variation in axial tension along their length. To calculate the torsional stiffness of each section within the spring–disc representation the axial force on each section must be known. It is assumed to be constant along the length of the TRPT. When the rotor thrust or force from the lift kite changes, the axial tension along the length of the TRPT will vary, however, this variation is not considered in the spring–disc model. In contrast the multi–spring representation is able to capture the variation in axial tension along

Wind Speed (m/s)	Change in Torque RMSE	Change in Tension RMSE
6	0.056	0.332
8	0.038	0.271
10	0.019	0.186
12	0.019	0.119

Table 5.8: Comparison between the multi–spring and spring–disc models

the length of the TRPT, a change in rotor thrust or lift kite force will therefore propagate along the TRPT in the multi–spring model. This leads to an increased difference between the two models when a change in axial tension is applied in comparison to a change in torque.

It can also be seen from Table 5.8 that as the wind speed increases the error between the two response series reduces. As the wind speed increases the thrust from the rotor and force from the lift kite increases, the axial force on the TRPT is therefore larger. This increases the torsional and axial stiffness of the TRPT. The increase in axial stiffness results in reduced difference between the outputs of the two models. This is due to the assumption, made within the spring–disc representation, of constant axial tension along the length of the TRPT , which is more valid for axially stiffer systems.

5.2.3   Impact of Tensile Rotary Power Transmission Length

In this section, the effect that TRPT length has on the the two models is compared. A longer TRPT will be less axially stiff. The TRPT length is increased from 10.3m to 30m in simulation settings. This is achieved by expanding the constant radius sections towards the ground station end of TRPT–4. 38 sections are added, to the original 8 sections, that each has a radius of 0.32m and a section length of 0.52m. Similar simulations to introduce changes in torque and axial tension, as introduced previously, are conducted with the longer TRPT at wind speeds of 8 m/s and 12 m/s. Figure 5.20

(a) 8 m/s

(b) 12 m/s
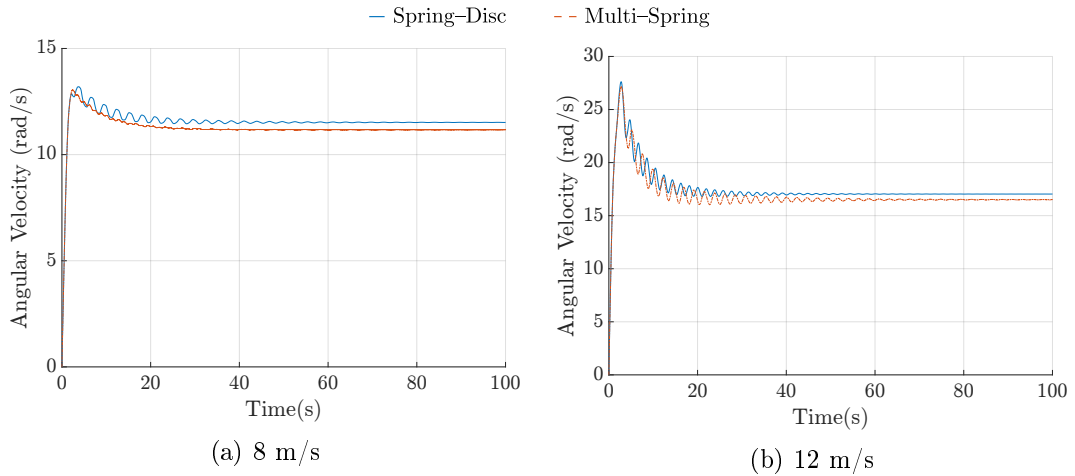
Figure 5.20: Angular velocity of the rotor for the spring–disc and multi–spring representations for a TRPT length of 30m.

shows the response of the two representations.

It can be seen from Figure 5.20 that for a longer TRPT there is a larger difference between the spring–disc and multi–spring models. For the response simulated at 8 m/s the steady state angular velocity is 11.5 rad/s for the spring–disc model and 11.2 rad/s for the multi–spring model. At 12 m/s the steady state angular velocity is 17.0 rad/s for the spring–disc model and 16.5 rad/s for the multi–spring model. For the initial length of 10.3m the difference between the two models is negligible. For the TRPT length of 30m the difference between the two models has become more visible.

Figure 5.21 shows the response of the angular velocity of the two representations for the 30m TRPT subject to changes in torque and axial tension, respectively. Figure 5.21(a) shows the response of the two models to a reduction in generator torque, Figure 5.21(b) shows the response to an increase in axial tension. These two step changes are the same as those introduced in Section 5.2.2. It can be seen from Figure 5.21 that the amplitude values of the responses for both models are similar, more close than for the shorter TRPT. However, there is a phase shift in oscillations between the two models. The phase difference is larger when the step change is introduced to the axial tension as shown in Figure 5.21(b). By comparing the results for the 10.3m TRPT (Figure 5.19)

189

(a) Response to a change in torque

(b) Response to a change in axial tension
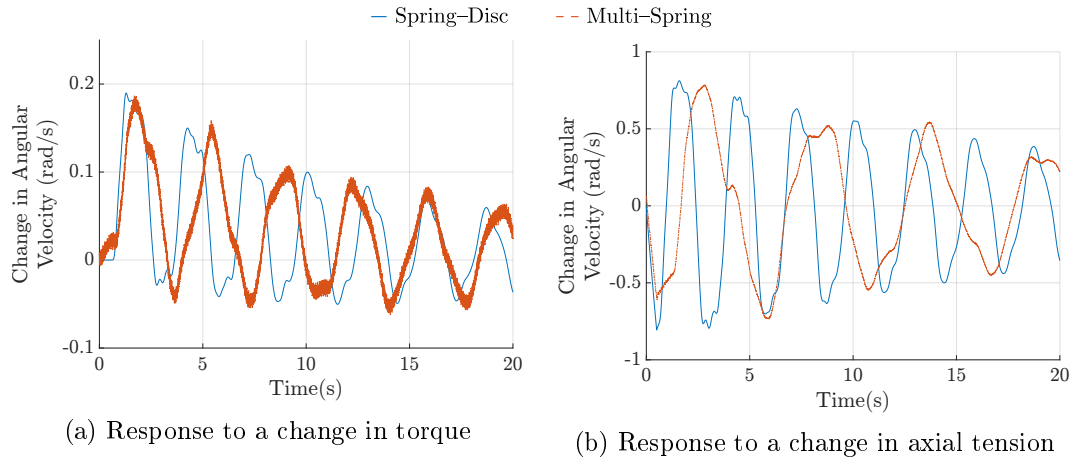
Figure 5.21: Change in angular velocity of the rotor for the spring–disc and multi–spring representations for a TRPT length of 30m to changes in torque and axial tension at a wind speed of 8 m/s.

and the 30m TRPT (Figure 5.20), it can be stated that the longer TRPT oscillates at a lower frequency. The RMSE between the two representations using the 30m TRPT is 0.027 for the change in torque and 0.290 for the change in axial tension at 8 m/s, and 0.020 and 0.234 respectively at 12 m/s. These are similar to the errors for the shorter TRPT shown in Table 5.8.

It can be seen that as the TRPT length increases so does the difference between the two representations, mostly in oscillation phase difference in the transient part and also in the steady state. As highlighted previously the main feature added to the multi–spring representation is that it accounts for the change in axial tension along the length of the TRPT. As the system becomes less axially stiff, the assumption of constant axial tension along the length of the TRPT, in the spring–disc representation, increases the error when compared to the multi–spring representation.

5.2.4   Model Comparison using Experimental Data

In this section, the previous simulation results comparing the spring–disc and multi–spring models to the measured data, given in Sections 5.1.2 and 5.1.3 respectively, are

further analysed to compare the two representations. It is noted that the low pass filter is not applied in these comparisons.

Figure 5.22 shows the results from experimental data Case 1. It can be seen that the results of the two developed mathematical representations are very similar, which can be checked by the magnified plot shown in Figure 5.22(b). Responses from both representations contain high frequency oscillations with similar phase values. The power spectral density of the ground station angular velocities are shown in Figure 5.23, from which it can be seen that the identification of the first natural frequency is consistent between the models.
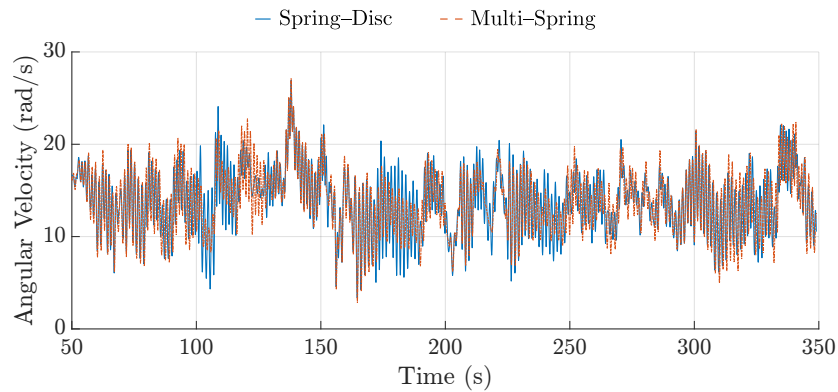
(a) Case 1: rigid wing, TRPT–4
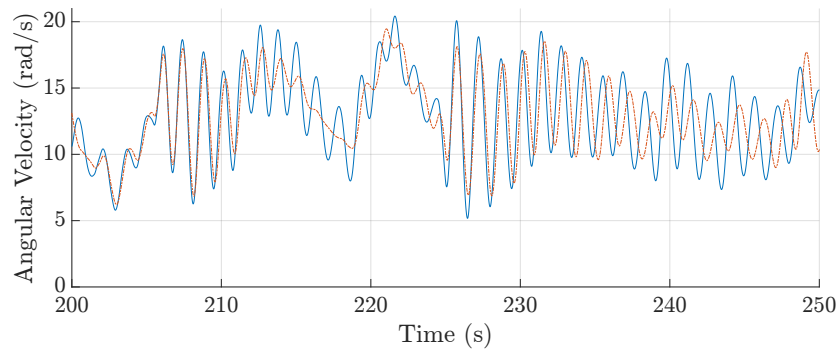
(b) Magnification of 5.22(a) for the selected period of 200 to 250 seconds

Figure 5.22: Angular velocity of the rotor for the spring–disc and multi–spring representations for experimental data case 1.

Table 5.9 shows the RMSE between the spring–
disc and multi-spring representations for the five
experimental cases. Figure 5.24 shows the com-
parison of ground station angular velocity for
cases 2–5.   It can seen from these results
that the two models are in close agreement
where the measured data is used for compari-
son.

Case	ω RMSE
1	2.80
2	0.30
3	0.24
4	0.42
5	0.10

Table 5.9:   RMSE between the
multi–spring and spring–disc mod-
els for the experimental data cases.

It has been shown that for the Daisy Kite proto-
types developed to date the two dynamic mathematical representations provide match-
ing responses as compared to experimental data. However, the complexity and therefore
the computational time required for the two models are largely different. As discussed
in Section 5.1.3 and shown in Table 5.6 the time step required for the multi–spring
model is much smaller than the spring–disc. To run a comparable simulation, the
multi–spring model takes over 50 times longer than the spring–disc model. For this rea-
son, the spring–disc representation is the preferred model when analysing the dynamic
behaviour of the current Daisy Kite prototypes. However, it should be noted that the
error between the spring–disc and multi–spring models increases with the increase of
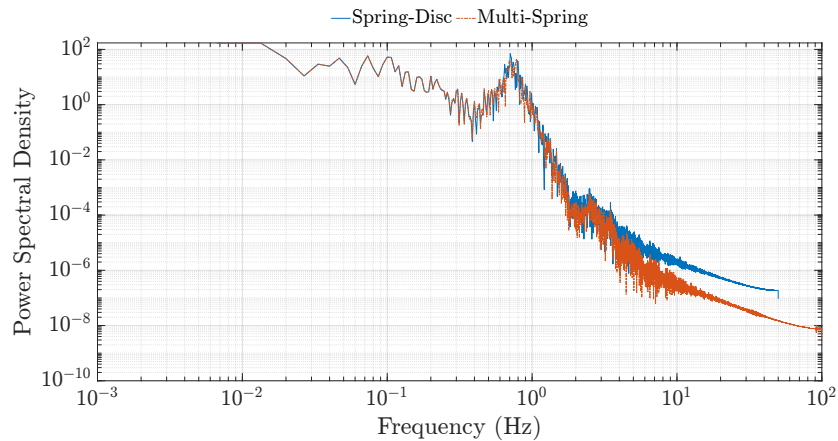
Figure 5.23: Comparison of the power spectral density plots of the spring–disc and
multi–spring models.
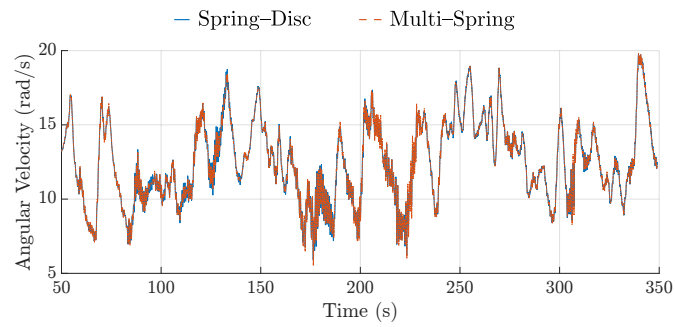
(a) Case 2: rigid wing, TRPT–3
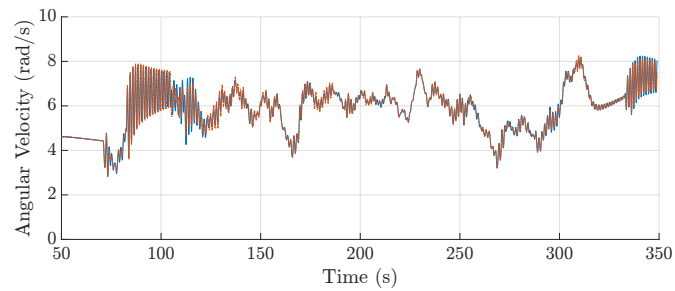
(b) Case 3: rigid wing, TRPT–3
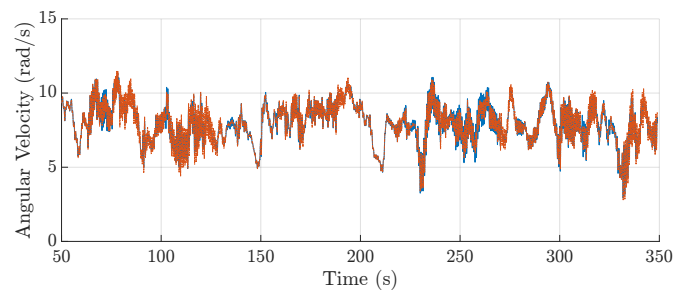
(c) Case 4: soft wing, TRPT–2
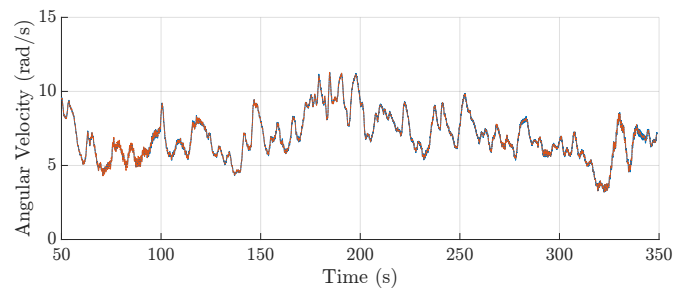
(d) Case 5: soft wing, TRPT–1

Figure 5.24: Comparison between the spring–disc and multi–spring model using the experimental data cases.

TRPT length, due to the reduction in the systems axial stiffness. The multi–spring representation is likely to be more suitable for modelling larger systems. It is also noted that the axial and torsional stiffness of a TRPT system is highly dependant on its geometry. Therefore, the spring–disc representation could be suitable for longer TRPT lengths when the geometry and operating state result in high stiffness of the system.

5.3   Analysis of Rotary Airborne Wind Energy System Design

To further understand the characteristics of rotary AWES a steady state analysis of the Daisy Kite's design has been undertaken and is detailed in this section. The TRPT and rotor designs are investigated in Sections 5.3.1 and 5.3.2 respectively. Their performance is analysed to identify any limitations and crucial design drivers. Given the importance that tether drag has on AWES, as shown in Section 2.1.5, the TRPT's tether drag is investigated in Section 5.3.3.

5.3.1   Tensile Rotary Power Transmission Design

The main role of a TRPT is to transfer the torque generated at the rotor down to the ground station. In Section 4.4, (4.31) is defined, this is used to calculate the static torque that a TRPT can transmit for a given TRPT geometry and operating condition, (4.31) is repeated below in (5.2).

$$Q = R_1 R_2 F_x \frac{\sin \delta}{\sqrt{l_t^2 - R_1^2 - R_2^2 + 2 R_1 R_2 \cos \delta}} \tag{5.2}$$

It can be seen from (5.2) that the amount of torsion that a single TRPT section can transmit is dependant on the TRPT's geometry, the axial force applied to it and the torsional deformation of the section. Figure 5.25 shows how the torque, Q, varies with the torsional deformation, δ, for a set geometry and axial force, for a single TRPT

194
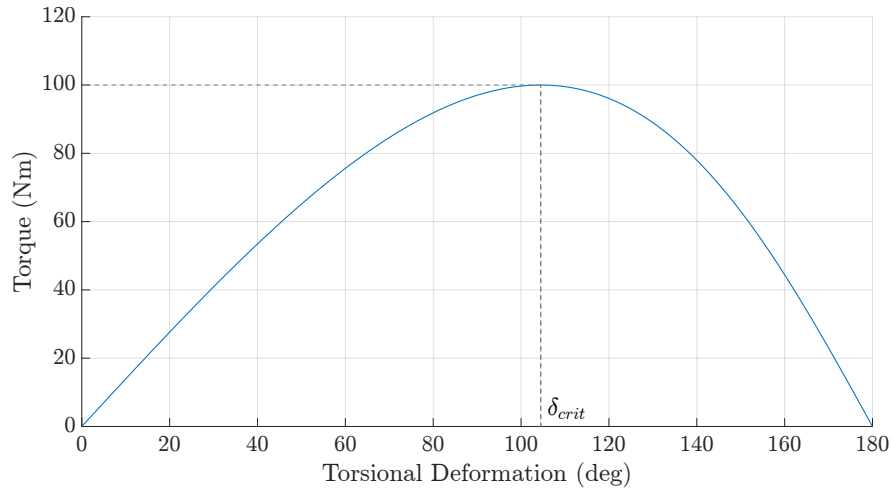
Figure 5.25: Amount of torque transmitted against the torsional deformation for a single section of the Daisy Kite's TRPT. The two rings of the section both have a radius of 0.4m, the tether length is 1m and the axial force is 500N.

section calculated using (5.2). In this case the two rings have the same radius (R_1, R_2) of 0.4m, the tether length (l_t) is 1m and the axial force, F_x, is set to 500N.

It can be seen from Figure 5.25 that the amount of torque that the TRPT section can transfer is highly dependant on its torsional deformation and that there is a non–linear relationship between the two. Initially as the torsional deformation is increased the transmittable torque increases, at a particular torsional deformation, δ_{crit}, a maximum torque value is reached. After this point, the ability for torque transmission reduces as the torsional deformation increases further. In the case shown in Figure 5.25 the maximum transmittable torque is 100Nm and δ_{crit} is equal to 104°. (4.34) shows that this critical value of torsional deformation is dependent on the TRPT geometry.

Figure 5.25 and (5.2) also show that with zero torsional deformation no torque can be transferred. In the case of the Daisy Kite's TRPT, it is not possible to transmit torque if adjacent rings have the same rotational position relative to one another. Some other TRPT designs are able to transfer torque without any torsional deformation occurring. As discussed in Section 3.5, if the torsional deformation between adjacent rings exceeds 180° the TRPT tethers will cross and it is no longer possible to transfer torque. Once

this occurs the TRPT fails as the torsional deformation will rapidly increase and the tethers will become excessively twisted.

One more observation from Figure 5.25 is that there are two possible torsional deformations for each torque value, one larger and one smaller than δ_{crit}. By investigating the torsional stiffness of the TRPT the two torsional deformations for each torque are analysed in more depth. Figure 5.26 shows how the torsional stiffness varies with torsional deformation, calculated using (4.33) in Section 4.4. The geometry and operational state used are the same as those in Figure 5.25.

It can be seen from Figure 5.26 that the torsional stiffness of a TRPT section decreases monotonically as the torsional deformation is increased. When the torsional deformation is equal to δ_{crit} the torsional stiffness of the TRPT section is equal to zero. For larger torsional deformations the torsional stiffness becomes negative. Therefore once the TRPT rotationally deforms beyond δ_{crit} there are no stable equilibrium conditions. With a positive torsional stiffness the TRPT is in equilibrium, where the tether force and torque oppose each other. A negative torsional stiffness shows that the TRPT is not in equilibrium as the tether forces and torque act in the same direction. When the deformation is larger than δ_{crit} the ability of the TRPT section to transmit torque col-
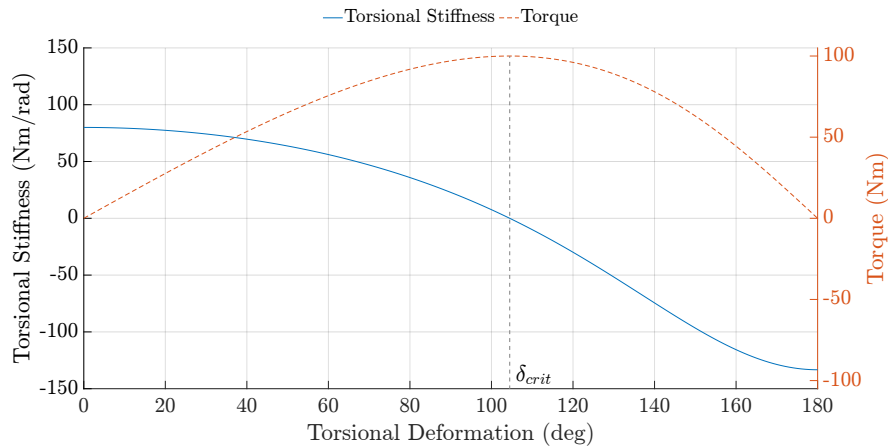
Figure 5.26: Torsional stiffness variation with torsional deformation for a single section of the Daisy Kite's TRPT. The two rings of the section both have a radius of 0.4m, the tether length is set to 1m and the axial force is set at 500N

lapses to zero. The first TRPT failure mode discussed in Section 3.1.3 is that *"Tethers cross due to excessive torsional deformation"*. Figure 5.26 shows that a TRPT section will fail prior to the tethers crossing. Once the torsional deformation is larger than δ_{crit} the rotational deformation will increase rapidly causing the tethers to cross and become excessively twisted. As mentioned in Section 3.1.3, although the tethers crossing is regarded as a failure mode, it is possible to recover the system and resume normal operation, so long as the tether twisting does not lead to the second or third failure mode, where the tether or ring components fail respectively.

During the systems operation, the torsional deformation must be kept below δ_{crit}. This provides a limit on the Daisy Kite's rotational deformation and can be used to ensure reliable operation. By measuring the tether angle or torsional deformation this could be used to ensure that the over twist scenario is avoided. Equally by measuring the axial tension it is possible to calculate a maximum torque that the TRPT is able to transmit, allowing limits to be set to avoid the tethers becoming twisted.

Figures 5.25, 5.26 demonstrate that it is possible to calculate operational limits for a given TRPT geometry. It is worth noting that this analysis can only be used to calculate the maximum torque when the tether length is larger than the TRPT diameter. If the tether length is less than the diameter of the TRPT then it is not possible for the TRPT to over twist to the point at which the tethers cross. In this case the maximum torque is determined by either the strength of the tethers or the strength of the rings. As described in Section 4.4, the limits are calculated based on the following assumptions:

1. The system is massless

2. The system is in static equilibrium

3. The tethers are straight and do not stretch

4. The TRPT rings are rigid

5. The TRPT rings are orthogonal to the axis of rotation and all share a common axis of rotation

TRPT Single Section Geometry Analysis

The static analysis has so far assumed that the geometry of the TRPT is known. It is more useful to design the dimensions of the TRPT to match the expected loads that it will experience. To achieve this the relationship between the geometry and the torque carrying ability of a single TRPT section is analysed. To start with, consider the case that the two rings of the TRPT have the same radius, R. The torque can be calculated by

$$Q = \frac{RF_x}{\sqrt{2}} \frac{\sin\delta}{\sqrt{\frac{l_t^2}{2R^2} + \cos\delta - 1}} \tag{5.3}$$

The critical deformation angle can be determined by $\dfrac{\partial Q}{\partial \delta} = 0$ which gives

$$\cos\delta_{crit} = 1 - \frac{\varphi^2}{2} + \frac{\varphi}{2}\sqrt{\varphi^2 - 4} \tag{5.4}$$

$$\varphi = \frac{l_t}{R} \tag{5.5}$$

Again, δ_{crit} is dependent on the TRPT's geometry only. It can be seen from (5.4) that when the radius of the two rings for a single TRPT section are the same, δ_{crit} is dependent only on φ, the ratio of the tether length to the ring's radius. Figure 5.27 shows the relationship between δ_{crit} and φ calculated using (5.4).

Below a φ value of 2 it is not geometrically possible for the torsional deformation to reach 180°. The tethers are therefore not able to cross. In this situation the material strength of the tethers and rings will dictate the failure point. In the case where φ is less than 2, it is possible for the axial distance between two rings to reduce to zero, although in practise the rings or tethers will fail prior to this occurring. It can be seen in Figure 5.27 that the minimum value of δ_{crit} is 90°. It can be stated that if φ is less than 2 or the torsional deformation is lower than 90° the operation is stable, unless the torque and axial forces are larger than the strength of the tethers or rings can withstand.
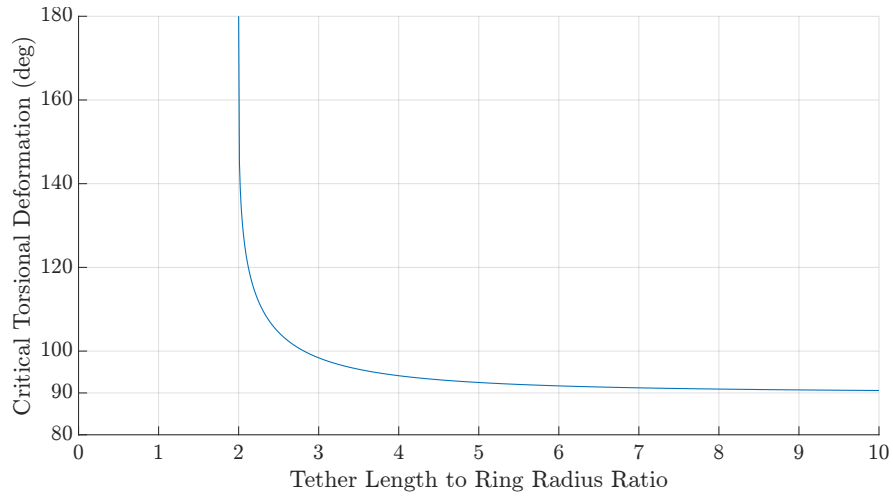
Figure 5.27: Critical torsional deformation for different tether length to ring radius ratios.

The amount of torque that a TRPT can transmit is directly proportional to the axial force applied to it. Given this linear relationship between the axial force and the amount of torque that can be transferred, the ratio between the two is a useful metric when analysing the TRPT design. The force ratio refers to the ratio between the tangential force due to torque acting at the ring, $\frac{Q}{R}$, and the axial force applied to the TRPT section, F_x. Figure 5.28 shows how this ratio changes with respect to the torsional deformation, for a single TRPT section. For the case shown in Figure 5.28 the radii of the two rings are 0.4m and the tether length 1m. The force ratio is at a maximum when the torsional deformation is equal to δ_{crit}. The maximum value of the force ratio remains constant independent of the magnitudes of the torque and axial force. For a given TRPT geometry, limits can be calculated for the maximum force ratio that will avoid TRPT failure. In the case shown in Figure 5.28 this value is 0.5.
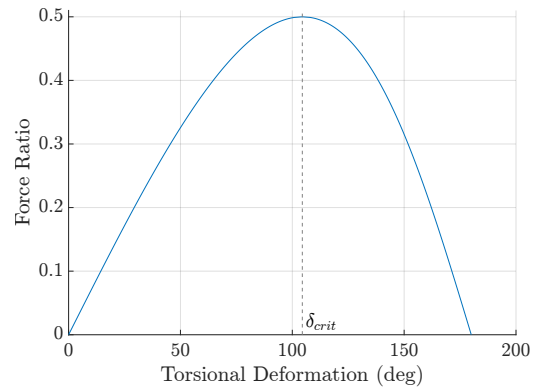
Figure 5.28: Force ratio against torsional deformation
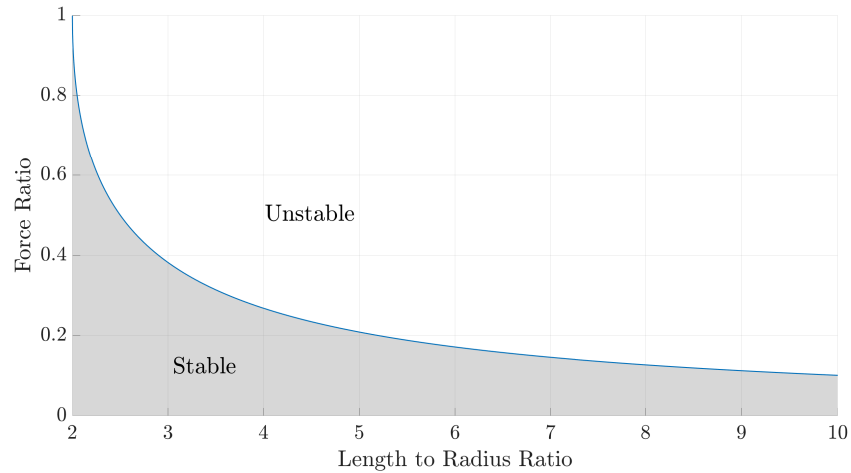
Figure 5.29: Force ratio against the length to radius ratio.

The crucial relationships for a TRPT section, with constant ring radius, are the force ratio and φ. The value of δ_{crit} is dependant on φ and it determines the maximum force ratio that can be achieved. Knowing this maximum force ratio allows the maximum transferable torque for a given axial tension to be calculated. Figure 5.29 shows the relationship between φ and the force ratio.

The graph shown in Figure 5.29 acts as a useful tool when designing the Daisy Kite's TRPT. The shaded region on the graph indicates the TRPT geometries and operating conditions that are stable. The line along the top of the shaded region represents δ_{crit} and therefore above this line the ability of the TRPT to transmit torque has collapsed to zero. If the amount of torque to be transmitted is known, along with the corresponding axial tension, all stable TRPT geometries can be identified. There are multiple TRPT geometries for each force ratio that will result in stable operation. In general, the shorter the TRPT section and the larger the radius i.e. smaller length to radius ratio, the larger the amount of torque that can be transmitted.

Variable Ring Radius

So far only TRPTs with a constant radius have been analysed. Figure 5.30 shows how a variable radius TRPT affects the ability of a single section to transfer torque. The dashed line in Figure 5.30 represents the maximum force ratio a set of rings with different radius can achieve, if the tether length allows for a torsional deformation of 180°. The force ratio against the length to radius ratio is depicted by solid lines for several different rings radius ratio, as labelled. Both the length to radius ratio and the force ratio are defined relative to the smaller one of the two rings. The line that corresponds to a radius ratio of 1 is identical to Figure 5.29.

It can be seen from Figure 5.30 that as the ratio between the two rings increases so does the force ratio and therefore the amount of torque that the TRPT section is able to transmit. It can be stated that the amount of torque a constant radius section can transmit scales up linearly with its geometry. For example, if the ring radius and tether length are scaled up by a factor of 2, the force ratio will decrease by a factor of 2 for a given torque and axial tension. The maximum force ratio remains unchanged. The maximum amount of torque that can be transmitted, for the same axial tension will therefore double. It can be seen from Figure 5.30 that if a single ring is scaled up by a factor of 2, i.e. the radius ratio increases by a factor of 2, the maximum torque that
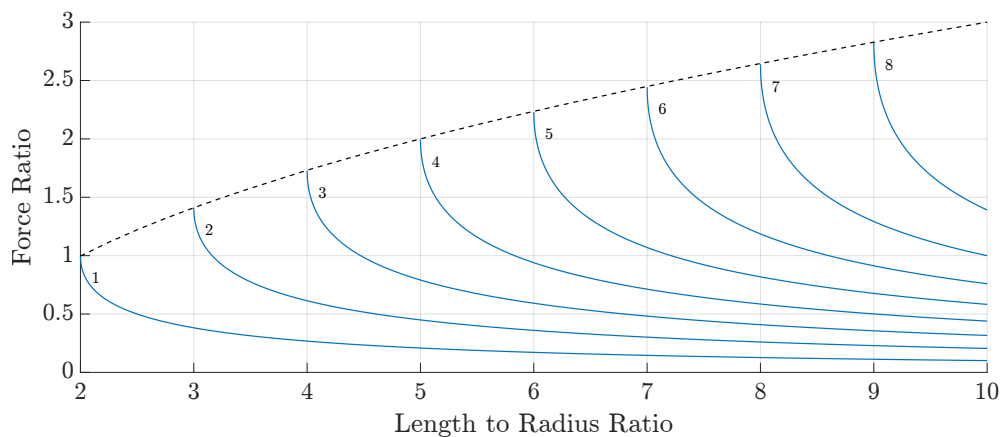
Figure 5.30: Force ratio against the length to radius ratio for rings with different radius. Each solid line corresponds to a different radius ratio between the two rings.

the section can transmit, for the same axial tension, increases by around 40%.

Figure 5.30 also shows that as the ring radius ratio increases the tether length to ring radius ratio, at which the maximum force ratio occurs, also increases. As the relative radius of the rings becomes larger the tether length required to allow a torsional defor-mation of 180° also increases. Similar to the constant ratio case, the maximum force ratio can only be identified for TRPT geometries that allow a torsional deformation of 180 °. In cases where this cannot occur the maximum force ratio is determined by the strength of the tethers or rings.

This section has identified various relationships important to the design of a TRPT. To design a TRPT based on this analysis it is necessary to know the magnitude of the forces applied to it in different conditions. The output from a rotary AWES rotor and lift kite, if the system includes one, will dictate the magnitude of these forces. The following section investigates the Daisy Kite's rotor design.

5.3.2   Rotor Design

The rotor of a rotary AWES is responsible for extracting the power from the wind, and it is a crucial component in any rotary system. The design of the Daisy Kite's rotor is analysed in this section.

System Elevation Angle

AWES rotors share many similarities with HAWT's. A key difference between HAWTs and rotary AWES is the misalignment of the rotors axis of rotation and the incoming wind. The need to fly the rotor on the top end of a tether, avoiding ground strikes and reaching higher altitudes, means that the flying rotor must be tilted into the wind. As discussed in Section 4.2.1 the tilting of the entire rotor into the wind will impact the rotor's performance, most crucially the amount of power that can be extracted from the
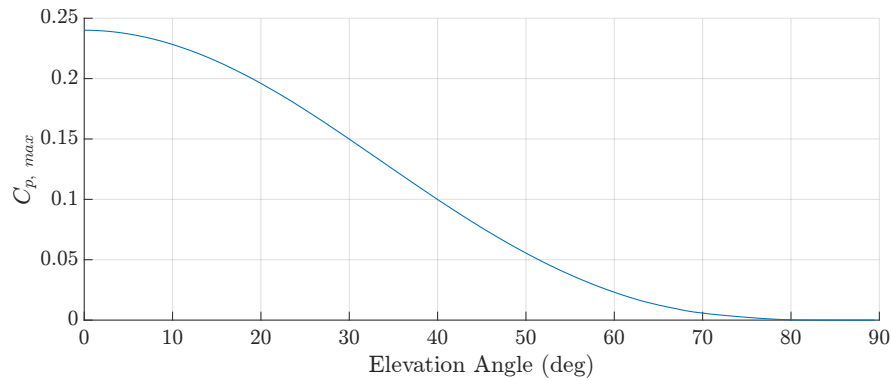
Figure 5.31: Variation of C_{pmax} with system elevation angle

wind. Figure 5.31 shows how the Daisy Kite's three bladed rigid rotors maximum power coefficient $C_{p,max}$ is affected by the rotors elevation angle. It suggests the advantage of reducing the elevation angle for the purpose of power production. For example, at an elevation angle of 20° $C_{p,max}$ is just below 0.2, increasing the elevation angle to 40° almost halves the $C_{p,max}$ value to 0.1.

Although Figure 5.31 shows the advantage of reducing the systems elevation angle it does not take into account the TRPT length or operating altitude. As the elevation angle increases the TRPT length required to reach a given altitude reduces. A shorter TRPT length will have less tether drag and therefore a higher efficiency. Section 5.4.1 furthers this analysis by looking at both the elevation angle and TRPT length to maximise the power output.

Blade Pitch Angle

As discussed in Section 4.2.1 the misalignment of the rotors axis of rotation and the incoming wind results in the rotor seeing an asymmetric flow field. The magnitude and direction of the apparent wind speed that a blade section sees will therefore vary as its rotational position within the rotor changes. Figure 5.32 shows the profile of the apparent wind velocity and the angle of attack for the mid point on one of the Daisy Kite's rigid blades as it rotates. The rigid blades inner and outer tip radius are at 1.22m and

(a) Apparent wind speed
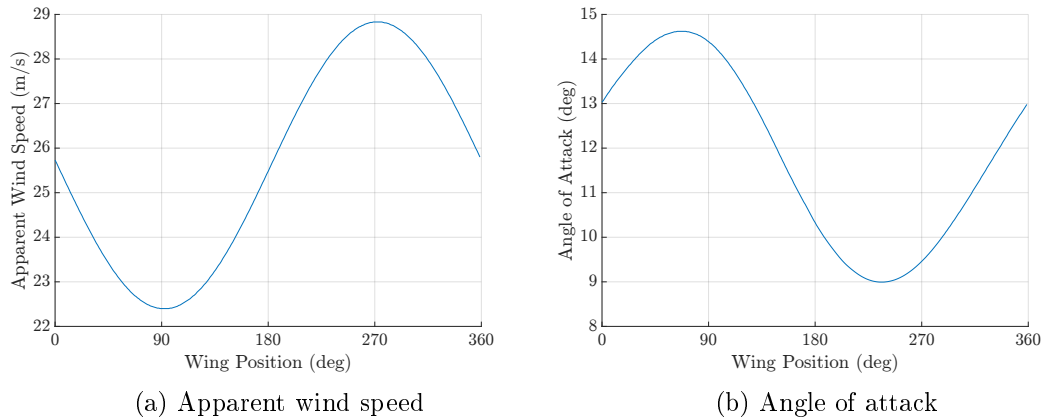
(b) Angle of attack

Figure 5.32: Variation of apparent wind speed and angle of attack with wing rotational position

2.22m respectively. The blades mid point therefore corresponds to a radius of 1.72m. The elevation angle is set to 25°, a uniform wind speed of 8 m/s is applied, TRPT–4 is used and the rotor speed corresponds to a tip speed ratio of 4. A blade position of 0° corresponds to the blade pointing directly upwards in the rotor plane.

It can be seen that at the blades mid point the apparent wind speed varies from 22.4 m/s to 28.8 m/s and the angle of attack from 9° to 14.6 °. This leads to variations in the aerodynamic forces produced by the blade section as it rotates. The combined effect causes the fluctuations in the torque and thrust generated by the rotor as it rotates, increasing the fatigue loading on components. This will require more attention as rotary AWES progress beyond prototype systems and towards commercial products.

As introduced in Section 3.1.1 the wings are attached onto the carbon fibre ring of the rotor using a 3D printed cuff. The pitch angle of the blades are dictated by this 3D printed cuff. During the experimental campaign two different rotor cuffs were used. The first with a pitch angle of 0° and the second with 4° pitch. At present the blades do not incorporate any twist. As shown in Figure 5.32(b) the angle of attack on each blade section varies as the system rotates, as with HAWT the angle of attack varies along the wing's span. The angle of attack and the apparent wind speed will vary both radially and as the system rotates. With the current design each blade section will only
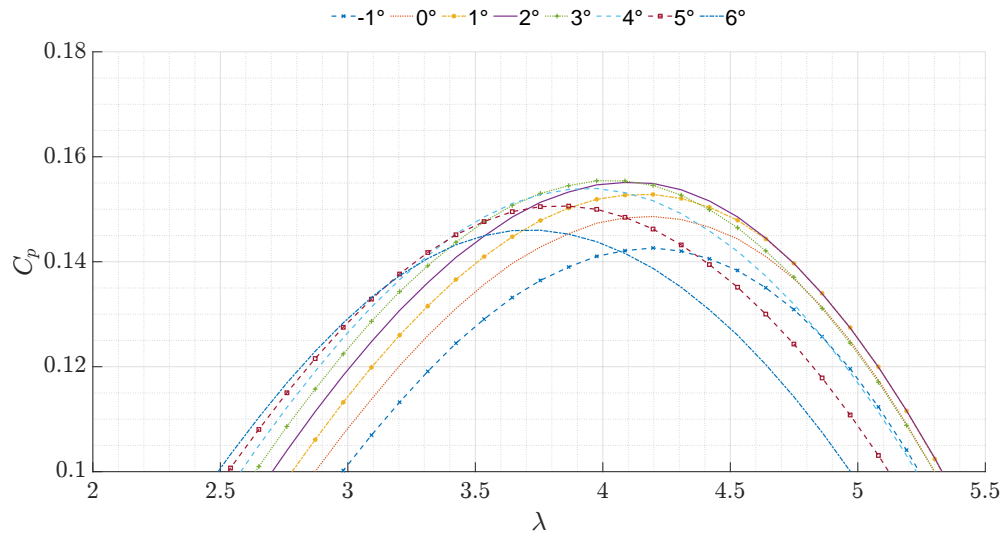
Figure 5.33: Effect of wing pitch angle on C_p vs λ curve

be operating in optimal conditions for a short period of time. Despite this there will be a pitch angle that is optimal for the current rotor design. To investigate what pitch angle is most advantageous in terms of power output, several simulations were run with different pitch angles. Figure 5.33 shows these results.

It can be seen from Figure 5.33 that a pitch angle of 3° produces the maximum power coefficient value. It is noted that positive pitch angles correspond with pitching to feather. A pitch angle of 3° gives an increase in $C_{p,max}$ of around 5% compared to the 0° case. It can also be seen from Figure 5.33 that by increasing the pitch angle, the tip speed ratio that corresponds to $C_{p,max}$ is reduced. As discussed in Section 5.3.3 a lower tip speed ratio will reduce the tether drag experienced within the TRPT, thus further improving the system's efficiency.

Rotor Solidity

Within the experimental campaign two different rigid rotors were manufactured and tested. The first used three rigid blades, the second six rigid blades. In both cases the same blade design was used. To assess the impact of the rotor solidity on the systems
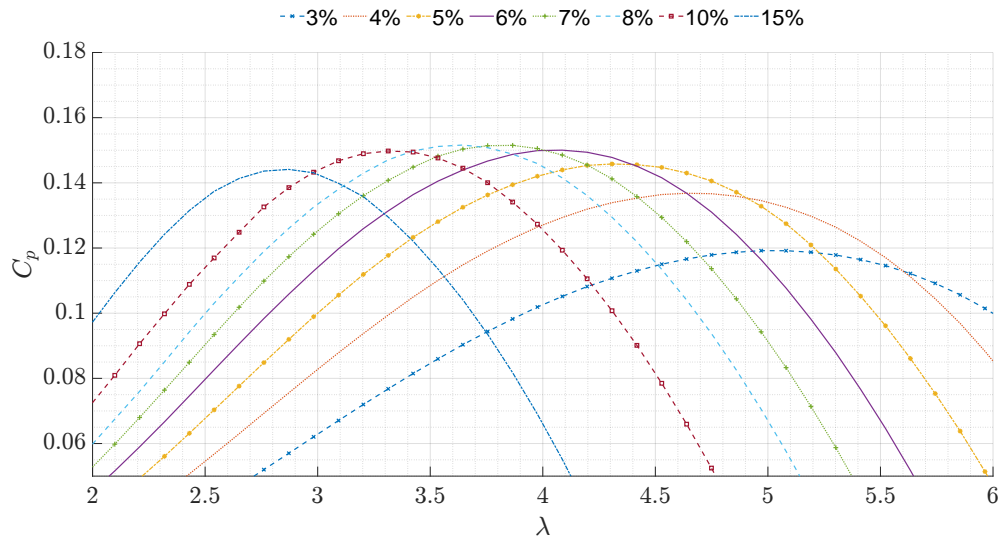
Figure 5.34: Effect of rotor solidity on the C_p vs λ curve

performance several simulations were run. The solidity is calculated by the ratio of the blade area to the rotors swept area. The rigid three bladed prototype has a rotor solidity of 5.6%, the rigid six bladed rotor has a solidity exactly double this. As discussed in Section 5.1.1, it is not possible to model more than three blades within the current rotor aerodynamics module used in the models. The chord length of the blades, for a three bladed rotor, is varied to simulate changes in rotor solidity. The rotor solidity was varied from 3% up to 15%, Figure 5.34 shows how the solidity affects the power capture performance. Again the elevation angle is set to 25° and TRPT–4 is used.

It can be seen from Figure 5.34 that a rotor solidity of 7–8% produces a higher $C_{p,max}$ value. The current rigid Daisy Kite rotor has a swept area of 10.81 m^2 and each blade has an area of 0.2 m^2. A solidity of 7–8% therefore corresponds to a four bladed rotor using the current blade design. Figure 5.34 also shows that by increasing the rotors solidity the tip speed ratio that corresponds to the $C_{p,max}$ is reduced. This is similar to the effect seen when increasing the blades pitch angle and again improves the efficiency within the TRPT.

Blade length

The outer blade portions of a rotor produce the most power. A blade section of a set span will sweep out a larger area the farther it is from the rotor centre. For a unit span the outer potions of the blade therefore sweep a larger area given them access to more wind power. A motivation behind AWE is to save material and cost by only building the outer portion of the blades and replacing the inner portion with a tether. This is the reason why the Daisy Kite's rotor uses blades that have a span that is less than the rotors radius, leaving the rotors centre open. However, the tip/end of any blade is also one of the least efficient blade sections. As the blade tip is approached the aerodynamic performance reduces, this is usually referred to as tip losses. By leaving the rotor centre open the blades have two tips and a short blade may be significantly impacted by the tip losses. To assess this effect different blade lengths have been modelled, the outer tip radius remains constant. Figure 5.35 shows how the $C_{p,max}$ and rotor power output are effected by different blade lengths based on the current Daisy Kite rigid rotor and blade design. The x-axis in Figure 5.35 shows the point on the rotor radius, r, that the blade starts, for example, a r/R value of 0.5 corresponds to the blades inner tip being half way between the rotor centre and outer tip radius R. The power output is shown as a percentage of the power produced by a rotor with a blade length equal to the rotor radius, $r/R = 0$. The elevation angle is 25° and TRPT–4 is used.

(a) $C_{p,max}$ (b) Power Output
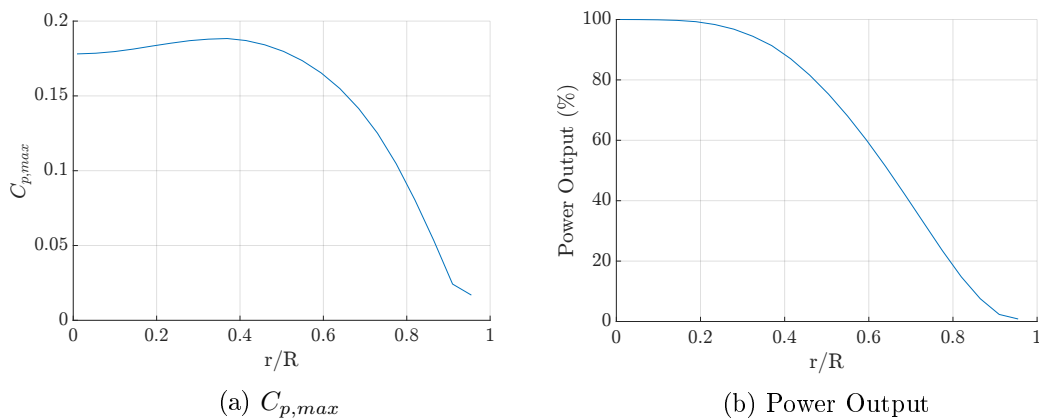
Figure 5.35: Effect of blade length on rotor power output and $C_{p,max}$

The value of $C_{p,max}$ obtained for each blade length, shown in Figure 5.35(a), shows the impact of making the blades too short. Beyond a relative inner radius value of about 0.5, $C_{p,max}$ reduces. It can also be seen that the largest value of $C_{p,max}$ is obtained when the blades start at a radius that corresponds to an inner radius of 0.37 of the outer radius. It is therefore suggested that the blade length is no less than half the rotor radius and that to maximise the blades performance the inner blade tip is located at 37% of the outer radius such that the blade length is equal to 63% of the rotor radius.

On the prototypes trailed during the experimental campaign the rigid blades start at a r/R value of 0.55 and the soft blades at a value of 0.48. For the rigid rotor a r/R value of 0.37 corresponds to a blade length of 1.4m.

Rotor Optimisation

This section has so far identified design changes that should be implemented to optimise the Daisy Kite's rigid rotor based on the current rotor radius and blade design. For the optimised rotor the blade pitch angle is 3° the solidity is 7.5% and the blade length is 1.4m. Figure 5.36 shows the comparison between the Daisy Kite rigid rotor used with prototype configuration 8 compared to the optimised design. The elevation angle is set to 25° and TRPT–4 is used. The optimised design increases the maximum power coefficient of the system from around 0.15 up to around 0.18, an increase of 20%. Figure 5.36(b) shows the system's power curve based on this value of $C_{p,max}$ and a rated wind speed of 12 m/s. The rated power of the system can be either increased, as shown in Figure 5.36(b), or obtained at a lower wind speed.

This optimised rotor design is based on the current blade profiles. It is envisaged that the current blade profiles could be improved to further increase the power capture of the Daisy Kite's rotor. The NACA 4412 blade profiles, used for the current rigid blades, were selected based on their use on small HAWTs. However, given the required rotor tilt and open centre, the conditions that the blades experience are different from that

(a) C_p vs λ (b) Power Output
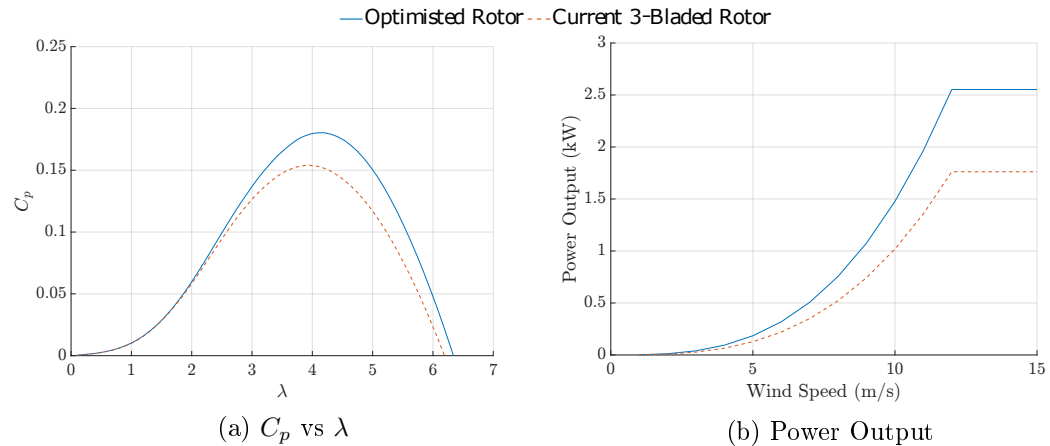
Figure 5.36: Optimised rotor design compared to the rotor used in prototype configuration 8

of a HAWT. It is likely that the blade geometry and rotor design could be improved to match the operating conditions better. More research is required into the aerodynamics of the rotor to further refine the rotor and blades design.

The rotor and TRPT have both been analysed using the steady state models. The final aspect of rotary AWES to be investigated using the developed steady state representation is the tether drag. It is known that tether drag causes significant losses within AWES, it is therefore crucial to analyse the impact that it will have on any proposed AWES.

5.3.3   Assessment of Tether Drag

The tether drag experienced by AWES can have a large impact on their performance. It is therefore crucial that the tether drag is investigated for the Daisy Kite and other rotary AWES. The tether drag in TRPT is assessed using the tether drag representations described in Section 4.5.

Simple Tether Drag

The simple tether drag model, introduced in Section 4.5.1, is used for an initial analysis. In this representation the key assumptions are as follows:

1. The TRPT has a constant radius

2. There is no torsional deformation within the TRPT

3. All tethers are straight, do not stretch and are of equal length and diameter

4. Any forces applied to the system are shared equally between all tethers

5. The wind is uniform in space and time

With these assumptions the torque loss per unit length of a TRPT due to tether drag can be calculated by (5.6).

$$Q_{loss} = R\rho V_w^2 \sqrt{\frac{N_t F_{x_{max}}}{\sigma_{max}\pi}} C_{D_t} \left(\lambda_t^2 + \frac{\sin^2 \beta}{2} \right) \tag{5.6}$$

From (5.6) it can be stated that under steady state conditions the torque loss due to tether drag is dependant on the following design variables:

1. The systems elevation angle, β

2. The maximum stress of the tether material, σ_{max}

3. The maximum total axial force $F_{x_{max}}$

4. The number of tethers, N_t

5. The tether speed ratio, λ_t

6. The TRPT radius, R

The torque loss is also directly proportional to the tether drag coefficient, C_{D_t}, which could also be considered a design variable as the tether shape could be varied to alter its drag coefficient.

As shown in Figure 5.31, the lower the elevation angle the more power the rotor is able to harvest from the wind. It can be seen from (5.6) that the torque loss within the TRPT is proportional to $\sin^2 \beta$. Lower elevation angles therefore increase the rotors power capture and reduce the torque loss per unit length of TRPT. However, a lower elevation angle results in a longer length of TRPT to reach the same altitude for rotor operation.

The torque loss is also proportional to $\dfrac{1}{\sqrt{\sigma_{max}}}$, therefore a tether material with a higher yield stress will result in a more efficient TRPT, as the tether cross section can be reduced. It is also proportional to $\sqrt{F_{x_{max}}}$, showing that as the maximum axial force increases the torque loss per unit length of TRPT also increases. When designing the TRPT it is likely that safety factors would be applied to σ_{max} and $F_{x_{max}}$. Both of these terms along with the number of tethers determine the required tether diameter as shown by (4.36).

It can also be seen from (5.6) that the torque loss increases with $\sqrt{N_t}$. Initially it may be expected that the torque loss is directly proportional to the number of tethers. However, as the number of tethers is increased the load on each tether is reduced, allowing for smaller diameter tethers to be used. The torque loss still increases with the increase in tether number making it advantageous to use fewer tethers in the design.

Lastly it can be seen that the torque loss is proportional to λ_t^2. This highlights the influence that the TRPT radius has on the torque loss. From (5.7) and (5.6) it can be seen that the overall torque loss is proportional to R^3. This shows the importance of reducing the TRPT's radius in relation to torque losses. It can be stated that the radius affects the torque loss more than any of the other factors in (5.6).

$$\lambda_t = \frac{\omega R}{V_w} \tag{5.7}$$

From a full system point of view it is useful to note that by assuming the angular velocity, ω, and the wind speed, V_w, being constant, the tether tip speed ratio can be

defined in terms of the rotor's tip speed ratio and the ratio between the TRPT and rotor radii, τ.

$$\lambda_t = \lambda \ \tau \tag{5.8}$$

where

$$\tau = \frac{R_{trpt}}{R_{rotor}} \tag{5.9}$$

Thus, the torque loss is proportional to λ^2. In terms of reducing tether drag it is therefore advantageous to design a rotor that has a lower optimal tip speed ratio.

Equation (5.6) allows the identification of the factors that affect the torque loss, it also allows for an initial estimation of the TRPT's overall torque loss. The efficiency of the power transmission between the flying rotor and the ground station can then be calculated. For example, at an elevation angle of 25° with a uniform wind speed of 8 m/s, the three bladed rigid winged rotor used in the Daisy Kite prototype produces a torque of 45.1Nm, when operating at a tip speed ratio of 4.0. Using TRPT–4, which has a length of 10.3m, the torque loss due to tether drag using (5.6) is 7.4Nm. The tether drag for each section is calculated using the tether radius at the mid point of the section. $F_{x_{max}}$ and σ_{max} are taken to be 37 kN and 3.5 GPa respectively. The yield stress is chosen to represent Dyneema SK76 [137] and the maximum axial force is chosen to correspond to a tether diameter of 1.5mm. This initial estimate shows that 17% of the energy captured by the rotor is lost in the TRPT. Therefore, given the operating conditions stated above the power transmission of TRPT–4 is estimated to have an efficiency of 83%, when operating at its optimal tip speed ratio.

Improved Tether Drag

To enhance upon the simple tether drag model the improved tether drag model was developed, described in Section 4.5.2. The improved model is able to account for variations in TRPT radius and torsional deformation. It therefore removes the first two assumptions for the simple tether drag model listed previously. Figure 5.37 shows how

the steady state torque loss, relative to the torque loss with no torsional deformation, varies for two TRPT sections with different geometries. The solid line corresponds to a radius of 0.4m and a tether length of 1m, the dashed line corresponds to a radius of 0.32m and a tether length of 0.52m. The geometry of the TRPT in the dashed line case matches the geometry towards the ground station end of TRPT–4. The elevation angle is 25°.

It can be seen from Figure 5.37 that as the torsional deformation increases, initially the torque loss also increases before reaching a peak. There are two key elements that cause this. Firstly, as the TRPT section deforms torsionally, the tethers will cross inside the outer radius of the TRPT. This reduces the radius of the tether sections. The smaller radius results in the tether section seeing a reduced apparent wind speed, the tether drag force acting at a smaller radius also reduces the torque force generated. Secondly, as the torsional deformation increases, the angle of attack between the tether and the apparent wind increases leading to increased aerodynamic force due to tether drag. This increases the tether drag force component, $F_{D,\tau}$, that acts perpendicular to the tether – see Figure 4.9 in Section 4.5.2. Figure 5.37 shows a typical response, where the torque loss increases initially with the increase in torsional deformation before reach-
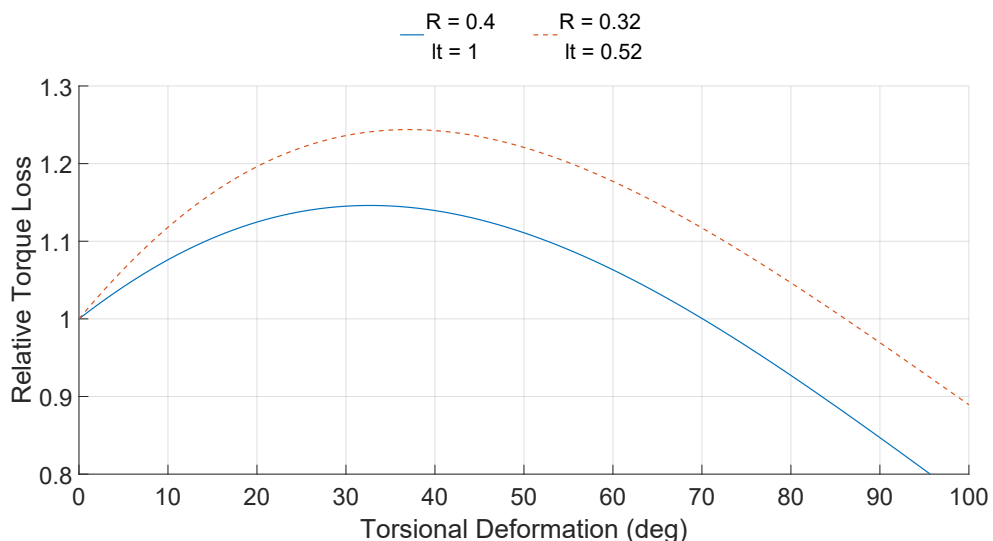
Figure 5.37: Effect of TRPT torsional deformation on the torque loss due to tether drag

ing a maximum value, after which it decreases with the increase of deformation angle. The elevation angle and TRPT geometry determine at what torsional deformation the maximum torque loss is reached.

With the improved tether drag model the estimate of torque loss and the efficiency of a TRPT can be refined. Using the same input conditions for the torque loss with the simple tether drag model, the torque loss is calculated with the improved model. To assess the impact of the torsional deformation, the torque loss is also calculated neglecting any torsional deformation, δ, within the improved model. The results comparing the models are shown in Table 5.10.

It can be seen from Table 5.10 that the initial figures show the simple tether drag model has over estimated the torque loss compared to the improved model. It can also be seen that by neglecting any torsional deformation within the improved model the torque loss is under estimated, in the case analysed the steady state torsional deformations of the sections within TRPT–4 vary from 33° to 46°. The sections that have the same geometry as the dashed line in Figure 5.37 have a torsional deformation of 46°. It can be seen from Figure 5.37 these sections are close to their maximum torque loss. With a torsional deformation of 46° the torque loss is greater than when the torsional deformation is zero. The error caused by neglecting the torsional deformation will vary depending on the system's operating state and the TRPT geometry.

Calculating the tether drag neglecting any torsional deformation is less computation-

Model	Torque Loss (Nm)	TRPT–4 Efficiency (%)
Simple	7.6	83.2
Improved (δ neglected)	4.9	89.2
Improved	5.1	88.6

Table 5.10: Comparison of the tether drag models

ally expensive. When including the torsional deformation the angular position of each TRPT ring must be found, this requires running a dynamic TRPT model for a specific input until the steady state is reached, as the torsional deformation is not a priori known. The case listed in Table 5.10 shows that the error caused by neglecting the torsional deformation is small. Figure 5.37 shows that in the example case the error is likely to be higher than other cases as the majority of the TRPT sections are operating at torsional deformations that significantly increase the torque loss. It is therefore concluded that for the initial steady state analysis under a range of operating conditions, the torsional deformation within the TRPT can be neglected to keep the model simple.

The simple tether drag model has allowed the identification of the key factors that affect the aerodynamic losses within the TRPT. However, it has been shown to over estimate the drag within the TRPT. The improved tether drag model has therefore been used within the spring–disc and multi–spring representations. It is noted that when used within the multi–spring representation the assumption that the tethers do not stretch is removed, the axial degrees of freedom within the multi–spring model allow for any axial force that arises due to tether drag to be considered.

The Impact of tether drag on Daisy Kite Operation

Up to now the tether drag has only been analysed when the rotor is operating at its optimal tip speed ratio. To understand how the tether drag will impact all steady operating conditions, the full range of possible tip speed ratios are analysed. Figure 5.38 shows the three bladed rigid rotor C_p vs λ curve when the rotor is combined with TRPT–4, as in the Daisy Kite prototype configuration 8. In these simulations the elevation angle is set to $25°$ and the torque loss is calculated using the improved tether drag model neglecting any torsional deformation.

Figure 5.38 shows that the tether drag within the TRPT affects the rotors optimal operating conditions when it is incorporated into the full system. The rotor in isolation
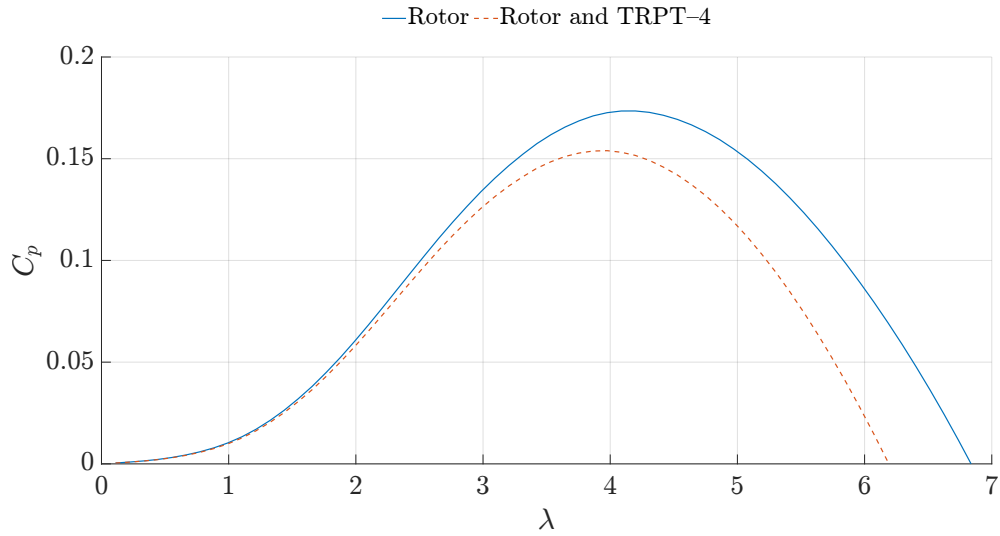
Figure 5.38: Effect of tether drag on the performance of rotary AWES

has a $C_{p_{max}}$ value of just over 0.17 which occurs when λ is 4.2. The rotor and TRPT combined have a $C_{p_{max}}$ of just over 0.15 which occurs at a lower tip speed ratio of 4.0. This represents a decrease of 11.5% in $C_{p_{max}}$ due to tether drag within the TRPT. It can also be seen from Figure 5.38 that the tether drag has more impact at higher tip speed ratios, confirming the observations made using (5.6) regarding the relationship between the system's tip speed ratio and the torque loss due to tether drag. Tether drag reduces the optimal tip speed ratio of the system compared to the rotor in isolation.

To further analyse the impact of tether drag, the torque loss and corresponding efficiency of the TRPT during the 5 cases taken from the experimental data are calculated. Table 5.11 shows the mean torque loss within the TRPT, the mean tip speed ratio and the TRPT efficiency for each of the experimental cases used previously. The results shown are based on the spring–disc representation. The TRPT efficiency is calculated based on the mean rotor torque and the mean torque loss.

It can be seen from Table 5.11 that the averaged efficiency of the TRPT over a set of operations is lower than those for an individual operating state shown in Table 5.10. Of the five cases the three that used a rigid rotor, cases 1, 2, and 3, all operated at

Case	Mean Torque Loss (Nm)	λ	TRPT Efficiency (%)
1	5.6	5.6	31.9
2	4.6	4.8	54.4
3	1.0	4.8	58.0
4	2.1	2.9	61.2
5	1.6	2.9	52.0

Table 5.11: Torque loss in the 5 experimental cases

tip speed ratios above the rotors optimal value of around 4. It is known that operating at higher tip speed ratios decreases the power output from the rotor and increases the losses within the TRPT. This is best seen comparing case 1 to cases 2 and 3. The mean tip speed ratio over the 5–minutes window in case 1 is 5.6, in cases 2 and 3 it is 4.8. The calculated efficiency for the higher tip speed ratio is almost half that of the lower tip speed ratios. This again highlights the impact that the tip speed ratio has on the tether drag.

Given the high torque losses within the TRPT, the drag on each section within the TRPT is analysed. Figure 5.39 shows the torque loss, relative to the overall torque loss, imposed on each ring within TRPT–4 for the results given in Table 5.10 using the improved model including torsional deformation. Section 1 corresponds to the rotor
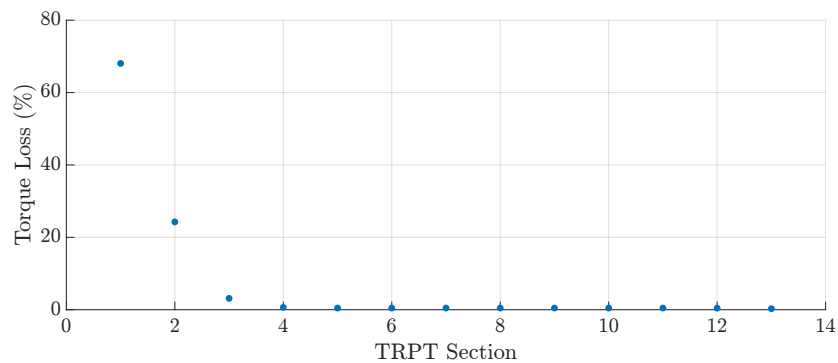
Figure 5.39: Relative torque loss for each section of TRPT–4 under optimal operating conditions.

and 13 the ground station. It can be seen from Figure 5.39 that the first section of the TRPT causes the majority of the overall torque loss. The first two rings, at two ends of the first TRPT section, see 92% of the overall losses. Figure 3.12(c) gives a schematic of the TRPT–4 geometry. The first TRPT section has a much larger radius compared to those closer to the ground station. This again shows the impact that the TRPT radius has on the efficiency and confirms the need to reduce the radius of the TRPT to improve the power transmission efficiency.

Tether Drag Coefficient

From the simple tether drag model the tether drag is directly proportional to the tether drag coefficient, C_{Dt}. To further assess the impact of the tether drag on the system model a sensitivity analysis of the steady state results was conducted. The tether drag coefficient was varied from 0.5 up to 5. Figure 5.40(a) shows the change in the system's maximum power coefficient as the tether drag coefficient is altered. It can be seen that it is close to a linear relationship between the maximum power coefficient of the system and the tether drag coefficient. The tether drag coefficient is directly proportional to the tether drag and corresponding torque loss. With a tether drag coefficient of 1.2 the torque loss within TRPT–4 operating at the optimal tip speed ratio of 4.0 is 4.9Nm. When the drag coefficient is increased to 2.7 the torque loss within TRPT–4, operating at the optimal tip speed ratio of 3.8, is 9.9Nm.

Figure 5.40(b) shows the RMSE between the simulated steady state C_p vs λ curve and that of one–minuted averaged experimental data for Daisy Kite prototype configuration 8, the experimental data used is the same as that in Figure 5.2(e) which shows the comparison with the tether drag coefficient set to 1.2. It can be seen from Figure 5.40(b) that the error is lowest when the tether drag coefficient is set to 2.7. This is over double the value of 1.2 used in all other simulations. For the results shown in Figure 5.40(b) the torque loss was calculated using the improved tether drag model neglecting any torsional deformation within the TRPT. As shown in Table 5.10 neglecting the

(a) Tether drag coefficient against the maximum power coefficient

(b) Tether drag coefficient against the error between the spring–disc model and experimental data
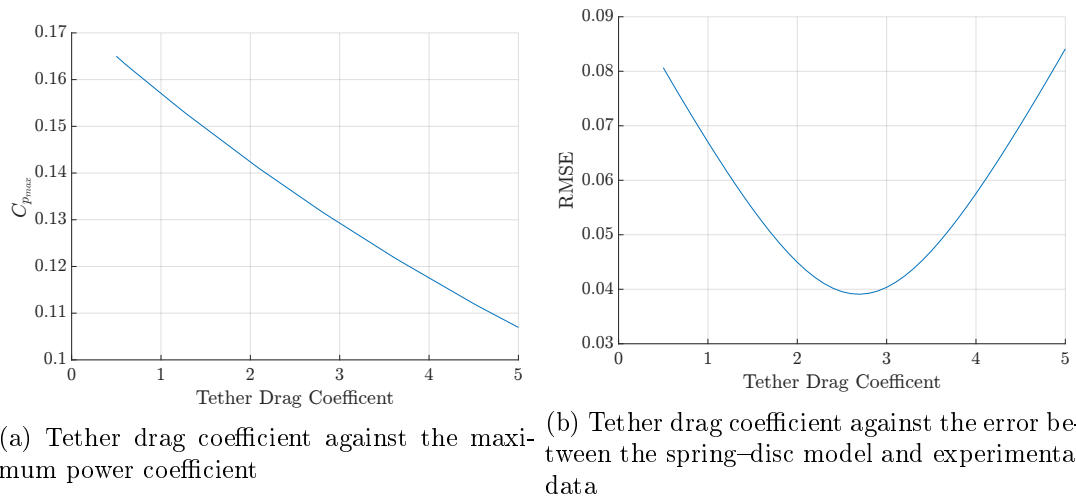
Figure 5.40: Effects of tether drag coefficient

torsional deformation results in a slight underestimate of the torque loss due to tether drag compared to taking the torsional deformation into account. This would result in a slightly larger tether drag coefficient being required to obtain the same torque loss. This, however, does not explain the significant increase in C_{Dt} required to minimise the error to the experimental data.

Given the result shown in Figure 5.40(b) it appears that the models, in general, under estimate the drag within the Daisy Kite system. However, with the experimental data available it is not possible to determine where within the model the drag is being underestimated. It may be that the drag on the rotor blades is being underestimated and therefore the rotor module is overestimating the torque output from the rotor. The model only takes into account the main lines within the TRPT, in reality there will be a number of other components that contribute to the torque loss, for example, the carbon fibre rings and the blades/kites bridle lines. In the models it is assumed that the drag on all other components is negligible compared to the main TRPT lines.

On the rigid rotors each blade has two bridle lines. The first connects the inner tip of the blade to the closest main TRPT line, the second joins the closest main line at 0.35m from the blade tip. Both lines are therefore connected to the same main TRPT line

below the rotor ring. Both bridle lines are one metre in length. To assess the impact that these additional tethers have on the torque loss the improved tether drag model is used. The calculation is based on an elevation angle of 25°, a constant wind speed of 8 m/s, a tip speed ratio of 4.0 with torsional deformation neglected. Under these settings the bridle lines for the three blades cause a combined torque loss of 3.7Nm. This is a significant amount of additional torque loss that is not currently accounted for within the models. As shown in Table 5.10 the model calculates a torque loss of 4.9Nm for the stated operating conditions. Although the bridle lines have a relatively short length compared to the main TRPT tethers they operate at a larger radius. The radius at the mid point on the bridle lines are 1.3m and 1.6m for the inner and outer lines respectively. As shown previously in this Section, the radius that a tether section operates at is a key factor in determining the tether section's contribution to the over-all torque loss. The torque loss caused by the relatively short bridle lines highlights this.

Incorporating the drag on the bridle lines increases the overall torque loss in the op-erating conditions described above from 4.9Nm to 8.6Nm. The bridle lines within the current Daisy Kite design therefore cannot be neglected when considering the tether drag. Future design should aim to remove bridle lines or minimise their length and radius.

Tether Drag Reduction

The tether drag has been shown to significantly impact the operation of rotary AWES. It should be considered in all aspects of the design, particularly when selecting the ge-ometry of the TRPT and the systems operating strategy. It has been shown that the tether drag causes significant torque losses within the TRPT. Within the experimental cases analysed, the mean efficiency of any TRPT tested is calculated to be at maximum just above 60%, see Table 5.11. It is envisaged that the torque loss within the TRPT can be reduced for the current and future rotary AWES. Several of the factors that influence the torque loss can be altered to improve efficiency.

By using the optimised rotor from Section 5.3.2 at a uniform wind speed of 8 m/s, elevation angle of 25° , tip speed ratio of 4.0 and with TPRT–4, the rotor torque produced is 61.8Nm and the torque loss within the TRPT is 5.1Nm. The torque loss is calculated using the improved tether drag model with the torsional deformation neglected. This gives a TRPT efficiency of 92% compared to 89% in Table 5.10 for the current three bladed rigid rotor. By altering the rotor the efficiency of the TRPT during operation can be improved. It was identified that to increase the TRPT efficiency the optimal tip speed ratio of the rotor should be kept low. As discussed in Section 3.4.2 this will likely result in a rotor with higher solidity compared to HAWTs. It was also shown that the elevation angle should be minimised to reduce the tether drag.

Perhaps the most important factor that affects the torque loss is the radius of the TRPT. The torque loss increases proportional to R^3. To reduce the torque loss the radius should therefore be kept low. However, in Section 5.3.1 it was shown that a larger radius TRPT is able to transmit more torque. This presents a compromise between the radius being large enough to transfer the required torque but kept small to reduce the tether drag. It was also shown that the axial tension applied to the TRPT is proportional to the amount of torque that can be transmitted, and that the tether drag is proportional to the square root of the maximum axial tension. To increase the torque carrying ability of the TRPT it is therefore more advantageous to increase the axial tension instead of the TRPT's radius. At present all AWES that utilise TRPT also incorporate a lift kite. The axial force on the TRPT could therefore be increased though improving the aerodynamic characteristics or increasing the lift kites area. It is envisaged that as systems scale up in size the lift kite would no longer be held static. By flying with crosswind motion the lift force produced for a given kite area is increased.

The tether drag coefficient is directly proportional to the torque loss. This could be reduced by altering the profile of the tethers or adding a profiled shroud to them. The use of an aerodynamically shaped fairing may be of particular interest for TRPTs. Given that the tethers are of relatively short length compared to other AWES, they will be

less likely to twist. The orientation of tethers within a TRPT are more consistent, therefore an aerodynamic fairing on the tethers is more likely to have the desired effect of reducing tether drag. The primary role of the rigid components within a TRPT are to keep the various tethers apart. In the case of the Daisy Kite's TRPT the rings keep points on the tethers a set radius from the axis of rotation. It may be possible for any aerodynamic profile or shroud on the tethers to create an aerodynamic force that acts to prevent the tethers from collapsing towards the axis of rotation. This could lead to longer lengths between rings or allow for a smaller radius TRPT.

It is not possible to completely remove the tether drag from an AWES. Any reduction in tether drag will often come by compromising the device's performance in other aspects. It is clear that rotary AWES, similar to all AWES, are susceptible to large losses due to the aerodynamic forces on the tethers. By considering this into design, particularly the geometry of the TRPT, the losses can be reduced.

5.4   Improved Design and Operation

This section provides details for an improved design for the Daisy Kite system. This is based on the steady state analysis described in the previous section. Following this the Daisy Kite's operational behaviours are discussed using observations and collected data from the experimental campaign along with simulation results from the mathematical models.

5.4.1   Design of Rotary Airborne Wind Energy Systems

The individual elements of the Daisy Kite design were investigated within Section 5.3. By using this analysis the design of the Daisy Kite system can be improved. An optimised rotor design was given in Section 5.3.2. Building on the optimised rotor the rest of the system design is refined.

Optimised Daisy Kite System Design

To design the TRPT the expected axial force and torque that it will experience must be calculated. Using the optimised rotor design, operating at its optimal tip speed ratio of 4.3, and an elevation angle of 25° the rotors thrust and torque coefficients are 0.5 and 0.05 respectively. The thrust and torque coefficients are dependant on the tip speed ratio, their magnitude is proportional to the wind speed squared. The force from the lift kite, for a given elevation angle, is also proportional to the wind speed squared. Therefore, the force ratio applied to the top of the TRPT will be constant for all wind speeds, assuming the tip speed ratio remains unchanged. Although it is desirable that the system operates at or close to to the optimal tip speed ratio, all possible operating points must be considered when designing the TRPT geometry. The relationship between the force ratio applied to the top of the TRPT, with a radius of 1.52m, will vary with the tip speed ratio. Figure 5.41 shows this relationship.

Figure 5.41 shows that the maximum force ratio reached using the optimised Daisy Kite rotor and the current single skin lifter is 0.17, at a tip speed ratio of 2.6. Higher force ratio values correspond to larger amounts of torque being transmitted relative to the axial force on the TRPT. For a given geometry, larger force ratios will result in more torsional deformation, and the TRPT will be operating closer to the point of over twist.
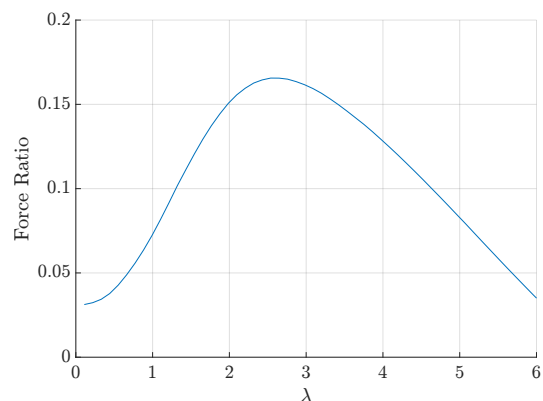
Figure 5.41: Force ratio against the tip speed ratio for the optimised Daisy Kite rotor.

It can be seen from Figure 5.41 that the maximum force ratio occurs at a tip speed ratio of 2.6, less than the rotor's optimal value of 4.3. The TRPT will have maximum torsional deformation, and will be closest to failure, when the system operates at a tip speed ratio of 2.6. With a constant TRPT radius of 1.52m, the radius of the rotor's

carbon fibre ring, the expected maximum force ratio is 0.17. Figure 5.29 is used to identify suitable length to radius ratios.

It can be seen from Figure 5.29 that, with a force ratio of 0.17, the length to radius ratio of the TRPT can be as high as 6 to provide stable operation. This is much bigger than the sections within the current TRPT prototypes. Although large TRPT sections are advantageous to reduce the amount of material, the tether drag must be considered. As shown in Figure 5.39 the sections of the TRPT with the largest radius cause the majority of the losses within the TRPT. As discussed in Section 5.3.3 the torque loss within the TRPT is proportional to R^3. The radius should therefore be minimised to maximise the TRPT's efficiency. The radius of the current TRPTs are decreased slowly from the rotor towards the ground station to avoid any abrupt changes in diameter. Given the advantage of reducing the TRPT radius a new TRPT design is proposed. By reducing the TRPT radius down to a minimum at the rotor the tether drag can be reduced. In the proposed TRPT design the first TRPT ring is in the plane of the rotor and the TRPT has a constant radius along its length.

As the TRPT radius is decreased the force ratio will increase thus requiring a smaller length to radius ratio. The lower sections of TRPT–5, the most recent TRPT prototype, have a radius of 0.35m. If this radius was used a maximum force ratio of 0.72 would be expected, which corresponds to a maximum length to radius ratio of 2.11. The maximum force ratio identified is based on the system's steady state. During dynamic operation it is likely that this force ratio will be exceeded. Equally it is not desirable to operate close to TRPT failure. If a TRPT length to radius ratio of 2.11 were to be used with a TRPT radius of 0.35m, the TRPT would likely fail during operation. To account for this the radius must be increased or the section length decreased. Figure 5.42 shows the maximum force ratio for different TRPT radii. Figure 5.42 also shows how the per unit length TRPT efficiency varies with TRPT radius. The efficiency is calculated using the simple tether drag model assuming a tether diameter of 1.5mm, a wind speed of 8 m/s and with the system operating at the rotor's optimal tip speed
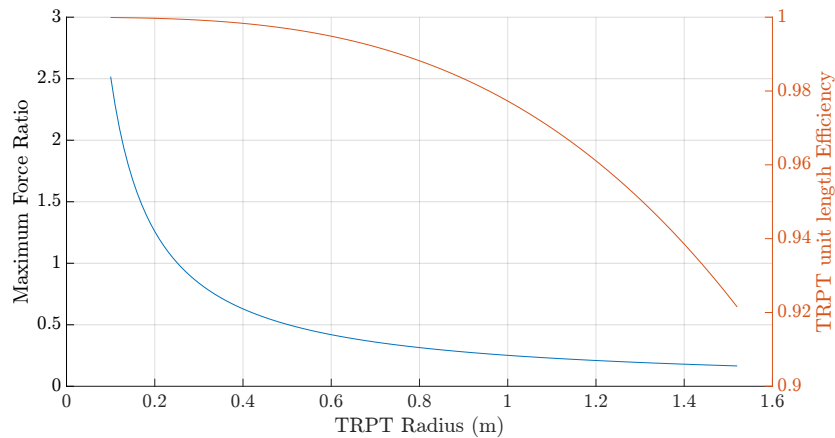
Figure 5.42: Maximum force ratio and TRPT efficiency variation with TRPT radius.

ratio of 4.3.

Figure 5.42 shows the compromise that must be made when selecting the TRPT radius. A larger radius results in lower force ratios, allowing for longer TRPT sections or for the TRPT to operate with lower torsional deformations and further from over twisting. However, a larger radius also leads to lower TRPT efficiencies. In this case a radius of 0.5m is selected as a trade off between the TRPT's torque transmission ability and its efficiency. This results in a force ratio of 0.5 and a per unit length efficiency of 99.7%, a length to radius ratio of 2.5, and section length of 1.25m.

Optimal Elevation Angle and Tether Length

The optimised rotor and new TRPT geometry are used to find the optimal TRPT length and elevation angle. A key motivation for AWES is their ability to reach higher altitudes, compared to HAWT, where stronger and more consistent winds are available. In order to reach higher altitudes longer tether lengths are required. The tether length required to reach the desired altitude is dependant upon the system's elevation angle. Although a larger elevation angle corresponds to a shorter tether, it also results in lower power capture at the rotor, as shown in Figure 5.31. To find the optimal elevation angle and TRPT length for the improved Daisy Kite design detailed above, an actuator disc

rotor model is used along with the simple tether drag model.

At an elevation angle of 25° the optimised rotor design has a maximum C_p value of 0.20 at $\lambda = 4.3$. Using these values multiple TRPT lengths are simulated to find the optimal length and corresponding operational altitude. The wind shear exponent is taken to be 0.2 with a reference wind speed of 8m/s at an altitude of 10m. The TRPT radius is 0.5m and the section length is 1.25m. The tethers have a diameter of 1.5mm.

Figure 5.43: Power output for the optimised Daisy Kite rotor for different TRPT lengths.

Figure 5.43 shows the power output at the bottom of the TRPT for a range of TRPT lengths given an elevation angle of 25°. The power output reaches a maximum of just over 1.4kW when the TRPT length is 126m. This corresponds to the rotor operating at an altitude of 53m.

The above analysis assumes that the elevation angle and tip speed ratio are constant at 25° and 4.3 respectively. These are varied to find the optimal values to maximise the power output. As shown in Figure 5.38, due to the TRPT tether drag, the optimal tip speed of the rotor is not necessarily the optimal tip speed of the system. To account for this difference, a look-up table, calculated using the rotor BEM model, of the tip speed ratio and corresponding power coefficient for the optimised rotor is used. The MATLAB function *fminsearch* is used to maximise the power output dependent on the elevation angle, TRPT length and tip speed ratio.

With the optimised rotor and new TRPT geometry an initial guess for the elevation angle, tether length and tip speed ratio of 25°, 125m and 4.3 respectively are used. The results of the multiple parameter optimisation are shown in Table 5.12 along with the proposed rotor and TRPT geometries. The optimal elevation is relatively

low at 18.5° and the overall TRPT length is fairly high at 190m. This results in an operating altitude of 60m, far beyond the operating height of a HAWT with a power output of a few kW. With a wind speed of 8 m/s at the reference height of 10m the power output is 1.6kW at the bottom of the TRPT. The optimal altitude for the rotor is highly dependent upon the wind shear, for example if a shear exponent of

Rotor radius	2.22m
Blade length	1.4m
TRPT radius	0.5m
TRPT section lengths	1.25m
Elevation angle	18.5°
TRPT total length	190m
Tip speed ratio	3.5

Table 5.12: Proposed Daisy Kite System Design

0.1 is used the optimal height drops to 25m, with an elevation angle of 15° and a TRPT length of 100m. The optimal TRPT length and elevation angle will therefore vary depending on the site and wind conditions. The optimal tip speed ratio is 3.5. A lower tip speed ratio reduces the tether drag but also results in a larger force ratio within the TRPT, as shown by Figure 5.41. A TRPT will therefore operate closer to the over twist scenario as the TRPT length is increased and the optimal tip speed ratio reduced.

The above analysis has lead to an optimised Daisy Kite system design, shown in Table 5.12, based on the current rotor radius and the steady state performance. The next section uses the mathematical representations to analyse some of the operational characteristics of the Daisy Kite system.

5.4.2   Operational Behaviour

The motion of the rotor combined with the varying stiffness and tether drag within the TRPT lead to complicated behaviour. This section briefs the Daisy Kite's operational behaviour using the spring–disc model and observations made during the experimental campaign.

Effect of Wind Speed on TRPT Response

As shown in Section 5.3.1 the torsional stiffness of a single TRPT section is determined by its operating state. The torsional stiffness is dependent on the TRPT geometry, the axial force and the torsion applied to it. The axial force and torsion applied vary with the wind speed. As the wind speed varies the torsional stiffness of the TRPT will change, this will alter its operating characteristics. To investigate this the settling time of the response of TRPT–4 is analysed. The results from the simulations used to compare the response of the spring–disc and multi–spring models in Section 5.2.2 are used for this analysis.

Table 5.13 shows the torsional stiffness range for the entire TRPT and settling time for the spring–disc representation at different wind speeds. The generator torque is set such that the device operates at a tip speed ratio of 4.0. Once the steady state has been reached the generator torque is reduced by 1Nm for a period of 0.5 seconds. The settling time is the time starting from when the input signal (torque reduction) is introduced to the time at which the ground station rotational speed remains within $\pm$ 2% of the steady state speed.

It can be seen that as the wind speed increases the torsional stiffness increases and the settling time becomes shorter. The system responds more quickly at higher wind speeds. This is due to the increase in axial force. As the wind speed increases the thrust from the rotor and the force from the lift kite increases. The torsional stiffness is directly proportional to the axial force. The rotor thrust and force from the lift kite both increase with the square of the wind speed. It can be seen from Table 5.13 a close-to

Wind Speed (m/s)	Torsional Stiffness (Nm)	Settling Time (s)
6	35-60	200
8	65-110	167
10	100-170	136
12	145-245	106

Table 5.13: Effect of wind speed on Daisy Kite response

linear relationship between the square of the wind speed and the torsional stiffness. It is the variation in axial force with wind speed that drives the change in torsional stiffness and leads to the difference in response time.

Multiple Steady State Complexity

By coupling the rotor aerodynamics module into the system model the interaction between the rotor and TRPT was analysed. Using the spring–disc model a series of simulations are run to investigate the steady state response of the rigid rotor and TRPT–4 system. The elevation angle is set to 20°, a constant uniform wind speed of 8 m/s is used and the generator torque is set to zero. Figure 5.44 shows the angular velocity of the rotor for three simulations, in each case the system is given a different initial angular velocity.

Figure 5.44 shows that two different steady state angular velocities are possible. The initial angular velocity determines which of the two values the system reaches. This suggests there are two equilibrium states for the rigid rotor and TRPT–4 system. At a wind speed of 8 m/s, shown in Figure 5.44, these angular velocities are 4.5 rad/s and 19 rad/s which correspond to tip speed ratios of 1.2 and 5.3 respectively. In this case a threshold of 5 rad/s for the initial angular velocity is identified. Below this value the lower equilibrium speed of 4.5 rad/s is reached, above it the higher equilibrium speed of 19 rad/s reached. This phenomenon was also experienced during the experimental campaign. On occasions it was necessary to drive the system using the generator as a motor to reach higher angular velocities. In general, this situation only occurred during light winds.
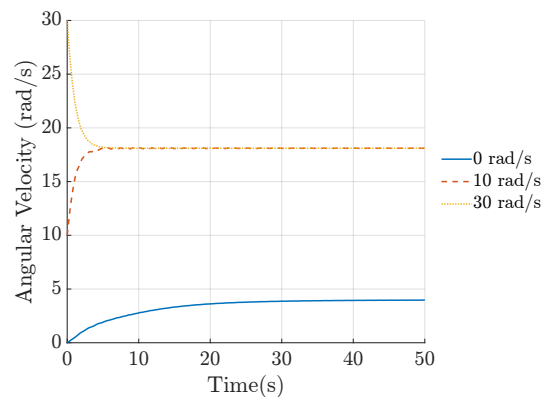
Figure 5.44: Angular velocity of the rotor for several initial angular velocities in a constant wind speed of 8m/s.

An equilibrium angular velocity is reached when the rotor torque equals the sum of the generator torque and the torque loss due to aerodynamic drag. In this case the generator torque is set to zero, therefore the rotor torque is equal to the torque loss due to tether drag at the two angular velocities discussed above. The combination of the rotor and the TRPT leads to this phenomenon. Figure 5.45 shows the torque coefficient against the tip speed ratio for both the rotor in isolation and the rotor coupled with TRPT–4. When the torque generated by the rotor equals the torque loss within the TRPT the torque coefficient becomes zero. It can be seen that for this system the torque coefficient drops below zero at tip speed ratios of 1.2 and 5.3, matching the equilibrium velocities seen in Figure 5.44.

Figure 5.45(a) also shows that the torque coefficient of the rotor in isolation does not drop below zero until the tip speed ratio is over 6. The multiple steady state equilibrium points arise due to the combination of the rotor and TRPT. This indicates that it is possible to design the system such that the lower equilibrium speed does not occur. For example, when TRPT–4 is coupled to the optimised rotor, described in Section 5.3.2, only one equilibrium speed is obtained. The speed corresponds to the higher angular velocity found in the case above.

(a)

(b) Magnified region of 5.45(a).
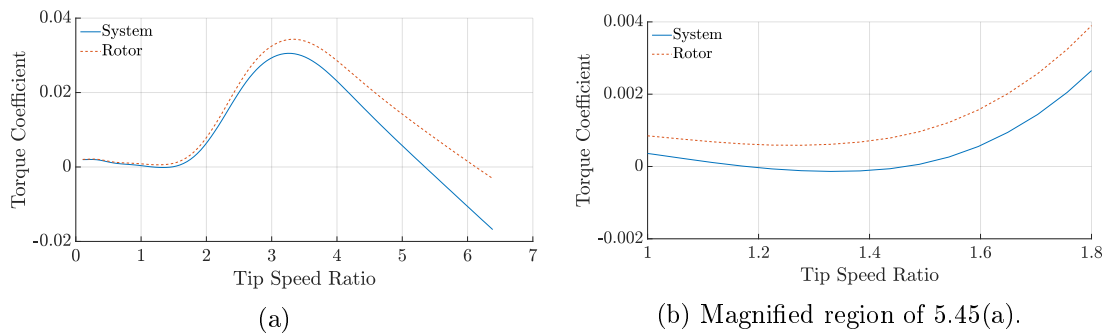
Figure 5.45: Torque coefficient against tip speed ratio for an elevation angle of $20°$

5.5   Summary

This chapter has used the data collected during the experimental campaign, described in Chapter 3, and the mathematical representations, detailed in Chapter 4. The six different single rotor prototypes tested during the experimental campaign were used for an initial comparison with the spring–disc system model. This showed that the spring–disc representation is able to match the experimental data over a range of different system configurations. However, it was found that when modelling rotors with more than three blades the difference between the simulation and experimental results is larger.

To test the overall performance of the mathematical representations five 5–minute windows from the experimental data were compared to both the spring–disc and multi–spring models. Through this comparison study both models were refined. By incorporating the change in axial position of the rotor, and therefore the relative wind speed experienced by the rotor, the difference between the simulated and measured results was reduced. It was shown that by assuming the rings being rigid within the multi–spring model the computational time is reduced by a factor of around 6 with negligible impact on the results.

The comparison with experimental data shows that both system models are able to match the measured data. Despite the differences between the spring–disc and multi–spring models their results, when modelling the Daisy Kite's prototypes, are similar. However, the difference between them increases for longer TRPTs. Given the much larger computational time required for the multi–spring representation, the spring–disc model is used to analyse the current Daisy Kite system.

A steady state analysis of the TRPT provided an insight into its design and operation. A critical rotational deformation was identified, beyond which the ability of a TRPT section to transmit torque collapses to zero. This critical rotational deformation is determined by the sections geometry, for a section with constant radius it is determined by the ratio of the section length to its radius. For a given TRPT geometry the torsional

deformation is dictated by the torque and axial force applied to it. The ratio of tangential force due to torque to axial force can be used to identify stable TRPT geometries.

A steady state analysis of the Daisy Kites rigid rotor leads to an optimised rotor design. In the optimised rotor design the fixed blade pitch is 3° and the rotor solidity is 7.5%, which could be achieved by using the current chord length of 0.2m and increasing the number of blades to 4. The blade length is increased to 1.4m to further increase the rotors power coefficient.

The simple tether drag model was used to identify the key factors affecting the torque loss due to tether drag. It was shown that the most important factor is the TRPT radius, R, as the torque loss increases with R^3. It is therefore advantageous to keep the TRPT radius small. Using the improved tether drag model the efficiency of the TRPT–4, operating under steady state conditions at a tip speed ratio of 4.0, is shown to be 89%. However, the mean efficiency from the simulations used for comparison with the five 5–minute windows of experimental data was calculated to be between 32% and 61%. It is envisaged that the tether drag can be reduced for future TRPT systems by keeping the TRPT radius small and potentially using tethers with a more aerodynamic profile. As keeping the TRPT radius small is advantageous to reduce torque losses a new TRPT design is proposed. The suggested TRPT has a constant radius along its length. Based on the optimised rotor the TRPT radius is 0.5m with each TRPT section having a length of 1.25m.

Using the improved Daisy Kite design with the optimised rotor and new TRPT, a multi parameter optimisation was done to find the optimal combination of elevation angle, TRPT length and tip speed ratio. The results concluded that an elevation angle of 18.5°, a TRPT length of 190m and a tip speed ratio of 3.5 maximised the power output of the system.

The final section of this chapter investigated the operational behaviour of the Daisy Kite

system using experience gained from the experimental campaign and the mathematical models. The complex dynamic nature of the system was highlighted. As the wind speed increases the torsional stiffness increases and the response time of the system decreases. The natural frequencies of the system are determined by the torsional stiffness. It was found that the first natural frequency varies over a wide range in a relatively short space of time. These fluctuations cause the device to have a highly variable dynamic response. It was also found that, under certain system designs, two equilibrium steady state rotational speeds could be obtained.

This chapter has presented the comparison between experimental data and the mathematical representations. The measured data and simulation results have been used to identify key design drivers, the systems operational behaviour and a new system design has been proposed. The next and final chapter of this thesis concludes this work.

Chapter 6

Conclusions and Future Work

This final chapter summaries the major contributions of this thesis work, future work is also detailed including a discussion of potential control strategies for the Daisy Kite and other similar rotary AWES.

Experimental Campaign and Design Improvements

Chapter 3 presented the field tests conducted on the nine different Daisy Kite system configurations. This experimental campaign resulted in over 120 hours of recorded data and represents the most comprehensive testing of any rotary AWES that incorporates TRPT. Samples of this data has been used to confirm the accuracy of the mathematical representations developed as part of this thesis work. This comparison was able to provide confidence in the accuracy and reliability of the simulation results.

The desire for reliable experimental data, along with the experience gained through the multiple test flights, resulted in a series of design improvements throughout the campaign. The most crucial of these, with respect to robust operation and to facilitate the collection of reliable data, was the development of a bespoke ground station. The new ground station proving to be more stable and less susceptible to failure. A key design change, with regard to power output, was the use of rigid wings. The more aerody-namically efficient rigid wings increased the power coefficient of the Daisy Kite, they

also highlighted the complex dynamic operation of the device. The increased knowledge on the operation of the device, in particular the response of the TRPT to changes in wind speed e.g. during a gust, was also highlighted. The experimental campaign also included practical testing on operation strategy improvements. For example, yawing the rotor away from the downwind position to reduce the power output and using the generator torque or mechanical brake to reduce or stop the rotor rotating during take–off and landing. These proof of concepts provide confidence in any strategy change prior to them being incorporated into future systems.

At the start of the field tests a triple rotor, soft winged, 3–bladed prototype achieved a maximum power output of just over 300W. By the end of testing a single rigid winged, 3–bladed rotor had achieved a maximum power output of 1.4kW. This highlights the impact of the several design improvements made during the experimental campaign. W&I have continued to develop the Daisy Kite system and are currently working on the design of a 10kW system. Once complete this will be the largest rotary AWES that incorporates TRPT.

Mathematical Representations

A major contribution of this thesis work is the developed mathematical representations of the Daisy Kite system described in Chapter 4. The modular framework of the representations allowed for multiple versions of the rotor, tether aerodynamics and TRPT dynamics modules. This resulted in three full system models referred to as the steady–state, spring–disc and multi–spring representations. The use of lightweight tethers to transfer torque is both innovative and novel. It is not seen outside of AWE. The modelling focused on this unique method of power transmission. The steady–state, spring–disc and multi–spring models are analysis tools that can be used to investigate the operation and design of future TRPT systems. The spring–disc and multi–spring models are the first dynamic representations of a rotary AWES that incorporates TRPT.

Several assumptions were made to allow the development of the full system models. Improvements could be made to the representations by relaxing or removing some of these. This may be required as larger scale systems are modelled. For example, within the spring–disc model it is assumed that the axial force is constant along the length of the TRPT. The spring–disc model could be improved by removing this assumption. The Daisy Kite TRPT design represents one possible TRPT geometry, future work should involve the modelling and analysis of other possible TRPT configurations, for example that used by someAWE's airborne turbine. It was shown that the bridle lines used in the rigid rotor set ups cannot be neglected when calculating the torque loss due to tether drag. Future work should involve analysis of the components that contribute towards tether drag and possible ways of reducing the drag e.g. line fairing.

Simulation and Analysis of Rotary AWE Systems

One of the aims during the experimental campaign was to collect empirical data for comparison against the mathematical models. In Chapter 5 measured data from the six single rotor prototypes provided an initial comparison while a selection of 5–minute windows from the measured data allowed for a more in depth analysis. The more in depth analysis resulted in alterations being made to both dynamic representations. The change in length of the TRPT was accounted for within the rotor module as this affects the relative wind speed that the rotor experiences and therefore the torque and thrust generated. The multi–spring representation was also adapted, by assuming that the TRPT rings are rigid the computational time required is reduced. The empirical data has shown that the mathematical models are able to produce accurate and reliable results. Simulations to compare the two dynamic representations showed that the results from each are similar but that the difference between the two models increases as the TRPT length increases. Due to the lower computational time it was concluded that the spring–disc model is preferred for analysis of the Daisy Kite system.

The steady–state representation was used to identify the critical rotational deforma-

tion, beyond which the TRPT is no longer able to transmit torque. This leads onto analysis to identify the range of suitable TRPT geometries, dependent upon the torque and axial force applied to the TRPT. The radius of the TRPT was found to be the most important factor that influences the torque loss due to tether drag. It was also shown that, due to the losses within the TRPT, the optimal tip speed ratio for the rotor is higher than the optimal tip speed ratio for the combined rotor and TRPT system. Analysis of the Daisy Kite rotor resulted in a more optimal rotor design being proposed with the optimal blade pitch, rotor solidity and blade length being identified for the current Daisy Kite rigid winged rotor. A TRPT geometry was then selected based on the optimised rotor design. The new design was used to assess the optimal TRPT length and elevation angle for the system.

The steady–state model has been used to propose a new Daisy Kite design. The dynamic representations were used to identify key operating characteristics of the current prototypes. Most crucially the complex response of the TRPT. It was found that the torsional stiffness of the TRPT can vary by relatively large amounts over short periods of time. This causes the first natural frequency of the system to vary and therefore the system's response. These fluctuations imply complex dynamic behaviour. It was also shown that, due to the coupling of the rotor and TRPT, two equilibrium states are possible depending on the system design and the initial conditions.

The developed mathematical representations and the experimental tests have resulted in improved knowledge regarding the design and operational characteristics of rotary AWES that use TRPT. The understanding of TRPT is still in its infancy. The mathematical representations provide a systematic way to further explore this novel method of power transmission, for example, different TRPT configurations could be investigated to establish which are the most advantageous for AWES. In future work the mathematical representations could also be used for developing and analysing possible control systems. Possible control methods to investigate are discussed in the following section.

6.1   Discussion of Potential Control Strategies

Currently the two leading airborne wind designs are those that use a pumping cycle and Fly–Gen crosswind systems. Both of these architectures require sophisticated control systems. They use a single wing flying in a crosswind motion. The wing must be controlled so that it follows the desired flight path. Pumping cycles in particular must regularly transition between reel–out and reel–in phases. The required control systems can be complex, therefore research into AWES often focuses on the control of these two systems.

In contrast past and present Daisy Kite prototypes have operated with very little, and in some cases no, active control system in place. With the wings networked together the flight path of each individual wing is constrained, making it possible to operate the Daisy Kite and similar rotary systems without any active control. It is only in the most recent iteration of the Daisy Kite ground station that the ability to control the generator speed and torque was implemented. Almost all previous Daisy Kite prototypes operated without any automated control system. This represents one of the largest advantages that rotary AWES have over other AWES

As the Daisy Kite and other rotary systems increase in size, control systems must be developed and implemented. As the size of the device increases the requirement to accurately control its operation becomes more important. This is to maximise the systems energy output, minimise the cost and prolong the working life of the device. Given the importance that control systems are likely to have on future iterations of the Daisy Kite and other similar rotary AWES, potential control strategies for the key operating regions of the Daisy Kite are discussed next. The potential strategies focus on increasing the systems autonomy to allow for larger scale systems.

Take–Off and Landing

The Daisy Kite currently relies on a manual launch and landing process. The lift kite is released into the air, once it has stabilised the back line, downwind of the rotor, is slowly let out. In doing so the lift kite pulls the rotor and TRPT into the air. The reverse process is used to land the system. For the small scale prototypes this has proved to be a simple and robust method for launch and landing. However, due to the need for an operator to manually release and retrieve the back line, wind speeds that can be safely testing in are constrained by the force needed to retract the line. As the back line is attached to a static back anchor the system must be landed for the anchor to be moved for example, if the wind direction changes. As systems increase in size, the force on the back line will increase. The desire for longer flights requires a system that can adapt to changes in wind direction and eventually launch and land autonomously, without any operator intervention.

It is proposed that for small scale systems launch and landing procedures are similar to the current methods. For simplicity it is envisaged that the lift kite will still be launched manually. The backline release and retrieval will however be performed by an electric winch, this to remove the need for manual intervention particularly when landing the system in high winds. The electric winch will be located on an arched track, the track may form a circle or only a portion of one. As the wind direction changes the winch can move along the track to ensure that the backline remains downwind of the ground station. To avoid excessive movement the winch will be held in place with a mechanical brake, this will be released automatically when the winch position needs to be altered. Once the backline is realigned in the downwind position the mechanical brake will be reapplied. A simple lift kite controller, capable of steering the lift kite, will be used to land the lift kite when required. The launching of the system will still require an operator, but once airborne and operational the system will be able to maintain its downwind alignment and land when required. As the system increases in size further improvements will be needed to the launch and landing process.

The use of a backline downwind of the rotor allows for a more safe system. It provides a second point of contact with the ground and is crucial in the current launch and landing process. However, it increases the land space that the system requires. For smaller devices this is acceptable but if larger systems are to be realised it may be advantageous to remove the backline. The ground infrastructure would then all be located at the ground station. This would require a complete redesign of the launch and landing procedures. It is envisaged that the rotor would be stored on the ground station when not operational. To launch, power would be supplied to the rotor so that it rotated and provided sufficient lift to support itself in the air. The TRPT would be slowly reeled out from the ground station as the rotor gained altitude. Once the relative wind speed of the rotor passed a lower limit the rotor could transition from being powered into autorotation. The system could then begin generating power, this is similar to the launch and landing procedure proposed by BladeTip Energies [11]. The opposite process would be used for landing the device. This launch and landing procedure proposed for larger systems would also remove the need for a lift kite. Even if the lift kite is not required for launch and landing it may be advantageous to retain the lift kite to allow the rotor to operate at lower elevation angles.

Over speed Protection

A key feature currently missing from the Daisy Kite prototypes is automated over speed protection. This limits the use of the device in higher wind speeds. Over speed protection is now crucial to develop the design further and enable larger scale systems. In the first instant it is proposed that a lift kite controller is used to prevent overloading system components. Through the use of lift kite control the position of the rotor would be moved away from the downwind position relative to the ground station. This may cause the rotor to yaw away from the downwind position, reducing the power that it produces. During the experimental campaign this process was used on several occasions to slow the rotors rotation prior to landing, in this situation the backline was used to pull the rotor away from the downwind position. It is envisaged that a similar effect

would be achieved by steering the lift kite. The lift kite steering could be achieved through the use of a small control pod suspended below the kite. This would alter the relative tensions on the kite's bridle lines to steer it. The elevation angle could also be increased to reduce the rotor's power output.

It is envisaged that for much larger systems, active pitching of the rotor blades will be required. This would allow for quicker response than yawing or altering the elevation angle of the entire system. Another possible solution for larger systems is to alter the swept area of the rotor. As the centre of the rotor is open it is possible to expand or retract the blades relative to the rotors centre. This would alter the swept area of the rotor and the power generated. A variable rotor radius could also reduce the land use of the ground station as the rotor radius could be minimised during take–off, landing and when stored on the ground.

Operational Control

Initially the development of robust launch, landing and over speed control is the priority for the control system. Moving towards higher levels of automation will allow for systems with larger power outputs and for extended field tests. As the systems scale in size the operational control will become more crucial. Being able to extract the maximum amount of energy while also maximising the component life and minimising the systems cost will lead to the lowest cost of energy.

At present the operational control of the Daisy Kite uses only the generator torque to set the rotational speed of the system. This is used to keep the system operating at close to a set tip speed ratio in below rated wind speeds. It is likely that torque control will be used in all future system designs. This will include further investigation into the dynamic behaviour of the TRPT. The torque and thrust produced by the rotor are related and preliminary analysis has shown that the system responds more quickly to a a change in tension than a change in torque. It has been proposed that the tension at

the bottom of the TRPT could be used as an input to set the generator torque.

Generator torque control is only suitable for lower wind speeds. As the wind speed increases the maximum generator torque will be exceeded, alternative control methods are therefore required for higher wind speeds. As introduced previously, yawing or tilting the system to increase the misalignment of the rotor and the incoming wind will reduce the rotors power output. For small scale systems it is envisaged that this method will be used to regulate the system in higher wind speeds. This will be achieved by using the back anchor and line along with the lift kite to position the rotor. As the system increases in size it is proposed that variable pitch blades would be incorporated into the design, similar to HAWT. As with the over speed protection it may be possible to alter the radius of the rotor, particularly in higher wind speeds, to control the systems power output.

The development of a lift kite controller will enable the position of the rotor to be controlled. For small scale systems altering the rotor's position, and therefore the rotor's orientation to the oncoming wind, provides a simple solution to reducing the forces generated by the rotor in higher wind speeds. It also provides a method of minimising the rotor's rotational speed during launch and landing. It is envisaged that for small scale systems the lift kite will remain static. However, as the size of the systems increase it may be advantageous to fly the lift kite in a crosswind motion. The aerodynamic forces produced by a wing in crosswind flight are larger in comparison to it remaining static. As the size of rotary systems increases using a crosswind motion would reduce the size of the lift kite required. Although it may be feasible for a rotary AWES to operate without a lift kite, a lift kite allows for a lower elevation angle and increased tension within the TRPT. It may prove to be advantageous for larger rotary AWES to incorporate a lift kite.

The aim of this thesis work was to improve the design and operation of rotary AWES that utilise TRPT and to assess the systems performance based on mathematical mod-

elling and experimental data. This has been achieved. Three mathematical models have been produced and their accuracy has been confirmed using data collected during an experimental campaign on the Daisy Kite system. Several design and operational improvements were made during the experimental campaign. Analysis using the developed models resulted in a new Daisy Kite design being proposed, the design is aimed at increasing the systems power output. Analysis of simulation results and experimental data, along with observations made during field tests, has lead to the identification of several operational characteristics of rotary AWES that incorporate TRPT.

Appendix A

Tensile Rotary Power Transmission Laboratory Experiments – Felicity Levett Final Report

Airborne Wind Energy Systems

DISCOVERING THE OPTIMAL LENGTH OF
TETHER TO TORQUE RATIO

Felicity Levett | University of Strathclyde | Tuesday 1st August

As the United Kingdom's need for energy rises, standard forms of energy such as Coal, Nuclear and mainly Gas are used increasingly. Other forms of energy have to be considered to meet the demand. Of the total energy supplied to the UK in 2016, 75.4% was taken to produce electricity. From this, only 18.8% of the energy was renewable. The UK plans to have a 20% of the total energy produced by renewables 2020. Of the renewable energy produced in 2016, 18.6% came from wind energy [1].
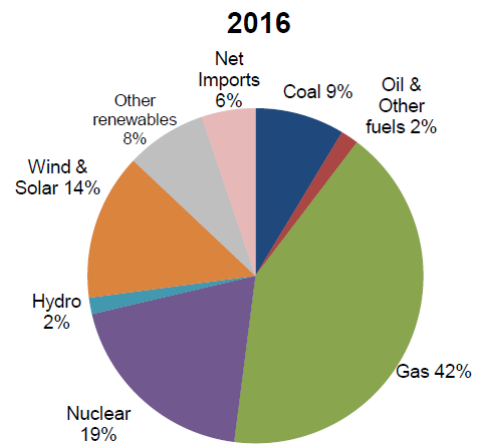
Wind turbines can range in the amount of energy they produce. From lower producing turbines that have a maximum power output of around 50kW with projects costing around £32000; to large turbines that can produce a power of 3MW but with projects costing £3.1 million [2]. To supply the amount of (renewable) power needed to reach the UK's target of 20%, large wind farms are being constructed across the UK.

One of the largest UK wind farms is the Dunmaglass Wind Farm in Scotland. Its construction was finished in Spring 2017 and when fully operational, Dunmaglass has the potential to produce 94.05 MW. With SSE estimating the cost of the project to equal around £200 million [3] it is evident that to supply energy quickly, a cheaper alternative has to be found.

Airborne Wind Energy looks at the ways in which usable power can be generated from systems that are free flying in the air or tethered to the ground like a kite [4]; this is in contrast to wind turbines, which are firmly planted to the ground by an expensive tower and foundations. With wind, the more powerful, clean air is situated higher up, therefore the towers for turbines get taller and taller to capture more energy. The wind is stronger higher up due to jet streams of clean air uninterrupted by the environment. Wind is treated as a fluid as what happens in one area effects other surrounding areas. This increase of height requires more material and therefore a bigger budget. However, theoretical Airborne Wind Energy Systems (AWES), are lightweight and can achieve greater heights provided they have enough stability in their design to stay safely airborne.

The power generated by a kite is surprisingly large depending on its lift mode. Miles Lloyd from San Francisco in 1980's investigated crosswind kites. Lloyd formulated that the useful power of a kite can be approximated by using:

$$P = \frac{2}{27} \rho A v_w^3 C_L (\frac{C_L}{C_D})^2$$

The formula suggests that power (P) is equal to the product of the density of air (ρ), the area (A), the velocity of the wind cubed (v_w^3), the lift coefficient (C_L) and the lift-to-drag ratio$(\frac{C_L}{C_D})^2$.

However this relationship is not definitively proven experimentally but is supported computationally. However in new systems, tether drag poses a large problem and so one of the main design features of a system is to take into account the number of tethers. A main aim is to reduce the number contained within the system and so reduce the drag which mathematically increases the lift-to-drag ratio, generating more power.

The problems with kites is that they can only be used in certain conditions. Once they have been manually released, they undergo passive control to keep them in working condition. However an advantage to kites is that they can be brought down easily for maintenance and released soon after.

For my internship, alongside Oliver Tulloch, I will be looking at the Daisy Stack model as created by Rod Read.

Wind Turbines versus Kites

When trying to calculate the kinetic energy possessed by a moving solid, the formula:

$$E_k = \frac{1}{2} m v^2$$

However, wind is treated as a fluid. It is possible to quantify the amount of energy in a space. If given a cylinder, the energy possessed by the wind filling the shape is:

$$E_k = \frac{1}{2} (\rho V_c) v^2$$

Rather than looking at the mass of air, we substitute the density of air and the volume of the cylinder. However, due to the continuum assumption which states assumes that fluids are infinitely continuous, it is inaccurate to quantify the amount of energy in a cylinder at one point. Therefore, looking at the cross sectional area of a cylinder is then taken, and the rate of energy passing through this per second can then be calculated using:

$$P = \frac{1}{2}(\rho \pi R^2)v^3$$

The above equation suggests that the larger the radius, the larger the power that can be harvested by the turbine. This explains why Turbines are made larger so that the blades sweep a larger area. The formula also shows that the higher the velocity of wind, the larger the power. However Wind Turbines have limits to when they can operate. Approximately, for a wind turbine to be operational, wind speed must be $> 4mph$ but remain $< 20mph$ otherwise the turbine is turned off to prevent damages.
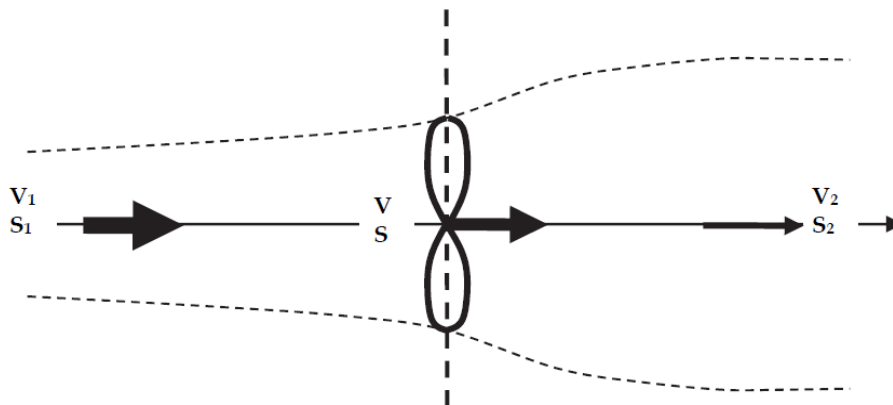
Wind turbines have a limit to how much kinetic energy they can capture from the wind. This limit is called the Betz Limit. A turbine can only convert a maximum 59.26% [5] of the power of the wind. It is independent of the design and is caused by the area of the wind before the turbine blades is smaller than the area after. From the diagram above, the dotted line shows the path of the air flow. The velocity of the air decreases directly following the blade showing the loss of energy but the velocity of the outer boundaries of the area has to increase due to the conservation of mass (has further distance to travel in the same amount of time as the central area of air).

With a limit of how much power can be extracted from the air, it is paramount that the energy we extract is done efficiently and at a low cost.

Kites, although not currently efficient are a low cost way of extracting energy from the wind as it does not involve building huge concrete structures that costs hundreds of thousands of pounds. Airborne Wind Energy Systems are able to reach greater heights where they can find clean air for a more constant, uninterrupted air flow.

Some systems work with pairs of kites that fly in a figure of eight. As the move up and down respectively, their partner does so too. This twisting motion caused by the up and down movement of the kites, turns a generator to produce power.

However, with Rod Read's design, the Daisy Ring Kite system is tethered to a grounded generator and relies on a spinning motion around a central shaft that transmits the tension from the lifting kite. As the kites make the system start to spin, the tethers are made to skew between the rings. This changes the force from acting perpendicularly to the ring, to acting at an angle. By doing so, a component acts in the plane of the ring causing torsion. This torque is transferred down along the system. An important point to note is that torque is lost as you make your way down the system through factors such as line drag and friction between different parts of system.

Therefore the aim of this internship was to see that the factors we consider to be negligible when creating a computational model of the design, are just that in real life.

Methodology

By placing two bike wheels opposite each other and applying a tension along the tethers, it is possible to simulate the lower rings of the concept.

Before the system was put into motion, the two wheels were covered in alternating tape with a width of 20mm. This way, when looking back at the photos during data analysis, it is easy to see the displaced length of the tether and so work out the angle of skew more

quickly. As you can see from the photo on the right, we had our tape alternating red, white and blue and on these segments numbered them. An excel spreadsheet was created that could then calculate the angle of skew from inputting the number of tape segment being pointed at by the pink arrows.

The tension was provided by hanging bags of rubble off a rope. The bags of were separated into two bags of 20kg, one bag of 10kg, one of 5kg and one of 15kg. They were weighed by hanging them from the weighing scale and the pulley. The bags of rubble had to be quite large as it was easier if there were fewer bags to hang freely from the pulley without touching the pillar. If the weight were to touch the pillar, not all of the force would be being transmitted as tension along the rope.

Behind the moving motor, a pulley system was setup to apply tension to the rig. From the base of the trolley, the polypropylene rope (we used this type of rope to prevent it from stretching) was run to a pillar. At the bottom of the pillar, a ratchet was securely tightened with rubber squares to stop it from slipping. A pulley was then attached to the corner of the strap and the rope was ran through this and up to another pulley on the furthest side of the pulley from the system. To give enough clearance, multiple bolts were placed along the rod. By having them flush to one another, the essentially increases the diameter of the rod, and therefore increases the tensile strength so it is able to hold more mass. However, as you can see from the picture, although the rod was able to hold mass, it still bent. Loops were then placed along the length of the rope so that the bags of mass could be hung off it easily without touch the wall.

Start with tethers that are smaller than the diameter in the bike wheel because the system is able to take more torque before failing. Rather than tying the tethers straight onto the wheel, smaller pieces of rope were tied. On these smaller pieces of rope, 2cm away from the rim, measured using a caliper, a knot was tied. This meant that the longer pieces of rope could easily be attached and unattached and swapped for other lengths more easily. It is also easier to then check that the longer lengths of rope are the same length rather than checking once they are tied onto the wheels. Then start the power supply.

At the power supply there are two dials. One controls the speed and the other the torque. Begin the experiment by running one wheel at a constant speed. For this experiment, we

chose 60 rpm. Then gradually in regular increments, increase the torque. One wheel is set to a constant speed, the opposite, the torque. Before increasing the torque at the power supply, a quick excel sheet was created to approximate what level or torque could be achieved before the system failed. The below table shows an approximation for how much torque each tether can take for a length of 0.646m which was the first length of tether used.

After setting each torque, take a photo of the wheels so that the angle of skew can be

Length of Tether	Tension	Torque	Angle/Deg	Angle/Rad	Radius/m	Chord
0.65	100.00	4.64	180.00	3.14	0.30	0.60
0.65	100.00	4.57	160.00	2.79	0.30	0.59
0.65	100.00	4.36	140.00	2.44	0.30	0.56
0.65	100.00	4.02	120.00	2.09	0.30	0.52
0.65	100.00	3.56	100.00	1.75	0.30	0.46
0.65	100.00	2.99	80.00	1.40	0.30	0.39
0.65	100.00	2.32	60.00	1.05	0.30	0.30
0.65	100.00	1.59	40.00	0.70	0.30	0.21
0.65	100.00	0.81	20.00	0.35	0.30	0.10
0.65	100.00	0.00	0.00	0.00	0.30	0.00

calculated using the excel spreadsheet. Throughout the experiment we were unable to record two sets of data simultaneously from the torque transducers on one laptop. So, instead, we were recorded the data from one so it would create a spreadsheet of data. Then by having a gopro camera set towards the laptop screen whilst the experiment is running, on the spreadsheet, it is possible to fill out the missing torques from the other transducer. Also between each change in torque, record the load measured by the scale attached to the back of the moving trolley. As the torque increases, so should the load until there is enough force to overcome friction in the pulley system and then it should remain constant.

Weight on Pulley	Weight between Wheels	Weight on Back of System
5	4.5	8.5
10	7	13.5
15	12.5	19
20	17.5	23
25	21.5	29.5
30	27.5	32.5
35	32	38.5
40	37	43.5
45	44.5	49
50	48	52
55	55	57.5
60	60	60
65	66	62.5
70	67	72.5

As it is clear from the picture above, before the system is even started, there are losses in tension in the system. This may be due to friction within the pulley system. Based on this table, when inputting the tension on the system into the final calculations, the load measured on the back of the trolley was roughly converted into the load felt between the wheels.

Results

The first mass we used was 5kg with a tether length of 0.646m. The graph below shows that though our measured values follow a similar pattern to those calculated, the two results are very far apart. Additionally, the system failed very quickly at a low torque due to the grub screw holding the wheel in place sheared.
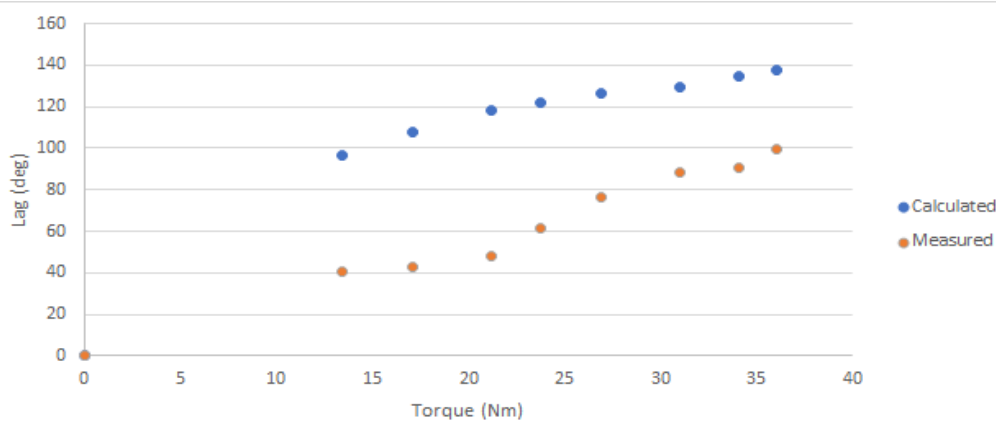
The second mass that we tested was 10kg. In comparison to the 5kg result, you can see that the two sets of data, one for calculated and one for measured have got closer together. Though the measured is still below the calculated data which can be expected due to losses in the system, they still follow the same pattern suggesting that the collected data is reliable. The system was able to surpass the safety angle of 120 degrees and continue up to a torque of around 320Nm.
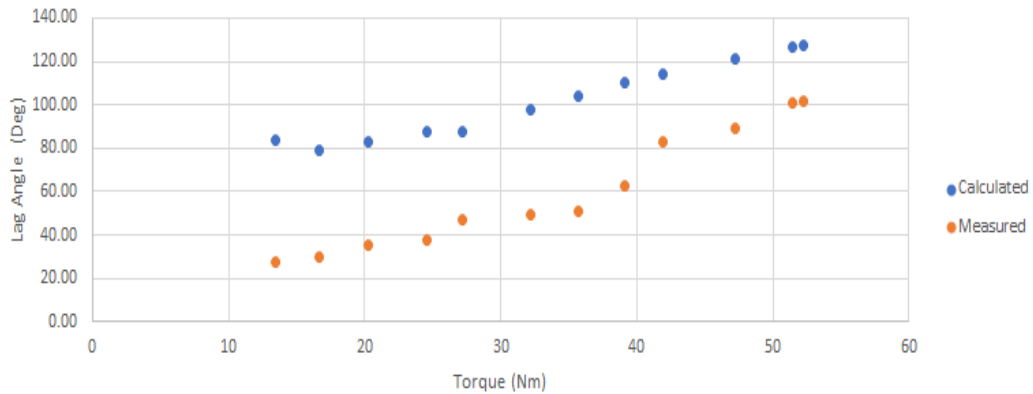
The third test completed was for a mass of 20kg. Already the two sets of data are closer together. This suggests that higher masses, with greater tension in the system, the rig is quicker to overcome the force of friction and react to the torsion.
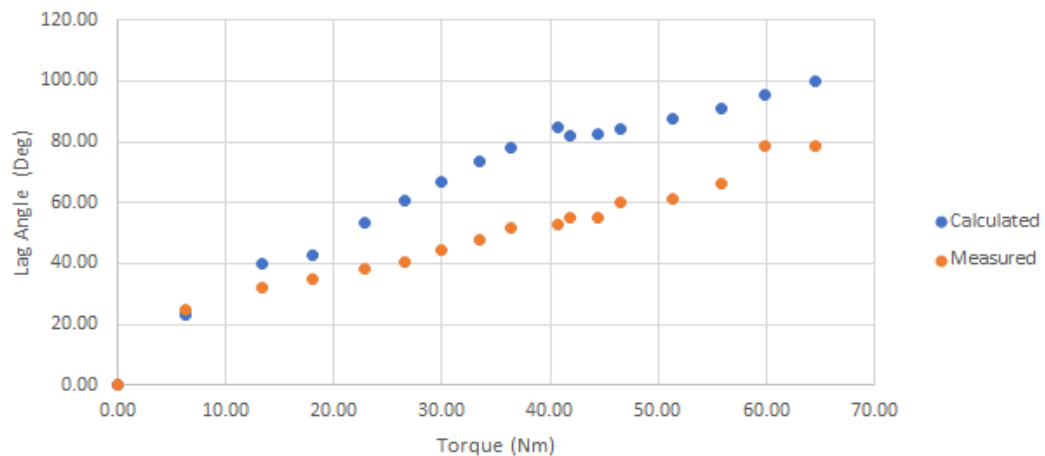
Our final test was based on 30kg. The load cell was quicker to reach a point and remain constant. However, as shown by the graph below, after 60N, the measured data becomes slightly erratic and fails to correlate with the calculated data. When performing the experiment, the wheel began to stop resisting the torque induced in the system. This is the point that is believed to be at which the grub screw of one of the wheels sheared.
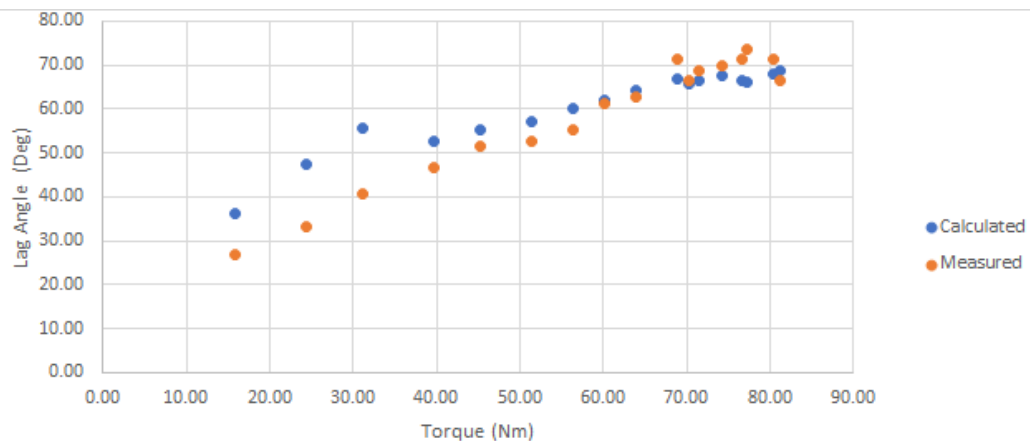
Conclusion

To conclude, the higher the mass the more accurate the results. This is because the tension is enough to overcome the friction in the system. Moreover, at higher weights, the calculated and measured results are similar that we can assume that the factors such as line drag can be considered negligible when making calculations on the concept.

However, to improve the experiment, the tests need to be repeated with wheels that have been reinforced so that there is no risk of shearing. Moreover, the set of the experiment is set diagonally across the room. With the rig being so heavy, it is hard to easily move it about. Therefore, once the stationary rig was set, it was unable to be shifted so that it ran directly in line to the corner of the pillar where the pulley was situated. It was also be more accurate to have two torque logs running simultaneously into one excel spreadsheet so the loss in torque between the two rings can easily be seen as data would have been recorded at the same time. With regards to photos, it would be better have had them taken directly above the wheels to reduce the error in parallax. Also, the torque shown on the power supply differed from that measured by the torque log. Furthermore, when reading the data, towards higher torques, the increasing by the same increments at the supply, the logs recorded it to be smaller. This suggests that the dial is nonlinear. To solve this, it may be better to have a computer system that set both the speed and torque. When planning the experiment, we expected to test within the range of 500-700N as that is approximately the tensions experienced by the actual kite. To reach these tensions within the experiment, more weight needed to be added to the pulley. It may have been better for the experiment

as a whole if it began at higher tensions, and this was slowly decreased. That way, the rig would be quicker to fail so it would be possible to see the limit of the length of tether quicker.

Appendix B

Summary of Experimental Data

Table B.1: Summary of data collected during the Daisy Kite test campaign.

Date	Rotor	TRPT	Test Length	Comments
1st May 2017	Single Soft	1	04:33	First test with power meter
22nd May 2017	Single Soft	1	03:08	
12th June 2017	Single Soft	1	04:54	
13th June 2017	Single Soft	1	07:54	
18th June 2017	Single Soft	1	02:48	First test with wind data
27th June 2017	Single Soft	1	04:20	
11th July 2017	Dual Soft	1	00:47	First dual rotor test
13th July 2017	Dual Soft	1	04:10	
30th Aug 2017	Dual Soft	1	02:30	
2nd Sept 2017	Dual Soft	1	02:53	
5th Sept 2017	Dual Soft	1	05:13	

Date	Rotor	TRPT	Test Length	Comments
6$^{\text{th}}$ Sept 2017	Dual Soft	1	05:12	
16$^{\text{th}}$ Sept 2017	Dual Soft	2	03:25	
4$^{\text{th}}$ Dec 2017	Triple Soft	2	00:54	First triple rotor test
5$^{\text{th}}$ Jan 2018	Triple Soft	2	00:31	
23$^{\text{rd}}$ Jan 2018	Triple Soft	2	03:28	
18$^{\text{th}}$ Mar 2018	Single Soft	2	03:28	First test with VESC
21$^{\text{st}}$ Mar 2018	Single Soft	2	00:29	
21$^{\text{st}}$ Mar2018	Dual Soft	2	00:04	
30$^{\text{th}}$ Mar 2018	Single Soft	2	00:18	
10$^{\text{th}}$ Apr 2018	Single Soft	2	01:06	
10$^{\text{th}}$ Apr 2018	Dual Soft	2	01:58	
10$^{\text{th}}$ Apr 2018	Triple Soft	2	01:41	
30$^{\text{th}}$ Apr 2018	Triple Soft	2	05:42	
19$^{\text{th}}$ May 2018	Triple Soft	2	04:40	
5$^{\text{th}}$ June 2018	Single Soft	2	09:05	Constant speed
13$^{\text{th}}$ June 2018	Single Soft	2	01:21	Constant speed
17$^{\text{th}}$ Aug 2018	Single Soft	3	00:27	Mast mounted constant speed
22$^{\text{nd}}$ Aug 2018	Single Soft	3	05:37	Mast mounted constant speed
23$^{\text{rd}}$ Aug 2018	Single Rigid	3	04:14	Mast mounted constant speed

Date	Rotor	TRPT	Test Length	Comments
27$^{\text{th}}$ Aug 2018	Single Rigid	3	01:13	Mast mounted
28$^{\text{th}}$ Aug 2018	Single Soft	3	03:09	Mast mounted
31$^{\text{st}}$ Aug 2018	Single Rigid	3	01:12	Mast mounted
20$^{\text{th}}$ Sept 2018	Single Rigid	3	01:10	Mast mounted, 4° blade pitch
13$^{\text{th}}$ Dec 2018	Single Rigid	4	01:32	4° blade pitch
17$^{\text{th}}$ May 2019	Single Rigid	4	03:13	4° blade pitch
17$^{\text{th}}$ May 2019	Dual Rigid	4	00:27	4° blade pitch
5$^{\text{th}}$ June 2019	Single Rigid	4	07:31	4° blade pitch
6$^{\text{th}}$ June 2019	Single Rigid	4	01:24	4° blade pitch
24$^{\text{th}}$ Aug 2019	Single Rigid	4	02:59	4° blade pitch
8$^{\text{th}}$ Sept 2019	Single Rigid	4	00:38	4° blade pitch
29$^{\text{th}}$ Apr 2020	Single Rigid	5	00:10	Mast mounted 6 wing rotor
16$^{\text{th}}$ May 2020	Single Rigid	5	01:12	Mast mounted 6 wing rotor

Appendix C

AeroDyn Input Files for Soft Rotor

```
-----  AeroDyn Driver v1.00.x Input File  --------------------------------------
HQ ram air kite rotor
-----  Input Configuration  ----------------------------------------------------
False          Echo              -  Echo input parameters to "<rootname>.ech"?
"ad_primary_Daisy.inp"    AD_InputFile    -  Name of the primary AeroDyn input file
-----  Turbine Data  -----------------------------------------------------------
        3      NumBlades         - Number of blades (-)
        1.16   HubRad            - Hub radius (m)
        4.5    HubHt             - Hub height (m)
        0      Overhang          - Overhang (m)
        25     ShftTilt          - Shaft tilt (deg)
        0      Precone           - Blade precone (deg)
-----  I/O Settings  -----------------------------------------------------------
"AeroDyn"      OutFileRoot       - Root name for any output files (use "" for .dvr rootname) (-)
True           TabDel            - When generating formatted output (OutForm=True), make output
tab-delimited (fixed-width otherwise) (flag)
"ES10.3E2"     OutFmt            - Format used for text tabular output, excluding the time channel.
Resulting field should be 10 characters. (quoted string)
True           Beep              - Beep on exit (flag)
-----  Combined-Case Analysis  -------------------------------------------------
    1          NumCases          - Number of cases to run
WndSpeed       ShearExp    RotSpd       Pitch       Yaw         dT          Tmax
(m/s)          (-)         (rpm)        (deg)       (deg)       (s)         (s)
8.000000E+00 2.000000E-01 1.250000E+02 0.000000E+00 0.000000E+00 2.500000E-02 1.000000E+01
```

```
------- AERODYN v15.04.* BLADE DEFINITION INPUT FILE -------------------------------------
Blade file for HQ ram air kites
======  Blade Properties =================================================================
    41              NumBlNds             - Number of blade nodes used in the analysis (-)
  BlSpn      BlCrvAC    BlSwpAC    BlCrvAng   BlTwist    BlChord    BlAFID
  (m)        (m)        (m)        (deg)      (deg)      (m)        (-)
  0.0000     0.0        0.0        0.0        0.000      0.160      1
  0.0318     0.0        0.0        0.0        0.000      0.181      1
  0.0635     0.0        0.0        0.0        0.000      0.201      1
  0.0953     0.0        0.0        0.0        0.000      0.222      1
  0.1270     0.0        0.0        0.0        0.000      0.242      1
  0.1588     0.0        0.0        0.0        0.000      0.263      1
  0.1905     0.0        0.0        0.0        0.000      0.283      1
  0.2223     0.0        0.0        0.0        0.000      0.304      1
  0.2540     0.0        0.0        0.0        0.000      0.324      1
  0.2858     0.0        0.0        0.0        0.000      0.345      1
  0.3175     0.0        0.0        0.0        0.000      0.365      1
  0.3493     0.0        0.0        0.0        0.000      0.386      1
  0.3810     0.0        0.0        0.0        0.000      0.406      1
  0.4128     0.0        0.0        0.0        0.000      0.427      1
  0.4445     0.0        0.0        0.0        0.000      0.447      1
  0.4763     0.0        0.0        0.0        0.000      0.468      1
  0.5080     0.0        0.0        0.0        0.000      0.488      1
  0.5398     0.0        0.0        0.0        0.000      0.509      1
  0.5715     0.0        0.0        0.0        0.000      0.529      1
  0.6033     0.0        0.0        0.0        0.000      0.550      1
  0.6350     0.0        0.0        0.0        0.000      0.570      1
  0.6668     0.0        0.0        0.0        0.000      0.550      1
  0.6985     0.0        0.0        0.0        0.000      0.529      1
  0.7303     0.0        0.0        0.0        0.000      0.509      1
  0.7620     0.0        0.0        0.0        0.000      0.488      1
  0.7938     0.0        0.0        0.0        0.000      0.468      1
  0.8255     0.0        0.0        0.0        0.000      0.447      1
  0.8573     0.0        0.0        0.0        0.000      0.427      1
  0.8890     0.0        0.0        0.0        0.000      0.406      1
  0.9208     0.0        0.0        0.0        0.000      0.386      1
  0.9525     0.0        0.0        0.0        0.000      0.365      1
  0.9843     0.0        0.0        0.0        0.000      0.345      1
  1.0160     0.0        0.0        0.0        0.000      0.324      1
  1.0478     0.0        0.0        0.0        0.000      0.304      1
  1.0795     0.0        0.0        0.0        0.000      0.283      1
  1.1113     0.0        0.0        0.0        0.000      0.263      1
  1.1430     0.0        0.0        0.0        0.000      0.242      1
  1.1748     0.0        0.0        0.0        0.000      0.222      1
  1.2065     0.0        0.0        0.0        0.000      0.201      1
  1.2383     0.0        0.0        0.0        0.000      0.181      1
  1.2700     0.0        0.0        0.0        0.000      0.160      1
```

```
!------------------------ AIRFOIL INPUT FILE ------------------------------------
! "Prediction of Aerodynamic Characteristics of Ram-Air Parachutes, M. Ghoreyshi et al. 2016"
! "Clark Y-M15 Aerofoil, Re = 0.2 million for AoA 0 - 30, extrapolated using NRELs AerofoilPrep"
! -------------------------------------------------------------------------------
"Default"     InterpOrd        ! Interpolation order to use for quasi-steady table lookup
{1=linear; 3=cubic spline; "default"} [default=3]
! -------------------------------------------------------------------------------
          1   NonDimArea       ! The non-dimensional area of the airfoil (area/chord^2) (set to
1.0 if unsure or unneeded)
          0   NumCoords        ! The number of coordinates in the airfoil shape file (including an
extra coordinate for airfoil reference).  Set to zero if coordinates…
! ......... x-y coordinates are next if NumCoords > 0 .............
! x-y coordinate of airfoil reference
!   x/c         y/c
! -------------------------------------------------------------------------------
          1   NumTabs          ! Number of airfoil tables in this file.  Each table must have
lines for Re and Ctrl.
! -------------------------------------------------------------------------------
! data for table 1
! -------------------------------------------------------------------------------
        0.2   Re               ! Reynolds number in millions
          0   Ctrl             ! Control setting (must be 0 for current AirfoilInfo)
True          InclUAdata       ! Is unsteady aerodynamics data included in this table? If TRUE,
then include 30 UA coefficients below this line
!....................................... "Taken from example file, only used if AFAeroMod = 2"
       -2.5   alpha0           ! 0-lift angle of attack, depends on airfoil.
         30   alpha1           ! Angle of attack at f=0.7, (approximately the stall angle) for
AOA>alpha0. (deg)
        -30   alpha2           ! Angle of attack at f=0.7, (approximately the stall angle) for
AOA<alpha0. (deg)
          1   eta_e            ! Recovery factor in the range [0.85 - 0.95] used only for UAMOD=1,
it is set to 1 in the code when flookup=True. (-)
     2.1211   C_nalpha         ! Slope of the 2D normal force coefficient curve. (1/rad)
  "Default"   T_f0             ! Initial value of the time constant associated with Df in the
expression of Df and f''. [default = 3]
  "Default"   T_V0             ! Initial value of the time constant associated with the vortex
lift decay process; it is used in the expression of Cvn. It depends on…
  "Default"   T_p              ! Boundary-layer,leading edge pressure gradient time constant in
the expression of Dp. It should be tuned based on airfoil experimental…
  "Default"   T_VL             ! Initial value of the time constant associated with the vortex
advection process; it represents the non-dimensional time in semi-…
  "Default"   b1               ! Constant in the expression of phi_alpha^c and phi_q^c.  This
value is relatively insensitive for thin airfoils, but may be different…
  "Default"   b2               ! Constant in the expression of phi_alpha^c and phi_q^c.  This
value is relatively insensitive for thin airfoils, but may be different…
  "Default"   b5               ! Constant in the expression of K'''_q,Cm_q^nc, and k_m,q.  [from
experimental results, defaults to 5]
  "Default"   A1               ! Constant in the expression of phi_alpha^c and phi_q^c.  This
value is relatively insensitive for thin airfoils, but may be different…
  "Default"   A2               ! Constant in the expression of phi_alpha^c and phi_q^c.  This
value is relatively insensitive for thin airfoils, but may be different…
  "Default"   A5               ! Constant in the expression of K'''_q,Cm_q^nc, and k_m,q. [from
experimental results, defaults to 1]
          0   S1               ! Constant in the f curve best-fit for alpha0<=AOA<=alpha1; by
definition it depends on the airfoil. [ignored if UAMod<>1]
          0   S2               ! Constant in the f curve best-fit for        AOA> alpha1; by
definition it depends on the airfoil. [ignored if UAMod<>1]
          0   S3               ! Constant in the f curve best-fit for alpha2<=AOA< alpha0; by
definition it depends on the airfoil. [ignored if UAMod<>1]
          0   S4               ! Constant in the f curve best-fit for        AOA< alpha2; by
definition it depends on the airfoil. [ignored if UAMod<>1]
     1.3492   Cn1              ! Critical value of C0n at leading edge separation. It should be
extracted from airfoil data at a given Mach and Reynolds number. It…
```

```
  -1.0600   Cn2                ! As Cn1 for negative AOAs.
 "Default"   St_sh             ! Strouhal's shedding frequency constant.  [default = 0.19]
    0.0404   Cd0               ! 2D drag coefficient value at 0-lift.
   -0.0328   Cm0               ! 2D pitching moment coefficient about 1/4-chord location, at
0-lift, positive if nose up. [If the aerodynamics coefficients table does…
         0   k0                ! Constant in the \hat(x)_cp curve best-fit; = (\hat(x)_AC-0.25).
[ignored if UAMod<>1]
         0   k1                ! Constant in the \hat(x)_cp curve best-fit.  [ignored if UAMod<>1]
         0   k2                ! Constant in the \hat(x)_cp curve best-fit.  [ignored if UAMod<>1]
         0   k3                ! Constant in the \hat(x)_cp curve best-fit.  [ignored if UAMod<>1]
         0   k1_hat            ! Constant in the expression of Cc due to leading edge vortex
effects.  [ignored if UAMod<>1]
 "Default"   x_cp_bar          ! Constant in the expression of \hat(x)_cp^v. [ignored if UAMod<>1,
default = 0.2]
 "Default"   UACutout          ! Angle of attack above which unsteady aerodynamics are disabled
(deg). [Specifying the string "Default" sets UACutout to 45 degrees]
 "Default"   filtCutOff        ! Cut-off frequency (-3 dB corner frequency) for low-pass filtering
the AoA input to UA, as well as the 1st and 2nd derivatives (Hz)…
!......................................
! Table of aerodynamics coefficients
        46   NumAlf            ! Number of data lines in the following table
!Alpha  Cl        Cd        Cm
!(deg)  (-)       (-)       (-)
-180    0.0000    0.3162    0.0000
-170    0.2834    0.3566    0.4000
-160    0.5668    0.4726    0.4489
-150    0.8501    0.6488    0.5303
-140    0.7577    0.8620    0.4788
-130    0.6592    1.0835    0.4653
-120    0.5308    1.2831    0.4589
-110    0.3703    1.4327    0.4456
-100    0.1876    1.5097    0.4185
-90     0.0000    1.5000    0.3750
-80     -0.1876   1.5097    0.3412
-70     -0.3703   1.4327    0.2909
-60     -0.5308   1.2831    0.2294
-50     -0.6592   1.0835    0.1616
-40     -0.7577   0.8620    0.0885
-30     -0.8501   0.6488    0.0000
-20     -0.4878   0.4460    -0.0895
-10     -0.1255   0.2432    -0.0943
0       0.2368    0.0404    0.0000
2       0.3064    0.0495    0.0000
4       0.3868    0.0602    0.0000
6       0.4564    0.0699    0.0000
8       0.5295    0.0902    0.0000
10      0.6064    0.1004    0.0000
12      0.6759    0.1214    0.0000
14      0.7345    0.1456    0.0000
16      0.7932    0.1718    0.0000
18      0.8518    0.2201    0.0000
20      0.9177    0.2675    0.0000
25      1.0843    0.4306    0.0000
30      1.2145    0.6488    0.0000
40      1.0825    0.8620    -0.1079
50      0.9418    1.0835    -0.1850
60      0.7582    1.2831    -0.2484
70      0.5290    1.4327    -0.3016
80      0.2680    1.5097    -0.3443
90      0.0000    1.5000    -0.3750
100     -0.1876   1.5097    -0.4185
110     -0.3703   1.4327    -0.4456
120     -0.5308   1.2831    -0.4589
```

261

```
130    -0.6592  1.0835  -0.4653
140    -0.7577  0.8620  -0.4788
150    -0.8501  0.6488  -0.5303
160    -0.5668  0.4726  -0.4489
170    -0.2834  0.3566  -0.5000
180     0.0000  0.3162   0.0000
```

```
------- AERODYN  INPUT FILE -----------------------------------------
Input for 3 blades HQ ram air kite Daisy Kite rotor
======  General Options
===============================================================================
False         Echo              - Echo the input to "<rootname>.AD.ech"?  (flag)
"Default"     DTAero            - Time interval for aerodynamic calculations {or "default"} (s)
        1     WakeMod           - Type of wake/induction model (switch) {0=none, 1=BEMT}
        2     AFAeroMod         - Type of blade airfoil aerodynamics model (switch) {1=steady
model, 2=Beddoes-Leishman unsteady model} [must be 1 when linearizing]
        0     TwrPotent         - Type tower influence on wind based on potential flow around the
tower (switch) {0=none, 1=baseline potential flow, 2=potential flow…
False         TwrShadow         - Calculate tower influence on wind based on downstream tower
shadow? (flag)
False         TwrAero           - Calculate tower aerodynamic loads? (flag)
False         FrozenWake        - Assume frozen wake during linearization? (flag) [used only when
WakeMod=1 and when linearizing]
False         CavitCheck        - Perform cavitation check? (flag)
======  Environmental Conditions
===============================================================================
     1.225    AirDens           - Air density (kg/m^3)
  1.467E-05   KinVisc           - Kinematic air viscosity (m^2/s)
       340.3  SpdSound          - Speed of sound (m/s)
     101325   Patm              - Atmospheric pressure (Pa) [used only when CavitCheck=True]
       2000   Pvap              - Vapour pressure of fluid (Pa) [used only when CavitCheck=True]
        0.6   FluidDepth        - Water depth above mid-hub height (m) [used only when
CavitCheck=True]
======  Blade-Element/Momentum Theory Options
==================================================== [used only when WakeMod=1]
        2     SkewMod           - Type of skewed-wake correction model (switch) {1=uncoupled,
2=Pitt/Peters, 3=coupled} [used only when WakeMod=1]
True          TipLoss           - Use the Prandtl tip-loss model? (flag) [used only when
WakeMod=1]
True          HubLoss           - Use the Prandtl hub-loss model? (flag) [used only when
WakeMod=1]
True          TanInd            - Include tangential induction in BEMT calculations? (flag) [used
only when WakeMod=1]
True          AIDrag            - Include the drag term in the axial-induction calculation? (flag)
[used only when WakeMod=1]
True          TIDrag            - Include the drag term in the tangential-induction calculation?
(flag) [used only when WakeMod=1 and TanInd=TRUE]
     5E-05    IndToler          - Convergence tolerance for BEMT nonlinear solve residual equation
{or "default"} (-) [used only when WakeMod=1]
        100   MaxIter           - Maximum number of iteration steps (-) [used only when WakeMod=1]
======  Beddoes-Leishman Unsteady Airfoil Aerodynamics Options
=================================== [used only when AFAeroMod=2]
        2     UAMod             - Unsteady Aero Model Switch (switch) {1=Baseline model
(Original), 2=Gonzalez's variant (changes in Cn,Cc,Cm), 3=Minemma/Pierce…
True          FLookup           - Flag to indicate whether a lookup for f' will be calculated
(TRUE) or whether best-fit exponential equations will be used (FALSE);…
======  Airfoil Information
===============================================================================
        1     InCol_Alfa        - The column in the airfoil tables that contains the angle of
attack (-)
        2     InCol_Cl          - The column in the airfoil tables that contains the lift
coefficient (-)
        3     InCol_Cd          - The column in the airfoil tables that contains the drag
coefficient (-)
        4     InCol_Cm          - The column in the airfoil tables that contains the
pitching-moment coefficient; use zero if there is no Cm column (-)
        0     InCol_Cpmin       - The column in the airfoil tables that contains the Cpmin
coefficient; use zero if there is no Cpmin column (-)
        1     NumAFfiles        - Number of airfoil files used (-)
"ad_airfoil_Daisy_v3.inp"    AFNames          - Airfoil file names (NumAFfiles lines) (quoted
```

```
strings)
======  Rotor/Blade Properties
===================================================================
True          UseBlCm           - Include aerodynamic pitching moment in calculations?  (flag)
"ad_blade_Daisy.inp"    ADBlFile(1)        - Name of file containing distributed aerodynamic
properties for Blade #1 (-)
"ad_blade_Daisy.inp"    ADBlFile(2)        - Name of file containing distributed aerodynamic
properties for Blade #2 (-) [unused if NumBl < 2]
"ad_blade_Daisy.inp"    ADBlFile(3)        - Name of file containing distributed aerodynamic
properties for Blade #3 (-) [unused if NumBl < 3]
======  Tower Influence and Aerodynamics
========================================================== [used only when TwrInflnc/=0, or
TwrAero=True]
          5   NumTwrNds          - Number of tower nodes used in the analysis  (-) [used only when
TwrInflnc/=0, or TwrAero=True]
TwrElev       TwrDiam       TwrCd
(m)           (m)           (-)
0.0000000E+00  6.0000000E+00  0.0000000E+00
2.0000000E+01  5.5000000E+00  0.0000000E+00
4.0000000E+01  5.0000000E+00  0.0000000E+00
6.0000000E+01  4.5000000E+00  0.0000000E+00
8.0000000E+01  4.0000000E+00  0.0000000E+00
======  Outputs
===============================================================================
False         SumPrint          - Generate a summary file listing input options and interpolated
properties to "<rootname>.AD.sum"?  (flag)
          0   NBlOuts           - Number of blade node outputs [0 - 9] (-)
          0   BlOutNd           - Blade nodes whose values will be output  (-)
          0   NTwOuts           - Number of tower node outputs [0 - 9]  (-)
          0   TwOutNd           - Tower nodes whose values will be output  (-)
              OutList           - The next line(s) contains a list of output parameters.  See
OutListParameters.xlsx for a listing of available output channels, (-)
"RtSpeed, RtAeroPwr, RtAeroFxh, RtAeroMxh, B1Azimuth, RtAeroCp, RtAeroCq, RtAeroCt, RtArea, RtTSR,
B1N1Cl, B1N1Cd, B1N1Alpha"

END of input file (the word "END" must appear in the first 3 columns of this last OutList line)
------------------------------------------------------------------------------------
```

Bibliography

[1] G. Pocock, *The Aeropleustic Art or Navigation in the Air by the use of Kites, or Bouyant Sails*. London, UK: W. Wilson, 1827.

[2] R. H. Luchsinger, D. Aregger, F. Bezard, D. Costa, C. Galliot, F. Gohl, G. Hanna, J. Heilmann, S. Hessberger, and C. Houle, "Twingtec's roadmap from full proof of concept to the first commercial product," in *8th International Airborne Wind Energy Conference (AWEC2019)*, R. Schmehl and O. Tulloch, Eds. Delft University of Technology and University of Strathclyde, 2019, pp. 103–107, https://doi.org/10.4233/uuid:57fd203c-e069-11e9-9fcb-441ea15f7c9c.

[3] R. Schmehl. Airborne wind energy - an introduction to an emerging technology. http://www.awesco.eu/awe-explained [Accessed: 27 April 2020].

[4] R. Schmehl and O. Tulloch, Eds., *8th International Airborne Wind Energy Conference (AWEC2019)*. Delft University of Technology and University of Strathclyde, 2019, https://doi.org/10.4233/UUID:57FD203C-E069-11E9-9FCB-441EA15F7C9C.

[5] Ampyx Power. Airborne wind energy ampyx power is developing airborne wind energy systems (AWES). https://www.ampyxpower.com [Accessed: 10 Jan 2020].

[6] G. Helgason. The Focke Achgelis FA330 Bachstelze (Wagtail). http://www.uboat.net/technical/bachstelze.htm [Accessed: 24 May 2017].

[7] P. Benhaïem and R. Schmehl, "Airborne wind energy conversion using a rotating reel system," in *Airborne Wind Energy: Advances in Technology Development and*

Research, R. Schmehl, Ed. Singapore: Springer Singapore, 2018, pp. 539–577, https://doi.org/10.1007/978-981-10-1947-0_22.

[8] C. Beaupoil, "Practical experiences with a torsion based rigid blade rotary airborne wind energy system with ground based power generation," in *8th International Airborne Wind Energy Conference (AWEC2019)*, R. Schmehl and O. Tulloch, Eds. Delft University of Technology and University of Strathclyde, 2019, pp. 146–167, http://resolver.tudelft.nl/uuid:c50f7eb6-f116-4158-9e9b-aa1b05092ab2.

[9] Some Airborne Wind Energy. https://www.someawe.org [Accessed: 25 Feb 2019].

[10] M. Diehl, R. Leuthold, and R. Schmehl, Eds., *The 7th International Airborne Wind Energy Conference 2017: Book of Abstracts*, 2017, https://doi.org/10.4233/uuid:4c361ef1-d2d2-4d14-9868-16541f60edc7.

[11] Bladetips Energy. http://bladetipsenergy.com/en/home [Accessed: 25 Feb 2019].

[12] D. Selsam. Selsam - innovation in alternative energy. http://www.selsam.com [Accessed: 4 Dec 2017].

[13] Sky WindPower. https://www.skywindpower.com [Accessed: 27 March 2019].

[14] R. Harburg, "Coaxial multi-turbine generator," US patent US5 040 948A, 1990.

[15] M. Ghoreyshi, K. Bergeron, J. Seidel, A. Jirasek, A. J. Lofthouse, and R. M. Cummings, "Prediction of aerodynamic characteristics of ram-air parachutes." *Journal of Aircraft*, vol. 53, no. 6, p. 1802, 2016, https://doi.org/10.2514/1.C033763.

[16] C. Ostowari and D. Naik, "Post-stall wind tunnel data for NACA 44xx series airfoil sections," Texas A and M Univ., College Station (USA). Dept. of Aerospace Engineering, Tech. Rep., 1985, https://doi.org/10.2172/5791328.

[17] NACA 4412 (naca4412-il) Xfoil prediction polar at RE=200,000 Ncrit=5. http://airfoiltools.com/polar/details?polar=xf-naca4412-il-200000-n5 [Accessed: 4 April 2020].

[18] Varun, I. Bhat, and R. Prakash, "LCA of renewable energy for electricity generation systems—a review," *Renewable and Sustainable Energy Reviews*, vol. 13, no. 5, pp. 1067 – 1073, 2009, https://doi.org/10.1016/j.rser.2008.08.004.

[19] A. Cherubini. Fundamentals of airborne wind energy a course for engineering students and researchers. http://www.antonellocherubini.com/awe-course.html [Accessed: 6 April 2018].

[20] G. M. Masters, *Renewable and Efficient Electric Power Systems.* Hoboken, NJ, USA: John Wiley & Sons, Inc., 2005.

[21] D. Yinke, *Ancient Chinese Inventions.* Cambridge, UK: Cambridge University Press, 2011.

[22] Oxford University Press. English Oxford Dictionaries Definitions. www.en.oxforddictionaries.com [Accessed: 24 May 2017].

[23] G. Webster. (2003) Kite for a Purpose (The Golden Age of Kites?). http://www.thekitesociety.org.uk/PDF/Golden%20Years.PDF [Accessed: 6 Jan 2019].

[24] M. Diehl, "Airborne wind energy: Basic concepts and physical foundations," in *Airborne Wind Energy*, U. Ahrens, M. Diehl, and R. Schmehl, Eds. Berlin, Heidelberg: Springer Berlin Heidelberg, 2013, pp. 3–22, https://doi.org/10.1007/978-3-642-39965-7_1.

[25] International Energy Agency. Data and statistics. https://www.iea.org/data-and-statistics/data-tables [Accessed: 8 Jan 2020].

[26] X. Lu, M. B. McElroy, and J. Kiviluoma, "Global potential for wind-generated electricity," *Proceedings of the National Academy of Sciences of the United States of America*, vol. 106, pp. 10 933–10 938, 2009, https://doi.org/10.1073/pnas.0904101106.

[27] C. de Castro, M. Mediavilla, L. J. Miguel, and F. Frechoso, "Global wind power potential: Physical and technological limits," *Energy Policy*, vol. 39, no. 10, pp. 6677–6682, 2011, https://doi.org/10.1016/j.enpol.2011.06.027.

[28] T. Burton, *Wind Energy Handbook*, 2nd ed. Chichester, West Sussex: Wiley, 2011, https://doi.org/10.1002/9781119992714.

[29] C. L. Archer and K. Caldeira, "Global assessment of high-altitude wind power," *Energies*, vol. 2, no. 2, pp. 307–319, 2009, https://doi.org/10.3390/en20200307.

[30] K. Marvel, B. Kravitz, and K. Caldeira, "Geophysical limits to global wind power," *Nature Climate Change*, vol. 3, no. 2, pp. 118–121, 2013, https://doi.org/10.1038/nclimate1683.

[31] P. Bechtle, M. Schelbergen, R. Schmehl, U. Zillmann, and S. Watson, "Airborne wind energy resource analysis," *Renewable Energy*, vol. 141, pp. 1103 – 1116, 2019, https://doi.org/10.1016/j.renene.2019.03.118.

[32] UK Government Department for Business, Energy and Industrial Strategy, "Contracts for difference allocation round 3 results," 2019, https://assets.publishing.service.gov.uk/government/uploads/system/uploads/attachment_data/file/838914/cfd-ar3-results-corrected-111019.pdf [Accessed: 21 March 2021].

[33] S. Mann, "An introduction to airborne wind technology and cost reduction trends," 2019, https://ore.catapult.org.uk/analysisinsight/an-introduction-to-airborne-wind/ [Accessed: 21 March 2021].

[34] S. Wilhelm, "Life cycle assessment of electricity production from airborne wind energy," in *Airborne Wind Energy: Advances in Technology Development and Research*, R. Schmehl, Ed. Singapore: Springer Singapore, 2018, pp. 727–750, https://doi.org/10.1007/978-981-10-1947-0_30.

[35] F. Bauer. Which energy technology has the lowest CO2-footprint? https://www.medium.com/kitekraft/which-energy-technology-has-the-lowest-co2-footprint-8dd55ba590a3 [Accessed: 29 Dec 2019].

[36] UK Government Department for Business, Energy and Industrial Strategy, "Contracts for difference allocation round one outcome," 2 2015, https://assets.publishing.service.gov.uk/government/uploads/system/uploads/attachment_data/file/407059/Contracts_for_Difference_-_Auction_Results_-_Official_Statistics.pdf [Accessed: 21 March 2021].

[37] Renewable Energy Policy Network for the 21st Century, *Renewables 2019 Global Status Report.* Paris, France: Paris: REN21 Secretariat, 2019, https://www.ren21.net/wp-content/uploads/2019/05/gsr_2019_full_report_en.pdf [Accessed: 21 March 2021].

[38] R. Schmehl, Ed., *Airborne Wind Energy: Advances in Technology Development and Research.* Springer, 2018, https://doi.org/10.1007/978-981-10-1947-0.

[39] A. Cherubini, A. Papini, R. Vertechy, and M. Fontana, "Airborne wind energy systems: A review of the technologies," *Renewable and Sustainable Energy Reviews*, vol. 51, p. 1461, 2015, https://doi.org/10.1016/j.rser.2015.07.053.

[40] L. Fagiano and M. Milanese, "Airborne wind energy: An overview," in *2012 American Control Conference (ACC)*, 2012, pp. 3132–3143, https://doi.org/10.1109/ACC.2012.6314801.

[41] E. Lunney, M. Ban, N. Duic, and A. Foley, "A state-of-the-art review and feasibility analysis of high altitude wind power in Northern Ireland," *Renewable and Sustainable Energy Reviews*, vol. 68, pp. 899–911, 2017, https://doi.org/10.1016/j.rser.2016.08.014.

[42] Enerkite. https://www.enerkite.de [Accessed: 10 Jan 2020].

[43] M. Ippolito. Kitegen carousel. http://www.kitegen.com/en/products/kite-gen-carousel [Accessed: 21 March 2021].

[44] kiteKRAFT. http://www.kitekraft.de [Accessed: 10 Jan 2020].

[45] kitepower. https://www.kitepower.nl [Accessed: 10 Jan 2020].

[46] W. J. Ockels, "Laddermill, a novel concept to exploit the energy in the airspace," *Aircraft Design*, vol. 4, no. 2, pp. 81 – 97, 2001, https://doi.org/10.1016/S1369-8869(01)00002-7.

[47] Kiteswarms. https://www.kiteswarms.com [Accessed: 10 Jan 2020].

[48] Altaeros. http://www.altaeros.com/index.html [Accessed: 10 Jan 2020].

[49] Windlift. https://www.windlift.com/ [Accessed: 16 Jan 2021].

[50] SkySails Power. https://www.skysails-power.com [Accessed: 16 Jan 2021].

[51] F. Fritz, "Application of an automated kite system for ship propulsion and power generation," in *Airborne Wind Energy*, U. Ahrens, M. Diehl, and R. Schmehl, Eds. Springer, 2013, pp. 359–372, https://doi.org/10.1007/978-3-642-39965-7_20.

[52] Windswept & Interesting Ltd. https://www.windswept-and-interesting.co.uk/ [Accessed: 10 Jan 2020].

[53] U. Ahrens, M. Diehl, and R. Schmehl, Eds., *Airborne Wind Energy*, ser. Green Energy and Technology. Springer, 2013, https://doi.org/10.1007/978-3-642-39965-7.

[54] M. L. Loyd, "Crosswind kite power (for large-scale wind power production)," *Journal of Energy*, vol. 4, no. 3, pp. 106–111, 1980, https://doi.org/10.2514/3.48021.

[55] Makani kites: airbrone wind energy. https://www.x.company/projects/makani/ [Accessed: 21 March 2020].

[56] Kite Power Systems. Kitemill buys KPS. http://www.kps.energy [Accessed: 23 March 2020].

[57] I. Argatov, P. Rautakorpi, and R. Silvennoinen, "Estimation of the mechanical energy output of the kite wind generator," *Renewable Energy*, vol. 34, no. 6, pp. 1525–1532, 2009, https://doi.org/10.1016/j.renene.2008.11.001.

[58] B. Houska and M. Diehl, "Optimal control of towing kites," *Proceedings of the IEEE Conference on Decision and Control*, pp. 2693–2697, 2006, https://doi.org/10.1109/CDC.2006.377210.

[59] S. Dunker, "Tether and bridle line drag in airborne wind energy applications," in *Airborne Wind Energy: Advances in Technology Development and Research*, R. Schmehl, Ed. Singapore: Springer Singapore, 2018, pp. 29–56, https://doi.org/10.1007/978-981-10-1947-0_2.

[60] A. Cherubini, "Advances in Airborne Wind Energy and Wind Drones," Ph.D. dissertation, Scuola Superiore Sant'Anna, Pisa, Italy, 2017, https://www.antonellocherubini.com/uploads/4/5/7/1/45719075/cherubini_phd _thesis_small.pdf [Accessed: 21 March 2021].

[61] M. Zanon, S. Gros, J. Andersson, and M. Diehl, "Airborne wind energy based on dual airfoils," *IEEE Transactions on Control Systems Technology*, vol. 21, no. 4, pp. 1215–1222, July 2013, https://doi.org/10.1109/TCST.2013.2257781.

[62] J. De Schutter, R. Leuthold, T. Bronnenmeyer, R. Paelinck, and M. Diehl, "Optimal control of stacked multi-kite systems for utility-scale airborne wind energy," in *2019 IEEE 58th Conference on Decision and Control (CDC)*. IEEE, 2019, pp. 4865–4870, https://doi.org/10.1109/CDC40024.2019.9030026.

[63] G. Saul, L. Peter, M. Don, and H. Corwin, "Faired tether for wind power generation systems," US patent US20 090 289 148A1, 2009-11-26.

[64] B. Tigner, "Multi-tether cross-wind kite power," US patent US8 066 225B1, 2011-11-29.

[65] P. R. Payne and C. Mccutchen, "Self-erecting windmill," US patent US3 987 987A, 1976-10-26.

[66] T. Ansboro, "Kite," US patent US464 412A, 1891-12-01.

[67] A. R. S. Bramwell, G. Done, and D. Blamford, *Bramwell's Helicopter Dynamics*. Oxford, UK: Butterworth-Heinemann, 2001.

[68] H. Glauert, "A general theory of the autogyro. R. & M. no. 1111," *British ARC*, 1926.

[69] P. U. Poulsen, "Windmill," US patent US4 242 043A, 1980-12-30.

[70] C. M. Fry and H. W. Hise, "Wind driven, high altitude power apparatus," US patent 4 084 102A, 1978-04-11.

[71] C. A. J. Fletcher and B. W. Roberts, "Electricity generation from jet-stream winds," *Journal of Energy*, vol. 3, no. 4, pp. 241–249, 1979, https://doi.org/10.2514/3.48003.

[72] B. W. Roberts, "Quad-rotorcraft to harness high-altitude wind energy," in *Airborne Wind Energy: Advances in Technology Development and Research*, R. Schmehl, Ed. Singapore: Springer Singapore, 2018, pp. 581–601, https://doi.org/10.1007/978-981-10-1947-0_23.

[73] J. D. Schutter, R. Leuthold, and M. Diehl, "Optimal control of a rigid-wing rotary kite system for airborne wind energy," in *2018 European Control Conference (ECC)*, 2018, pp. 1734–1739, https://doi.org/10.23919/ECC.2018.8550383.

[74] A. W. Stahl, *Transmission of Power by Wire Ropes*. D. Van Nostrand New York, 1877.

[75] J. J. Flather, *Rope-Driving: A treatise on the transmission of power by means of fibrous ropes*. J. Wiley & Sons, 1895.

[76] R. Read and O. Tulloch, "Practical experimentation on rotary network AWES," in *8th International Airborne Wind Energy Conference (AWEC2019)*, R. Schmehl and O. Tulloch, Eds. Delft University of Technology and University of Strathclyde, 2019, p. 121, http://resolver.tudelft.nl/uuid:910395f8-1a3a-4ad0-ba10-d801380f874b.

[77] R. Read, "Kite networks for harvesting wind energy," in *Airborne Wind Energy: Advances in Technology Development and Research*, R. Schmehl, Ed. Singapore: Springer Singapore, 2018, pp. 515–537, https://doi.org/10.1007/978-981-10-1947-0_21.

[78] Kite Winder. https://kitewinder.fr/ [Accessed: 25 Feb 2019].

[79] J. Carroll, A. McDonald, and D. McMillan, "Failure rate, repair time and unscheduled o&m cost analysis of offshore wind turbines," *Wind Energy*, vol. 19, no. 6, pp. 1107–1119, 2016, https://doi.org/10.1002/we.1887.

[80] R. Queen, *Build and Test a 3 Kilowatt Prototype of a Coaxial, Multi-rotor Wind Turbine: Independent Assessment Report*. California Energy Commission, 2007.

[81] A. K. de Souza Mendonça, C. R. Vaz, Á. G. R. Lezana, C. A. Anacleto, and E. P. Paladini, "Comparing patent and scientific literature in airborne wind energy," *Sustainability*, vol. 9, no. 6, p. 915, 2017, https://doi.org/10.3390/su9060915.

[82] A. S. Mcdonald, M. A. Mueller, and H. Polinder, "Structural mass in direct-drive permanent magnet electrical generators," *IET Renewable Power Generation*, vol. 2, no. 1, pp. 3–15, 2008, https://doi.org/10.1049/iet-rpg:20070071.

[83] B. Newman, "Multiple actuator-disc theory for wind turbines," *Journal of Wind Engineering and Industrial Aerodynamics*, vol. 24, no. 3, pp. 215–225, 1986, https://doi.org/10.1016/0167-6105(86)90023-1.

[84] M. Bastankhah and F. Porté-Agel, "Experimental and theoretical study of wind turbine wakes in yawed conditions," *Journal of Fluid Mechanics*, vol. 806, p. 506–541, 2016, https://doi.org/10.1017/jfm.2016.595.

[85] J. Breuer, "Information report kitepower tether failure on Thursday the 30th of May 2019," https://kitepower.nl/wp-content/uploads/2019-05-30_tether_failure_information.pdf [Accessed: 1 May 2020].

[86] R. Read, "Autogyro kite networks with torque transfer to ground-based generators," in *Wind Energy Science Conference 2019*, https://doi.org/10.5281/zenodo.3357444.

[87] Directorate-General for Research and Innovation (European Commission), ECO-RYS, "Study on challenges in the commercialisation of airborne wind energy systems," 2018, https://doi.org/10.2777/87591.

[88] K. Petrick, "Policies for airborne wind energy: Preparing the grounds for AWE specific incentive schemes (scoping study)," 2018, https://doi.org/10.5281/zenodo.2613535.

[89] A. F. de O. Falcão, "Wave energy utilization: A review of the technologies," *Renewable and Sustainable Energy Reviews*, vol. 14, no. 3, pp. 899 – 918, 2010, https://doi.org/10.1016/j.rser.2009.11.003.

[90] L. Fagiano, "Automation challenges in airborne wind energy systems and the role of academic research," in *8th International Airborne Wind Energy Conference (AWEC2019)*, R. Schmehl and O. Tulloch, Eds. Delft University of Technology and University of Strathclyde, 2019, p. 35, http://resolver.tudelft.nl/uuid:f1a524b1-d0db-4fca-bb78-1ccf9612b298.

[91] L. Fagiano and S. Schnez, "On the take-off of airborne wind energy systems based on rigid wings," *Renewable Energy*, vol. 107, pp. 473–488, 2017, https://doi.org/10.1016/j.renene.2017.02.023.

[92] L. Fagiano, E. N. Van, and S. Schnez, "Linear take-off and landing of a rigid aircraft for airborne wind energy extraction," in *Airborne Wind Energy: Advances in Technology Development and Research*, R. Schmehl, Ed. Singapore: Springer Singapore, 2018, pp. 491–514, https://doi.org/10.1007/978-981-10-1947-0_20.

[93] B. Rieck, M. Ranneberg, A. Candade, A. Bormann, and S. Skutnik, "Comparison of launching and landing approaches," in *Book of Abstracts of the Airborne Wind Energy Conference 2017*, M. Diehl, R. Leuthold, and R. Schmehl, Eds.

Freiburg, Germany: Albert Ludwigs University of Freiburg and Delft University of Technology, 2017, p. 123, http://resolver.tudelft.nl/uuid:746d1263-9685-452a-b26b-d26b6a138c65.

[94] D. Y. Leung and Y. Yang, "Wind energy development and its environmental impact: A review," *Renewable and Sustainable Energy Reviews*, vol. 16, no. 1, pp. 1031 – 1039, 2012, https://doi.org/10.1016/j.rser.2011.09.024.

[95] S. Abbasi, Tabassum-Abbasi, and T. Abbasi, "Impact of wind-energy generation on climate: A rising spectre," *Renewable and Sustainable Energy Reviews*, vol. 59, pp. 1591 – 1598, 2016, https://doi.org/10.1016/j.rser.2015.12.262.

[96] L. Bruinzeel, E. Klop, A. Brenninkmeijer, and J. Bosch, "Ecological impact of airborne wind energy technology: Current state of knowledge and future research agenda," in *Airborne Wind Energy: Advances in Technology Development and Research*, R. Schmehl, Ed. Singapore: Springer Singapore, 2018, pp. 679–701, https://doi.org/10.1007/978-981-10-1947-0_28.

[97] G. Vallejo, E. Klop, and J. Bosch, "Avian collision risk modelling: A comparison of methods for airborne wind energy devices," in *8th International Airborne Wind Energy Conference (AWEC2019)*, R. Schmehl and O. Tulloch, Eds. Delft University of Technology and University of Strathclyde, 2019, pp. 58–59, http://resolver.tudelft.nl/uuid:910395f8-1a3a-4ad0-ba10-d801380f874b.

[98] Department for Business Energy and Industrial Strategy, "Renewable energy planning database," https://www.gov.uk/government/collections/renewable-energy-planning-data [Accessed: 21 March 2021].

[99] M. Harper, B. Anderson, P. A. James, and A. S. Bahaj, "Onshore wind and the likelihood of planning acceptance: Learning from a Great Britain context," *Energy Policy*, vol. 128, pp. 954 – 966, 2019, https://doi.org/10.1016/j.enpol.2019.01.002.

[100] S. Watson, A. Moro, V. Reis, C. Baniotopoulos, S. Barth, G. Bartoli, F. Bauer, E. Boelman, D. Bosse, A. Cherubini, A. Croce, L. Fagiano, M. Fontana, A. Gambier, K. Gkoumas, C. Golightly, M. I. Latour, P. Jamieson, J. Kaldellis, A. Mac-

donald, J. Murphy, M. Muskulus, F. Petrini, L. Pigolotti, F. Rasmussen, P. Schild, R. Schmehl, N. Stavridou, J. Tande, N. Taylor, T. Telsnig, and R. Wiser, "Future emerging technologies in the wind power sector: A European perspective," *Renewable and Sustainable Energy Reviews*, vol. 113, p. 109270, 2019, https://doi.org/10.1016/j.rser.2019.109270.

[101] R. Read, "Daisy & AWES networks: Scalable, autonomous AWES with continuous power output," in *7th International Airborne Wind Energy Conference (AWEC2017)*, M. Diehl, R. Leuthold, and R. Schmehl, Eds. Albert Ludwig University Freiburg and Delft University of Technology, pp. 35–37, http://resolver.tudelft.nl/uuid:1c6b790b-79dc-416b-bd07-6887ed45b087.

[102] J. Manwell, J. McGowan, and A. Rogers, *Wind Energy Explained.* Wiley, 2002.

[103] HQ Kites. SYMPHONY BEACH III 1.3 RNBOW. http://hqkitesusa.com/proddetail.asp?prod=11768050 [Accessed: 5 Feb 2019].

[104] Kaixuan kite Official Store. 3 SQM peterlynn one skin kite, lifter, pilot kite from Kaixuan kite factory. https://www.aliexpress.com/item/32601207908.html?gps-id=pcStoreJustForYou&scm=1007.23125.137358.0&scm_id=1007.23125.137358.0&scm-url=1007.23125.137358.0&pvid=9d5c369d-f6a5-4562-aafe-8ac59af57594&spm=a2g0o.store_home.smartJustForYou_819224023.19 [Accessed: 11 Jun 2020].

[105] B. Vedder. VESC project. https://vesc-project.com/ [Accessed: 6 Feb 2019].

[106] Quarq power meters. https://www.quarq.com/dzero/#sm.0001mr3ju1pktd57 qde19rnfjf0fp [Accessed: 21 Nov 2017].

[107] Windfinder. Wind & weather statistics stornoway airport. https://www.windfinder.com/windstatistics/stornoway [Accessed: 23 Nov 2017].

[108] Vector Instruments. A100l2 low power anemometer (analog+pulse outputs). http://www.windspeed.co.uk/ws/index.php?option=displaypage&Itemid=49&op=page [Accessed: 22 June 2020].

[109] J. Breukels and W. Ockels, "Analysis of complex inflatable structures using a multi-body dynamics approach," in *49th AIAA/ASME/ASCE/AHS/ASC Structures, Structural Dynamics, and Materials Conference, 16th AIAA/ASME/AHS Adaptive Structures Conference,10th AIAA Non-Deterministic Approaches Conference, 9th AIAA Gossamer Spacecraft Forum, 4th AIAA Multidisciplinary Design Optimization Specialists Conference*, 2008, p. 2284, https://doi.org/10.2514/6.2008-2284.

[110] S. Rimkus and T. Das, "An application of the autogyro theory to airborne wind energy extraction," in *ASME 2013 Dynamic Systems and Control Conference, DSCC 2013*, vol. 3.   American Society of Mechanical Engineers (ASME), 2013, https://doi.org/10.1115/DSCC2013-3840.

[111] S. Mackertich and T. Das, "A quantitative energy and systems analysis framework for airborne wind energy conversion using autorotation," in *2016 American Control Conference (ACC)*.   American Automatic Control Council (AACC), 2016, pp. 4996–5001, https://doi.org/10.1109/ACC.2016.7526145.

[112] B. Roberts, D. Shepard, K. Caldeira, M. Cannon, D. Eccles, A. Grenier, and J. Freidin, "Harnessing high-altitude wind power," *IEEE Transactions on Energy Conversion*, vol. 22, no. 1, pp. 136–144, 2007, https://doi.org/10.1109/TEC.2006.889603.

[113] A. Betz, *Introduction to the Theory of Flow Machines*.   Oxford: Pergamon, 1966, https://doi.org/10.1016/C2013-0-05426-6.

[114] B. Noura, I. Dobrev, R. Dizene, F. Massouh, and S. Khelladi, "Experimental study of yawed inflow around wind turbine rotor," *Proceedings of the Institution of Mechanical Engineers Part A Journal of Power and Energy*, vol. 226, pp. 664–673, 07 2012, https://doi.org/10.1177/0957650912445015.

[115] M. O. Hansen and H. A. Madsen, "Review paper on wind turbine aerodynamics." *American Society of Mechanical Engineers*, vol. 133, no. 11, p. 114001, 2011, https://doi.org/10.1115/1.4005031.

[116] D. Johnson, M. Gu, and B. Gaunt, "Wind turbine performance in controlled conditions: BEM modeling and comparison with experimental results," *International Journal of Rotating Machinery*, 2016, https://doi.org/10.1155/2016/5460823.

[117] D. Rancourt, F. Bolduc-Teasdale, E. D. Bouchard, M. J. Anderson, and D. N. Mavris, "Design space exploration of gyrocopter-type airborne wind turbines," *Wind Energy*, vol. 19, no. 5, pp. 895–909, 2016, https://doi.org/10.1002/we.1873.

[118] D. Micallef and T. Sant, "A review of wind turbine yaw aerodynamics," in *Wind Turbines*, A. G. Aissaoui and A. Tahour, Eds. Rijeka: IntechOpen, 2016, ch. 2, https://doi.org/10.5772/63445.

[119] F. Castellani, D. Astolfi, F. Natili, and F. Mari, "The yawing behavior of horizontal-axis wind turbines: A numerical and experimental analysis," *Machines*, vol. 7, no. 1, p. 15, 2019, https://doi.org/10.3390/machines7010015.

[120] H. Rahimi, M. Hartvelt, J. Peinke, and J. Schepers, "Investigation of the current yaw engineering models for simulation of wind turbines in BEM and comparison with CFD and experiment," in *Journal of Physics: Conference Series*, vol. 753, no. 2. IOP Publishing, 2016, p. 022016, https://doi.org/10.1088/1742-6596/753/2/022016.

[121] D. Micallef, M. Kloosterman, C. S. Ferreira, T. Sant, G. van Bussel, and D. Micallef, "Comparison and validation of BEM and free wake unsteady panel model with the mexico rotor experiment," in *Proceedings of Euromech*, vol. 508, 2009, http://resolver.tudelft.nl/uuid:33950a07-dbaf-492b-bfec-8833984afd2f.

[122] J. Holierhoek, J. De Vaal, A. Van Zuijlen, and H. Bijl, "Comparing different dynamic stall models," *Wind Energy*, vol. 16, no. 1, pp. 139–158, 2013, https://doi.org/10.1002/we.548.

[123] J. Jonkman. FAST. https://nwtc.nrel.gov/FAST [Accessed: 4 June 2020].

[124] J. M. Jonkman, G. J. Hayman, B. J. Jonkman, and R. R. Damiani, *AeroDyn v15 User's Guide and Theory Manual*, NREL, Denver, Colorado,

https://wind.nrel.gov/nwtc/docs/AeroDyn_Manual.pdf [Accessed: 21 March 2021].

[125] A. Ning, G. Hayman, R. Damiani, and J. M. Jonkman, "Development and validation of a new blade element momentum skewed-wake model within aerodyn," in *33rd Wind Energy Symposium*, 2015, p. 0215, https://doi.org/10.2514/6.2015-0215.

[126] S. Guntur, J. Jonkman, R. Sievers, M. A. Sprague, S. Schreck, and Q. Wang, "A validation and code-to-code verification of FAST for a megawatt-scale wind turbine with aeroelastically tailored blades," *Wind Energy Science*, vol. 2, no. 2, pp. 443–468, 2017, https://doi.org/10.5194/wes-2-443-2017.

[127] S. Ehrich, C. M. Schwarz, H. Rahimi, B. Stoevesandt, and J. Peinke, "Comparison of the blade element momentum theory with computational fluid dynamics for wind turbine simulations in turbulent inflow," *Applied Sciences*, vol. 8, no. 12, p. 2513, 2018, https://doi.org/10.3390/app8122513.

[128] S. Evans, D. Bradney., and P. Clausen, "Development and experimental verification of a 5kW small wind turbine aeroelastic model," *Journal of Wind Engineering and Industrial Aerodynamics*, vol. 181, pp. 104 – 111, 2018, https://doi.org/10.1016/j.jweia.2018.08.011.

[129] C. Hansen. Airfoilprep. https://nwtc.nrel.gov/AirFoilPrep [Accessed: 4 July 2020].

[130] C. L. Archer, "An introduction to meteorology for airborne wind energy," in *Airborne Wind Energy*, U. Ahrens, M. Diehl, and R. Schmehl, Eds. Berlin, Heidelberg: Springer Berlin Heidelberg, 2013, pp. 81–94, https://doi.org/10.1007/978-3-642-39965-7_5.

[131] B. Jonkman and L. Kilcher, "TurbSim user's guide: version 1.06. 00," *National Renewable Energy Laboratory: Golden, CO, USA*, 2012.

[132] IEC, "Wind turbines–part 1: Design requirements, IEC 61400-1," 2005.

[133] W. Bootle, "Forces on an inclined circular cylinder in supercritical flow," *AIAA Journal*, vol. 9, no. 3, pp. 514–516, 1971, https://doi.org/10.2514/3.6213.

[134] A. K. Chopra, *Dynamics of Structures Theory and Applications to Earthquake Engineering.* Prentice Hall, 1995, https://doi.org/10.1007/BF0042698.

[135] DSM, "Dyneema," https://www.dsm.com/products/dyneema/en_GB/home.html [Accessed: 17 Feb 2020].

[136] "Carbon fibre profiles," https://www.carbonfibreprofiles.com/ [Accessed: 17 Feb 2020].

[137] B. Sanborn, A. M. Dileonardi, and T. Weerasooriya, "Tensile properties of dyneema SK76 single fibers at multiple loading rates using a direct gripping method," *Journal of Dynamic Behavior of Materials*, vol. 1, pp. 4–14, 2014, https://doi.org/10.1007/s40870-014-0001-3.